

Table of Contents

Abstract.....	iii
Acknowledgements	iv
List of Figures.....	vii
List of Tables	xiii
Glossary of Abbreviations.....	xiv
1 Introduction.....	1
1.1 Motivation.....	1
1.2 Objectives	2
1.3 Cardiac Anatomy and Function Parameters	2
1.4 Data Acquisition	6
1.5 Construction of Heart Model	11
1.6 CMR Image Segmentation.....	14
1.7 Overview of the Thesis	24
1.8 Achievements in the Thesis	26
2 Automated Detection of the Left Ventricle on 4D CMR Images.....	28
2.1 Introduction.....	28
2.2 Method	30
2.3 Results.....	38
2.4 Discussions	42
2.5 Conclusions.....	45
3 Model-based Graph Cuts Method for Automated Segmentation	46
3.1 Introduction.....	46
3.2 Method	48
3.3 Implementation	52
3.4 Experiment.....	55
3.5 Discussions and Conclusions.....	57
4 Evaluation of Similarity Measures for Atlas-based Rigid-body	
Registration	59
4.1 Similarity Measures	60
4.2 SMPL Atlas-based Registration Framework	64
4.3 Protocol for Evaluation	71
4.4 Implementation	74
4.5 Results.....	83
4.6 Discussion.....	89
4.7 Conclusions.....	92
5 Atlas-based Segmentation of Cardiac MR Images	93
5.1 Introduction.....	93
5.2 Atlas Construction	95
5.3 Free-form Deformation for Non-rigid Registration.....	102
5.4 Energy Function.....	105
5.5 Optimisation.....	106
5.6 Capture Range Analysis.....	109
5.7 Large Dataset Analysis	114

5.8	Discussion and Conclusion	121
6	Modified Atlas-based Segmentation for Cardiac MR Images	125
6.1	Inclusion of High Level Information.....	125
6.2	Integration of the Boundary Term.....	127
6.3	Integration of Area Term.....	133
6.4	Results	135
6.5	Discussion	138
6.6	Conclusions	141
7	Model-based 3D Segmentation.....	142
7.1	Introduction	142
7.2	Feature-based 3D Registration Method.....	146
7.3	Segmentation on Other Short-axis Slices.....	156
7.4	Segmentation of the 4-chamber Long-axis slice	161
7.5	Results	165
7.6	Discussions.....	172
7.7	Conclusions	177
8	Conclusions	178
8.1	Thesis Summary	178
8.2	Further Work	181
9	Publications.....	184
10	References	185

List of Figures

Figure 1.1 Anatomy of heart in frontal and transverse views (adapted from [7])	4
Figure 1.2 ECG, volume change and phases in a cardiac circle (adapted from [7])	5
Figure 1.3 Manual planning of CMR acquisition. (a) definition of the three standard anatomical planes, (b) coronal image and planning for acquisition of an axial stack, (c) axial image and planning for acquisition of a single long axis oblique, (d) planning for acquisition of double oblique long axis scout, (e) planning for acquisition of SA cines and (f) middle SA slice and planning for acquisition of LA cines.	9
Figure 1.4 One SA slice and two LA slices with digitized points; green dots – epicardium, blue dots – RV endocardium and pink dots – LV endocardium.....	12
Figure 1.5 Digitization of two endocardial and one epicardial surfaces; green dots – epicardium, blue dots – RV endocardium and pink dots – LV endocardium.....	13
Figure 1.6 Three surfaces of the constructed model.	14
Figure 1.7 Flow chart showing the contents of each chapter.....	26
Figure 2.1 Flow chart of the LV localization.....	31
Figure 2.2 Manual definition of LV orientation. (a) centre of the LV on an apical SA slice, (b) centre of the LV on a basal SA slice, (c) RV insertion points for defining V_y and (d) right handed coordinate system.	32
Figure 2.3 Temporal analysis of two pixels: (a) image showing a pixel near a moving boarder inside the heart (P_{in}) and a pixel near a stationary boarder (P_{out}), (b) pixel intensity change in the time sequence.....	33
Figure 2.4 Comparison between P_{in} and P_{out} in Figure 2.3 for their magnitude of (a) the first seven frequency components and (b) the DC components.....	33
Figure 2.5 Temporal Fourier Transforms for each pixel in the time sequence: (a) DC (average) image, (b) H1 (first harmonic) image and (c) standard deviation image for comparison to H1 image.	33
Figure 2.6 Gaussian fitting and the cut for the 3D cylindrical ROI.....	35
Figure 2.7 Iterative approximation of the circular ROI for each SA slice of the H1 images (apex to base from left to right and the rows from top to bottom showing results after every 10 more iterations).	35
Figure 2.8 Calculation of the threshold level for LV segmentation; (a) search line shown on the ROI image, (b) intensity for each pixel showing a local minimum for the septum S , (c) intensity gradient for each pixel showing the position of the maximum gradient (max).	36
Figure 2.9 Locating the LV blood pool (a) LV blood pool detected on the middle SA slice by thresholding, (b) convex hull applied to the middle SA slice, (c) projection of the LV blood pool onto an adjacent slice, (d) thresholding and selection of the most similar binary object as the detected LV blood pool, and (e) convex hull applied to the new slice.	37
Figure 2.10 Example of the detected LV blood pool on all SA slices (apex to base from left to right).	38
Figure 2.11 The failure due to the improper ROIs computed from the H1 images: top row – H1 images and the ROIs, bottom row – DC image with ROIs.....	39
Figure 2.12 Distance plots (mm) of automatic V_x relative to Observer A (worst case) on apical, middle and basal SA slices for the ONTARGET dataset (mean and standard	

deviation shown for y and z directions under each plot). Dotted lines show limits of agreement ($\mu \pm 2\sigma$)	40
Figure 2.13 Distance plots (mm) of automatic V_x relative to Observer A (worst case) on apical, middle and basal SA slices for the ZEST dataset (mean and standard deviation shown for y and z directions under each plot).....	41
Figure 2.14 Distance plots (mm) of automatic V_x relative to Observer A (worst case) on apical, middle and basal SA slices for the CINE-SCOUT dataset (mean and standard deviation shown for y and z directions under each plot).....	41
Figure 3.1 Graph structure constructed from a 9-pixels image.....	48
Figure 3.2 Intersection of LV model and middle SA slice.....	52
Figure 3.3 Example of using prior for LV endocardial segmentation.....	53
Figure 3.4 Example of using a prior for LV epicardial segmentation.....	53
Figure 3.5 Results on ES, middle and ED frames of a middle SA slice. (a) initial contours for spatial priors, (b) detected endocardium, (c) detected endocardium and epicardium, (d) ground truth.	56
Figure 3.6 Box plots of the MHD for 9 sets of parameters.....	57
Figure 4.1 Example of sampling in parameter space (3D view): two parameter lines with M sampling points and the ground truth x_0	72
Figure 4.2 (a) 1D Error surface from a parameter line and (b) the negative gradient values on the left side of $x_{n,\max}$ and the positive gradient values on the right side of $x_{n,\max}$	72
Figure 4.3 (a) ED frame of a middle SA slice and (b) its atlas.....	75
Figure 4.4 1D Error surface of a translation-only parameter line of radius 20 pixels from the ground truth.	76
Figure 4.5 Close look at the global maximal area in Figure 4.4. (a)Nearest neighbor, linear, partial intensity interpolations and (b) partial volume interpolation.....	76
Figure 4.6 MI performance using partial volume interpolation on 20 randomly selected parameter lines.	77
Figure 4.7 Performance of each parameter in six measures.....	78
Figure 4.8 ACC performance of six measures with M from 21 to 221.....	80
Figure 4.9 NOM performance of six measures with M from 21 to 211 when $k = 20$ and $k = 80$	81
Figure 4.10 ACC performance of six measures with N from 20 to 600.	82
Figure 4.11 NOM performance of six measures with N from 20 to 600 when $k = 10$ and $k = 40$	82
Figure 4.12 ACC Performance of six measures.....	83
Figure 4.13 Box plot of DOG performances of six measures at different k	84
Figure 4.14 DOG performances of six measures when $k = 10$ and $k = 40$	85
Figure 4.15 Box plot of NOM performance of six measures at different k	86
Figure 4.16 Comparison of NOM performances when $k = 10$ and $k = 40$	87
Figure 4.17 Box plot of RON performance of six measures at different k	88
Figure 4.18 Comparison of RON performances when $k = 10$ and $k = 40$	89
Figure 4.19 Computational cost of each measure in second.....	90
Figure 5.1 (a) model centre and \mathbf{V}'_x defined by the H1 volume, (b) \mathbf{V}'_y defined by the collapsed H1 volume, (c) Initial estimate of the heart model based on the H1 volume.	97
Figure 5.2 Histogram of a middle SA slice with and without initial model. (a) middle SA slice and initial model, (b) histogram of the whole image, (c) histogram inside the model.....	99

Figure 5.3 EM estimation of the histogram in Figure 5.2c. Red curve – histogram, green curve – initial estimation, cyan curve – two estimated Gaussian distribution and pink curve – combined distribution.	100
Figure 5.4 An example used for showing artefact of linear interpolation; (a) middle SA image, green rectangle – region for atlas translation, red dot – ground truth of gravity centre; (b) atlas, red dot – gravity centre.	101
Figure 5.5 Artefact of linear interpolation in error surface; (a) shift one pixel each time, (b) shift half pixel each time.	101
Figure 5.6 Resampling at sub-pixel level: green dots – the pixel centres, red and blue dots – the new locations of the atlas points after sub-pixel resampling.....	102
Figure 5.7 Artefact reduced by sub-pixel sampling in comparison to Figure 5.5.	102
Figure 5.8 Definitions of T_x , T_y and R and examples with single maximal values. (a) $\nabla T_x = +30$, (b) $\nabla T_y = +30$ and (c) $\nabla R = +60$	110
Figure 5.9 An example of the registration process. The initial pose was formed with a large rotation error. 20 loops occur between two neighbouring images.....	111
Figure 5.10 Changes in the energy function and its individual terms from the example shown in Figure 5.9. E – energy function, ES – smoothing term, EI – intensity term including LV term EL , RV term ER and myocardium term EM	111
Figure 5.11 Examples of atlas-based registration results. Top row - starting positions, bottom row – positions after registration. (a) $\nabla T_x = 22$, $\nabla T_y = 10$, $\nabla R = 20$; (b) $\nabla T_x = 10$, $\nabla T_y = -26$, $\nabla R = 20$; (c) $\nabla T_x = 18$, $\nabla T_y = -18$, $\nabla R = -20$; (d) $\nabla T_x = -18$, $\nabla T_y = -6$, $\nabla R = -4$;	112
Figure 5.12 Histogram plot of modified Hausdorff distances (MHD) of 14147 registrations with different starting poses. (a) LV, (b) RV, (c) myocardium.	112
Figure 5.13 Iso-surfaces of MHD at 2 pixels. (a) LV, (b) RV, (c) myocardium.	113
Figure 5.14 Sub-pixel level ground truth data: (a) original image, (b) under-sampling ground truth and (c) ground truth contours after sub-pixel interpolation.	114
Figure 5.15 Multi-grid and multi-resolution strategy applied in the case of Figure 5.20. Top row – before registration, bottom row – after registration. (a) 2x2 mesh, high smoothing, (b) 3x3 mesh, medium smoothing, (c) 4x4 mesh, low smoothing, (d) 5x5 mesh, no smoothing.	117
Figure 5.16 Removal of papillary muscles from LV cavity; (a) SA image with LV contour, (b) binary image after thresholding, (c) binary image after convex hull, (d) potential papillary muscle pixels, (e) image after removing LV papillary muscles... ..	118
Figure 5.17 Removal of papillary muscles from RV cavity; (a) SA image with RV contour, (b) binary image after thresholding, (c) binary image after image filling, (d) potential papillary muscle pixels, (e) image after removing RV papillary muscles... ..	118
Figure 5.18 Two failed cases with large initial errors. (a) ground truth, (b) initial estimation, (c) registration result.	119
Figure 5.19 (a) MHD errors in pixels and (b) SI results of initial contours on the ED frames of middle SA slices for the ONTARGET dataset.....	120
Figure 5.20 The case with the largest RV error. (a) ground truth, (b) initial estimation, (c) registration result.	120
Figure 5.21 Box plot of MHD (unit: pixel) between the ground truth and the detected contours. (a) LV endocardium, (b) RV endocardium and (c) epicardium.....	121
Figure 5.22 Box plot of SI between the ground truth and the detected contours. (a) LV blood pool, (b) RV blood pool and (c) myocardium.	121
Figure 5.23 Box plot of SI with and without papillary muscle removal process. (a) LV blood pool, (b) RV blood pool and (c) myocardium.	123
Figure 5.24 A small epicardial contour because of no background information.....	123

Figure 5.25 Myopic problem in a case with high RV/LV ratio.	124
Figure 6.1 (a) atlas points: blue – myocardial points, red – RV points, pink – LV points; (b) boundary and anatomical information defined in atlas, green points – boundary points, black dots – two RV inserts, red contours – two special anatomical regions.	127
Figure 6.2 Edge distance maps derived from binary edge maps: (a) original image, (b) binary edge image with high threshold, (c) distance map from b, (d) binary edge image with low threshold and (e) distance map from d.	129
Figure 6.3 (a) pink - initial contour and blue – actual boundary, (b) edge distance map (3D) and (c) ROI distance map (3D) based on fast marching time-cross map.	130
Figure 6.4 Distance maps based on fast marching algorithm and its updates in each step of the multi-grid strategy (each row); (a) image with initial contours before registration (b) B_{LV} , (c) B_{RV} , (d) B_{LV} 3D view and (e) B_{RV} 3D view.	132
Figure 6.5 Example of a closed polygon with seven vertices	134
Figure 6.6 Comparison between the results of the method with and without boundary term; (a) ground truth, (b) initial contours, (c) method without boundary term and (d) method with boundary term.	136
Figure 6.7 MHD comparison of initial contour, registration based on intensity only and registration after adding boundary term. (a) LV, (b) RV and (c) epicardium.	136
Figure 6.8 SI comparison of initial contour, registration based on intensity only and registration after adding boundary term. (a) LV, (b) RV and (c) myocardium.	136
Figure 6.9 MHD comparison of using different area-term weights from 0 to 0.16. (a) LV, (b) RV and (c) epicardium.	138
Figure 6.10 SI comparison of using different area-term weights from 0 to 0.16. (a) LV, (b) RV and (c) epicardium.	138
Figure 6.11 MHD comparison of initial contour and each level of the coarse-to-fine strategy, 1 st level: 2x2 mesh, 2 nd level: 3x3 mesh, 3 rd level: 4x4 mesh, 4 th level: 5x5 mesh. (a) LV, (b) RV and (c) epicardium.	139
Figure 6.12 SI comparison of initial contour and each level of the coarse-to-fine strategy, 1 st level: 2x2 mesh, 2 nd level: 3x3 mesh, 3 rd level: 4x4 mesh, 4 th level: 5x5 mesh. (a) LV, (b) RV and (c) myocardium.	139
Figure 6.13 MHD Comparison of the registrations with 5x5 mesh and 4x4 mesh used in the last level of the coarse-to-fine strategy.	141
Figure 7.1 Flow chart showing the process of automated 3D model-based CMR segmentation process.	144
Figure 7.2 Contour points (red) detected in last chapter and their corresponding points (green) on the model surfaces (a) RV endocardium, (b) LV endocardium, (c) epicardium.	147
Figure 7.3 Model hosted by 3x3x3 mesh, the contours (red) and their corresponding points (green) on the model surfaces.	149
Figure 7.4 Linear solution to the computation of local coordinates.	150
Figure 7.5 First three iterations in the fitting, (a) initial model, (b) after 1 st iteration, (c) after 2 nd iteration and (d) after 3 rd iteration.	153
Figure 7.6 Error function change in iterations.	153
Figure 7.7 Comparison of MHD results of using linear and cubic FFD; (a) LV, (b) RV, (c) myocardium.	154
Figure 7.8 SI results of using linear and cubic FFD; (a) LV, (b) RV, (c) myocardium.	154
Figure 7.9 MHD results of using different smoothing weights from 0.25 to 4; (a) LV, (b) RV, (c) myocardium.	155

Figure 7.10 SI results of using different smoothing weights from 0.25 to 4; (a) LV, (b) RV, (c) myocardium.	155
Figure 7.11 MHD results of using different mesh complexities from left to right 1x1x1, 2x2x2, 3x3x3, 4x4x4; (a) LV, (b) RV, (c) myocardium.	156
Figure 7.12 SI results of using different mesh complexities from left to right 1x1x1, 2x2x2, 3x3x3, 4x4x4; (a) LV, (b) RV, (c) myocardium.	156
Figure 7.13 Examples of variability of the atlas and the LV RV presentation on apical slices.	157
Figure 7.14 Examples of variability of the atlas and the LV RV presentation on basal slices.	158
Figure 7.15 Coarse-to-fine strategy for the atlas-based registration of a SA slice close to the apex, top row – before registration, bottom row – after registration.	160
Figure 7.16 Box plot of MHD errors of the experiments using different smoothing weights from 0.25 to 1.	161
Figure 7.17 (a) and (b) are two different LA planning shown on the middle SA slice, (c) the LV centre (orange), two RV inserts (magenta), the original V_y (cyan dot line) and the V_y rotated by θ (cyan solid line).	164
Figure 7.18 (a) atlas on the 4-chamber LA slice, (b) 2D view of LV distance map and (c) its 3d view.	165
Figure 7.19 Multi-grid and multi-resolution strategy for the atlas-based registration of the LA slice; pink – constraint points, green – mesh, magenta – atlas.	165
Figure 7.20 Contour comparisons on the middle SA slice used in the last chapter: (a) Ground truth contours, (b) initial model contours, (c) contours after atlas-based registration and (d) model contours after 3D fitting.	166
Figure 7.21 MHD comparison of initial contours, the contours after atlas-based registration and contours after 3D model fitting. (a) LV, (b) RV and (c) epicardium.	167
Figure 7.22 SI comparison of initial contours, the contours after atlas-based registration and the contours after 3D model fitting. (a) LV, (b) RV and (c) epicardium.	167
Figure 7.23 Top row – initial model shown on each SA slice, middle row – updated model with the contours computed from the middle SA slice, bottom row – updated model with the detected contours of the 3 rd to 5 th SA slices; magenta contour – the ground truth of LV endocardium.	168
Figure 7.24 Location of five specific slices: (a) first apical slice, (b) second apical slice, (c) middle slice, (d) second basal slice and (e) first basal slice.	169
Figure 7.25 Box plots of the modified Hausdorff distances between ground truth and the updated model, in comparison to the inter-observer errors.	169
Figure 7.26 MHD errors on the 4-chamber LA slice between the ground truth and (a) the contours before the registration, (b) the contours after registrations and (c) inter-observer error.	170
Figure 7.27 Improvement of using 4-chamber LA slice in comparison to the Figure 7.23.	170
Figure 7.28 Box plot of the modified Hausdorff distance of the correspondence between ground truth and Initial estimate, using the contours detected on Mid SA, All SA, SA+LA, and inter-observer manual error.	172
Figure 7.29 Two possible better LA acquisition plans; green – original slices, magenta – new slices added.	174

Figure 7.30 Covers above the basal slice and erroneous deformation at the base in a coarse-to-fine registration process; top row – before registration, bottom row – after registration; (a)3x3, (b)4x4, (c)5x5.	176
Figure 7.31 Two problems at the apex in current model; (a) thick myocardium, (b) RV apex lower than LV.	176

List of Tables

Table 2-1 Thresholds defined for leakage detection and improvement evaluation in each slice.....	38
Table 2-2 Comparison of the orientation errors (mean \pm standard deviation in degrees) relative to manual identification of the LV long axis orientation V_x . In the ONTARGET and ZEST datasets, the parallel SA scan planes were planned to be approximately orthogonal to V_x during image acquisition and should therefore have normals aligned with V_x . In the CINE-SCOUT dataset, the image orientations were fixed to \bar{V}_x	42
Table 4-1 Measures which appeared in three or more of the above articles.....	62
Table 4-2 Four aspects of an algorithm with good performance.....	74
Table 4-3 Standard deviations of the Gaussian curves fitted to the curves in Figure 4.7.....	79
Table 4-4 Relationships between T_x , T_y , R and S in five cases.....	79
Table 5-1 Modified Hausdorff distance and similarity index before and after registration.....	121
Table 6-1 MHD and SI comparison of initial contour, registration without and with boundary term.....	137
Table 7-1 MHD and SI comparison of initial contours, contours after atlas-based registration and contours after 3D registration.....	167
Table 7-2 Modified Hausdorff distance between the ground truth and the updated model after initial estimate, using the contours detected on Mid SA, All SA, SA+LA, and inter-observer manual error.....	172

Glossary of Abbreviations

AAM	Active Appearance Models
ACC	Accuracy
AMIR	Automatic Multi-modality Image Registration
AMRG	Auckland Magnetic Resonance Research Group
ASM	Active Shape Models
CAR	Capture Range
CMR	Cardiac Magnetic Resonance
CO	Cardiac Output
CR	Correlation Ratio
CSS	Chi Square Statistic
CT	Computed Tomography
DC	Direct Current
DICOM	Digital Imaging and Communication in Medicine
DOG	Distinctiveness of the Global Maximum
ECC	Entropy Correlation Coefficient
ECG	Electrocardiogram
ED	End-diastolic
EDI	Entropy of Difference Image
EDV	End-diastolic Volume
EF	Ejection Fraction
EH	Energy of Histogram
EM	Expectation Maximization
ES	End-systolic
ESV	End-systolic Volume
FFD	Free-form Deformation
FOV	Field of View
FT	Fourier Transform
GCC	Gradient Cross Correlation
GMI	Gradient Mutual Information
GVF	Gradient Vector Flow
H1	First Harmonic
HD	Hausdorff Distance
ICA	Independent Principle Component Analysis
ICP	Iterative Closest Point
JE	Joint Entropy
LA	Long Axis
LM	Levenberg-Marquardt
LV	Left Ventricle

LVEF	Left Ventricle Ejection Fraction
LVM	Left Ventricle Mass
MAP	Maximum a Posteriori
MHD	Modified Hausdorff Distance
MI	Mutual Information
MR	Magnetic Resonance
MRA	Magnetic Resonance Angiography
MRF	Markov Random Fields
MRI	Magnetic Resonance Image
MRIU	Modified Ratio of Image Uniformity
NCC	Normalized Cross Correlation
NMI	Normalized Mutual Information
NOM	Number of Minima
NP-hard	Nondeterministic Polynomial-time Hard
ONTARGET	Ongoing Telmisartan Alone and in combination with Ramipril Global Endpoint Trial
PCA	Principal Component Analysis
PDM	Point Distribution Models
PET	Positron Emission Tomography
PNI	Pattern Intensity
RIU	Ratio of Image Uniformity
ROI	Region of Interest
RON	Risk of Non-convergence
RV	Right Ventricle
SA	Short Axis
SI	Similarity Index
SMPL	Simple Multi-Property Labelled
SPECT	Single Photon Emission Tomography
SPM	Statistical Parametric Mapping
SSD	Sum of Squared Difference
SSFP	Steady State Free Precession
SV	Stroke Volume
WD	Wood Method
WT	Wall Thickness
ZEST	New Zealand Eplerenone Aortic Stenosis Trial

1 Introduction

Cardiovascular disease is the leading cause of death in the world. In New Zealand, it accounts for 40% of deaths annually (approximately 10,500). Every 90 minutes a New Zealander dies from a heart attack (17 deaths a day) [1]. Cardiac imaging is an established tool to provide qualitative and quantitative information about the morphology and function of the heart and great vessels. It plays an important role in guiding clinical diagnosis, treatment, and the follow-up of cardiac disease. However, a single cardiac examination results in a large amount of image data. This leads to the urgent requirement for efficient image segmentation algorithms to automatically extract clinically relevant parameters. The overall goal of this thesis is to provide clinically useful tools for the automatic extraction of cardiac performance parameters from cardiac magnetic resonance imaging (MRI) data.

This chapter presents the motivation and the objectives of this work, followed by an introduction to cardiac magnetic resonance (CMR) imaging and heart modeling. Current segmentation methods are reviewed and an overview of the structure of the thesis is provided. Finally, an overview of the achievements of this thesis is given.

1.1 Motivation

Three-dimensional (3D) (or at least spatially localised 2D) imaging of the heart and the cardiovascular system is now available with all main imaging modalities: X-ray computed tomography (CT); magnetic resonance (MR); positron emission tomography (PET); single photon emission tomography (SPECT); and ultrasound. The use of MR imaging in clinical practice is rapidly increasing, due to its ability to provide high resolution multiphase 2D cardiac images, illustrating cardiac anatomy and function. MR imaging is also free from radiation and, unlike echocardiography, can reliably image the entire heart. However, a single cardiac examination can result in a large amount of data.

There is an increasing demand for efficient image segmentation algorithms to automatically extract clinically relevant parameters. The ability to quantitatively analyse all of the acquired image data is still not routinely available in clinical applications. Much of the acquired data is therefore under-utilised because the current semi-manual analysis procedures are time-

consuming and are also prone to intra-observer and inter-observer variability. It is critical that methods for highly automated 2D and 3D cardiac image segmentation are developed.

Segmentation of the left and right ventricular boundaries is of the highest clinical importance for the quantitative assessment of cardiac function. Various methods have been proposed to solve this problem. However, most of them still experience a low success rate in comparison to manual segmentation. The main reasons for their failure are listed below [2]:

- 1) Image pixel intensities cannot adequately constrain the segmentation. Current limitations include limited temporal and spatial resolution and the lack of contrast between blood and muscle or muscle and other anatomical structures.
- 2) Image artefacts. Artefacts occur due to irregular heart rates, respiration, other patient motion, magnetic susceptibility, flow, coil inhomogeneity, metal in the imaging volume, and partial volume effects.
- 3) Prior information. The amount of prior knowledge incorporated into current methods is often insufficient. It has been reported by several studies [2-6] that spatial and temporal constraints can be useful in optimising segmentation.

1.2 Objectives

The aim of this thesis is to develop robust, accurate, automated, model-based methods for segmentation of the left ventricular (LV) and right ventricular (RV) blood pools and myocardium. The methods should be fully automated and supervision free. In order to achieve these objectives, the following sub-objectives should be fulfilled:

- 1) **Develop** robust methods for good initial estimation of the location and orientation of the heart.
- 2) **Develop** efficient model-based methods to accurately fit the model to the scanned data

1.3 Cardiac Anatomy and Function Parameters

In this section, for a better understanding of the remainder of this thesis, a brief introduction to cardiac anatomy and the cardiac cycle is provided. All the important parameters quantifying cardiac function in clinical usage and their relationships to image segmentation

are explained. An outline of CMR imaging, one of the best and most reproducible approaches for the accurate measurement of both LV and RV functions, is included.

1.3.1 Cardiac Anatomy

The heart (Figure 1.1) is a muscular organ which pumps blood throughout the body by contracting and relaxing in rhythmic cycles. The heart wall consists of the epicardium (outer layer), the myocardium (middle layer comprised of cardiac muscle tissue), and the endocardium (inner layer). The heart consists of four chambers: the LV, the RV, the left atrium and the right atrium. The LV pumps blood to the systemic circuit. Its free wall and the septum are much thicker than the RV free wall. It is separated from the left atrium by the mitral (bicuspid) valve. The RV is separated from the right atrium by the tricuspid valve. The closure of the mitral valve is controlled by papillary muscles and chordae tendineae to prevent valve leaflet prolapse.

Figure 1.1 shows the detailed anatomy of the heart. The two ventricles are clearly identified by the thick layer of myocardium that makes up their walls. The short axis (SA) slices used in CMR images have a similar appearance to the transverse view (below) where regular contours, consisting of two concentric circles, can be readily fitted to the LV endocardium and epicardium. This is very useful in cardiac image analysis.

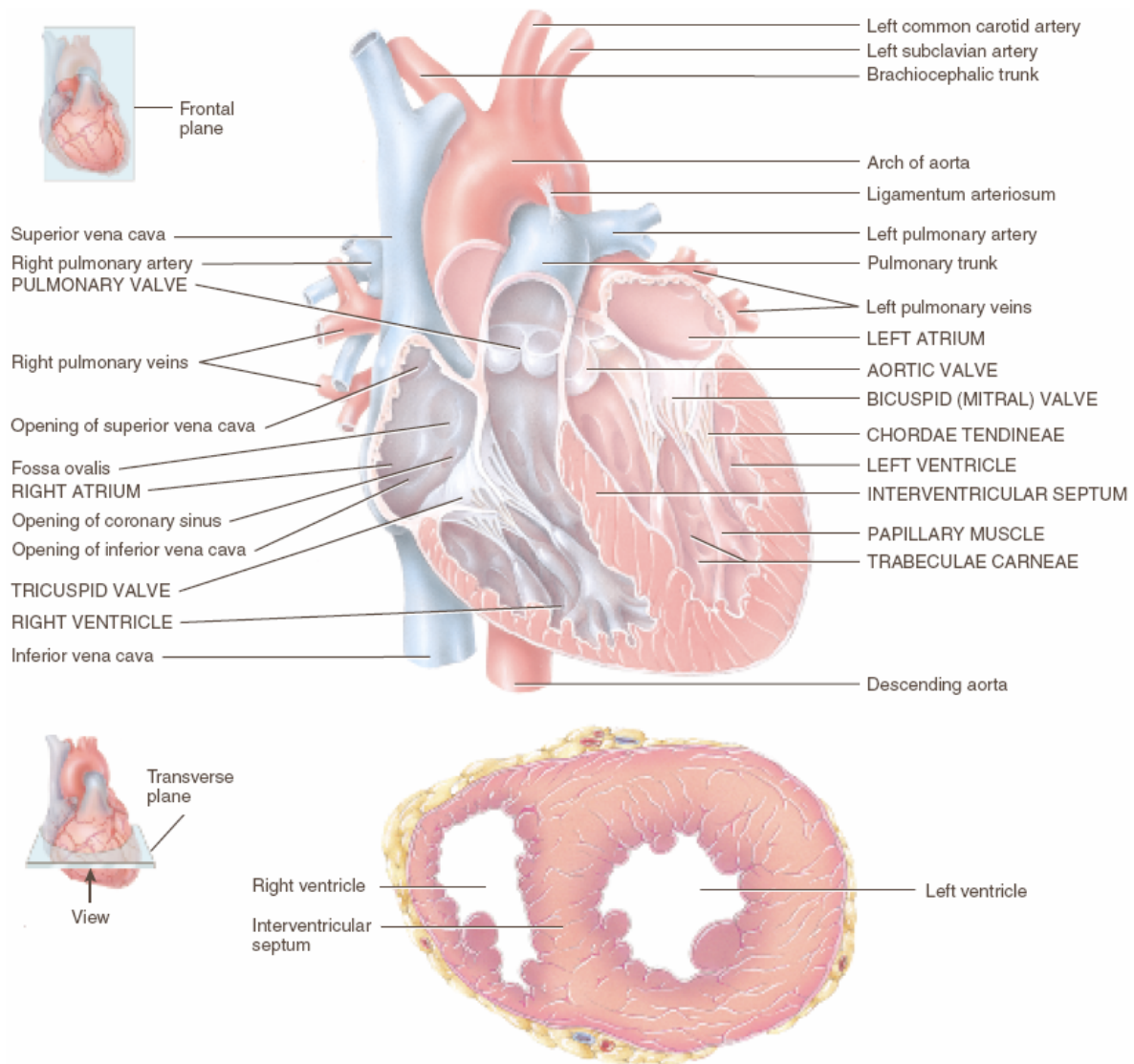


Figure 1.1 Anatomy of heart in frontal and transverse views (adapted from [7])

1.3.2 Cardiac Cycle

A cardiac cycle consists of the rhythmic contraction (systole) and relaxation (diastole) of both atria and ventricles. The cycle begins with atrial systole where blood is actively pumped from the atria into the ventricles. The end of the atrial systole marks the end of the ventricular diastole (Figure 1.2). The volume of blood (end-diastolic volume or EDV) contained in each of the ventricles reaches their maximum at end-diastole (ED). Ventricular systole causes the pressure inside the ventricles to rise sharply and ejection of blood from the heart through the aortic or pulmonary valves begins. The end-systolic volume (ESV) is computed at end-systole (ES) when the blood volume in the ventricles reaches a minimum. The volume changes during the entire cycle and the corresponding electrocardiogram (ECG) are presented in Figure 1.2.

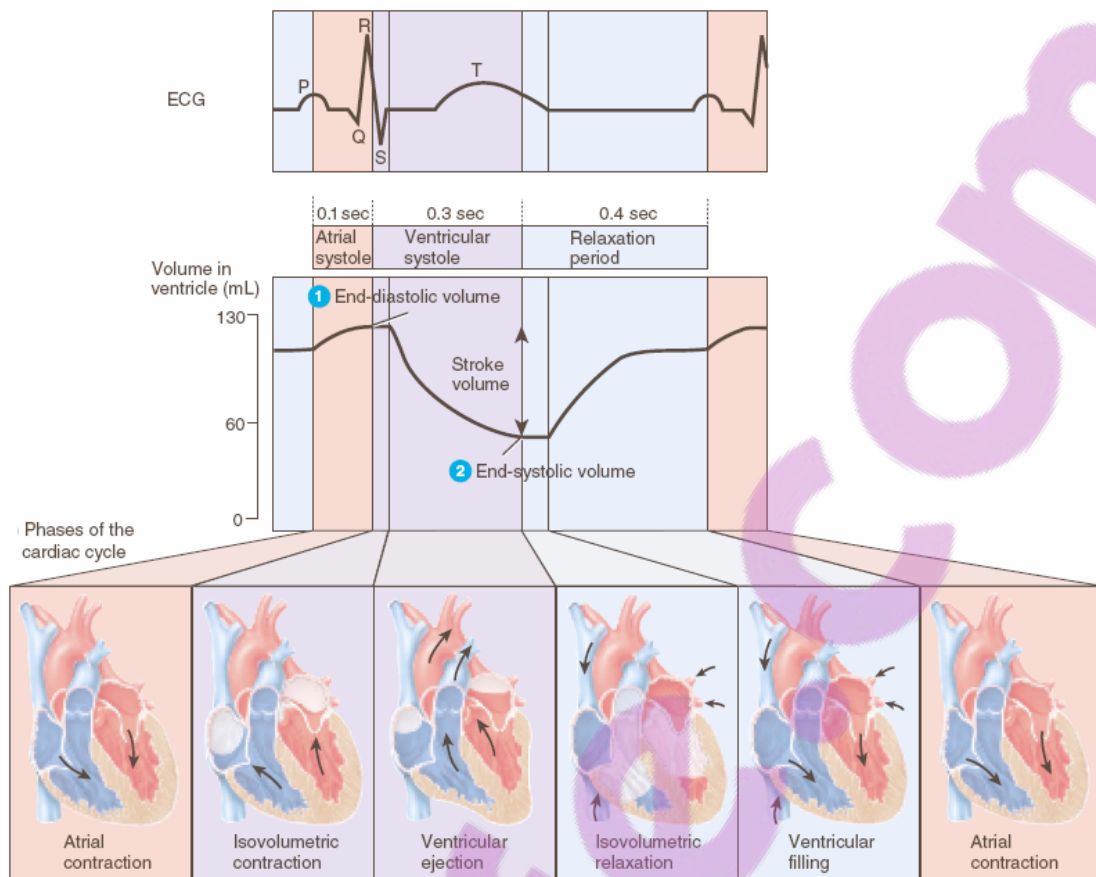


Figure 1.2 ECG, volume change and phases in a cardiac cycle (adapted from [7])

1.3.3 Cardiac Function Parameters

Cardiac functional parameters are very important in assessing the heart and diagnosing heart disease. They are classified into two groups, global functional parameters and regional functional parameters. Global parameters include general volumetric measures such as ventricular volumes (EDV and ESV), ventricular mass (LVM), ejection fraction (EF), stroke volume (SV), and cardiac output (CO). Regional parameters are related to the motion and deformation of a smaller part of region of the heart during the cardiac cycle, and include things such as local wall thickening, strain, and strain rate.

Global functional parameters, the left ventricular EF (LVEF) and LVM are two of the most useful global indices in clinical practice.

- 1) **LVEF**, a measure of LV pump function, is defined as the ratio of the difference between ESV and EDV to the EDV. The computation of EDV and ESV is based on segmentation of the LV endocardium.

$$\text{LVEF} = \frac{\text{EDV} - \text{ESV}}{\text{EDV}} \times 100\% \quad (1)$$

- 2) **LVM** is an important predictor of cardiovascular risk and higher mortality. LVM is calculated from the myocardial volume (possibly averaged over several phases of the cardiac cycle), multiplied by the specific gravity of myocardium (generally accepted to be 1.04-1.05 g/mL). The myocardial volume is computed by subtracting the LV chamber volume inside the endocardium from the total volume contained within the epicardial border of the ventricle.

In local cardiac functional analysis, wall motion and wall thickening (WT) have been quantitatively investigated with the development of CMR imaging technologies. It has been reported that WT is a more sensitive indicator of dysfunctional contraction than wall motion [8].

- 3) **WT** is measured, using endocardial and epicardial contours of each slice, by drawing chords perpendicular to the centre line that is equidistant to both contours [9]. This method can be extended to three-dimensional surfaces.

Each parameter requires knowledge about the endocardial and epicardial contours. Thus, the accurate segmentation of the endocardial and epicardial surfaces of the ventricles at ED and ES is essential for the calculation of these cardiac functional parameters.

It would also be desirable to include RV functional parameters since its function is known to be an important determinant of prognosis in coronary artery disease, heart failure and pulmonary disease [10]; however, global RV function is difficult to assess adequately due to its more complex shape and significant basal descent during systole. Though it has been shown that CMR imaging is one of the best and most reproducible approaches for the accurate measurement of both LV and RV function [11], most of the current research still focuses on LV because of its thicker wall and simpler symmetrical geometry.

1.4 Data Acquisition

1.4.1 Principles of Cardiac MR Imaging

MR imaging is a technique for obtaining high-resolution images of soft tissues by mapping the distribution and relaxation times of hydrogen nuclei. Images are formed by manipulating hydrogen's quantum property 'spin angular momentum'. Spin angular momentum describes

how an atom rotates about its own axis resulting in a weak magnetic field. Ordinarily, hydrogen nuclei are oriented randomly so that there is no net magnetic field but in the presence of a strong uniform external magnetic field the hydrogen atoms line up to create a detectable net magnetization. Different tissues have different strengths of magnetization which is proportional to the percentage of hydrogen atoms in that tissue. Location information can be encoded by a field with a smooth gradient in field strength, because the atoms at different field strength spin at different angular velocities and therefore emit different frequencies. The Fourier transform is then used to decode the location information from the measured frequencies. A two dimensional image can be obtained with two gradients which are perpendicular to each other. More detailed principles can be found in [12].

CMR imaging can provide detailed information on 3D ventricular shape and geometry, regional systolic and diastolic strain, material microstructure, blood flow, perfusion and viability [13]. It is considered the most accurate method to measure ventricular volumes and systolic function. The CMR technique known as steady state free precession (SSFP) has become the ‘gold standard’ in clinical LV function assessment. SSFP greatly improves the contrast between myocardium and blood by driving the magnetization to a steady state, and making the cines (sequential images in time) virtually independent of inflow enhancement.

1.4.2 Cardiac MR Image Acquisition

A standard clinical assessment of global cardiac structure and function normally comprises sequential 2D breath-hold cine SSFP imaging in multiple slices covering the heart. CMR scanners from all major manufacturers can sample the entire heart with a high contrast to noise ratio and acceptable spatial and temporal resolution (10-20 slices at 1x1x6 mm voxels and 20-50 msec temporal resolution) in 10-15 minutes [13]. On some modern scanners with improved hardware, a single cine can be acquired in one breath-hold of just 8 seconds, allowing the whole stack of images to be acquired in 5–10 minutes [10].

- **Acquisition Protocol**

The acquisition protocol described in this section is the standard protocol currently used at the University of Auckland Centre for Advanced MRI. It is very similar to the description in [10] and slightly different from [14].



Manual planning for CMR image acquisition starts from a coronal scout scan (see Figure 1.3b) to acquire a stack of axial scout scans which cover the entire heart. An axial scout scan (Figure 1.3c) showing the left ventricle is then selected. The centre of the mitral valve ring is then determined on this image and another scout scan planned through this and the tip of the apex to produce a single-oblique long-axis scan. Similarly, another plane through the centre of the mitral valve and the tip of the apex is planned for acquisition of a double oblique long-axis scout scan. Finally, a number of parallel SA cines are planned on the double oblique long axis to encompass the whole LV. The planning of the long-axis (LA) slices is based on the ED frame of the middle SA slice. In our protocol, all LA slices are positioned to pass through the centre of the LV chamber and rotated by 60° increments.

This manual planning procedure typically takes an experienced radiologist less than five minutes from the acquisition of the first set of localizer images to beginning the acquisition of correctly aligned breath-hold SA images.

▪ **Problems in Cardiac MR Imaging**

The quality of cardiac MR images can be affected by a large number of factors:

- 1) The constant 3D motion the heart undergoes during the cardiac cycle.
- 2) Motion artefacts due to respiratory movement or irregular heart rate. These occur if there is motion during the acquisition which violates the assumptions of the ECG gated image acquisition process. In some cases, patients are unable to hold their breath and this creates additional motion blurring in the images.
- 3) Slice misregistration due to respiratory movement. These may occur when one or more cines acquired in different breath-holds are displaced due to changes in the diaphragmatic position of the patient. This is particularly important where 3D reconstruction techniques which rely on accurate slice registration are used.
- 4) Partial volume effects. This occurs when a voxel contains two or more types of tissue and as a result the edges of the images are blurred. This problem is usually caused due to the anisotropic resolution of the images. The in-plane resolution can be high (1mm) but the through-plane resolution is usually low (6-8mm).

- 5) Some boundaries in CMR images may not be clear, for example the boundary between the lung and the myocardium is often indistinct. Susceptibility artefacts may also give rise to errors. Although not significant problems in manual analyses, these can be challenging for automatic methods.

Not all these problems can be solved with current imaging technologies. The misregistrations caused by separate breath-holds can be reduced by acquiring all slices during an end expiratory breath-hold; however, small differences between slices remain observable in many cases. Thus, a slice position correction process is required for 3D analysis.

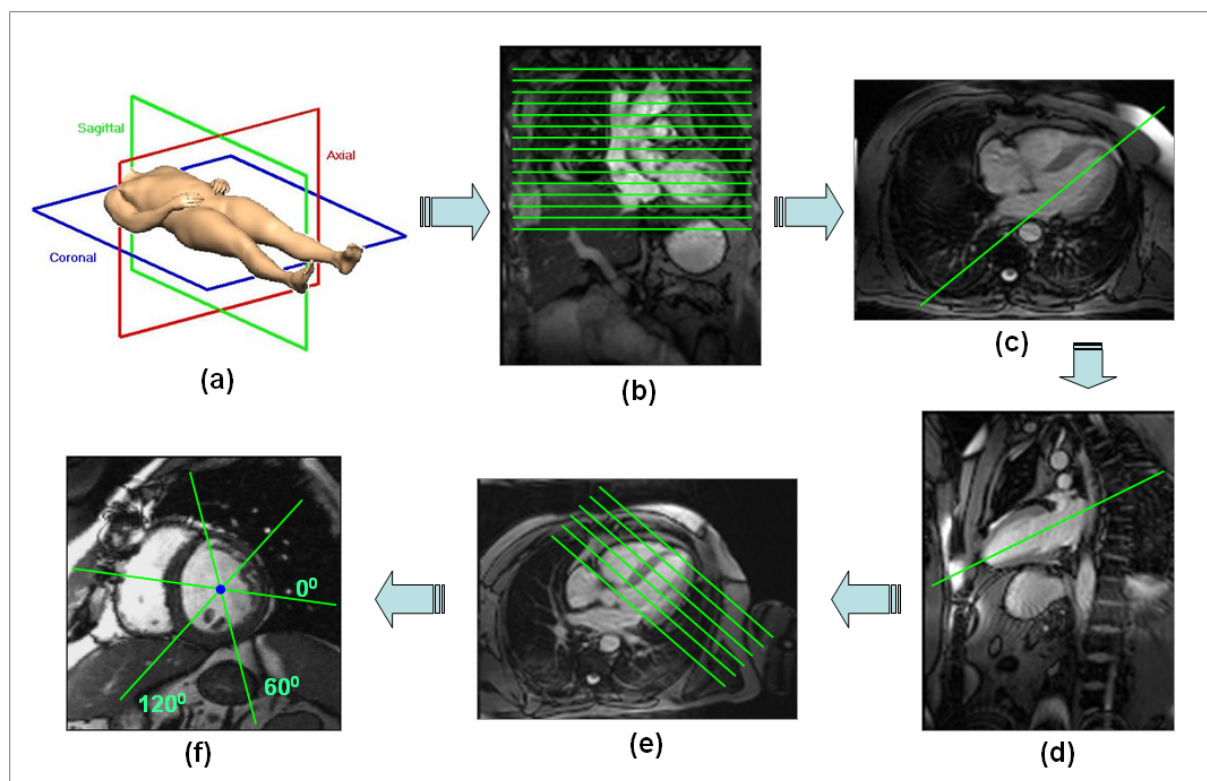


Figure 1.3 Manual planning of CMR acquisition. (a) definition of the three standard anatomical planes, (b) coronal image and planning for acquisition of an axial stack, (c) axial image and planning for acquisition of a single long axis oblique, (d) planning for acquisition of double oblique long axis scout scan, (e) planning for acquisition of SA cines and (f) middle SA slice and planning for acquisition of LA cines.

- **Slice Correction**

Experienced analysts inspect each slice in three dimensions by comparing them to all other LA and SA slices. If a large mis-registration is observed, the slice is manually registered by translating the slice in the plane of the image. In this process, no through-plane translation,

rotation or deformation is permitted in order to keep the registration as simple as possible. This simple method does not guarantee that the LA and SA slices completely match but it was found to be adequate for this study. Automated motion correction is possible but beyond the scope of the present study. Interested readers may find more details in [15].

1.4.3 Cardiac MRI Datasets

Three clinical datasets are utilized in this thesis. The ONTARGET (Ongoing Telmisartan Alone and in combination with Ramipril Global Endpoint Trial) dataset contained 330 patients with cardiac and vascular disease recruited from eight MR centres world-wide as enrolled in the CMR substudy to ONTARGET [16]. The second trial is from New Zealand and is known as ZEST (New Zealand Eplerenone aortic Stenosis Trial). The third trial, called CINE-SCOUT, is a small dataset collected from 14 asymptomatic volunteers by the AMRG (Auckland Magnetic-resonance Research Group) centre.

- **ONTARGET Dataset**

The rationale and patient details of this dataset are described in [16]. 330 patients at high risk for adverse events were imaged with a range of disease histories: 294 had coronary artery disease, 46 had peripheral arterial disease, 111 had diabetes, 202 had hypertension and 192 had suffered a previous myocardial infarction (with the total exceeding the number of patients due to multiple diagnoses). The patients were recruited and scanned at eight imaging centres in six countries (New Zealand, Australia, China Hong Kong, Thailand, Canada and Germany) using a standard SSFP imaging protocol on Siemens, Philips and GE scanners. Either prospectively or retrospectively gated images were acquired in six equally spaced SA locations from apex to base. Typical imaging parameters were TR/TE/flip/FOV = 30ms/1.6ms/ 60° / 360 mm with a slice thickness of 6 mm and an image matrix of 256×208. There were typically 25 temporal frames per slice, depending on the heart rate. All cines were acquired during breath-holds of 8–15 seconds duration.

- **ZEST Dataset**

The ZEST trial investigated patients with asymptomatic moderate or severe aortic stenosis. Baseline image data was acquired in 65 patients with aortic stenosis at three imaging centres within New Zealand using Siemens, Philips and GE scanners. The imaging protocol for the multislice SSFP cine acquisitions was identical to the ONTARGET protocol above.

- **CINE-SCOUT Dataset**

In order to evaluate the performance in lower resolution cine-scout images, 14 healthy volunteers were imaged with the protocol described above. An additional 8 slices with 10 frames/cycle were also acquired using a 15 second breath-hold SSFP retrospectively gated acquisition with TR/TE/flip/FOV = 86ms/1.5ms/71°/400x325mm, a slice thickness of 6mm, 7.2 mm slice gap, and an image matrix of 256x102. The orientation of these cine-scout scans was fixed to be normal to the average LV orientation found in the ONTARGET dataset.

1.4.4 Data Normalization

The original data were stored using the DICOM format which has a data range from 0 to 4096. However, a thorough investigation revealed that the data in most CMR images are clustered at the low end of the grey scale range, with only a small number of pixels with high intensity values - normally associated with the fat outside of the heart. These are not important for cardiac analysis and can cause a long tail in the histogram making automated analysis more difficult.

This effect was reduced by a linear scaling solution which assigned the top 2% of pixels to the 98th percentile value. The whole image was then normalized to the range of 0 to 1. In our experience, all SA slices can usually be combined and normalised using the same threshold. The LA slices needed to be dealt with separately because the image intensity distribution differed between the SA and LA slices. Further research is required to reduce the inhomogeneity between the SA and LA intensity distributions.

1.5 Construction of Heart Model

The standard approach to the construction of a geometric model is to represent the geometry of the object using simple blocks or elements that capture the required level of detail. The value of a quantity over an element is then determined by interpolating between the values at the element vertices.

The details of the construction of a heart model can be found in [17] and are also briefly described in this section. The construction process begins with the digitization of the CMR images to obtain the necessary surface points of the structures to be fitted. The data are then projected to the corresponding surfaces of an initial model. This triggers the deformation of the model to minimise the distance between the data and the model surfaces.

In this project, only the ED frame heart model was employed. The other frames were expected to be analysed by propagating the ED results over time. This is advantageous because

- 1) Papillary muscles are more easily segmented from the myocardium on ED frames.
- 2) There may be less motion artefacts on ED frames.
- 3) The statistical analysis of the intensity distribution is more accurate with the larger sizes of the blood pool.
- 4) ED is an important frame for the calculation of heart function.

The original heart model was developed from a normal CMR scan of a random healthy volunteer. More cases will be incorporated in the future for statistical analysis but this was not investigated in this thesis.

1.5.1 Data and Digitization

The human heart model used in this thesis was constructed previously at the Auckland Bioengineering Institute, from a CMR scan of a randomly selected healthy male aged in his 40s. The standard imaging protocol was applied to produce six SA and three LA cines. The images were ECG gated during breath-holding and the end-diastolic frames are selected for digitization (Figure 1.4).

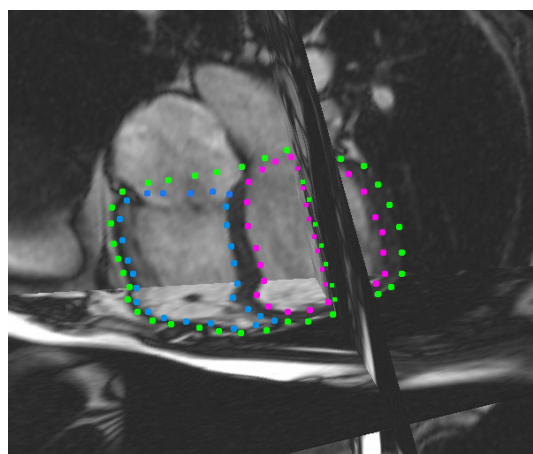


Figure 1.4 One SA slice intersecting with two LA slices with digitized points; green dots – epicardium, blue dots – RV endocardium and pink dots – LV endocardium.

The digitization was manually performed by an experienced operator. Both endocardial and epicardial surfaces were segmented from all SA and LA slices. In order to make a closed surface for each structure a surface was added along the closure points of each valve as shown in Figure 1.4 and Figure 1.5.

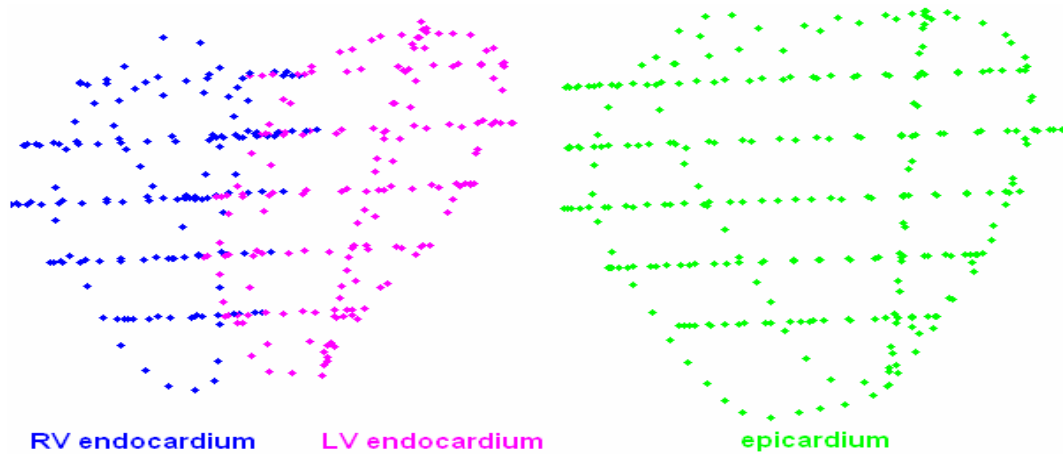


Figure 1.5 Digitization of two endocardial and one epicardial surfaces; green dots – epicardium, blue dots – RV endocardium and pink dots – LV endocardium.

1.5.2 Initial Model

The initial model was developed directly from the digitized data cloud. A small number of points scattered over the surfaces were selected to be the nodes to generate elements in a systematic manner for the initial polygonal mesh. The nodes were selected to construct a regular mesh with a minimal number of elements required for accurate optimisation. Cubic Hermite elements were then applied over the whole model with some collapsed elements defined at the apex and base. The advantage of this approach was that the linear mesh gave a good initial approximation, which could then be refined by optimizing over a higher order cubic interpolation. A cubic Hermite interpolation, in conjunction with Sobolev smoothing, was applied to provide smooth surfaces for the model even though a limited number of LA and SA slices were acquired.

1.5.3 Finite Element Fitting

The projection of a data point onto the surface was obtained by searching for the nearest point on the surface. The objective function was defined as the sum of squared distances between each data point and its projection onto the element. In the finite element model, the projected point can be interpolated as a function of nodal parameters. Thus, the distance between a data point and its projection onto the element is also a function of the element

parameters. Optimal nodal parameters are found by minimizing the objective function using a least squares approach. The final surfaces (Figure 1.6) are determined by the resulting element equations.

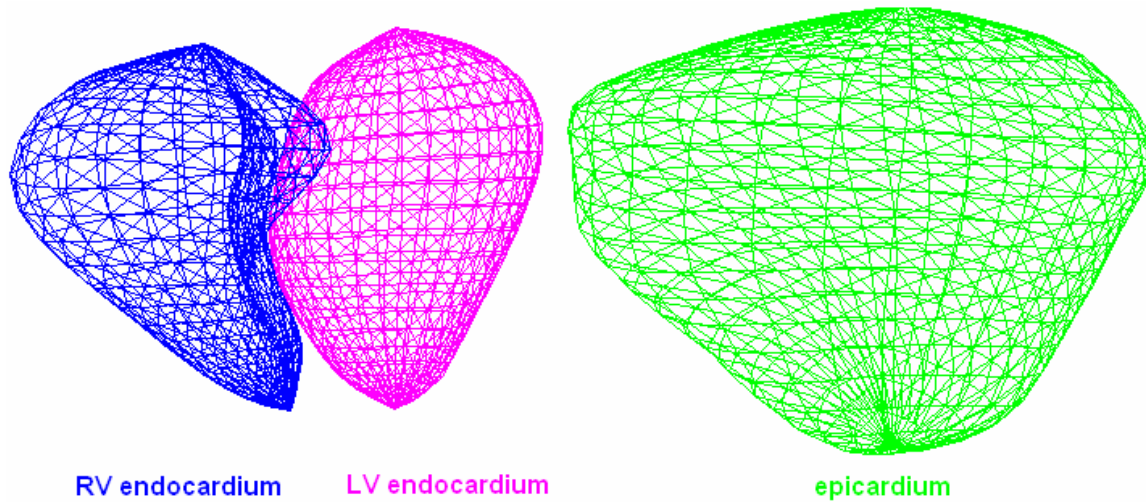


Figure 1.6 Three surfaces of the constructed model.

1.6 CMR Image Segmentation

This review focuses mainly on a number of currently published image segmentation methods applied to CMR images, which are pertinent to this thesis. Readers interested in general reviews on medical image segmentation are referred to [18, 19], and [9] for a review on cardiac modeling. The methods to be discussed below are categorized into five groups:

- 1) Deformable model based methods
- 2) Region based methods
- 3) Graph based methods
- 4) Statistical model based methods
- 5) Atlas based methods

Deformable model based methods and region based methods are two major categories of segmentation strategies. Graph based methods combine both region and boundary information into one framework. Most statistical model based methods can also be classified as deformable model based methods but are listed here in a separate category because of significant current interest. Atlas based registration methods can also be classified into either

deformable model or region based methods, depending on their energy functions, but they are considered here as a separate category. Although each technique is described separately, multiple techniques are often used together to obtain better solutions in many applications. In the rest of this section, an overview of each category is followed by a discussion of its advantages and disadvantages.

1.6.1 Deformable Model Based Methods

Deformable models are model based techniques for delineating region boundaries using 2D closed parametric curves or 3D surfaces which deform under the influence of internal and external forces [18]. Most algorithms require a good initial estimate to be near the desired boundaries. External forces, constructed from a feature space or directly from the image, drive the curve or surface towards desired image features like lines and edges. Internal forces maintain smoothness throughout the deformation. However, it has been reported that most deformable models are sensitive to initial conditions, and can be easily trapped in local optima. This is known as the ‘myopic problem’ [20]. There have been few reported applications to large medical image datasets and performance is often affected by artefacts, noise and poor image quality. Efforts have been made in recent years to solve the myopic problem by developing algorithms with wider capture range, greater robustness, more *a priori* knowledge, combining boundary and intensity information, and so on. A general review on deformable model based algorithms is given in [21].

- **Active Contours**

The active contour algorithm introduced by [22] is the basis of this category, in which the external force was determined by a smoothed gradient map. The parameters (control points), which represented the initial contour, evolved according to the deformation process. One significant problem with many implementations is that the capture range of the algorithm is normally very limited. Another problem is that control points may collapse in areas with high deformation.

- **Gradient Vector Flow**

The gradient vector flow (GVF) algorithm [26] made use of a new external force to provide a wider capture range than the original active contour. The force is based on a vector field $\mathbf{v}(\mathbf{x}, t)$ constructed by minimizing the following energy function:

$$E = \int \mu |\nabla \mathbf{v}(\mathbf{x}, t)|^2 + |\nabla I(\mathbf{x}, t)|^2 |\mathbf{v}(\mathbf{x}, t) - \nabla I(\mathbf{x}, t)|^2 d\mathbf{x}$$

where $\mathbf{x} = (x, y)$ represents each pixel on the image I and $\nabla \mathbf{v}(\mathbf{x}, t)$ is the gradient of the vector field. The first term becomes dominant where $\nabla I(\mathbf{x}, t)$ is small, which yields a slowly-varying field in homogenous regions. The second term creates an effect similar to the gradient of the edge map at areas close to boundaries.

The algorithm was applied in [27] to attract a 3D elastic LV model to the boundaries of SA slices. The GVF force field was reported to be more efficient in initialization and convergence. Instead of using a model, a manually traced rough polygon was used [28] as the starting contour. The algorithm was applied to the detection of the LV endocardium and epicardium in 4D (3D plus time) CMR images. GVF is also applied in [29] to construct a force field for local deformation in a level set framework.

- **Geodesic Active Contours**

The collapse problem in the original active contour algorithm was solved in the geodesic active contour algorithm [23, 24] by expressing the parameters implicitly. The evolution of this representation can then be handled by the level set framework, a powerful platform for integrating different information into one process. The algorithm called ‘active contours without edges’ in [25] is also based on a similar strategy. One disadvantage of these algorithms is that they do not integrate physiological knowledge of the underlying biological structures, which is often available in medical image analysis.

- **Level Set**

The level set method was introduced by Osher and Sethian [30, 31] and is a powerful technique which can easily integrate different information into one framework. The level set defines the contour as the zero level of a function ϕ of higher dimension. The function moves in its normal direction according to a speed function F . For 2D image segmentation, the evolution of ϕ is given by

$$\frac{\partial \phi(\mathbf{x}, t)}{\partial t} - F(\mathbf{x}) |\nabla \phi| = 0$$

with the initial image contours defined as $\phi(\mathbf{x}, t = 0)$. Interested readers are referred to [31, 32] for more details of the algorithm and its applications in medical image segmentation.

In [33], a variational level-set framework was proposed for the segmentation of the LV endocardium and epicardium. The framework was able to integrate boundary, intensity, shape and temporal information into one system. In [29], a level set non-rigid registration procedure was implemented to segment cardiac MR images with the help of an elastic model. A level set process was combined with statistical shape information based on the maximum a posteriori (MAP) approach in [34]. A level-set based method was employed in [35] for the segmentation of myocardial walls and the results applied to the quantitative evaluation of the LV blood flow in hypertrophic cardiomyopathy. Another level-set based method incorporating both gradient and region-based information was proposed in [36]. The initialization was implemented on a fast marching map (discussed below). The method in [37] minimizes an energy function that combines stochastic region-based and edge-based information with shape priors of the heart and local properties of the contour in a level-set platform.

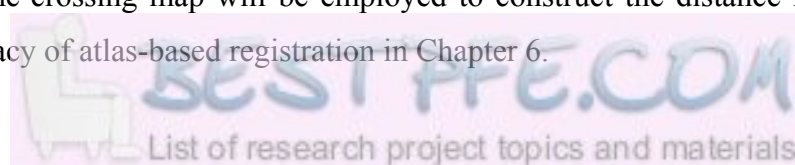
- **Fast Marching**

The fast-marching method is a particular case of the level-set approach introduced by Sethian [31]. The evolution of the initial contour is expressed in terms of the crossing time $T_M(x, y)$ of the contour at point (x, y) , which satisfies

$$\|\nabla T_M(x, y)\| = F(x, y)^{-1}$$

where $F(x, y)$ corresponds to the velocity of the moving front of the contours. The contours are advanced monotonically according to the propagation speed, normally a function of the image gradients. The time for the pixels inside initial curves is set to zero, while for all others it is set to infinity. The propagation of the interface is done via the construction of a time-crossing map based on image gradients. The construction algorithm selects the interface point having the smallest arrival time and calculates the arrival times of its neighbours, and so on until the interface has propagated across the whole region of interest. See [31] for details of the propagation.

The computational complexity of the algorithm is $N \log N$ where N is the number of pixels in the interested region. The algorithm is often used for initial estimates such as in [36]. In this thesis, the time-crossing map will be employed to construct the distance map used to improve the accuracy of atlas-based registration in Chapter 6.



1.6.2 Region Based Methods

Region based segmentation methods attempt to partition or group regions according to common image properties such as intensities, textures, patterns or spectral analysis of high dimensional data.

▪ Simple Algorithms

Thresholding is the simplest region based algorithm and is often used as an initial step in a sequence of image processing operations. Similarly, region growing is seldom used alone. [38] integrates an active shape model with region growing for LV endocardial segmentation of cardiac CT, and [39] combined some morphological operations for the segmentation of both LV and RV endocardial surfaces in CMR images. The advantage of these two algorithms is that they are extremely fast; however, they often require manual interaction to obtain the seed points [38, 40]. Leaking is another primary problem of the algorithm. Some special controls or local constraints must be applied such as the local examination method proposed in [38]. Large gaps between the SA slices of CMR scans also cause difficulties during 3D propagation in the long axis direction. Thus, region growing algorithms are better suited to CT images than CMR images.

▪ Algorithms with Training Data

Other histogram based algorithms such as maximum-likelihood and Bayes classifier methods are often used when training data is available. These algorithms can efficiently transfer the labels defined on the training data to the target image. Unfortunately, the training data is often required to be manually segmented. The algorithm is also not robust to intensity inhomogeneities; therefore it is often combined with other algorithms. For example, the region based term of the active contour scheme in [37] was based on the maximum-likelihood algorithm for the LV and RV segmentation on CMR images.

▪ Algorithms without Training Data

Clustering algorithms are able to train themselves without the use of training data, which make them easy to be used in different image modalities. Three common algorithms are K-means, fuzzy c-means and expectation-maximization (EM).

– K-means

This algorithm segments the image by iteratively classifying the image pixels to the nearest cluster centres. 15–20 independent cluster centres were used in [41] as the initial guess for the CMR segmentation. The pixels are iteratively clustered together until there are no movements between the classes. The number of clusters is then optimised by merging clusters with similar attributes.

- **Fuzzy c-means**

This algorithm, unlike K-means which directly classifies the pixels, gives the degrees of membership to each class based on fuzzy set theory. This was applied in [42] for the detection of LV endocardial and epicardial boundary points.

- **Expectation Maximization**

EM is a general method to estimate unknown parameters from given information, which is often used in image processing for histogram distribution estimation. It is assumed that the image histograms follow a statistical model, typically a Gaussian mixture model. It iteratively clusters the data by computing the posterior probabilities and the maximum likelihood estimates of each class. This has become a quite popular tool to estimate the intensity distribution of each tissue type in automated segmentations of CMR images [4, 6, 14, 43-45]. The advantage of EM over K-means and fuzzy c-mean techniques is its ability to provide a statistical model of the data and its capability to handle the associated uncertainties. The EM algorithm is also employed in our system for atlas construction and will be further discussed in Section 5.2.2. A disadvantage of the above three algorithms is that they do not incorporate any spatial modeling so they are sensitive to noise and inhomogeneities.

- **Markov Random Fields**

Markov random fields (MRF) was used in [46] for adding contextual constraint into the clustering algorithms. Such a constraint forces the algorithm to take into account the classification of neighbouring voxels. It has been shown that this method can efficiently remove isolated noisy pixels [4, 46]. This has been successfully applied for the CMR segmentation in [4] and [14]; however, the computational cost is often high.

1.6.3 Graph Cut Method

The graph cut method solves the image segmentation problem by constructing a graph that includes both the boundary and regional information of the image. A cut with minimal cost is then pursued which aims to separate the object nodes of the graph from the background. Typically, the maximum flow algorithm [47] is used to determine the minimum cut. A typical graph cut application for image segmentation requires object seeds, background seeds, and the estimates of both object and background intensity distributions as input, which are normally manually defined. The main advantage of the algorithm is that it is able to provide a global optimal solution. Another advantage is its flexibility to extend to 3D or even higher applications within the same formalism. The algorithm has promising applications in the interactive segmentation environment where the seeds and the intensity distributions can be easily obtained interactively. A good result had been reported in [48] for CMR image segmentation with manually defined seeds.

Automated selection of the seeds was also investigated in [49] for cardiac CT images and in [50] for CMR images. A rough region-of-interest (ROI) was first detected by using a scheme similar to the novel method developed in Chapter 2. A simple classification algorithm was then applied in the ROI to obtain the necessary seeds and the intensity distribution estimations for the graph cut. Some manual post-processing was still required since the obtained contours were quite irregular. The performance on large datasets is also unknown.

In order to develop an automated method based on graph cuts, *a priori* knowledge must be added to the algorithm to constrain the flexible cut. A shape constraint was added to the boundary term in [49] to guide the algorithm to cut the LV as convex blobs. This problem will also be investigated in Chapter 3.

1.6.4 Statistical Model-based Approaches

Statistical model-based approaches are able to provide anatomical constraints derived from a training set on the analysis. They have been known to greatly improve the results. The constraints can efficiently guide the model by preventing changes which are not physiologically likely. Active shape models (ASM) [51] and active appearance models (AAM) [52] are two successful schemes widely used in medical image analysis.

- **Active Shape Models**

ASM learns 2D or 3D shape variation from a training dataset. A reference shape in the dataset is often first selected and all the other images are then aligned in the same coordinate system. The statistical model can be based on point distribution models (PDM). A principal component analysis (PCA) or independent principal component analysis (ICA) [53] is performed to reduce the dimension of the shape vectors and keep most of the variability. In this way the deformation of the model during the fitting process is able to be restricted within trained statistical limits.

- **Active Appearance Models**

AAM extends ASM by taking into account image intensity values of the structures and surroundings. AAM has better convergence than ASM but is much slower. The combination of AAM and ASM was investigated in [54] for the segmentation of cardiac ventricles.

One significant disadvantage of these methods is that accurate segmentation of a large training set is required to cover the inter-patient variances in applications. A set of corresponding landmarks are also needed to be defined over the training set. The computational cost is another obstacle for these methods in high dimensional domains, particularly the AAM algorithm.

1.6.5 Atlas-based Methods

Atlas-based image segmentation treats segmentation as a special registration problem. The atlas is generally a labelled image generated by manually segmenting an actual image. It is then used to find the transformation that maps the pre-segmented atlas to the target image. After registration, all structural information defined in the atlas is transferred to the target image. The registration is classified as being “rigid” if only rotation and translation is involved in the transformation. “Affine” registration allows all linear transformations. Otherwise “non-rigid” registration is required if two images cannot be successfully registered without some localized stretching of the images [55].

The methods can be further classified into two groups based on their different energy functions.

- Feature-based Registration: feature-based registration computes the distance between the feature points detected on the target image and their corresponding points on the atlas, which is expected to reach the minimum when registered.
- Intensity-based Registration: intensity-based registration uses a function based on the intensity difference between the atlas and the target image. The advantage is that no pre-processing is required.

General reviews on medical image registration can be found in [55-59] and cardiac image registration in [60].

▪ **Feature-based Registration Methods**

In this approach, landmarks or feature points must be obtained from the target image before the registration. Boundaries or some easy detectable anatomical points are generally selected for this purpose. The points corresponding to these feature points on the atlas are automatically detected or manually defined. The atlas is transformed and/or deformed by the registration algorithm to reduce the difference between these correspondences. The segmentation methods discussed above can be employed for detection of the feature points.

This method was used for model fitting in [42]. The feature points were detected by the fuzzy c-means clustering algorithm discussed above and the iterative closest point (ICP) algorithm was applied to find the correspondence. A different strategy was employed in [61] for feature point detection. Instead of establishing a force field by gradient based algorithms, a region based method was used and the boundary points were searched along the normal direction of the vertices of the triangle meshes of the model surface. A similar strategy was studied in the registration algorithm of thoracic/abdominal structures in [62]. At least two advantages can be addressed for the methods in this sub-category:

- They are generally much faster than intensity based registration methods. Linear solutions may be available in some cases.
- They are more robust than intensity based registration methods in the cases where the intensity is not homogenous or well modelled by the atlas [63].

This scheme will be used in Chapter 7 for updating the model when endocardial and epicardial contours have been detected on each slice. These feature points on the contours

are automatically projected onto the model surface by the ICP algorithm. The registration method transforms or deforms the model to reduce the distance between the contours and the model.

- **Intensity-based Registration Methods**

Intensity-based registration methods have become the predominant approach in medical image segmentation and registration. The advantage of intensity-based registrations is that they do not need any pre-segmentation or boundary detection step, unlike feature-based registration. Registration is guided by the intensity difference between the atlas and the corresponding pixels on the target image. The atlas is an excellent tool to define and incorporate anatomical information.

The method has been widely used in brain and cardiac image segmentation. For CMR applications, a 3D statistical shape model of the LV and RV was constructed in [64] and registered to the SA images by minimizing the function of the intensity difference between the atlas and the target image in [65]. The atlas used in [65] contained three objects: LV, RV and myocardium. The intensity distribution of the background was also modeled; however the task was difficult because of the large variance between different cases. In order to avoid local minima caused by noise in the CMR images, an average image was created by registering different frames to the ED frame. The atlas was subsequently registered to the average image instead of each single frame. The validation of the method on large datasets is still unknown. The atlas was then extended to 4D registration in [4, 66, 67]. More details about the construction of probabilistic and statistical 4D cardiac atlas and its registration to patient images can be found in [68]. However, such a registration strategy was also reported to be not sufficient in accuracy [69-71], easily trapped into local optima [72] and computationally intensive [69]. A multiple resolution and multiple grid strategy was applied in [72] to avoid local optima.

This thesis primarily focuses on the investigation of atlas based segmentation methods in this sub-category. A new framework for atlas-based non-rigid registrations is proposed in Chapter 5. The framework enables easy integration of different types of information, such as intensity, boundary and anatomy, into the system to improve robustness and accuracy. A modified automated segmentation method is proposed in Chapter 6 and validation on large CMR datasets proves the efficiency of the new system.

1.7 Overview of the Thesis

This research is focussed on developing robust, model-based strategies for accurate automated segmentation of the LV, RV and myocardium. Figure 1.7 outlines the structure of the thesis. An initial estimate is derived in Chapter 2 from the temporal and spatial characteristics of heart pixels. An investigation on the integration of graph cut methods with LV models for CMR image segmentation is performed in Chapter 3. Due to limitations in its application to fully automated segmentation techniques, this method is not pursued further. The remainder of the thesis investigates atlas-based registration techniques in 2D and 3D spaces. An atlas-based 2D registration procedure is developed to detect the LV, RV endocardial and epicardial contours on each image in Chapters 4, 5 and 6. A feature-based 3D registration is used for updating the 3D model with the detected contours in Chapter 7. This procedure starts from the middle SA slice since the midventricular shapes are less variable and the model has a better initial position on that slice than the others. The detected contours on the middle slice are then used to update the 3D model. This provides a highly accurate initial model for the two SA slices next to the middle slice, which are then segmented by 2D atlas-based registration and the resulting contours are used to update the 3D model again. The model is iteratively deformed with the inclusion of more slices. Because of the uncertainty of the apical appearance on SA slices, due to partial volume effects, the 4-chamber LA slice is included to provide more accurate information at the apex. An overview of each chapter is given as follows:

Chapter 1. In this chapter, the motivation and the objectives of this work are first presented, followed by an introduction of CMR imaging and heart modeling. Current segmentation methods in CMR images are reviewed and the structure and achievements of this thesis are presented.

Chapter 2. This chapter proposes a fully automated method to estimate the location and orientation of the LV from multi-slice cine CMR images. The method relies on a novel combination of temporal Fourier analysis and simple contour detection to achieve a fast localization of the heart without user input. Quantitative validation performed on two large clinical datasets shows high agreement between the ground truth and the automatic results.

Chapter 3. Graph cut algorithms are investigated in this chapter for image segmentation problems. For automation, high level information must be included in the formulation to

guide the cut. This chapter proposes a new solution to the integration of model-based *a priori* information into the graph cut formulation. However, the method is found to work best for LV segmentation on middle SA slices, and further work will be necessary to apply this method robustly to all slices in a fully automated environment. Thus, RVLV atlas based solutions are sought in the following chapters.

Chapter 4. This chapter examines six widely used similarity measures in the context of rigid atlas based segmentation, using a comparison framework independent of the optimisation algorithm. The comparisons are based on a new Simple Multi-Property Labelled (SMPL) atlas-based registration framework, which enables simplifications in the computational complexity of the atlas registration problem. All six similarity measures are simplified for use in this framework. They are then quantitatively compared with each other using performance criteria derived from the literature.

Chapter 5. In this chapter, the SMPL atlas-based non-rigid registration framework is further developed. In the new framework, the atlas is treated as a set of mathematical points which have no size but are labelled with various properties. The chapter shows how the SMPL framework enables easy integration of different types of information into the system, thereby improving robustness and accuracy. The results also demonstrate that the accuracy is improved by sampling the atlas at sub-pixel level.

Chapter 6. The registration method in Chapter 5 can result in errors due to the myopic problem and lack of background information, if only intensity information is applied. In this chapter, the SMPL framework is extended to integrate intensity, boundary and anatomical information into a single process for CMR image segmentation. The results show that the extended method has better accuracy and robustness.

Chapter 7. In this chapter, an efficient feature-based 3D registration method is proposed to update the initial heart model with the contours detected by the 2D atlas-based registration of Chapter 6. The method integrates the iterative closest point algorithm with 3D free-form deformation. The model is iteratively updated by applying the 3D feature-based registration method and the 2D atlas-based registration method in sequence on each SA slice. The four chamber LA slice is also exploited for more accurate information at the apical area. The overall results are then evaluated and discussed.

Chapter 8. This chapter gives a thorough review of the thesis and discusses future improvements for automated clinical applications.

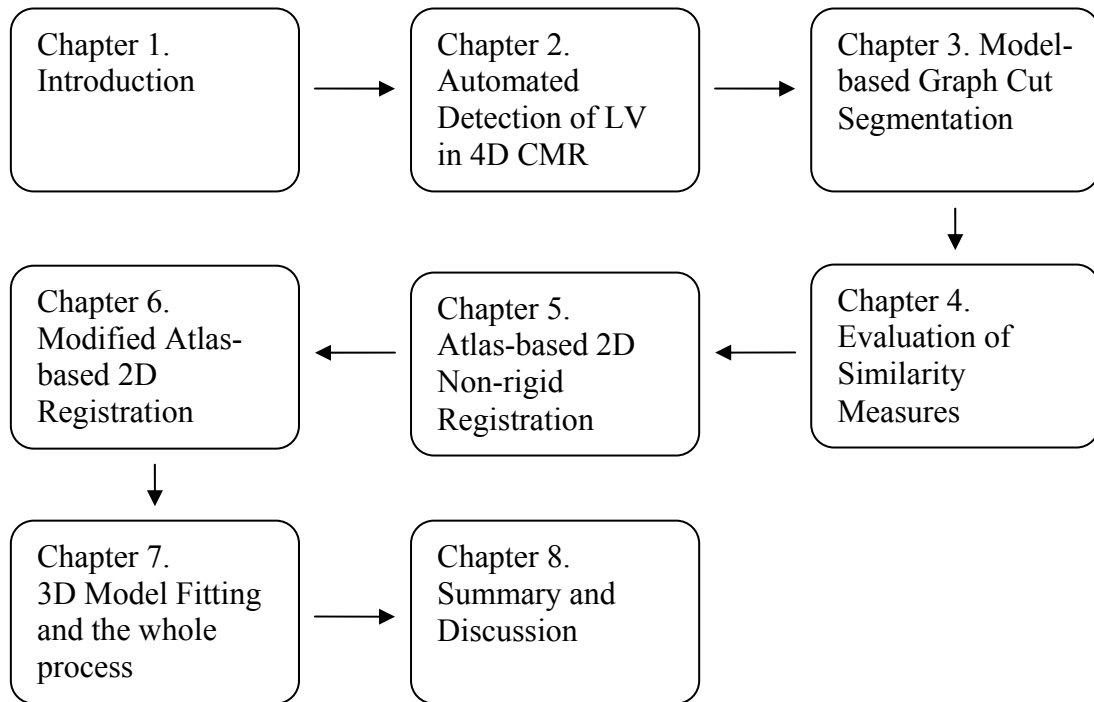


Figure 1.7 Flow chart showing the contents of each chapter.

1.8 Achievements in the Thesis

The thesis has made novel contributions in a number of areas, which are outlined below:

- 1) Proposed a novel approach to successfully localize the initial position of the model in fully automated segmentation procedures (Chapter 2). This is the first time a temporal Fourier analysis has been used to achieve a fast localization of the heart without user input. The method has been validated with large clinical datasets and can be used for initial estimation of pose and scale in cardiovascular segmentation or detection applications.
- 2) Developed a method for the incorporation of high-level information from a model into a low-level graph cut segmentation algorithm (Chapter 3). Although the method was not applied further in automated segmentation applications, it has the potential in the future for higher accuracy in good quality images.
- 3) Systematically examined the effect of different similarity measures for the objective function in atlas based segmentation (Chapter 4). Six popular measures in inter-

modality and intra-modality domains were investigated. The results show that no measure has an overall advantage over the others. The selection is not always straightforward and should depend on the system requirements, for example the relative priority of accuracy, robustness and capture range requirements.

- 4) Developed a new framework for 2D atlas based segmentation of the LV and RV (Chapter 5 & 6). The proposed framework was proven to have good performance, high accuracy and robustness with large clinical datasets. It also shows that the ability of integrating intensity, boundary and anatomical information into one framework provides better performance.
- 5) Developed and validated a new system for 3D feature based segmentation of the heart (Chapter 7). The system combines 2D atlas-based registration with 3D automated model fitting. The heart model was iteratively updated by the incremental addition of slices. The system was validated using large clinical datasets incorporating studies from different countries; it is therefore expected to be robust in future clinical applications.

2 Automated Detection of the Left Ventricle on 4D CMR Images

In this chapter, a fully automated method to estimate the location and orientation of the LV from multi-slice CMR images is developed and validated. The method is based on low-level image processing techniques that incorporate anatomical knowledge, and are able to provide rapid robust feedback for further processing. The method relies on a novel combination of temporal Fourier analysis and simple contour detection to achieve a fast localization of the LV without user input.

Quantitative validation was performed using two clinical datasets, obtained from a number of imaging centres around the world, containing 395 patients (63720 images) with a range of cardiac and vascular disease. Ground truth LV location and orientation were determined by two experienced observers and were compared with the automatic results.

The method failed in only one case. In the others, the average bias and precision was better than 5mm in the apical, middle and basal SA slices. These errors were similar to those associated with the original SA image orientations as planned by experienced technicians, indicating that the accuracy of the method is comparable with current clinical practice. The method also successfully detected LV position and orientation in lower resolution breath-hold cine-scout scans suitable for automated scan planning (bias and precision $< 6\text{mm}$).

2.1 Introduction

A robust, accurate and fully automatic method is required for the identification of heart location and orientation from CMR examinations. The method is targeted at clinical applications and therefore must be fast, efficient and reliable. It should be able to return the location, orientation and approximate contours of the LV in the absence of any user input. The method is expected to have two important applications. Firstly, the detected LV contours could be used as input to higher level segmentation methods such as deformable model based analyses. Secondly, the method could be used to speed up the image acquisition process by facilitating automatic planning of CMR examinations.

2.1.1 Fully Automated Left-ventricular Segmentation

Segmentation of the LV in CMR images is important for the quantitative assessment of cardiac function. Many automated approaches at different levels of image processing have been proposed to solve this problem. Low level techniques dependent on only local image intensity characteristics are fast but lack robustness. *A priori* knowledge can be incorporated into deformable model-based approaches; however, the efficiency and robustness of these methods is heavily dependent on the initial contours or models. Most semi-automatic methods still require manual initialization [28].

Fully automatic algorithms have been proposed but many of these are computationally intensive [4] or lack a wide range of clinical validation [2]. One [73] has been validated in 121 cases, but is limited in that it assumes the location of the heart is approximately at the centre of the MR image. Although specialized methods have also been proposed for tagged [74] and perfusion images [75], their application to patients with a wide range of clinical disease remains uncertain.

2.1.2 Automated Scan Planning

Automated CMR image planning has been proposed as a strategy for speeding up scan acquisition [14, 76, 77] and is also likely to improve the consistency of scan planning. The core requirement is for a fast and accurate calculation of the 3D position and orientation of the LV. A deformable template based method [76], which estimated the LV axis by fitting many feature points of the major thoracic organs in the localizer images, was computationally intensive. To avoid this problem, [77] proposed another method which employed *a priori* knowledge of the average LV direction to speed up the procedure. The scout images were then segmented by thresholding and both the LV and RV were localized by comparison with morphologic characteristics of the candidate objects. In our experience the inherent variability of images in patients with pathology compromised the robustness of this method.

2.1.3 Assumptions

This chapter focuses on fast, simple methods to automatically estimate heart location and orientation in order to provide rapid feedback to higher level processes. A novel feature of the method is that it relies on 4D images and detects characteristic features in the spatio-temporal behaviour of the cardiac structures. The assumptions of the method are listed

below. Any cases which violate these assumptions (e.g. congenital heart disease in which the LV and RV are transposed) would not be expected to be solved by this method.

- 1) The heart is the only large organ in the thorax with a temporal fundamental frequency equivalent to the cardiac cycle.
- 2) The orientation of the heart is similar across a wide variety of (non-congenital) cardiac pathology (this assumption is validated below).
- 3) The SA slices are acquired with SSFP ECG gated breath-hold cine sequences oriented approximately orthogonal to the long axis of the LV (it is shown below that this assumption is not restrictive, in that a standard fixed orientation also performs well).
- 4) The positions of the LV in adjacent slices are spatially and temporally coherent.
- 5) The septal myocardium is close to the centroid of the heart and has the LV and RV blood pools on each side. Also, the boundary between the LV blood pool and septal myocardium is not degraded by large papillary muscles or trabeculations (a reasonable assumption since these are not typically expected in this region anatomically).

The procedure was validated using two large datasets obtained in the course of clinical trials undertaken by our laboratory. In the first, images from 330 ONTARGET patients with vascular disease were used to optimize the method parameters and determine the average orientation of the heart relative to the magnet axes. The method was then tested on images from a second trial comprising of 65 ZEST patients with aortic stenosis, none of which were used to determine algorithm parameters. To determine the utility of the method for automated scan planning, it was also applied to the lower resolution, fixed orientation, CINE-SCOUT dataset of 14 healthy volunteers.

2.2 Method

The method is based on the novel combination of the Fourier transform (FT) in the temporal domain with *a priori* orientation and shape information in CMR coordinate system. The FT is employed to calculate an average (DC) image and first harmonic (H1) power image for each cine slice. The output of the FT is then used to derive a region of interest (ROI) and the

threshold level which robustly delineates the LV. This four step process is summarized below and a flow chart is shown in Figure 2.1:

- 1) Organize the temporal frames for each slice and apply the FT over time to obtain the DC and H1 images for each slice (Section 2.2.2).
- 2) Compute a ROI for each slice and the centroid for the whole heart from the H1 images (Section 2.2.3).
- 3) Find a pixel on the septal myocardium and compute the threshold level to delineate blood from myocardium in the midventricular DC image (Section 2.2.4).
- 4) Threshold the DC image and locate the LV on all slices (Section 2.2.5).

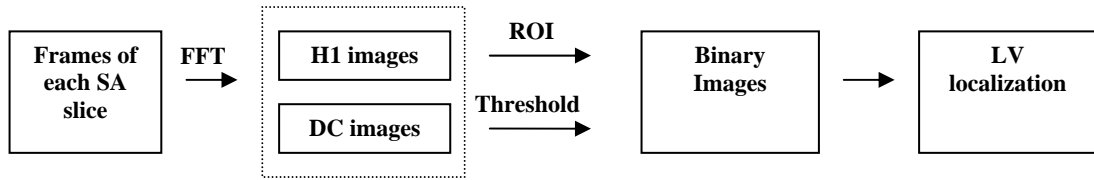


Figure 2.1 Flow chart of the LV localization

2.2.1 Patient Data and Ground Truth

Three clinical datasets are utilized in this study. The ONTARGET dataset contained 330 patients with cardiac and vascular disease recruited from eight MR centres world-wide as enrolled in the CMR substudy to ONTARGET. This study was the source of the *a priori* heart orientation information which is integrated into the method. Data from the ZEST dataset was used for independent validation purposes since no *a priori* knowledge was taken from that dataset. In order to evaluate the performance in lower resolution cine-scout images, the CINE-SCOUT dataset including 14 healthy volunteers was also tested. The orientation of these cine-scout scans was fixed to be normal to the average LA orientation found in the ONTARGET dataset, and all 8 low-resolution SA slices were obtained in a single breath-hold. This experiment was performed to ascertain the feasibility of future applications of the method in automated CMR scan planning.

The ground truth for the heart location and orientation was determined manually by two experienced technicians operating independently on the end-diastolic images. The 3D orientation of the LV long axis (\mathbf{V}_x) was defined by two points manually placed in the middle of the LV blood pool at the apex and the base respectively (Figure 2.2a and b). The

orientation of the RV (\mathbf{V}_y) was defined by the centroid of points placed on the endocardial insertions of the RV free wall to the LV on all SA slices showing the RV (Figure 2.2c). The remaining axis (\mathbf{V}_z) was oriented posteriorly to complete a right handed coordinate system (Figure 2.2d) [78]. The average manual directions $\bar{\mathbf{V}}_x$, $\bar{\mathbf{V}}_y$ and $\bar{\mathbf{V}}_z$ from all ONTARGET cases were then computed for use in the automated method below.

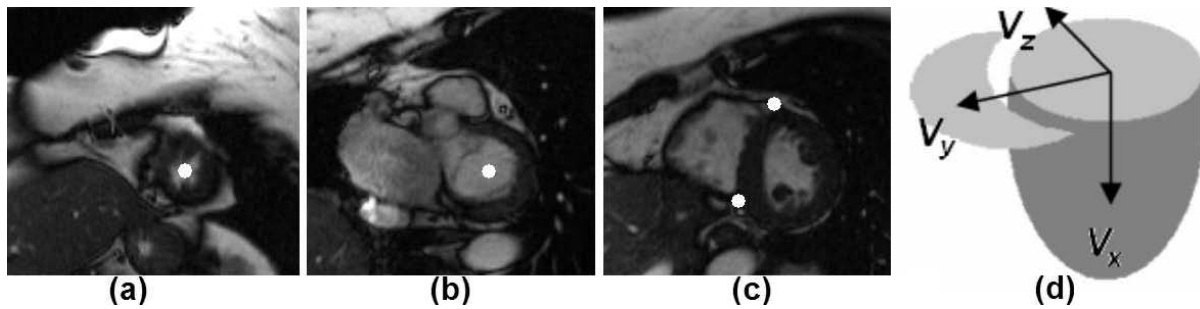


Figure 2.2 Manual definition of LV orientation. (a) centre of the LV on an apical SA slice, (b) centre of the LV on a basal SA slice, (c) RV insertion points for defining \mathbf{V}_y and (d) right handed coordinate system.

2.2.2 Fourier Transform over Time

The heart is the only large structure in the thorax with substantial motion at a frequency given by the heart rate. This characteristic makes the heart distinguishable by analyzing changes in pixel intensity. Figure 2.3 shows two typical pixel intensities through time. P_{in} is a pixel at the boundary between the LV blood pool and the septal myocardium and its intensity changes through a large range over time. P_{out} is also located close to the boundary of two different structures but outside of the heart. Its intensity changes are relatively minimal. Previously, the standard deviation of temporal pixel intensity signal has been used to locate the heart [11, 12], however it was found that in around 20% of ONTARGET cases the standard deviation images were contaminated by excessive high frequency noise (Figure 2.5c). The differences between P_{in} and P_{out} are most clearly appreciated in the magnitude of the first harmonic (H1) component of the temporal FT in comparison to the other components (Figure 2.4). The FT for every pixel in the image was therefore computed and the DC component (Figure 2.5a) and H1 image (Figure 2.5b) were employed in the subsequent analysis. This method provides excellent delineation of the cardiac structures, as well as the great vessels such as the aorta.

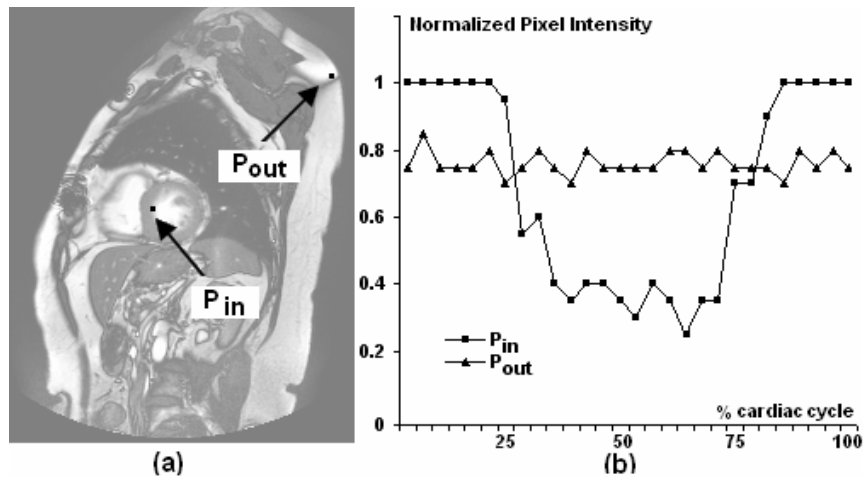


Figure 2.3 Temporal analysis of two pixels: (a) image showing a pixel near a moving boarder inside the heart (P_{in}) and a pixel near a stationary boarder (P_{out}), (b) pixel intensity change in the time sequence.

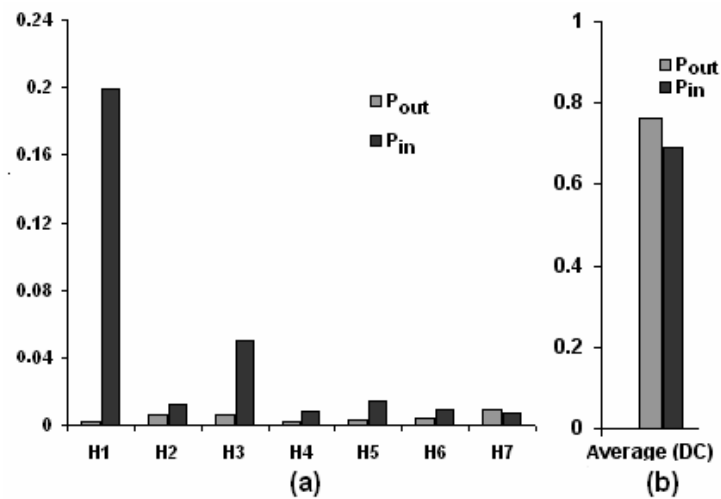


Figure 2.4 Comparison between P_{in} and P_{out} in Figure 2.3 for their magnitude of (a) the first seven frequency components and (b) the DC components.

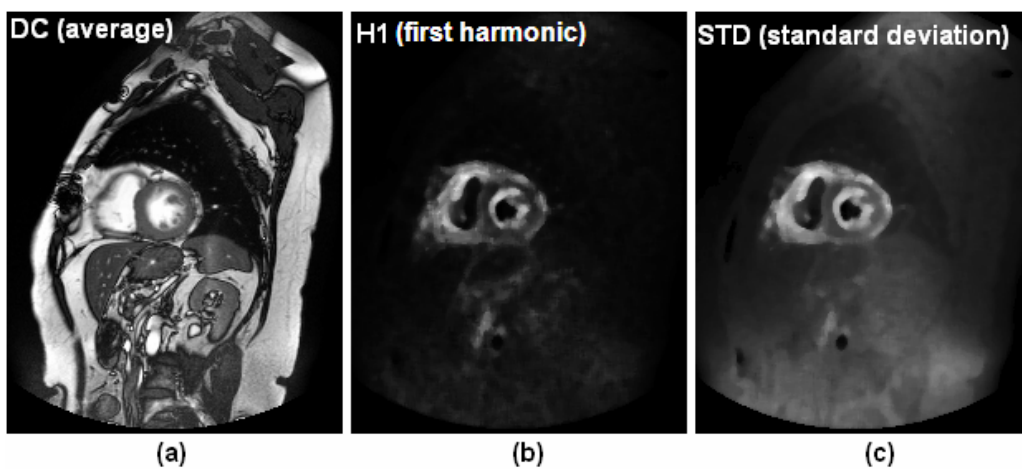


Figure 2.5 Temporal Fourier Transforms for each pixel in the time sequence: (a) DC (average) image, (b) H1 (first harmonic) image and (c) standard deviation image for comparison to H1 image.

2.2.3 Fast ROI Analysis

A cardiac centroid and ROI containing the heart were calculated from the H1 images for each slice as follows. Firstly, in order to reduce the effect of low level noise and signal from non-cardiac structures, the H1 images were filtered with a 5x5 median filter and all pixels with a magnitude less than 5% of the maximum magnitude within the overall 3D volume were set to zero. The 3D volume after thresholding is called the H1 volume.

Secondly, the ROI for each slice was iteratively refined using the following steps -

- 1) The centroid of the H1 image was computed for each SA slice.
- 2) A 3D line was fitted to the centroids of all the SA slices by linear least squares.
- 3) A distance distribution of all H1 pixels to the 3D line was calculated and weighted with each pixel's intensity value.
- 4) A Gaussian curve was fitted to this distribution and all pixels greater than a certain distance from the line were removed. The cut position to define this cylinder of interest was calculated using the following equation and is also shown in Figure 2.6:

$$r = \mu + \sqrt{2} \operatorname{erf}^{-1}(x)\sigma \quad (2)$$

where r is the radius of the cylinder of interest, x is the percentage of the pixels the cylinder should include (95% on our experiments), μ is the mean and σ is the standard deviation of the Gaussian distribution.

- 5) The 3D centroid of the H1 volume was then computed and compared to the previous 3D centroid.

Iteration terminated when the distance between successive 3D centroids was less than one pixel. In most cases, the iteration terminated after only one loop. Finally, the ROI was adjusted on each slice individually using the Gaussian fitting method to produce circular ROI of appropriate radius on each slice. Figure 2.7 shows that the iterative method successfully avoided high H1 signals from non-cardiac structure in a problem case which required more iterations than usual.

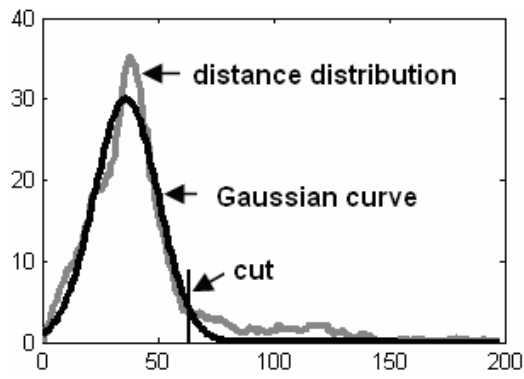


Figure 2.6 Gaussian fitting and the cut for the 3D cylindrical ROI



Figure 2.7 Iterative approximation of the circular ROI for each SA slice of the H1 images (apex to base from left to right and the rows from top to bottom showing results after every 10 more iterations).

2.2.4 Parameters for Blood Pool Segmentation

In order to provide an initial segmentation of the LV blood pool, as well as a separation of the RV and LV blood pools, the DC images were cropped by their respective circular ROI

(Figure 2.8a) to locate a pixel within the septal myocardium. Firstly, the mid-ventricular SA slice was defined as the closest slice to the 3D centroid of the H1 volume (designated the middle SA slice throughout this thesis). The centre of the ROI was obtained by intersecting the least squares 3D line (from Section 2.2.3) with the slice, marked C in Figure 2.8a. This point was almost always close to the inter-ventricular septum. A line passing through C was defined in the average direction of the RV (\bar{V}_y) which was constant for all patients. The intensity of the DC image along this line (Figure 2.8b) was used to locate the septal point S by searching for a local minimum within the region where the curve was less than the average intensity level (M_1 and M_2 are the two intersection points between the average intensity level and the curve in the neighbourhood of S). The LV could then be located on the $-\bar{V}_y$ side of the point S .

The threshold level which best discriminated the blood and myocardial signals was then determined by searching for the pixel with the maximum gradient between M_1 and M_2 (max in Figure 2.8c). To avoid the noise and uncertainty inherent in analyzing only a single line, eight additional lines at one pixel intervals parallel to \bar{V}_y were also analyzed, and the average value of these results was computed.

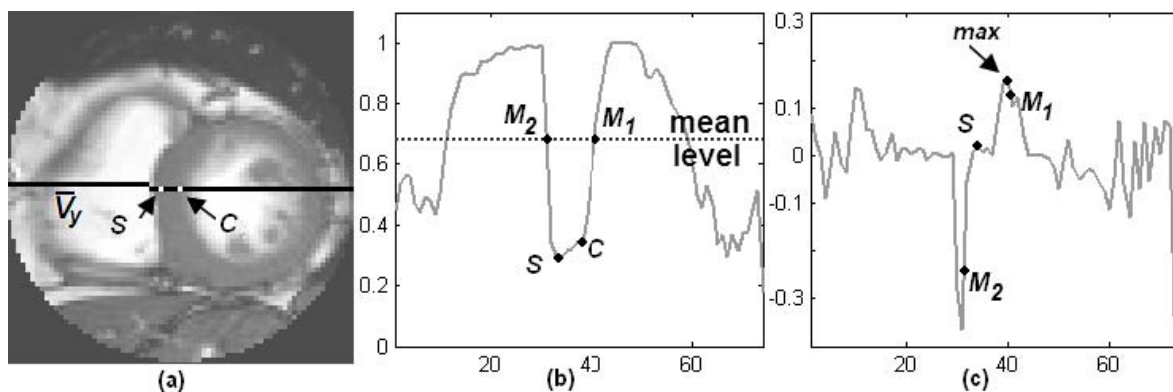


Figure 2.8 Calculation of the threshold level for LV segmentation; (a) search line shown on the ROI image, (b) intensity for each pixel showing a local minimum for the septum S , (c) intensity gradient for each pixel showing the position of the maximum gradient (max).

2.2.5 LV Localization

The LV blood pool in the middle SA slice was localized by thresholding (with the level computed above) and detecting the object on the $-\bar{V}_y$ side of S , as shown in Figure 2.9a. A

convex hull (Figure 2.9b) was then used to reduce the impact of the papillary muscles (as done in many other studies e.g. [74, 77]).

To find the LV blood pool in adjacent slices, a modification of the method proposed in [74] was employed. The analysis was based on binary images created by thresholding, assuming that the LV blood pool is spatially coherent between slices. The threshold segmentation from the middle SA slice was projected to its two neighbouring SA slices (towards the base and the apex) and the binary objects obtained were compared with the middle SA slice. Rather than project the region in the direction normal to the slice [74], the projection was performed in the average long axis direction \bar{V}_x in order to improve robustness to the orientation of the image planes. The binary object most similar to the projection in each slice was then selected. The similarity of the two objects was calculated by a measure called the similarity index (SI) which has been widely used for the segmentation evaluations [34, 79, 80]. The SI will also be applied in the following chapters as one of the important quantitative measures for evaluation of the segmentation methods. If C_1 and C_2 are two object contours and A is the area function, the SI can be formulated as:

$$SI(C_1, C_2) = \frac{A(C_1 \cap C_2)}{A(C_1) + A(C_2)} \quad (3)$$

Figure 2.9b shows a middle SA slice with the detected LV blood pool superimposed on it. This region is projected to its neighbouring slice in Figure 2.9c and the most similar object is then found in Figure 2.9d. Finally, the convex hull is applied to the new region in Figure 2.9e.

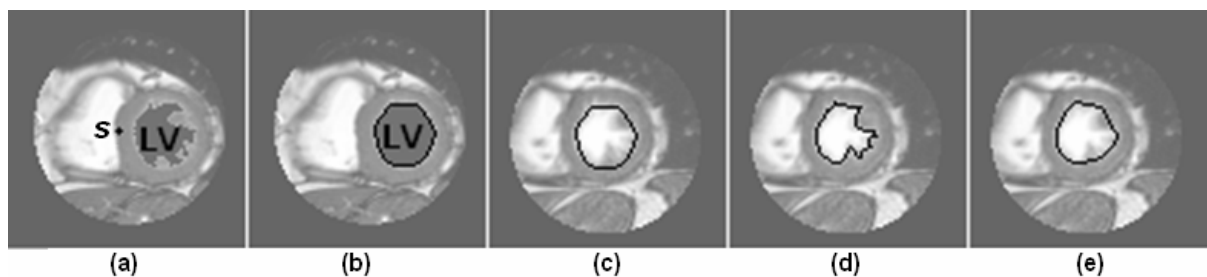


Figure 2.9 Locating the LV blood pool (a) LV blood pool detected on the middle SA slice by thresholding, (b) convex hull applied to the middle SA slice, (c) projection of the LV blood pool onto an adjacent slice, (d) thresholding and selection of the most similar binary object as the detected LV blood pool, and (e) convex hull applied to the new slice.

With this method, the LV regions on all slices were located (Figure 2.10). The similarity between the projected and binary regions could be very low on some SA slices because of leakage of the blood pool region through the valves during thresholding. A more robust measure than SI was applied. The erroneous connection between ventricles could be detected by evaluating the ratio of the LV perimeter on the current slice versus the middle SA slice. Once the value was larger than a trigger level (θ_{in} in Table 2-1, fixed by experience) then an iterative erosion operation was started to separate the two ventricles. When the erosion operation could not satisfy the acceptable level (θ_{out} in Table 2-1, fixed by experience) within 6 iterations, no LV region was reported, as shown in Figure 2.10f. A 3D line was then fitted to the centroids of the resulting LV regions to define the automated \mathbf{V}_x for each patient.

	Short-axis Slice	Trigger level θ_{in}	Acceptable level θ_{out}
Apex	other apical slice	1	0.55
	Middle - 2	1.3	0.7
	Middle - 1	1.4	0.8
	Middle + 1	1.6	1
	Middle + 2	1.8	1.1
Base	Other basal slice	1.3	0.9

Table 2-1 Levels defined for leakage detection and improvement evaluation in each slice.

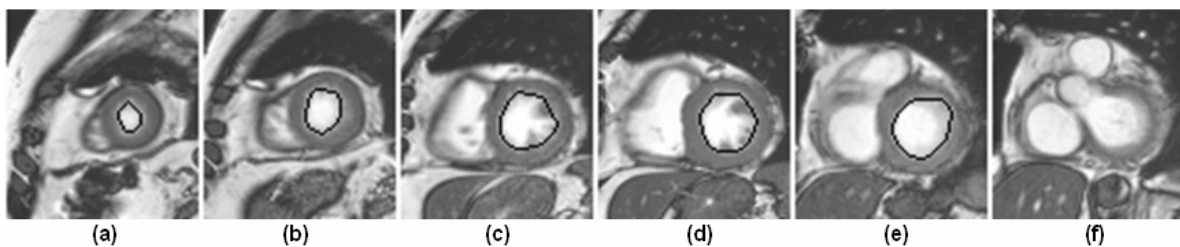


Figure 2.10 Example of the detected LV blood pool on all SA slices (apex to base from left to right).

2.3 Results

The fully automated method was implemented in Matlab and each case required approximately 4.13 seconds (not compiled) to run on a PC (Pentium IV 3.2GHz) for each case, excluding the DICOM file reading time. The first experiment was performed on the 330 cases in the ONTARGET dataset which had initially been used to define the average directions $\bar{\mathbf{V}}_x$, $\bar{\mathbf{V}}_y$ and $\bar{\mathbf{V}}_z$. Typical results of LV blood pool detection are shown in Figure 2.10. The algorithm failed to detect the LV in only one case, in which it found the RV

instead. To validate the robustness of the method with completely independent data, it was then tested against the ZEST and CINE-SCOUT datasets. These contained 79 independent cases which had not been used in any way during the development of the method. There were no failures in these groups. Errors between the manual and automatic methods are reported below.

2.3.1 ONTARGET Results

- **Failed Case**

The algorithm detected the RV instead of the LV in one case (Figure 2.11). The failure was due to the abnormal H1 images which caused the improper computation of the ROIs.

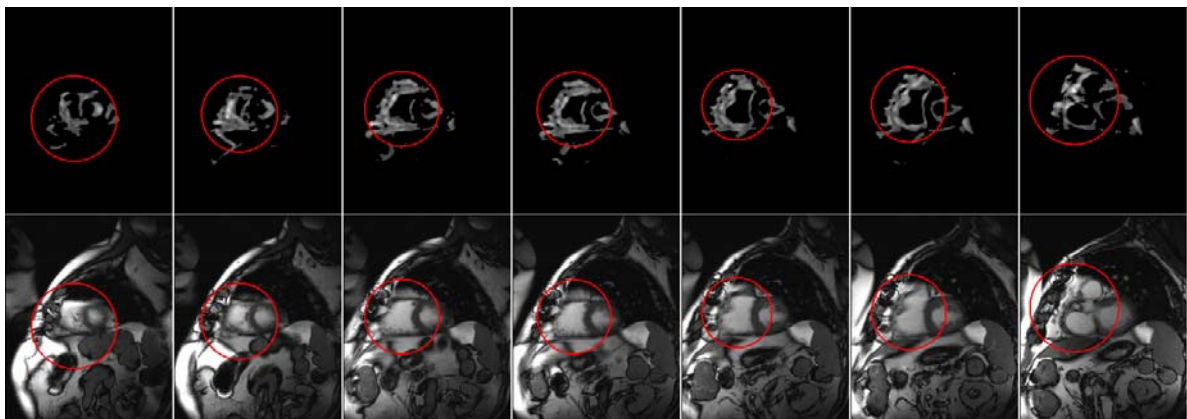


Figure 2.11 The failure due to the improper ROIs computed from the H1 images: top row – H1 images and the ROIs, bottom row – DC image with ROIs.

- **Angular Errors**

The average directions, \bar{V}_x , \bar{V}_y and \bar{V}_z computed by Observer A and Observer B show a good agreement with a difference between analysts of 0.4, 3.0 and 3.0° respectively. In 98% of cases, the average direction \bar{V}_x was within 24° of V_x (for Observer A, the worst case). These results show that the 3D LV orientation is remarkably consistent across patients, and validates assumption 2 in Section 2.1.3 above.

The inter-observer error of the orientation of V_x in ground truth was defined from the differences between Observers, which was $3.5 \pm 2.4^\circ$. The differences between the ground truth V_x (Observer A and B) and (i) the automatic method, and (ii) the normal to the original SA image planes defined by the technologist during scanning, are given in Table 2-2. The

magnitudes of the automatic errors were very similar to the errors associated with the manual positioning of SA scans during planning at the MRI scanner.

▪ **Position Errors**

In order to compute the position errors, both the ground truth \mathbf{V}_x and the automated \mathbf{V}_x were intersected with the image planes and the vector between the two intersections calculated relative to the ground truth reference. The slices closest to the apex and base and the slice midway between these two are presented for the purposes of comparison. Figure 2.12 shows the distribution of errors for the worst case (Observer A) for the ONTARGET data. It can be seen that the automatic results and the ground truth agree closely with each other. There is a small systematic bias in the \mathbf{V}_z direction which may be caused by conceptual differences between the manual and automatic methods (for example the ground truth \mathbf{V}_x was measured only at end-diastole while the automatic \mathbf{V}_x was based on images from throughout the cardiac cycle).

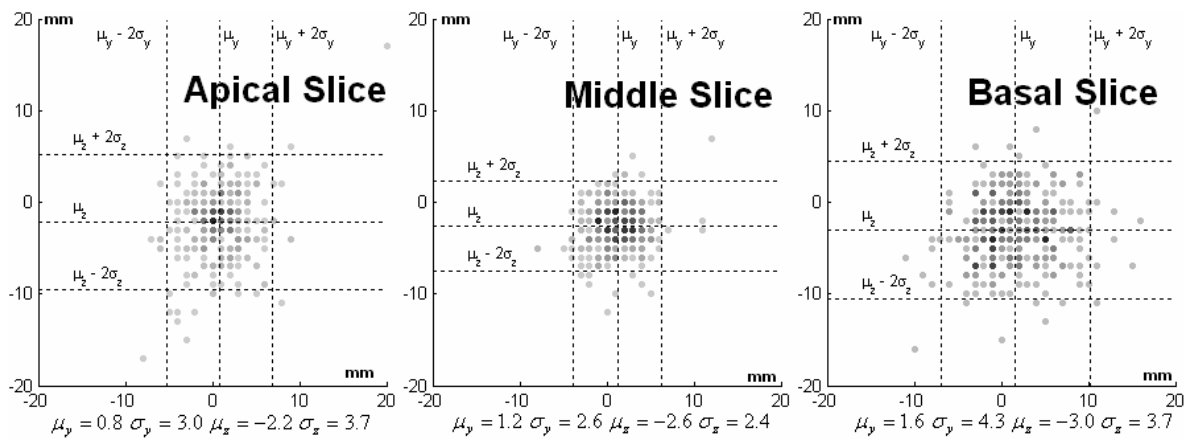


Figure 2.12 2D histogram (mm) between automatic \mathbf{V}_x and Observer A (worst case) on apical, middle and basal SA slices for the ONTARGET dataset (mean and standard deviation shown for y and z directions under each plot). Darker points refer to higher number of cases with errors located in these bins (size: 1mm x 1mm). Dotted lines show limits of agreement ($\mu \pm 2\sigma$).

2.3.2 ZEST Results

As the ONTARGET dataset had been used during the development of the method for the determination of $\bar{\mathbf{V}}_x$, $\bar{\mathbf{V}}_y$ and $\bar{\mathbf{V}}_z$, the ZEST dataset comprising 65 patients was used to provide an independent test. The same methods were used to calculate the angular and the position errors, which are also presented in Table 2-2 and in Figure 2.13. No failures occurred and the errors were similar to those from the ONTARGET dataset. The apparent

bias in this and the following datasets was not addressed further, due to the relatively small number of cases.

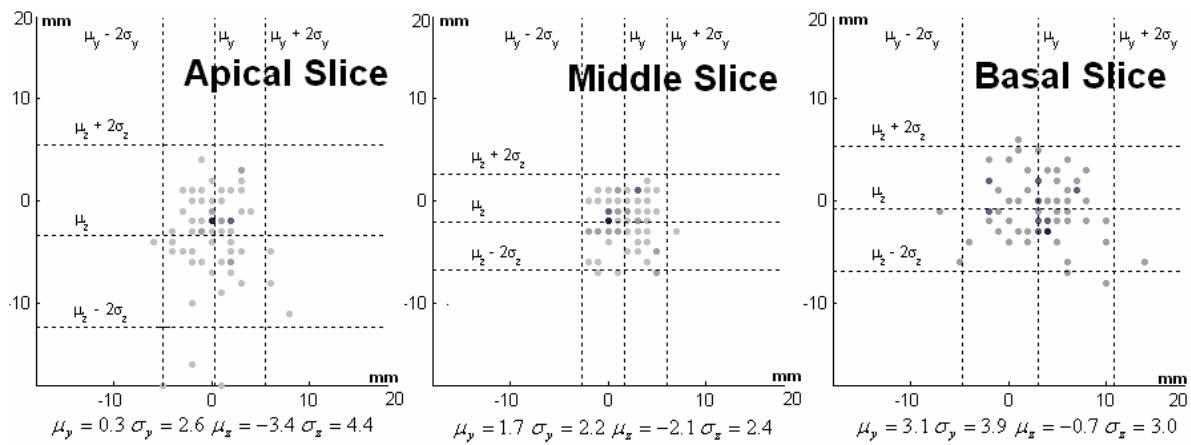


Figure 2.13 2D histogram (mm) between automatic V_x and Observer A (worst case) on apical, middle and basal SA slices for the ZEST dataset (mean and standard deviation shown for y and z directions under each plot).

2.3.3 CINE-SCOUT Results

To determine the utility of the method in automated scan planning, the method was applied to 14 healthy volunteers imaged in fixed orientations (given by the normal to \bar{V}_x) in a 8 slice, 10 frame single breath-hold acquisition. No failures occurred and the errors are presented in Table 2-2 and Figure 2.14.

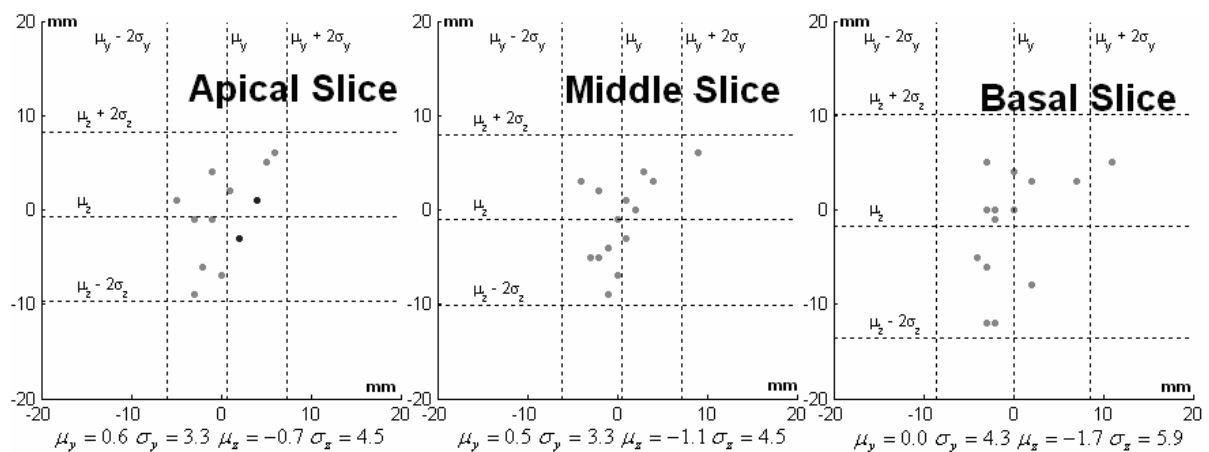


Figure 2.14 2D histogram (mm) between automatic V_x and Observer A (worst case) on apical, middle and basal SA slices for the CINE-SCOUT dataset (mean and standard deviation shown for y and z directions under each plot).

Dataset Name	Experts	Case numbers	Automatic V_x	Normal to SA scan plane
ONTARGET	Observer A	329	6.4 ± 4.4	6.3 ± 3.7
	Observer B	329	6.1 ± 4.1	6.8 ± 4.0
ZEST	Observer A	65	6.2 ± 4.7	6.5 ± 3.7
	Observer B	65	5.6 ± 4.1	7.6 ± 4.7
CINE-SCOUT	Observer A	14	7.1 ± 3.2	10.1 ± 4.5
	Observer B	14	7.6 ± 3.6	9.5 ± 4.4

Table 2-2 Comparison of the orientation errors (mean \pm standard deviation in degrees) relative to manual identification of the LV long axis orientation V_x . In the ONTARGET and ZEST datasets, the parallel SA scan planes were planned to be approximately orthogonal to V_x during image acquisition and should therefore have normals aligned with V_x . In the CINE-SCOUT dataset, the image orientations were fixed to \bar{V}_x .

2.4 Discussions

2.4.1 Achievements

A novel method is proposed for the automatic detection of the location and orientation of the heart in cine CMR image data. The method exploits the motion of the heart by first applying a pixel based Fourier analysis over time, and utilizes the dynamic characteristics of the heart to make the localization fast and efficient. Even in severely diseased hearts, this method successfully identifies the heart in most cases. The algorithm has many possible application areas. For example, it could be used in conjunction with low resolution cine-scout scans to design an efficient solution for heart location within an automated image scan planning process. It could also be employed to provide a high quality initial position for more detailed CMR segmentation algorithms. Applications to other cardiovascular objects or other modalities may also be possible. These application areas are discussed in more detail below.

- **Possible solution to CMR scan planning**

The standard scan planning process is designed to locate the heart and adjust the SA scan planes to be perpendicular to the central long axis of the LV. This procedure involves the acquisition of standard scout scans and manual identification of the canonical axes of the heart. The scan planning process could therefore be simplified with an automated scan

planning procedure. Previously, [76] used a deformable template method to estimate the LV long axis by fitting many feature points of major organs in the thorax to the scout images. This method is computationally intensive if a large number of feature points are selected; however, the number of failures and the accuracy of the result will be affected if fewer points are used. Variations in the shape and position of the other organs will also introduce errors to the results. Jackson *et al.* [14] employed *a priori* knowledge of the average LV axis to speed up the procedure and then used the EM algorithm to automatically detect the threshold of the blood pools. The LV and RV were localized by comparison of the morphologic characteristics of the binary objects that are obtained with thresholding. However, experiments performed using this method were insufficiently robust in both the step of computing the threshold and the morphologic comparison, most probably because of the lack of an efficient technique to define the ROI. The proposed method solves this problem by utilizing the H1 image from a temporal Fourier analysis. This provided excellent delineation of cardiac structures and can be used to define the ROI and approximate orientation of the heart.

The errors between the planned SA image orientations and the manually determined 3D central axis of the LV were similar to the errors associated with the automated detection method. This suggests that the method could be applied to low resolution cine-scout scans for the purposes of automatically determining the location of the high resolution SA cine images. Most CMR scanners now enable multiple low resolution cine images to be obtained during a breath-hold [81]. The above results showed that errors in LV orientation were only slightly increased when applied to lower resolution cine-scout images acquired in fixed orientations. Thus, this method shows promise in the application of automated scan planning using standard cine-scout acquisitions. Further work needs to be done to determine whether similar results are obtained in larger clinical datasets.

- **Initial estimate for high-level segmentation**

A review of model based LV functional analysis procedures can be found in [82]. These have considerable potential for accurate and robust segmentation and analysis of LV function in CMR images, due to the incorporation of *a priori* knowledge of heart shape and motion. Statistical variations in shape and motion can also be used to constrain the segmentation problem, using a database of models derived from many cases [83]. However, most of these methods require an initial estimation of the pose and scale (including position

and orientation) of the heart. The current method can be used to provide this initial estimate, and also provide a rough initial segmentation of the LV. The only *a priori* knowledge incorporated into the method at present is the average direction of the long axis of the LV $\bar{\mathbf{V}}_x$ and average direction of the RV $\bar{\mathbf{V}}_y$, as determined from the ONTARGET dataset. This information is necessary to make the method robust enough for clinical practice. However, more information would be useful in the future to improve the segmentation's accuracy and robustness. For example, a 3D LV model can be used to fit the contours detected in the method to solve the segmentation leakage problem which frequently occurred on basal slices, leading to no segmentation result being reported on these slices (e.g. Figure 2.10f).

In this thesis, the above method is extended in Chapter 5 to provide a high quality initial estimate for model based segmentation of both the LV and RV at the same time.

- **Applications in other areas**

In addition to these application areas, the success rate of the method (one failure in 395 cases) suggests that it may also be useful in other imaging modalities, such as ultrasound and CT. The characteristics of the H1 image also imply new applications in other areas. For example, large arteries such as the aorta have similar dynamic characteristics to the heart and the method may be used as an efficient tool for proximal vessel detection. Another possible application area is image registration, in which the localization is normally the first problem to be solved. It can also be used to solve other localization problems outside of the medical image processing area where the fundamental frequency of the target object's movement is approximately known and obviously different from the other objects and the background.

2.4.2 Limitations

The limitations of the method, in the application of LV segmentation, are that the detected LV contour is smaller than the real contour in many cases, and only a subset of slices can be segmented. This is because it is not possible to avoid blurring over time at the boundaries of the LV in the DC images, and the *a priori* knowledge incorporated in the method is limited. Chapter 5 provides one possible extension to incorporate higher level information. The algorithm employed in the current chapter to detect the boundary between the LV blood pool and the myocardium is simply based on the analysis of the intensity values of the line passing through the centroid of the H1 volume. To avoid segmentation errors, pixels at the blood pool side were selected for threshold computation when searching for the boundary

between the blood and myocardium. While this does not greatly affect the accuracy of the long axis orientation, the detected contour is not sufficiently accurate for LV functional analysis. However, this rough segmentation is designed only for use as an initialization for more accurate methods, which may include model-based analysis of RV and LV function (see Chapters 5-7).

2.5 Conclusions

In this chapter, a fully automatic method of determining the position and orientation of the LV from multislice cine MR images was presented. It has been found to be both efficient and robust. The errors in the automated method are similar to those found when the orientation of the normal to the short axis scan planes are compared with LV long axis ground truth data.

3 Model-based Graph Cuts Method for Automated Segmentation

Graph cuts have been proposed for image segmentation problems where the cost of the cut corresponds to an energy function which is globally minimized. However, only when the object and background seeds in the algorithm are carefully designed can the global minimum be expected to be the desired solution. It is much easier to define the seeds in an interactive environment than with a system where automated methods are required. For automation, high level information must be included to ensure the graph cuts occur at correct places, but this has been difficult to add because of the graph structure.

In this chapter, a new method is proposed to integrate model-based *a priori* information into the graph cuts formulation. The method currently works well for the segmentation of LV endocardium and epicardium on the middle SA slice, and may be extended to other slices in the future.

The remaining sections of this chapter are organized as follows. In Section 3.1, the traditional graph cuts method is introduced and the drawbacks are discussed when implementing it in the medical image domain. A new model-based graph cuts algorithm is proposed and implemented to solve the LV segmentation problem in Section 3.2. Experiments on the model-based graph cuts in the estimation of the endocardial and epicardial boundaries are presented in Section 3.3. Section 3.4 presents the results and the discussions and conclusions can be found in Section 3.5.

3.1 Introduction

3.1.1 Graph Cuts

Graph cuts are a framework for solving energy minimization problems, which can utilize efficient algorithms from graph theory. Here we focus on two-label segmentation algorithms; graph cut algorithms for more than two labels are still NP-hard. A specialized graph is constructed to represent the energy function to be minimized. The minimum cut of the graph represents the minimum value of the energy function, typically computed by the efficient max flow algorithm.

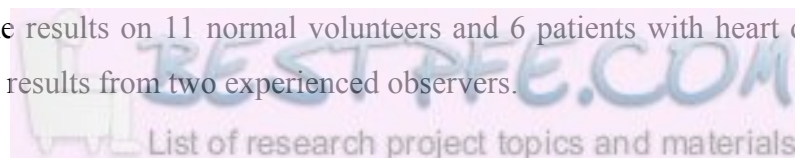
Fast graph cuts methods recently proposed in [48, 84] have proved to be efficient in practice. These algorithms have been used in many domains. In [84], it was used for 3D scene reconstruction from two views and was shown to be one of the top performers. Grabcut [85] is an efficient image editing tool based on the graph cuts concept. These studies show that the graph cuts method has high flexibility in interactive environments. Graph cuts methods can be found in a large variety of image analysis applications, and [48-50] show its application in CMR.

3.1.2 Disadvantages in Medical Image Analysis

Graph cuts methods have been widely used in image segmentations due to its ability to compute globally optimal solutions. For image segmentation, the graph is normally constructed from pixels and the graph cuts method results in a global minimum over the whole image. This solves the myopic problem that deformable model based methods often meet. It was reported in [84] that graph cuts can be applied only to a limited set of energy functions. Two kinds of low-level information constraints, boundary and regional constraints have been successfully integrated into the graph cuts framework. [48, 49] reported its successful application on CMR, liver CT, kidney MR and lung CT data using an interactive platform. Relatively few applications have been found that develop automated methods. A fully automated method for CMR segmentation was presented in [50]. All information used for constructing the graph was obtained directly from the image and thus no training was required. A simple spatial model was also used for finding good seeds, but was not actually integrated into the energy function. Without high-level constraints, the graph cuts method is insufficiently constrained to derive “good” solutions. Post-processing was reported to be necessary in [50]. Thus, it is desirable to include high level information into the graph cuts formulation.

3.1.3 Proposed Solution

This chapter proposes a method which is able to integrate model-based *a priori* information into a graph cuts formulation. A 2D LV spatial prior is pre-calculated for each frame from a 4D model prior which contains the LV endocardium and epicardium (Figure 3.2). The spatial prior is then combined with pixel intensity data and edge information in the graph cuts optimisation. Both epicardial and endocardial contours can be found using variations of this procedure. The results on 11 normal volunteers and 6 patients with heart disease were compared with the results from two experienced observers.



3.2 Method

3.2.1 Traditional Graph Cuts

▪ Graph Structure

The graph structure used in image segmentation is based on pixels. Suppose a graph Δ with vertices V and edges E , $\Delta = (V, E)$, is a directed graph with nodes corresponding to pixels $p \in P$ of a 2D image. Figure 3.1 shows a simple example constructed for an image of 3x3 size. The vertex set V includes not only the set P but also two additional nodes, the object terminal s and the background terminal t (shown as a red and a green node respectively in Figure 3.1). The edge set E includes two kinds of links, n-links N and t-links T . The t-links connect the pixels to the two terminals s and t . They indicate the individual label-preference of pixels. The red line t_1 and the pink line t_2 in Figure 3.1 are two t-links of the pixel p to s and t . The n-links are the connections between all neighbouring pixels, which encourage spatial coherence by penalizing discontinuities between neighbouring pixels [84]. The blue lines n_1 and n_2 are two n-links between p and one of its neighbours q but with opposite directions. The energy function built in such a graph cuts framework is described as the following:

$$E(f) = \lambda \sum_{p \in P} R(f_p) + \sum_{\{p, q\} \in N} B(f_p, f_q) \quad (4)$$

$R(f_p)$ is called region properties term and is governed by the t-links t_1 and t_2 . $B(f_p, f_q)$ is the boundary properties term, which is governed by the n-links n_1 and n_2 . λ is the weight balancing the two terms.

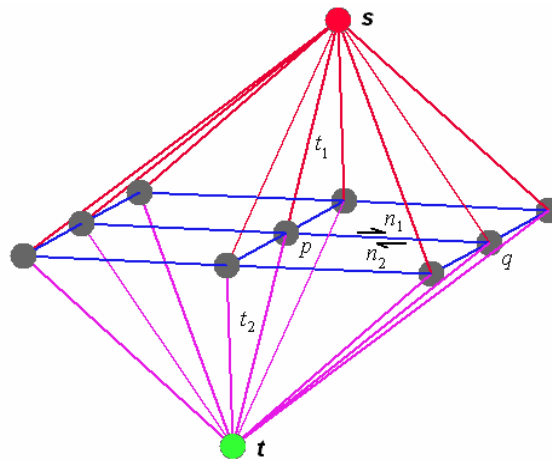


Figure 3.1 Graph structure constructed from a 9-pixels image.

- **Process of Graph Cuts**

Either t_1 or t_2 will be cut for every pixel in the solution. Also, n_1 and n_2 will both be cut if \mathbf{p} and \mathbf{q} belong to the different terminals. Each pixel will therefore be assigned to either object or background after calculation. The global cost of a cut is the sum of the costs of the edges which are cut by the solution. A minimum cost cut generates a segmentation that is the global optimal solution. The max-flow algorithm was reported to be able to solve this problem in polynomial time.

In order to reduce the process time and increase the robustness of the algorithm, initial object and background sets are often pre-defined. They can be manually defined through an interactive interface or automatically assigned by simple thresholding. The thresholding assigns correct labels to the pixels which definitely belong to the object O or background G set. The uncertain pixels are then determined by the graph cuts.

The definition of the values of the n-links and t-links is an active area of research. The approach described in [48, 84] is employed in this chapter. Assume I_p and I_q are the intensities of \mathbf{p} and \mathbf{q} . n_1 and n_2 are normally set equal and computed by:

$$n_1 = n_2 = \exp\left(-\frac{(I_p - I_q)^2}{2\sigma^2}\right) \cdot \frac{1}{\text{dist}(\mathbf{p}, \mathbf{q})} \quad (5)$$

where $\{\mathbf{p}, \mathbf{q}\} \in N$ and σ is a parameter based on the intensity range which can be the standard deviation of all pixels. t_1 and t_2 are defined by:

$$t_1 = \begin{cases} -\ln(\Pr(I_p|G)) & \mathbf{p} \notin O \cup G \\ K & \mathbf{p} \in O \\ 0 & \mathbf{p} \in G \end{cases} \quad (6)$$

$$t_2 = \begin{cases} -\ln(\Pr(I_p|O)) & \mathbf{p} \notin O \cup G \\ 0 & \mathbf{p} \in O \\ K & \mathbf{p} \in G \end{cases} \quad (7)$$

where K is a constant larger than n_1+n_2 . $\Pr(I_p|O)$ and $\Pr(I_p|G)$ are the probability of \mathbf{p} being an object or background based on its intensity. If the intensity distribution of objects is assumed to be a normal distribution with μ_o and σ_o , the probability can be computed by

$$\Pr(I_p | O) = \frac{1}{\sqrt{2\pi\sigma_o^2}} \cdot \exp\left(-\frac{(I_p - \mu_o)^2}{2\sigma_o^2}\right) \quad (8)$$

The value of the constant part $1/\sqrt{2\pi\sigma^2}$ in t_1 and t_2 are very similar after the log operation, so that it can be considered as a constant and ignored in practice. The same assumption can be used in $\Pr(I_p | G)$. Thus, if $p \notin O \cup G$ t_1 and t_2 are simplified to

$$\begin{aligned} t_1 &= \frac{(I_p - \mu_G)^2}{2\sigma_G^2} \\ t_2 &= \frac{(I_p - \mu_o)^2}{2\sigma_o^2} \end{aligned} \quad (9)$$

- **Disadvantages**

The disadvantage with this approach is that there are only two terms in the energy function to be minimized. It has been proven that the problem is NP-hard if more than two terminals are required in the graph shown in Figure 3.1 [86]. The structure of the graph also prevents integration of high level knowledge, such as curvature-driven terms or anatomy-driven constraints into the energy function, which has been proven useful in [20]. The model-based graph cuts method for LV segmentation proposed here is able to integrate spatial information provided by the cardiac model into the graph cuts, without introducing more terms into the energy function.

3.2.2 Model-based Graph Cuts Method

Typically, t-links are assigned weights based on the information of the pixels themselves while n-links are assigned weights based on the interaction between neighbouring pixels. *A priori* spatial information for each image can be derived from the intersection of the image plane and the initialized cardiac model. This defines two spatial priors for each image. The object spatial prior defines the probability of being an object for each pixel location. The background spatial prior defines the probability of being a background pixel.

- **Probability Representation**

Assume S_p is the spatial information of p , then the value at S_p in the object spatial prior is the probability of p being an object at that position, written as $\Pr(S_p|O)$. If the probability of p being a background at that position is written as $\Pr(S_p|G)$, it follows that

$$\Pr(S_p|O) + \Pr(S_p|G) = 1. \quad (10)$$

Since $\Pr(I_p|O)$ and $\Pr(S_p|O)$ do not affect each other, they represent two independent events. The probability of p being part of the object $\Pr(p|O)$ can now be given by the multiplication of the spatial and intensity probabilities:

$$\Pr(p|O) = \Pr(I_p|O) \cdot \Pr(S_p|O).$$

A weight β can be added to specify the relative confidence of these two probabilities. So, the probability of a pixel being an object is

$$\Pr(p|O) = \Pr(I_p|O)^{1-\beta} \cdot \Pr(S_p|O)^\beta. \quad (11)$$

If the log-like functions are employed for the t-links as in [48], they can be written as

$$\begin{aligned} t_1 &= -\ln\left(\Pr(I_p|G)^{1-\beta} \cdot \Pr(S_p|G)^\beta\right) \\ t_2 &= -\ln\left(\Pr(I_p|O)^{1-\beta} \cdot \Pr(S_p|O)^\beta\right) \end{aligned} \quad (12)$$

where p is any pixel except seeds. Thus, the t-links functions then become

$$\begin{aligned} t_1 &= (1-\beta) \cdot \frac{(I_p - \mu_G)^2}{2\sigma_G^2} - \beta \cdot \ln(\Pr(S_p|G)) \\ t_2 &= (1-\beta) \cdot \frac{(I_p - \mu_o)^2}{2\sigma_o^2} - \beta \cdot \ln(\Pr(S_p|O)) \end{aligned} \quad (13)$$

- **Construction of Spatial Prior with Model**

The model prior is constructed on the basis of anatomical knowledge. The great merit of the model-based segmentation method is the ability to integrate historical information into a probabilistic map. Given a database of previously analyzed cases, an average shape and motion can be found which can be applied to new cases [78].

The spatial prior is established by scaling and orienting the historical model prior to match the length and orientation of the particular subject. This step is performed by placing fiducial markers on the apex and base of the LV and at the insertions of the right ventricular free wall. The intersection of the model with each image plane gives two prior LV contours. The inner lines are the endocardial prior contour C_{endo}^o and the outer lines are the epicardial prior contour C_{epi}^o Figure 3.2.

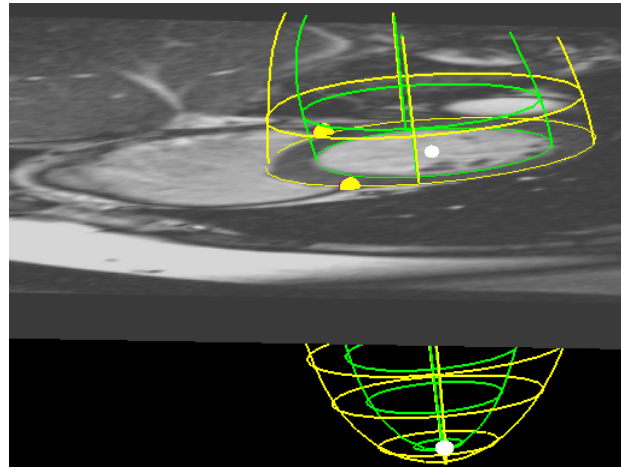


Figure 3.2 Intersection of LV model and middle SA slice.

3.3 Implementation

The middle SA slice was selected for this experiment because on that slice the position of the spatial prior was closer to the ground truth. The LV shape was also more regular than other slices.

3.3.1 Segmentation Process

The model-based graph cuts segmentation process consists of two steps. The first step is to detect the boundary of the endocardium. In this step, quality of the spatial prior does not affect the result too much because of the thick LV wall. In order to cover a majority of the blood pool, a spatial prior constructed from C_{epi}^o (Figure 3.3b) is used in this step instead of C_{endo}^o . The area inside of C_{epi}^o was filled and then smoothed with a 7×7 Gaussian smoothing kernel to form the spatial prior. The size of the kernel is based on the size of C_{epi}^o . The result with and without using the spatial prior are also shown as two yellow curves in Figure 3.3c and Figure 3.3d, while the red dots give the ground truth. The ground truth includes the papillary muscles in the blood pool, which is found to be more reproducible than not

including the papillary muscles. With the force derived from the spatial prior, the endocardial contour expands in radial directions. The detected contour is much closer to the ground truth in comparison to the contour without using the prior.

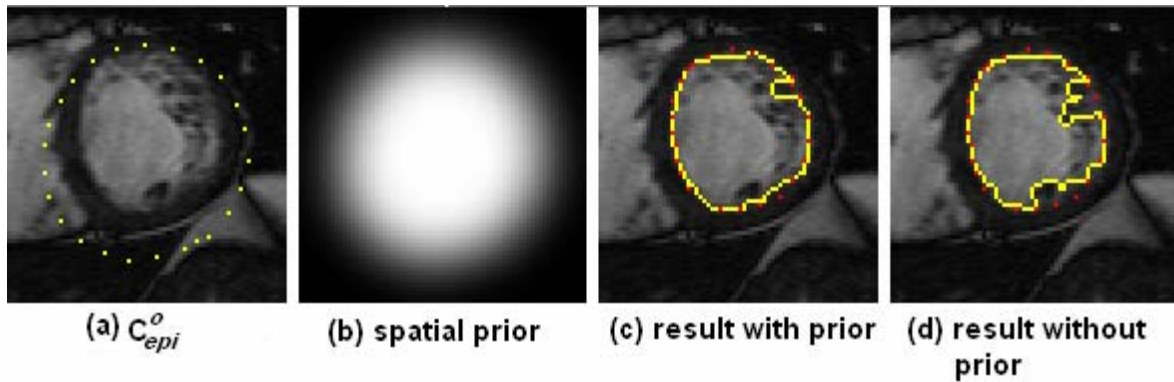


Figure 3.3 Example of using prior for LV endocardial segmentation.

After the estimation of the endocardial contour is finished, the same graph cuts method is used for the detection of the epicardial contour. In this case the spatial prior is obtained by spreading and smoothing the endocardial contour (Figure 3.4). The idea is motivated by the anatomical constraint used by Paragios et al. in their level set method [20], and assumes that the distance between the two contours is relatively constant. The distance was estimated from the thickness of the septal myocardium. In this step, the spatial prior provides the main distinction between LV myocardium and RV myocardium. Thus, spatial priors not only integrate spatial information into the graph cuts but also introduce anatomical constraints such as uniform wall thickness.

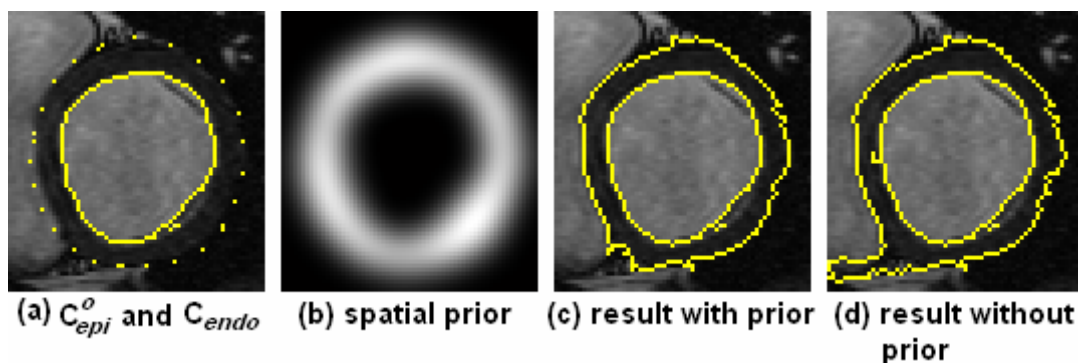


Figure 3.4 Example of using a prior for LV epicardial segmentation.

3.3.2 Evaluation Measure

A weighted modified Hausdorff distance function was used to quantitatively evaluate the estimated contours.

- **Hausdorff Distance**

The Hausdorff distance (HD) is a common measure for the evaluation of contour matching. It measures the longest distance from an arbitrary point in one contour to the corresponding nearest point in the other contour and vice-versa. Assume $A = \{\mathbf{a}_1, \mathbf{a}_2, \dots, \mathbf{a}_n\}$ and $B = \{\mathbf{b}_1, \mathbf{b}_2, \dots, \mathbf{b}_m\}$ are the point sets of two contours, the HD between A and B is

$$\text{HD}(A, B) = \max(d(A, B), d(B, A)) \quad (14)$$

where $d(A, B)$ is defined by

$$d(A, B) = \max_{\mathbf{a}_i \in A} d(\mathbf{a}_i, B) \quad (15)$$

and

$$d(\mathbf{a}_i, B) = \min_{\mathbf{b}_j \in B} \|\mathbf{a}_i - \mathbf{b}_j\| \quad (16)$$

Unfortunately, HD is sensitive to any noisy point on the contours.

- **Modified Hausdorff Distance**

The modified Hausdorff distance (MHD), proposed in [6], was reported to be more robust than the HD, which used the average instead of the maximal function in Eq. 15:

$$d(A, B) = \frac{1}{N_A} \sum_{\mathbf{a}_i \in A} d(\mathbf{a}_i, B) \quad (17)$$

Thus, the MHD is

$$\text{MHD}(A, B) = \max(d(A, B), d(B, A)) \quad (18)$$

where $d(A, B)$ follows Eq. 17.

If there exist two ground truth contours B and C , the error is computed by averaging:

$$\text{MHD}(A, B, C) = \frac{1}{2} [\text{MHD}(A, B) + \text{MHD}(A, C)] \quad (19)$$

- **Weighted Modified Hausdorff Distance**

Each image is treated equally in the above equation regardless of image quality. However, problems such as partial-voluming, movement of structure and low flip-angle will cause different image quality. For a more accurate evaluation, weights that are proportional to image quality should be added. It can be noticed that the MHD between two experts is smaller in high-quality images than in low-quality images. So, the weights can be inversely proportional to the MHD between B and C :

$$\text{MHD}_{\text{avg}} = \frac{\sum_{i=1}^N w_i \cdot [\text{MHD}(A_i, B_i) + \text{MHD}(A_i, C_i)]}{2 \sum_{i=1}^N w_i} \quad (20)$$

where

$$w_i = \frac{1}{\text{MHD}(B_i, C_i)} \quad (21)$$

A prerequisite condition of using this measure is that two ground truths need to exist; however, they are not always available. Thus, application of this measure is limited to this chapter and the MHD will be used in the following chapters.

3.4 Experiment

3.4.1 Data

The proposed method was applied to 17 cases, 11 normal cases and 6 cases from patients with heart disease. Each case had at least 6 SA slices and each slice had 28 frames in average. The image size of each frame was 256 x 208.

3.4.2 Result

The model produces prior contours for each phase on each slice. The left column of the images in Figure 3.5 shows the initial contours C_{endo}^o and C_{epi}^o . A group of spatial priors were obtained by smoothing each C_{epi}^o . Then the endocardial contours C_{endo} were computed (2nd column). Another group of spatial priors for the epicardium segmentation were obtained by dilating each C_{endo} before the epicardial contours were calculated (3rd column). The contours detected by the algorithm were reasonable in comparison to the gold standard

contours (4th column) from experts. Figure 3.5 also shows the behaviour of the algorithm in the presence of papillary muscles. If the papillary muscles are adherent to the myocardium, they are considered as part of the myocardium. If the connection between the papillary muscle and the myocardium was not so strong, it may be cut.

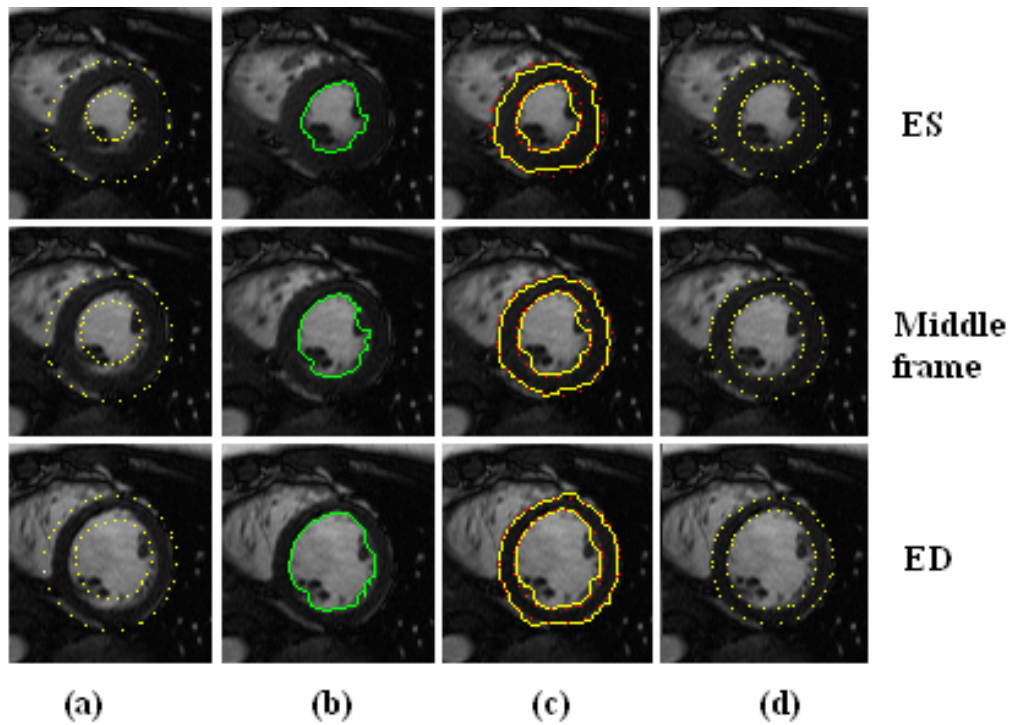


Figure 3.5 Results on ES, middle and ED frames of a middle SA slice. (a) initial contours for spatial priors, (b) detected endocardium, (c) detected endocardium and epicardium, (d) ground truth.

3.4.3 Parameter Optimisation

Two weights are required to be optimized: λ which balances the boundary and regional terms and β which is the weight of the spatial probability in the regional term. Nine sets of parameters with different values of λ from 0.5 to 2 and β from 0.3 to 0.7 were selected for parameter optimisation and an average error was obtained for each patient with each parameter set. Box and whisker plots (or called box plots) of the data are shown in Figure 3.6. The best pair was number 3 which is $\lambda = 2$ and $\beta = 0.7$.

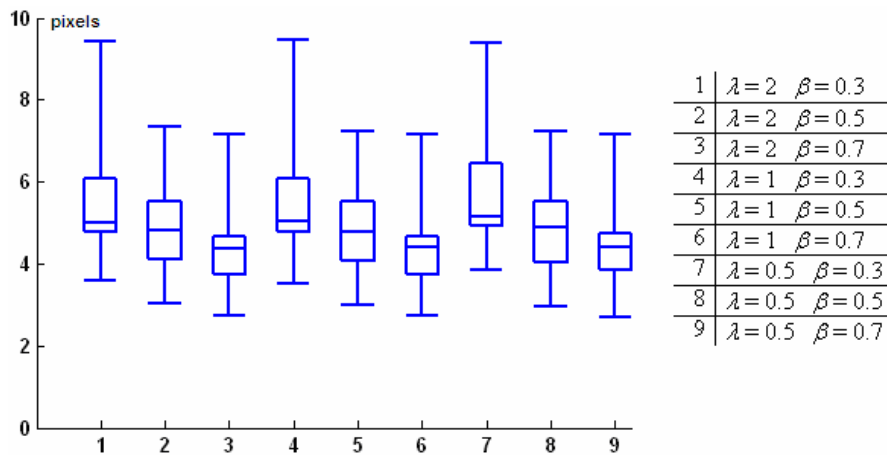


Figure 3.6 Box plots of the MHD for 9 sets of parameters.

3.5 Discussions and Conclusions

3.5.1 Achievements

The algorithm is a demonstration of the integration of high-level model-based knowledge into the graph cuts algorithm. It inherits the ability of the graph cuts to provide a global optimum for the entire image, while overcoming the limitation of using only low-level data. The spatial prior derived from the model contains not only spatial information but also some anatomical knowledge. This feature is particularly important when the low-level information is unable to determine the correct segmentation: for example in the cut between the RV myocardium and the LV myocardium. A modified Hausdorff distance measure showed good agreement between the model-based graph cuts and the expert observers in a midventricular slice.

3.5.2 Further Work

An iterative process can be performed if more accurate results are required. The results obtained from the graph cuts algorithm can be considered as the initial data for the model fitting. The parameters of the model, such as shapes, sizes, positions and orientations will be updated by tailoring the model to fit the data. The updated model can then provide more accurate initial contours for further image analysis.

The analysis could also be considered in the context of propagation from image to image. The shape of the contours does not change too much from one image to the next, either in the spatial domain or in the temporal domain. The contours propagated from neighbouring images may greatly help the process in practice.

3.5.3 Limitations

Further development and improvement is required to solve failures in some cases. It has been found that because only the septum was used to extract the thickness of the myocardium, the algorithm often failed when the septal myocardium was much thinner than the free wall. Another problem comes from the attached papillary muscles, which affects the dilation step to obtain a good spatial prior for the epicardium. Furthermore, the current model only includes the LV so it is unable to segment the RV. Even if LV RV model is used, the method may still have difficulty in the RV segmentation. The thin RV free wall will cause leaking problems if parts of the boundaries are blurred. The spatial prior can provide proper constraints for the algorithm only when correct location information is available, which is difficult in the RV free wall area.

It has been shown that the algorithm has limitations in the context of fully automated CMR segmentation, and may perform better in an interactive environment than a fully automated one. Thus, it was not implemented in the automated segmentation procedures studied in the remainder of this thesis.

4 Evaluation of Similarity Measures for Atlas-based Rigid-body Registration

Atlas-based segmentation treats image segmentation as a registration problem. The registration algorithm finds the transformation that maps the pre-segmented atlas image on to the target image (the image that requires segmenting). The segmentation defined on the atlas is transformed to the target image, thereby performing the segmentation of the target image. The method has been widely used in many medical applications: the neurosystem [63, 70-72, 79, 80, 87-99], cardiovascular system [4, 64-67, 100-104], bone system [70, 105], prostate [70] and lung [106]. The selection of an efficient similarity measure is one of the key tasks in atlas-based image registrations because it determines the error surface to be minimized by the registration algorithm. The success of the algorithm is greatly improved if an energy function has a large capture range, few local optima and high accuracy at the global optimum. A lot of effort has been focused on developing new measures to solve different image registration problems. Many studies have recently been performed to evaluate these measures in specific registration domains; however, a detailed evaluation of atlas-based registration in CMR segmentation has not yet been performed. This chapter examines similarity measures in the context of rigid atlas based segmentation, using a comparison framework independent of the optimisation algorithm.

Atlas-based registration can be considered as intermediate between intra-modality¹ and inter-modality² registration domains. Six similarity measures widely used in both domains are investigated and evaluated. A new Simple Multi-Property Labelled (SMPL) atlas-based registration framework is introduced which can simplify the computational complexity of the registration algorithms based on different similarity measures. These were quantitatively compared with each other using performance criteria derived from the literature. Brute-force examination of the global optimum's neighbourhood and the evaluation of non-rigid registrations are computationally prohibitive, therefore only rigid-body registrations are considered in this chapter.

¹ Registration of images from the same imaging modality, for example, CT to CT

² Registration of images from different imaging modalities, for example, CT to MRI

Results show that mutual information (MI) and normalized mutual information (NMI) have better performance at the areas close to the global optimum while sum of squared difference (SSD) and normalized cross-correlation (NCC) have wider capture range and less local optima in the total region of interest. The results of this chapter are used in subsequent chapters to further develop the new atlas-based non-rigid registration framework for segmentation.

The chapter is organized as follows. Section 4.1 reviews the existing literature on comparisons of different measures in various registration domains. Six measures are considered to have strong potential in atlas-based registration. In Section 4.2, these six measures are simplified for use in the new atlas-based registration framework. Section 4.3 describes how to establish the evaluation platform and how the measures are quantitatively evaluated. Detailed implementations can be found in Section 4.4. The results are presented in Section 4.5. The discussions and the conclusions can be found in Section 4.6.

4.1 Similarity Measures

Each similarity measure has its own specific properties and application domains. A similarity measure which performs well in intra-modality registrations may not be suitable for inter-modality studies. Comparisons between them are essential and have been well studied.

In this section, the recent literature is reviewed with the main intention of comparing different similarity measures in both intra-modality and inter-modality domains. Similarity measures applied in current atlas-based registration applications are also investigated. MI and NMI are two measures often used in this domain; however, with no quantitative comparison, the performances of other measures are still unknown. Six measures widely used in both the intra-modality domain and the inter-modality domain are selected for the experiments.

4.1.1 Review of Similarity Measure Comparisons

This has been an area of extensive research over the last two decades. Recently published articles are reviewed in this section (previous comparisons can be found in [56, 57]) with a focus on the measures selected for comparison rather than their results.

Six measures of registering 3D magnetic resonance angiography (MRA) images to 2D x-ray angiography images were compared in [107]. These were NCC, MI, gradient cross-correlation (GCC), entropy of difference image (EDI), pattern intensity (PNI) and a combination of the GCC and PNI methods. NCC is a standard algorithm that estimates the degree to which two images match. GCC is the application of NCC on the gradient map of an image. MI is based on the information theory relating marginal entropies and joint entropy (JE) of two registration images. EDI measures the entropy of the difference between two registration images (called the difference image). PNI aims to minimise the number of patterns present in the difference image. However, methods based on gradient maps or difference images miss most of the information contained in the original images and are seldom used in atlas-based registration.

[108] compared five measures for the registration of SPECT and MR images: MI, Wood's method (WD), correlation ratio (CR), automatic multi-modality image registration (AMIR) and statistical parametric mapping (SPM). CR is based on the concept that the co-occurrence of intensity values between two images should be maximized when they are registered. A very similar concept was applied in WD. AMIR also uses a similar cost function but requires the images to be pre-segmented. SPM converted the inter-modality problem to intra-modality problem by using statistical parametric mapping techniques.

In [109], eight different measures were studied for the rigid body registration of 3D brain MR images over time. These were SSD, EDI, MI, NCC, NMI, PNI, ratio of image uniformity (RIU) and a variant of the RIU measure (MRIU). RIU seeks to minimise the variance of the ratio image, the division between two registration images. MRIU improved RIU by adding a constant to both the numerator and the denominator to reduce the bias. However, similar to difference images, ratio images are seldom used in atlas-based registration.

MI, JE, RIU and NCC were compared in [110] for registration between different weighted MR images. Four measures, CR, NCC, MI and chi-square statistic (CSS), were examined in [111] for registration of portal images and 3D CT images. CSS was based on the Pearson's chi-square test between the joint histogram and the matrix product of two marginal histograms. Unfortunately, the method was not robust enough for global registration [112]. [113] provided a comparison of five common measures for the inter-modal registration of

brain images: WD, CR, JE, MI and NMI. They showed that only CR, MI and NMI performed well in heavily misaligned cases.

The latest comparison for rigid registration of MR images can be found in [114]. It examines six measures and three optimisations. The measures included SSD, NCC, CR, MI, NMI and gradient mutual information (GMI). GMI combines the gradient map and MI [115].

[116] proposed a new protocol to independently evaluate measures. Nine measures were compared for the intra-modality registration of head images, including MI, NMI, WD, CR, JE, entropy correlation coefficient (ECC), energy of histogram (EH) and two feature-based MI measures. ECC is a variant of the of NMI method. EH computes the energy of the joint histogram, which is found not frequently used as a measure. Their further study on non-rigid registration in [117] focused on six of these nine measures: MI, NMI, CR, JE, EH and one feature-based measure. The comparison protocol developed in [116, 117] is employed in this chapter to construct the comparison framework for atlas-based CMR registration.

A detailed comparison in atlas-based registration environment has not been widely discussed. A comparison was found in [89] but the measures selected for comparison are not in the current mainstream. A close study on the comparison of the performances of NMI, MI, NCC and SSD in brain registration was just investigated in [118]. However, only accuracy was compared in their work.

Seven similarity measures which appeared in three or more of the above articles are summarized in Table 4-1:

Measures	Acronym	Articles
Mutual Information	MI	[107] [108] [109] [110] [111] [113] [114] [116] [117] [118]
Correlation Ratio	CR	[108] [111] [113] [114] [116] [117] [118]
Normalized Mutual Information	NMI	[109] [113] [114] [116] [117] [118]
Normalized Cross Correlation	NCC	[107] [109] [110] [111] [114] [118]
Joint Entropy	JE	[110] [113] [116] [117]
Sum Squared Difference	SSD	[109] [114] [118]
Wood Method	WD	[108] [113] [116]

Table 4-1 Measures which appeared in three or more of the above articles.

4.1.2 Similarity Measures in Atlas-based Registrations

Atlas-based registration can be considered as an intermediate between intra and inter-modality registration. Choosing a measure to adapt to atlas-based registration is not always straightforward. Major considerations for the successful application of a measure are:

- 1) How successful can the intensity relationship between atlas and the objects in the image can be modelled? Similarity measures for inter-modality registrations may be more suitable when the relationships are not easily modelled, otherwise it may be better to use intra-modality measures.
- 2) How accurate can the atlas's initial estimate be? The size of capture range becomes important if the initial estimate is not close to the final solution, alternatively the accuracy may become the dominant factor in the selection of a measure if the initial estimation is close.
- 3) Other factors such as the computational cost and the background modeling processes also need to be considered.

- **Cardiac applications:**

A joint-probability based similarity measure was used in [64] for the registration of a 3D statistical shape model to CMR images. A similar strategy was applied in [65]. A detailed cardiac atlas was constructed which not only contained two ventricles but also the background. NMI was selected as the similarity measure for the registration. NMI has also been used in [4, 66, 67, 104]. A platform based on the NMI was developed in [119] for virtual cardiac surgeries.

- **Brain applications:**

NMI and MI are used extensively in brain registration [70, 80, 87, 92, 93]. SSD was applied as the similarity measure in [72] for both rigid and non-rigid registrations of 3D brain MR images. The quasi-Newton method was used for optimisation since analytic derivatives are available for SSD. The method was reported to be efficient and fast.

Unfortunately, no detailed comparison of all aspects of a measure's performance has been found for atlas-based registration. Thus, the true difference in performance between each measure, particularly in CMR segmentations, is still unknown.

4.1.3 Similarity Measures Selected for Comparison

For general application, only the most common measures were considered for the comparisons performed in this chapter. Six of the seven measures shown in Table 4-1 were selected: SSD, NCC, WD, CR, MI and NMI. JE was excluded since JE, MI and NMI are inherently similar and JE's performance in all four cited articles was worse than MI or NMI. These six measures are separated into two categories:

- intra-modality measures: SSD and NCC;
- inter-modality measures: WD, CR, MI and NMI.

4.2 SMPL Atlas-based Registration Framework

Traditional atlas-based registration algorithms map pixels in the target image onto pixels in the atlas [93] by minimizing a particular similarity measure. A new framework, SMPL (Simple Multi-Property Labelled) atlas based registration, was proposed in this thesis to obtain higher accuracy with lower computational cost (Chapter 4) and to integrate intensity, anatomical and boundary information (Chapter 5 and 6). In the SMPL framework, the atlas is no longer represented as an image but is treated as a set of mathematical points that have various properties such as intensity values, confidence weights and anatomical labels. The registration procedure maps each point from the atlas onto its best corresponding position in the target image. Linear interpolation in the target image is implemented to give sub-pixel resolution to the results. Advantages of the new framework include -

- 1) only objects of interest, rather than the whole image, are included in the atlas thereby reducing computational burden.
- 2) each atlas object has a fixed number of points so similarity measures can be simplified.
- 3) the atlas can be sampled at sub-pixel resolution (relative to the target image) to reduce artefacts caused by linear interpolation.
- 4) weights can be defined for all points in the atlas if statistical or probabilistic information is available.

- 5) boundary points and other features can be specified in the atlas and used to provide additional information for the registration process.
- 6) anatomical information such as identification of sub-regions of the heart muscle can be included.

The current chapter discusses the first two advantages. The six similarity measures are reformulated to integrate these two advantages and are compared to their general representation used in image registration. The other advantages will be exploited where appropriate in the next chapter.

In general, it is assumed that two registration images X and Y have an overlapping of M pixels. (x_m, y_m) where $m = 1, 2, \dots, M$ are the intensity pairs of corresponding pixels after interpolation. In the SMPL atlas-based registration framework, the number of pixels for computation is greatly reduced because only objects of interest, rather than the whole overlapping area, are considered. Assume that the atlas I_a consists of K objects of interest I_{ak} where $k = 1, 2, \dots, K$. I_{ak} is assumed to have n_k points with the same intensity label λ_k . The coordinates of these points are defined as a_{ki} where $i = 1, 2, \dots, n_k$. The total number of atlas points is $N = \sum_{k=1}^K n_k$ and the percentage of the number of each object's points I_{ak} is given by w_k which is:

$$w_k = \frac{n_k}{N} \quad (22)$$

w_k is not changed during the registration. Let I_t denote the target image and T the transformation of the registration. The coordinates of a_{ki} after registration can be written as $a'_{ki} = T(a_{ki})$ and the target intensity value of that point is $I_t(a'_{ki})$. Thus, the corresponding points of I_{ak} in I_t are represented as:

$$I_{tk} = \{I_t(a'_{ki}) | i = 1, 2, \dots, n_k\} \quad (23)$$

which consists of the corresponding points of I_a :

$$I_{ta} = \{I_{tk} | k = 1, 2, \dots, K\} \quad (24)$$

4.2.1 Sum of Squared Difference

SSD is the simplest measure and one of the most widely used measures in intra-modality registration. The availability of the analytical expression for the derivative gives more options for optimisation. The general SSD form between X and Y is given by

$$\text{SSD}(X, Y) = \sum_{m=1}^M (y_m - x_m)^2$$

The representation is changed in the SMPL atlas-based framework to:

$$\text{SSD}(I_a, I_{ta}) = \sum_{k=1}^K \sum_{i=1}^{n_k} (I_t(a'_{ki}) - \lambda_k)^2 \quad (25)$$

To be consistent with the other measures, a negative sign is added to the formula:

$$\text{SSD}(I_a, I_{ta}) = - \sum_{k=1}^K \sum_{i=1}^{n_k} (I_t(a'_{ki}) - \lambda_k)^2 \quad (26)$$

4.2.2 Normalized Correlation Coefficient

NCC is another popular measure in intra-modality applications. It provides a quantitative measure of general least squares fitting of two images. The measure is suitable to cases where the intensities of corresponding pixels are linearly related, which is possible in atlas-based registration. The general NCC formula is

$$\text{NCC}(X, Y) = \frac{\text{Cov}(X, Y)}{\sqrt{\text{Var}(X)}\sqrt{\text{Var}(Y)}}$$

where the variance $\text{Var}(X)$, $\text{Var}(Y)$ and the covariance $\text{Cov}(X, Y)$ are defined by:

$$\text{Var}(X) = \frac{1}{M} \sum_{m=1}^M x_m^2 - \bar{X}^2 \quad \text{where} \quad \bar{X} = \frac{1}{M} \sum_{m=1}^M x_m$$

$$\text{Var}(Y) = \frac{1}{M} \sum_{m=1}^M y_m^2 - \bar{Y}^2 \quad \text{where} \quad \bar{Y} = \frac{1}{M} \sum_{m=1}^M y_m$$

$$\text{Cov}(X, Y) = \frac{1}{M} \sum_{m=1}^M (x_m - \bar{X})(y_m - \bar{Y})$$

These are simplified in the SMPL framework as follows:

$$\text{NCC}(I_a, I_{ta}) = \frac{\text{Cov}(I_a, I_{ta})}{\sqrt{\text{Var}(I_a)}\sqrt{\text{Var}(I_{ta})}} \quad (27)$$

$$\text{Var}(I_a) = \sum_{k=1}^K w_k \lambda_k^2 - \bar{I}_a^2 \quad \text{where} \quad \bar{I}_a = \sum_{k=1}^K w_k \lambda_k \quad (28)$$

$$\text{Var}(I_{ta}) = \frac{1}{N} \sum_{k=1}^K \sum_{i=1}^{n_k} I_t^2(a'_{ki}) - \bar{I}_{ta}^2 \quad \text{where} \quad \bar{I}_{ta} = \frac{1}{N} \sum_{k=1}^K \sum_{i=1}^{n_k} I_t(a'_{ki}) \quad (29)$$

$$\text{Cov}(I_a, I_{ta}) = \frac{1}{N} \sum_{k=1}^K \left((\lambda_k - \bar{I}_a) \sum_{i=1}^{n_k} (I_t(a'_{ki}) - \bar{I}_{ta}) \right) \quad (30)$$

4.2.3 Correlation Ratio

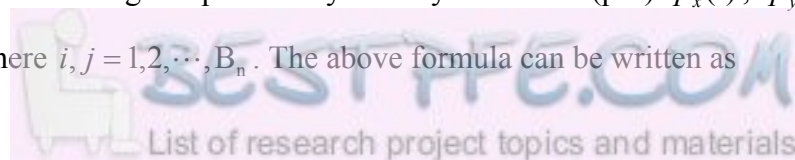
CR, proposed in [120], is mostly used for inter-modality applications [108, 110, 111, 121-125]. The measure computes the co-occurrence of intensity pairs between X and Y . Intensity pairs are constructed by the pixels in X and their corresponding pixels in Y . If X is clustered into several intensity bins, the intensity distribution of the corresponding pixels of each bin in Y can provide quantitative evaluation of the registration by using the standard deviation. This measure is not directly related to the intensity values so it can be used in inter-modality registrations. MI is similar to CR but MI uses the entropy to measure the co-occurrence instead. MI is more complicated than CR and not necessarily better in inter-modality registration applications such as [122, 124]. The general formula proposed in [120] is:

$$\text{CR}(X, Y) = 1 - \frac{\text{Var}(Y - E(Y|X))}{\text{Var}(Y)}$$

This is converted to the formula below for computation in practice:

$$\text{CR}(X, Y) = 1 - \frac{E_x(\text{Var}(Y|X = X_i))}{\text{Var}(Y)}$$

where X_i are the bins pre-defined in X . Assume both X and Y are categorized to B_n bins for the computation of the marginal probability density functions (pdf) $p_x(i)$, $p_y(j)$ and the joint pdf $p(i, j)$ where $i, j = 1, 2, \dots, B_n$. The above formula can be written as



$$\text{CR}(X, Y) = 1 - \frac{1}{\text{Var}(Y)} \sum_{i=1}^{B_n} \text{Var}(Y_i) p_x(i) \quad (31)$$

where

$$\text{Var}(Y) = \sum_{j=1}^{B_n} j^2 p_y(j) - \bar{Y}^2, \quad \bar{Y} = \sum_{j=1}^{B_n} j p_y(j) \quad (32)$$

$$\text{Var}(Y_i) = \frac{1}{p_x(i)} \sum_{j=1}^{B_n} j^2 p(i, j) - \bar{Y}_i^2, \quad \bar{Y}_i = \frac{1}{p_x(i)} \sum_{j=1}^{B_n} j p(i, j) \quad (33)$$

In atlas-based registrations, each object defined in I_a can be treated as a bin of the atlas. A different number of bins is defined in I_t . Each atlas bin has a fixed number of points in the new framework so the above formula can be simplified as below:

$$\text{CR}(I_a, I_{ta}) = 1 - \frac{1}{\text{Var}(I_{ta})} \sum_{k=1}^K w_k \text{Var}(I_{tk}) \quad (34)$$

The computation of $\text{Var}(I_{tk})$ can use Eq. 29. Unlike Eq. 33, Eq. 29 is bin-free:

$$\text{Var}(I_{tk}) = \frac{1}{n_k} \sum_{i=1}^{n_k} I_t^2(a'_{ki}) - \bar{I}_{tk}^2, \quad \bar{I}_{tk} = \frac{1}{n_k} \sum_{i=1}^{n_k} I_t(a'_{ki}) \quad (35)$$

4.2.4 Wood's Method

WD could be considered as an early version of the CR measure. The general format of the formula can be found in [126]. In the new framework, the main difference between CR and WD is that the denominator $\text{Var}(I_{ta})$ in CR is replaced by \bar{I}_{tk} in WD:

$$\text{WD}(I_a, I_{ta}) = \frac{1}{N} \sum_{k=1}^K w_k \frac{\sqrt{\text{Var}(I_{tk})}}{\bar{I}_{tk}} \quad (36)$$

However, this change does not make sense in atlas-based registration and causes poor performance, as shown in the following experiments. Like SSD, a negative sign is added to the formula to convert it to a global maximum:

$$\text{WD}(I_a, I_{ta}) = -\frac{1}{N} \sum_{k=1}^K w_k \frac{\sqrt{\text{Var}(I_{tk})}}{\bar{I}_{tk}} \quad (37)$$

4.2.5 Mutual Information

Similar to CR, MI makes no assumptions regarding the nature of the relationship between the intensity distributions in the pair of images being investigated. The measure of the co-occurrence of X and Y in MI is based on the theoretic notion of entropy according to the following equations:

$$\text{MI}(X,Y) = H(X) + H(Y) - H(X,Y) \quad (38)$$

where $H(X)$ and $H(Y)$ are the marginal entropy of X and Y respectively, and $H(X,Y)$ is their joint entropy:

$$H(X) = -\sum_{i=1}^{B_n} p_x(i) \log p_x(i) \quad (39)$$

$$H(X,Y) = -\sum_{j=1}^{B_n} \sum_{i=1}^{B_n} p(i,j) \log p(i,j) \quad (40)$$

where $p_x(i)$ and $p(i,j)$ is the marginal pdf and the joint pdf respectively. Interested readers are referred to [58], [127] and [57] for detailed explanations.

MI is sensitive to the interpolation scheme selected. Some interpolation algorithms will create obvious artefacts if new bins are introduced during the interpolation. This effect is discussed further in the implementation section. MI is also very computationally intensive. Most of the time is spent on the computation of the JE which has a very high computational complexity.

The computational cost of MI is greatly reduced in the SMPL framework because there are a limited number of bins B_n defined in the atlas with a fixed number of points in each. The computation of JE can be replaced by several marginal entropies. The entropy of I_{ta} and I_{tk} is respectively given by

$$H(I_{ta}) = -\sum_{j=1}^{B_n} p_{ta}(j) \log p_{ta}(j) \quad (41)$$

$$H(I_{tk}) = -\sum_{j=1}^{B_n} p_{tk}(j) \log p_{tk}(j) \quad (42)$$

The marginal entropy of I_a has a fixed value which is

$$H(I_a) = -\sum_{k=1}^K w_k \log w_k \quad (43)$$

The joint entropy can then be simplified as follows:

$$\begin{aligned} H(I_a, I_{ta}) &= -\sum_{k=1}^K \sum_{j=1}^{B_n} w_k p_{tk}(j) \log w_k p_{tk}(j) \\ &= -\sum_{k=1}^K \sum_{j=1}^{B_n} w_k p_{tk}(j) \log w_k - \sum_{k=1}^K \sum_{j=1}^{B_n} w_k p_{tk}(j) \log p_{tk}(j) \\ &= H(I_a) + \sum_{k=1}^K w_k H(I_{tk}) \end{aligned} \quad (44)$$

MI is written as

$$MI(I_a, I_{ta}) = H(I_{ta}) - \sum_{k=1}^K w_k H(I_{tk}) \quad (45)$$

4.2.6 Normalized Mutual Information

NMI was proposed [127] for the purpose of solving a known limitation of MI which occurs when the overlap between two images is small. The sum of the marginal entropies in MI may increase faster than the joint entropy. NMI has been proven to be less sensitive to changes in overlap when normalized using:

$$NMI(X, Y) = \frac{H(X) + H(Y)}{H(X, Y)} \quad (46)$$

The simplified NMI formula is:

$$NMI(I_a, I_{ta}) = \frac{H(I_a) + H(I_{ta})}{H(I_a) + \sum_{k=1}^K w_k H(I_{tk})} \quad (47)$$

Note that the area of overlap problem is avoided in the SMPL framework since the background is not considered. The atlas is completely warped inside the image and the area of overlap is constant.

4.3 Protocol for Evaluation

A comparison platform is required to evaluate the six measures. To independently compare the measures, optimisation algorithms should not be included in the platform; however, the close relationship between measure and optimisation makes them difficult to separate. [114] tried to find the best combination of measure and optimisation. One optimisation method was selected for all the measures in [122, 124].

The protocol proposed in [116] uses a brute-force examination of the neighbourhood of the global optimum. The performance of algorithms with respect to accuracy and capture range can be compared if enough samples are taken, but due to computational costs, it is difficult to use thorough sampling over the parameter space for analysis. Thus, a specific solution using small number of samples that still covers the whole space was proposed in the literature.

The similarity measures were evaluated using four criteria [116]: accuracy (ACC), distinctiveness of the global maximum (DOG), number of minima (NOM) and risk of non-convergence (RON). Another parameter called capture range (CAR), which was defined by the distance between the global optimum and the nearest local optimum [116], was not used in the current study because information about the capture range has already been taken into account by the NOM and RON. Thus, only these four properties were selected for the following experiments.

4.3.1 Sampling in Parameter Space

Assume that the evaluation has to be performed in K dimensional space if the algorithm contains K parameters (x_1, x_2, \dots, x_K) . Firstly, the space is normalized so that it can be considered as a unit hyper-sphere (Figure 4.1). A small step (sampling) change in any parameter will cause the same mean shift in voxels. The origin of the hyper-sphere \mathbf{x}_0 is the ground truth solution which is known. The hyper-sphere is then sampled in N directions which are randomly selected in term of the vectors $\{\mathbf{x}_n = (x_1^n, x_2^n, \dots, x_K^n) | n = 1, 2, \dots, N\}$. These lines are called parameter lines. On each line, M sampling points $\{\mathbf{x}_{n,m} | m = 1, 2, \dots, M\}$ are evenly distributed. Stable quantitative results can be observed when the numbers N and M are both increased to large enough values. The random selection strategy greatly reduces the required sampling number but the experiments still can cover the whole parameter space.

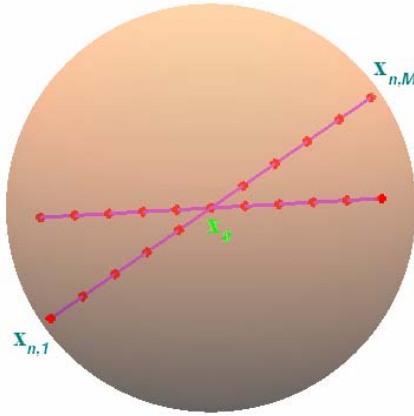


Figure 4.1 Example of sampling in parameter space (3D view): two parameter lines with M sampling points and the ground truth $x_{n,0}$.

4.3.2 Analysis of the Error Surface

A hyper-surface is formed when the results of all samples are calculated. A typical 1D error surface is shown in Figure 4.2a, which is obtained from one parameter line. The sample with the global maximal measure (on the parameter line) is denoted as $x_{n,max}$ in Figure 4.2a. The gradient $d_{n,m}$ is shown in Figure 4.2b. It should be noted that only the negative gradient values on the left side of $x_{n,max}$ and the positive gradient values on the right side of $x_{n,max}$ are of interest, since these correspond to the local minima. Both the absolute values and the number of $d_{n,m}$ are recorded. This information is used for the computation of the four properties, ACC, DOG, NOM and RON.

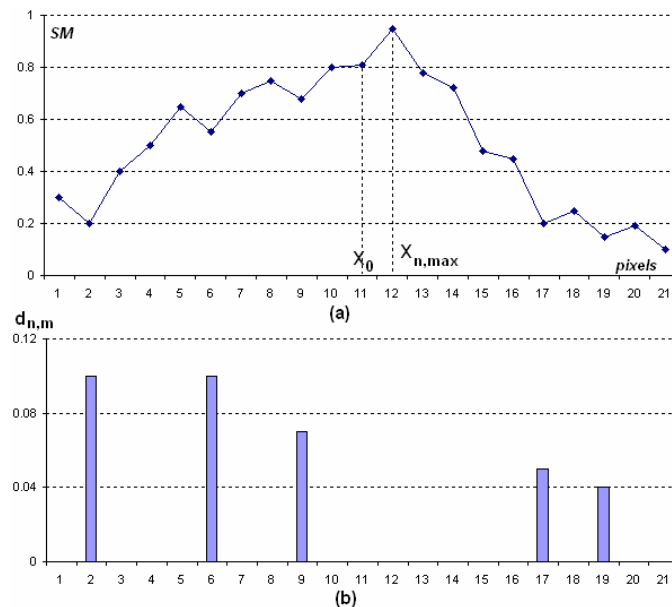


Figure 4.2 (a) 1D Error surface from a parameter line and (b) the negative gradient values on the left side of $x_{n,max}$ and the positive gradient values on the right side of $x_{n,max}$.

- **Accuracy (ACC)**

The ACC property of a similarity measure is defined as the root mean-square (RMS) of distances between \mathbf{x}_0 and $\mathbf{x}_{n,\max}$ of each parameter line where $n = 1, 2, \dots, N$ (Figure 4.2a). A smaller ACC means a better measure.

$$\text{ACC} = \sqrt{\frac{1}{N} \sum_{n=1}^N \|\mathbf{x}_{n,\max} - \mathbf{x}_0\|^2} \quad (48)$$

- **Distinctiveness of Global Maximum (DOG)**

DOG evaluates the behaviour of the algorithm in the neighbourhood of the global maximum. The sharper (more distinctive) the error surface around the global maximum, the less uncertainty there is about whether the true global maximum was found. DOG computes the average change of the measures near the global maximum. It is a function of distance r from $\mathbf{x}_{n,\max}$, where $r = k \cdot \delta$, δ is the sampling length and k is an integer:

$$\text{DOG}(r) = \frac{1}{2rN} \sum_{n=1}^N [2f_{\text{SM}}(\mathbf{x}_{n,\max}) - f_{\text{SM}}(\mathbf{x}_{n,\max-k}) - f_{\text{SM}}(\mathbf{x}_{n,\max+k})] \quad (49)$$

where f_{SM} represents any of the six measures. A large value for the DOG means a better measure.

- **Number of Minima (NOM)**

NOM describes how easily the algorithm could run into a local maximum. It counts the number of $d_{n,m}$ in Figure 4.2b. The property is also a function of distance r . If sgn is the sign function, the NOM formula is given by

$$\text{NOM}(r) = \frac{1}{N} \sum_{n=1}^N \sum_{m=\max-k}^{\max+k} \text{sgn}(d_{n,m} > 0) \quad (50)$$

Thus, for this property, a small NOM means the measure is better.

- **Risk of Non-convergence (RON)**

RON gives the information on how difficult it might be for the optimisation algorithm to jump out of a local maximum. As opposed to NOM, RON is based on the values of $d_{n,m}$ instead of the number.

$$\text{RON}(r) = \frac{1}{2rN} \sum_{n=1}^N \sum_{m=\max-k}^{\max+k} d_{n,m} \quad (51)$$

In summary, a good algorithm should have:

	ACC	DOG	NOM	RON
Good algorithm	low	high	low	low

Table 4-2 Four aspects of an algorithm with good performance.

4.4 Implementation

The experiments were based on the ED frame of the middle SA slices of nine CMR cases. One was from a healthy volunteer and the other eight cases were randomly selected from the ONTARGET dataset. The construction of an atlas for registration is described in Section 4.4.1. To obtain sub-pixel accuracy, interpolation algorithms are evaluated in Section 4.4.2. Section 4.4.3 presents how to normalize the parameter space in these specific experiments. Section 4.4.4 explains the details of sampling which include the selection of M and N.

4.4.1 Construction of an Atlas

In this experiment, the atlas used in each case was manually segmented directly from the image (the ED frame of middle SA slice in each case). The papillary muscles were included in the blood pool (Figure 4.3b). Three objects, LV, RV and myocardium, were delineated from the image. The centre of the heart, used for scaling and rotation, was also determined at the centre of gravity (green dot in Figure 4.3b). The grey level distributions associated with the blood and muscles of the atlas were calculated from the pixel intensities found within the atlas region on the patient images using the expectation maximum (EM) algorithm. Detailed implementations of these procedures will be described in the next chapter.

Since the atlas is treated as a set of mathematical points in the new framework, a sampling strategy is required to obtain these points from the atlas image. The points do not necessarily need to be extracted exactly at the centre of each pixel. A sub-pixel resampling can provide more robustness to the algorithm. Local optima caused by linear interpolation can be significantly reduced with sub-pixel resampling and will be discussed in more detail in the next chapter.

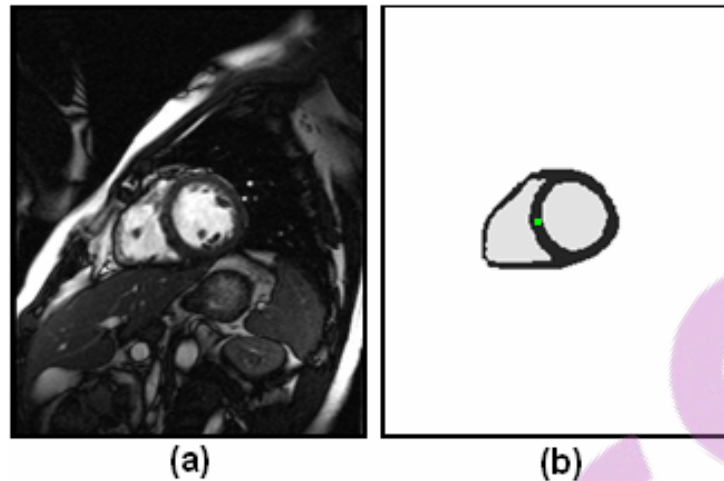


Figure 4.3 (a) ED frame of a middle SA slice and (b) its atlas.

4.4.2 Interpolation

Interpolation is required not only for sub-pixel resampling but also for the solution to have sub-pixel accuracy. The effect of interpolation on the shape of the error surface is discussed in this section.

- **Linear Interpolation**

Linear interpolation can be used in SSD, NCC, CR and WD. This provides sub-pixel accuracy at relatively low computational cost. Cubic or spline interpolation may improve the error surface by having less local optima, but the computational costs are much higher.

Linear interpolation is not suitable for entropy-based measures such as MI or NMI because it may produce new grey levels which do not belong to any structures in the image. These new levels may cause additional local optima in the error surface. Figure 4.4b shows the artefacts caused by linear interpolation in the 1D error surface of a translation-only parameter line. A close look at the area around the global maximum is shown in Figure 4.5a. A better interpolation is needed for MI and NMI.

- **Partial Intensity Interpolation**

Partial intensity interpolation proposed in [128] does not introduce new grey levels. It uses the linear interpolation result of each point to fractionally update two currently existing neighbouring grey levels. However, the artefacts in Figure 4.4c and Figure 4.5a show that the local optima problem is still serious with this interpolation.

- **Partial Volume Interpolation**

An efficient scheme called partial volume interpolation was proposed in [129], for details the reader is referred to [58, 130]. This uses the sub-pixel coordinates of each point to fractionally update the grey levels of its four spatial neighbours. The performance in Figure 4.4d and Figure 4.5b shows that this interpolation produces a much smoother error surface than the others. Some artefacts may still exist at the grid points since the total number of the histogram entries used for entropy computation is reduced at the grids. Local optima may be found at flat areas such as the range of $[-1, 0]$ in Figure 4.5b. Sub-pixel resampling or using high order interpolation was reported to be able to decrease the problem in [57, 131, 132] but the computational cost will increase. Partial volume interpolation was selected for the implementation of MI and NMI in the following experiments.

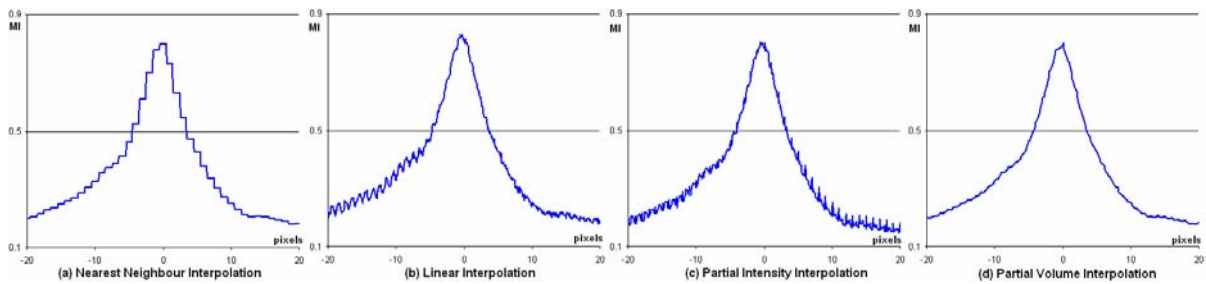


Figure 4.4 1D Error surface of a translation-only parameter line of radius 20 pixels from the ground truth.

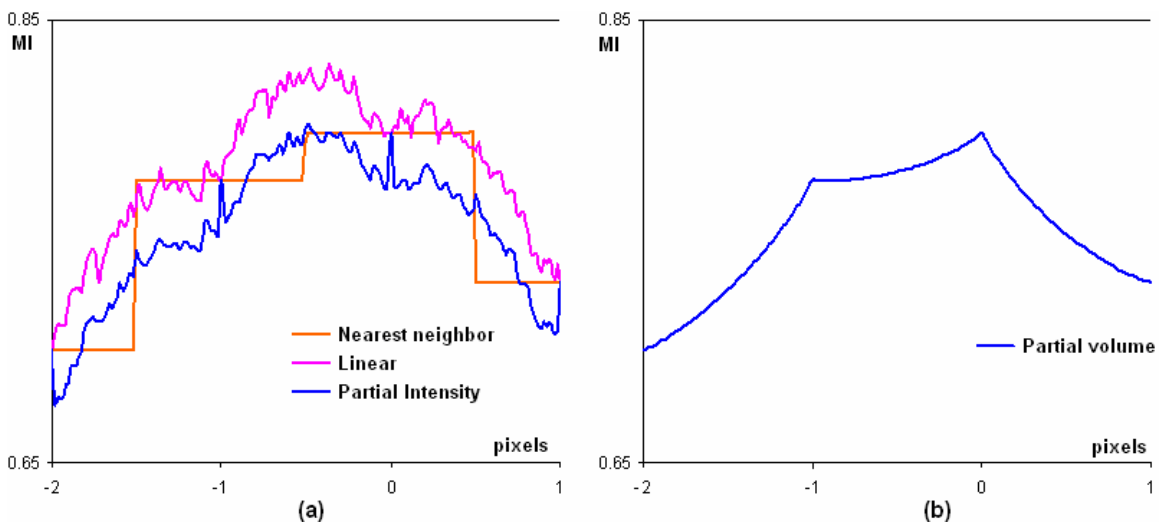


Figure 4.5 Close look at the global maximal area in Figure 4.4. (a) Nearest neighbor, linear, partial intensity interpolations and (b) partial volume interpolation.

The above translation-only example is in fact the worst case. The artefacts were decreased when rotations and scaling were included in the transformations. Figure 4.6 shows an

experiment of using the partial volume interpolation in the MI computation. Twenty parameter lines were randomly selected and the problem did not seriously affect the results.

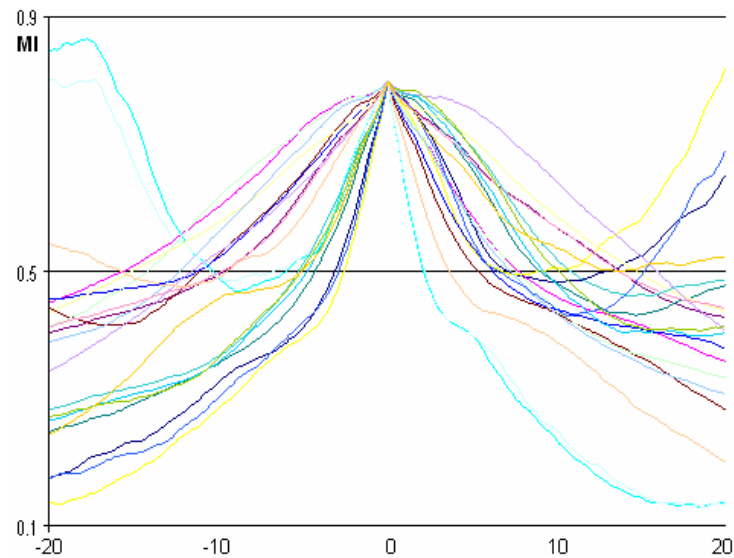


Figure 4.6 MI performance using partial volume interpolation on 20 randomly selected parameter lines.

4.4.3 Normalization of Parameter Space

The parameter space consisted of four parameters, two translations T_x and T_y , one rotation R and one scaling S . T_x was defined as the row direction of the image and T_y was the direction of column from image origin. The centre of rotation and scaling was defined at the centre of the gravity of the atlas (Figure 4.3b). In order to investigate all the parameters at the same time, a normalized parameter space was needed in which a step change in any parameter should cause a similar change in the result.

The parameters were independently inspected. For each test, only one parameter was changed and other parameters were kept as same as the ground truth. 201 samples were taken on each parameter line in this experiment. The 1D error surfaces (curves) from these tests were then compared in Figure 4.7. If the curves are assumed to follow a Gaussian function, the standard deviation σ of each curve provides a quantitative measure of the error space. The scaling relationships between these parameters can be found by the comparing their σ . The six measures were all tested and the results averaged.

A large region of interest was set for the parameters: the ranges of T_x and T_y were both -50 to +50 pixels away from the ground truth; the rotation range was -90 to +90 degrees; and the scaling ranged from 30% to 170%. Numerical results can be found in Table 4-3. In order to

avoid the impact of local optima in Figure 4.7, only the samples between $M = 51$ and 151 were used for the computation of parameter normalization scale factors.

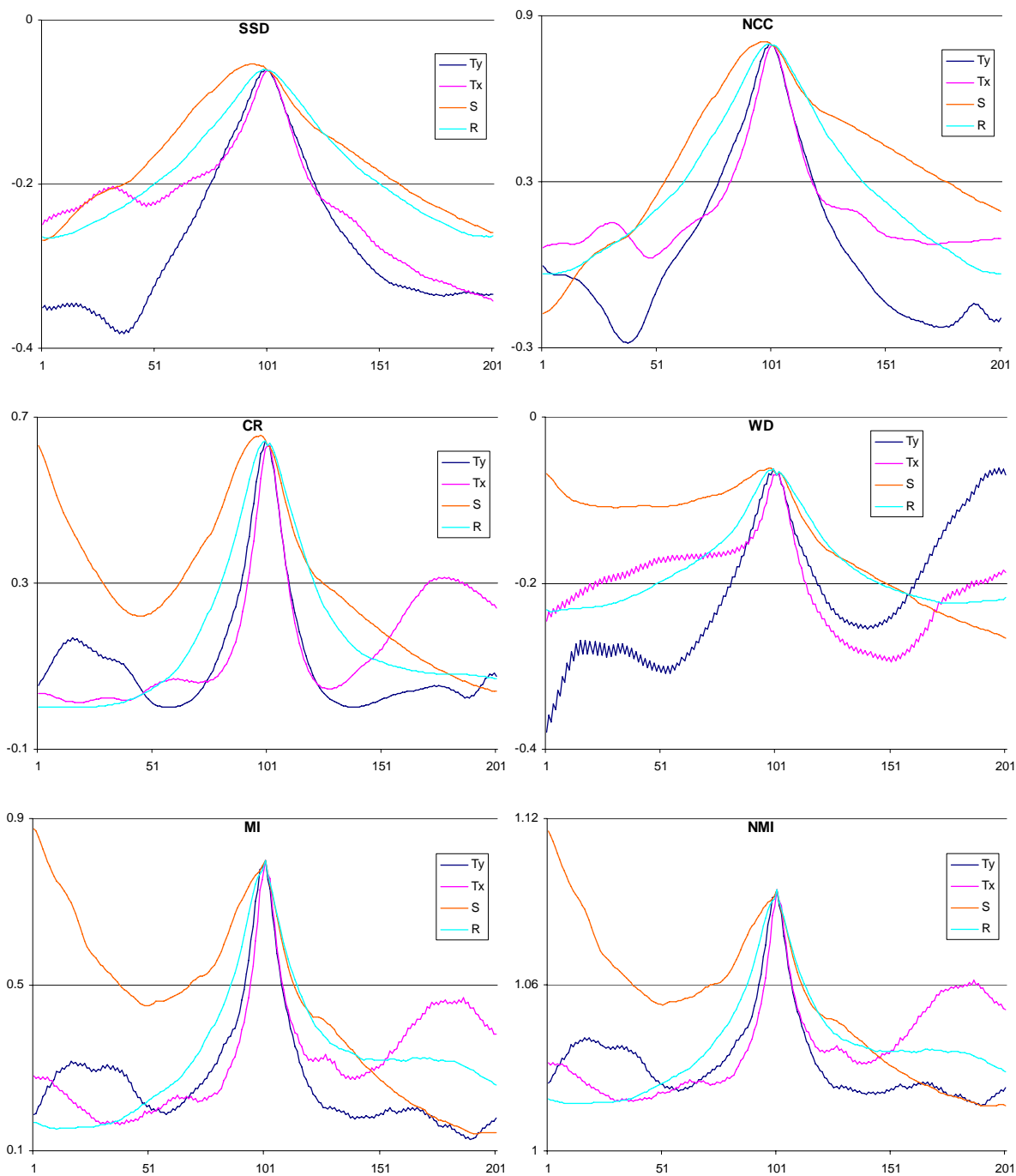


Figure 4.7 Performance of each parameter in six measures.

To make it robust, four patient cases were examined and the normalization relationships were determined from the average in Table 4-4. WD was not included because of its poor performance.

σ	T_y	T_x	S	R	T_x/T_y	S/T_y	R/T_y
SSD	14.53	16.23	32.26	26.96	1.12	2.22	1.86
NCC	14.14	13.86	31.59	24.41	0.98	2.23	1.73
CR	9.93	8.54	23.90	18.01	0.86	2.41	1.81
WD	14.05	18.40	32.78	25.62	1.31	2.33	1.82
MI	9.58	9.62	22.04	16.81	1.00	2.30	1.75
NMI	9.10	8.90	21.51	16.17	0.98	2.36	1.78
Average Ratio					0.99	2.31	1.79

Table 4-3 Standard deviations of the Gaussian curves fitted to the curves in Figure 4.7 and Relationships between T_x , T_y , R and S

	T_y/T_y	T_x/T_y	S/T_y	R/T_y
Patient 1	1	0.88	2.22	2.33
Patient 2	1	0.75	1.98	1.86
Patient 3	1	0.82	2.25	2.22
Patient 4	1	0.93	1.95	1.64
Healthy volunteer	1	0.99	2.31	1.79
Average	1	0.88	2.14	1.97

Table 4-4 Relationships between T_x , T_y , R and S in five cases.

The result showed that one pixel change in T_y is approximately equivalent to 0.88 pixels in T_x , 2.14% in S or a 1.97° in R . The novel localization method presented in the next chapter for the initialization of CMR segmentation, estimates the heart's initial position to be within 22 pixels of the ground truth on the middle slice. For consistency, the region of interest in the following tests is set to $[-22 \ 22]$ for T_x , which is equivalent to $[-25 \ 25]$ for T_y , $[-49.25 \ 49.25]$ for R and $[-46.5\% \ 153.5\%]$ for S . This space is finally normalized to a unit hyper-sphere.

4.4.4 Sampling in Parameter Space

In the hyper-sphere parameter space, N parameter lines passing through the origin are randomly extracted and M evenly distributed samples are taken for each line. Two experiments were investigated to answer the questions below:

- 1) What is the minimal requirement of M for stable results? Low M may result in sub-pixel local optima missed, which will affect the analysis results.
- 2) What is the smallest N for which stable results can be obtained? If N is not large enough erroneous conclusions may be made.

These experiments were based on the case shown in Figure 4.3. Two properties ACC and NOM are examined below. DOG and RON had similar results as NOM but are not shown. NOM is a property relating to the distance $r = k \cdot \delta$, where δ is the step length in parameter space and k is the number of steps. Two typical distances, one close to the ground truth and the other far away from ground truth, were defined to present NOM performances of the six similarity measures with different M or N.

- **Number of Sampling Points M**

Four hundred randomly selected parameter lines ($N = 400$) were used in this experiment. N was large in order to ensure that any errors introduced will not be because of N being too small. M was varied from 21 to 221 along each parameter line. The results shown in Figure 4.8 and Figure 4.9 were normalized for comparison. The step δ used in the horizontal and vertical axes of Figure 4.8 and the horizontal axis of Figure 4.9 is equal to $2/221$ length in the parameter space (equivalent to 0.20 pixels in T_x or 0.23 in T_y). It can be noticed that the curves form a plateau when M is greater than 120. Thus, M is set to 121 in the following tests.

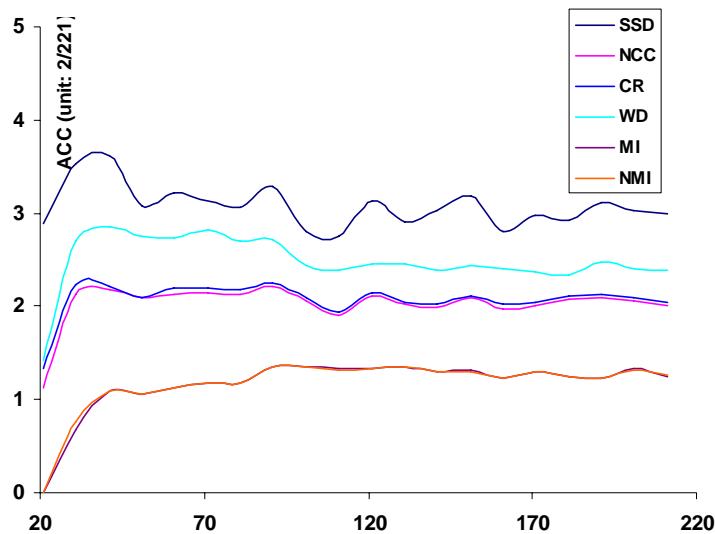


Figure 4.8 ACC performance of six measures with M from 21 to 221.

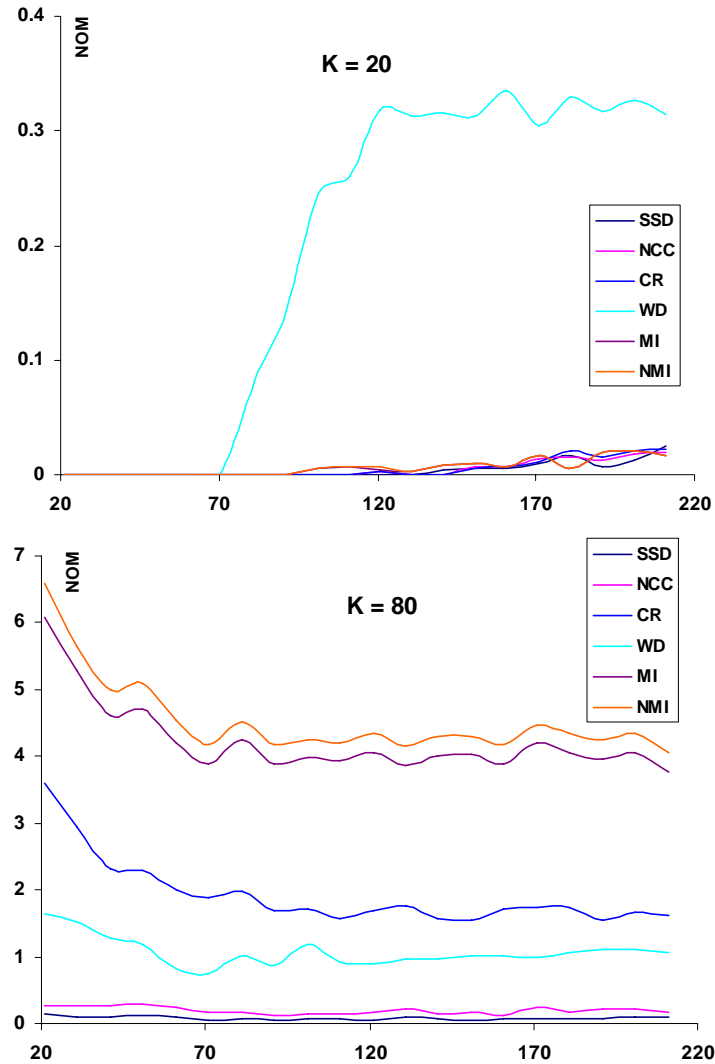


Figure 4.9 NOM performance of six measures with M from 21 to 211 when $k = 20$ and $k = 80$.

- **Number of Sampling Lines N**

A similar experiment was undertaken to determine the number of parameter lines N. N was varied from 20 to 600 in intervals of 20. M was set to 121, subsequently δ in the parameter space in this experiment was equivalent to 0.36 pixels in T_x or 0.41 in T_y . Figure 4.10 and Figure 4.11 show the ACC results and NOM performance of six measures when $k = 10$ and $k = 40$. The areas of $k = 10$ and $k = 40$ in this experiment are similar to the areas of $k = 20$ and $k = 80$ in the last experiment due to the different step applied. The results became stable when N is greater than 200. N is set to 200 in the following tests.

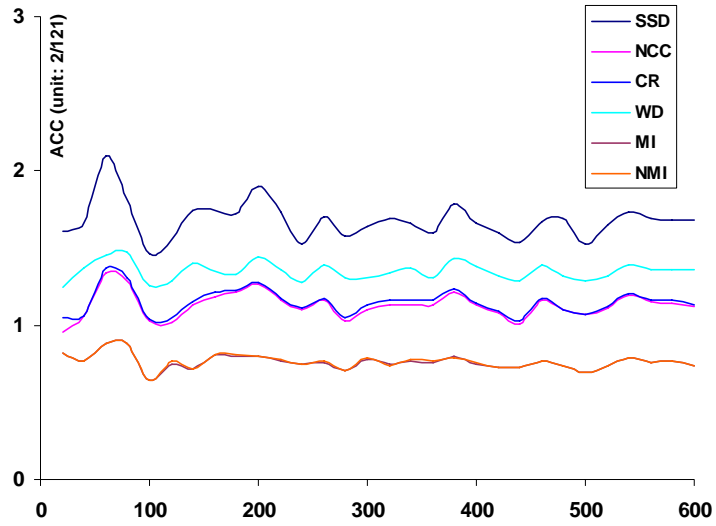


Figure 4.10 ACC performance of six measures with N from 20 to 600.

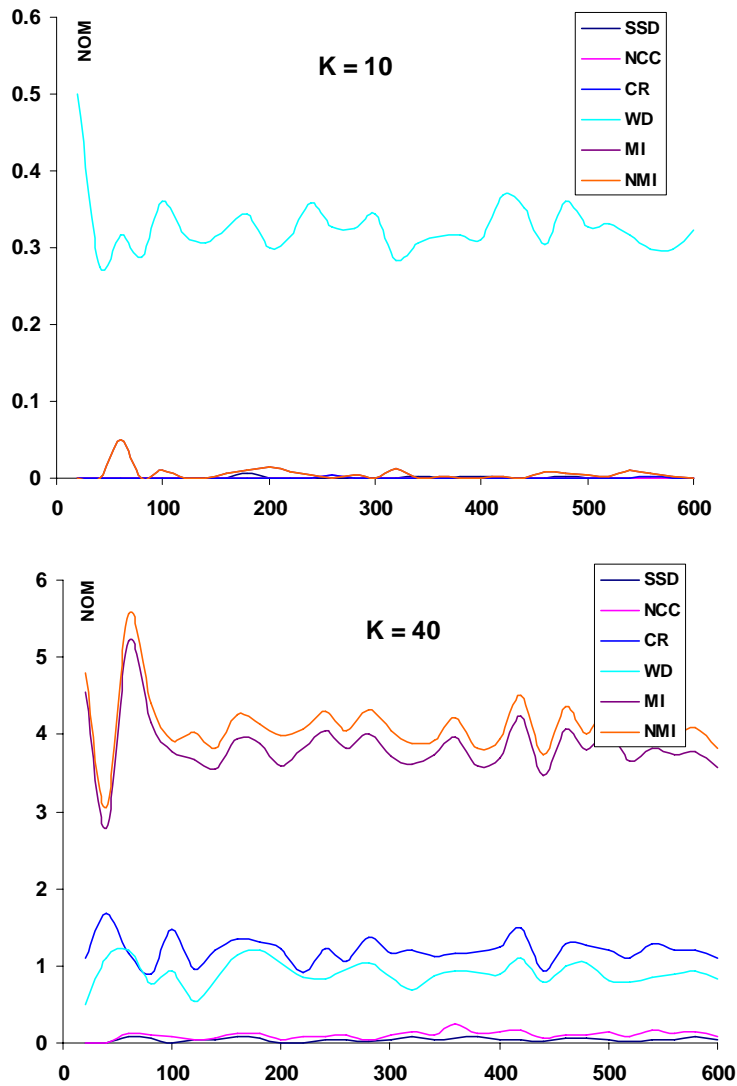


Figure 4.11 NOM performance of six measures with N from 20 to 600 when $k = 10$ and $k = 40$.

4.5 Results

Nine CMR cases were used for the experiments testing the performance of each similarity measures. Four properties, of the six measures were independently examined, ACC, DOG, NOM, and RON. The results were compared to demonstrate their advantages and disadvantages at the areas close to ($k = 10$) and far from ($k = 40$) the ground truth. It should be noted that the scales used in following figures may vary.

4.5.1 Accuracy

Figure 4.12 shows that all similarity measures had good accuracy. SSD had the worst performance with an average error of 1.66 steps (equivalent to 0.6 pixels in T_x). MI and NMI had the best performance with the errors of about 0.8 steps, which is half the SSD. MI showed slightly better results than NMI. The WD error was similar to the SSD. Two variance-based measures, NCC and CR, had similar performance.

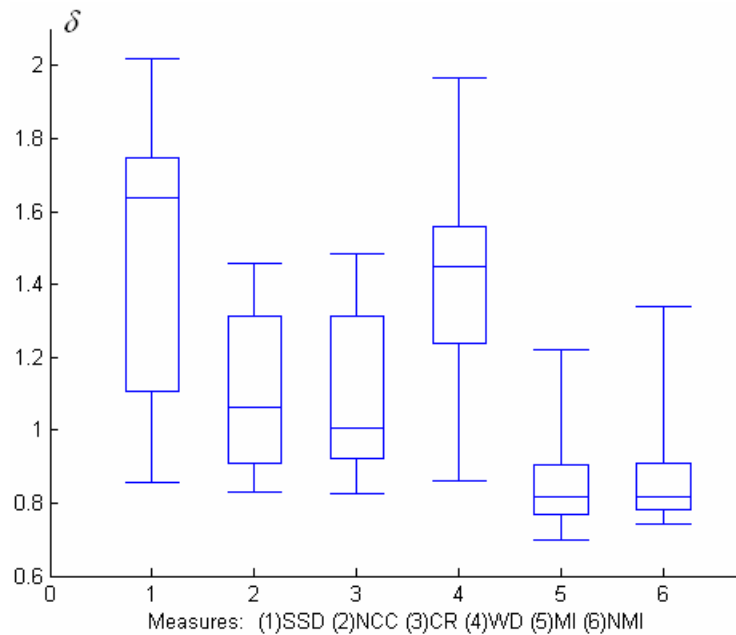


Figure 4.12 ACC Performance of six measures

4.5.2 Distinctiveness of Global Maximum

Figure 4.13 shows that CR, MI and NMI have large DOG values at areas close to the global optimum. The error surfaces are sharper in those areas compared to the areas far from the global optimum. In MI and NMI, the surface is still sharp within areas very close to the ground truth. This may lead to a fast convergence for a MI or NMI algorithm. The performance of SSD, NCC and WD are not as good as the other three measures at both low k

areas and high k areas (Figure 4.14). Their error surface may have a flatter peak around the global optimum and may explain why SSD has the worse ACC.

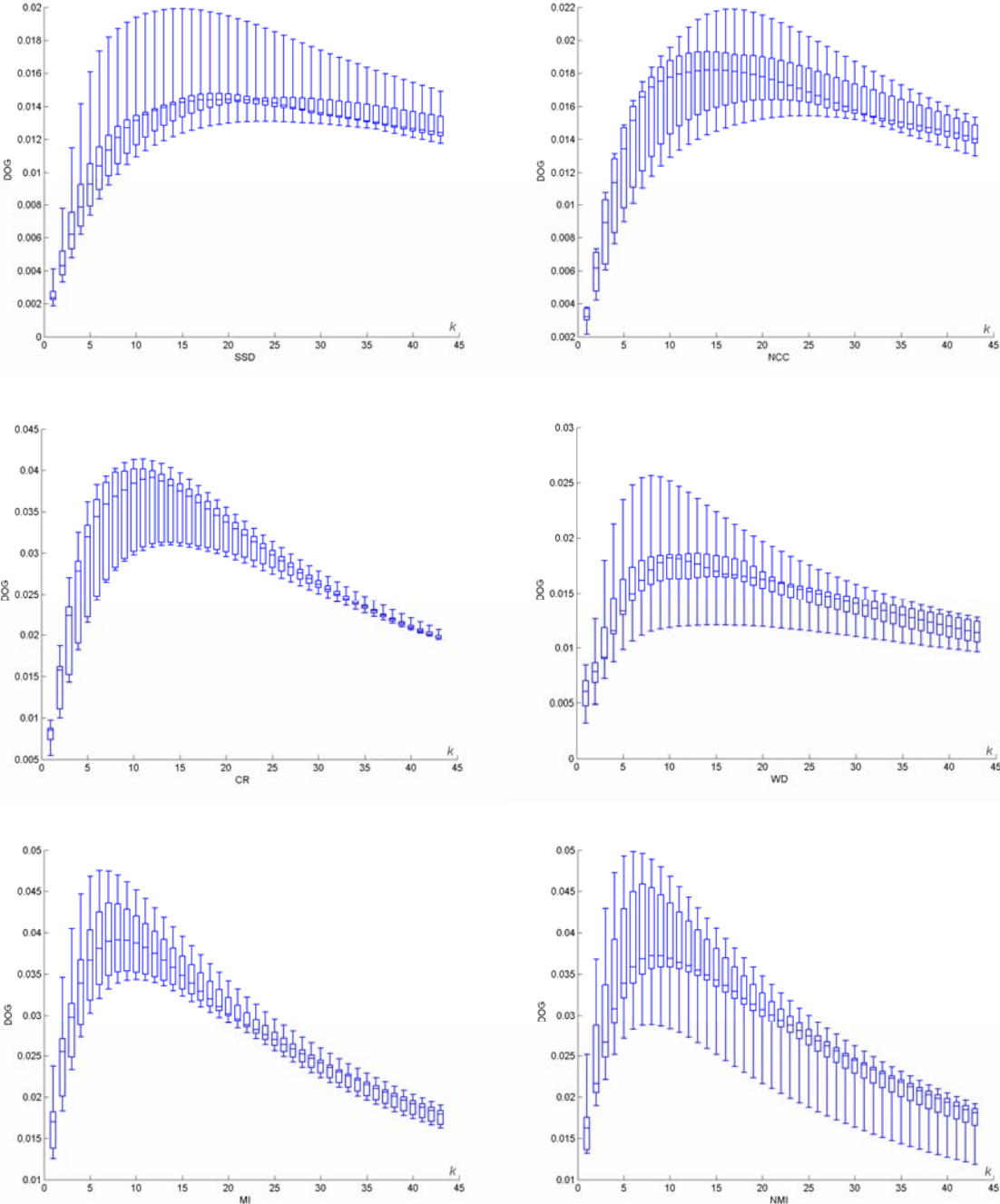


Figure 4.13 Box plot of DOG performances of six measures at different k .

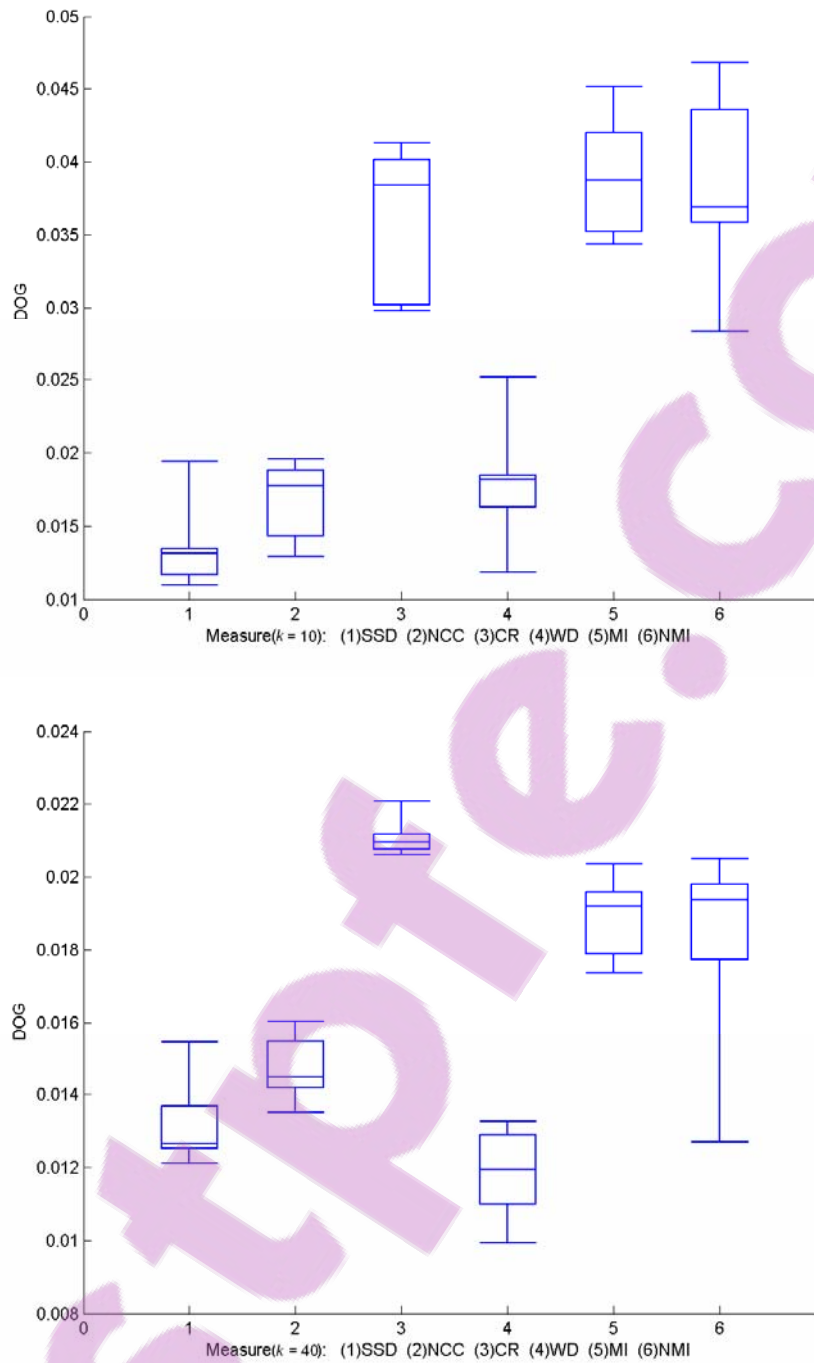


Figure 4.14 DOG performances of six measures when $k = 10$ and $k = 40$.

4.5.3 Number of Minima

Figure 4.15 shows the NOM of each measure. No obvious increases were observed before $k = 25$ and the values increase exponentially at the area where k is larger than 25. That is, the risk of being trapped by a local minimum will greatly increase if initial estimates cannot be within the area where $k < 25$.

SSD had an overall good performance in the total region of interest (Figure 4.16). Good performance was also found in NCC. The performance of CR, MI and NMI are similar though CR is slightly better than MI and NMI at high k areas. The performance of WD in the low k area was significantly worse than the others. This implies that a number of local optima must exist around the global optimum and consequently this measure is not recommended.

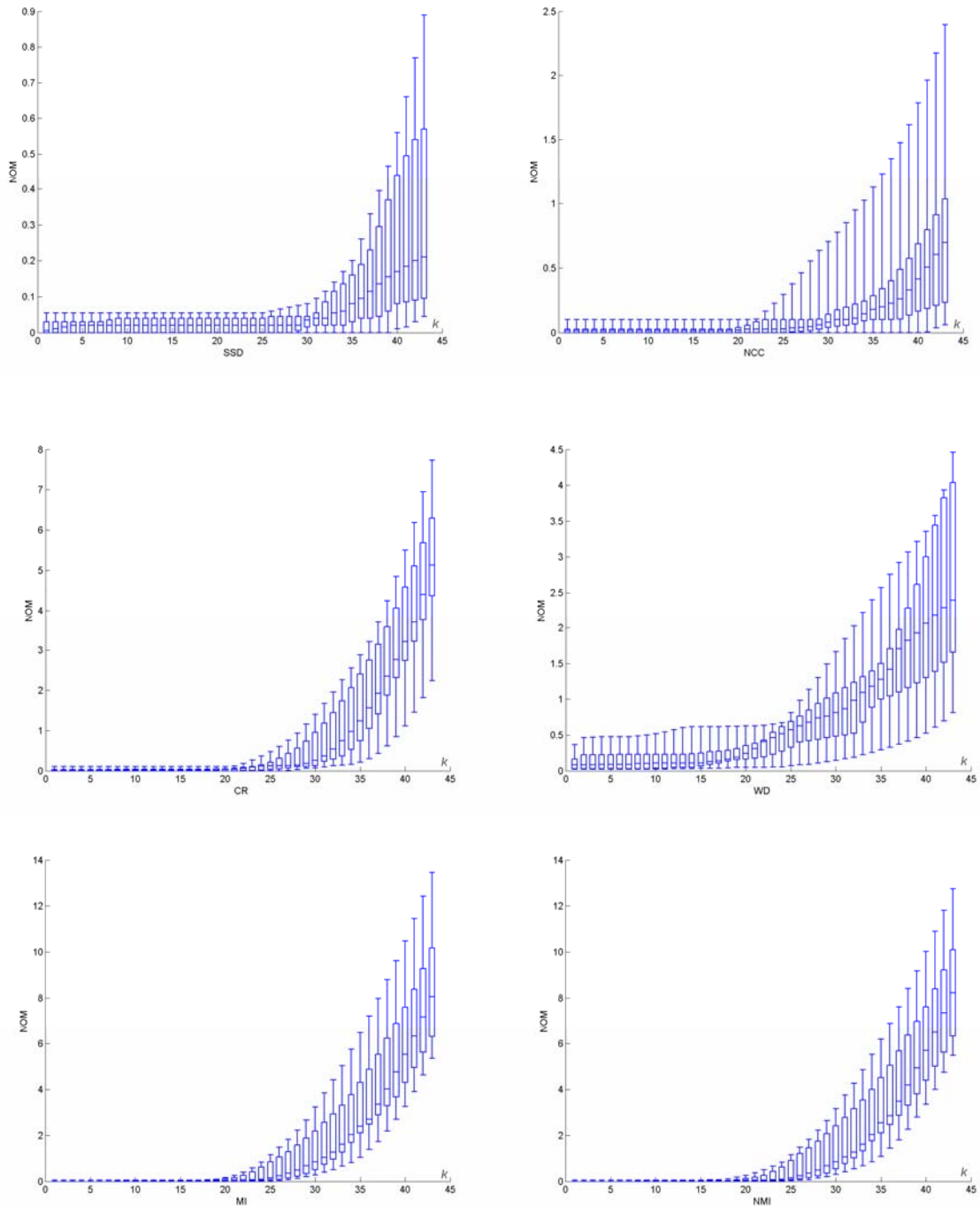


Figure 4.15 Box plot of NOM performance of six measures at different k .

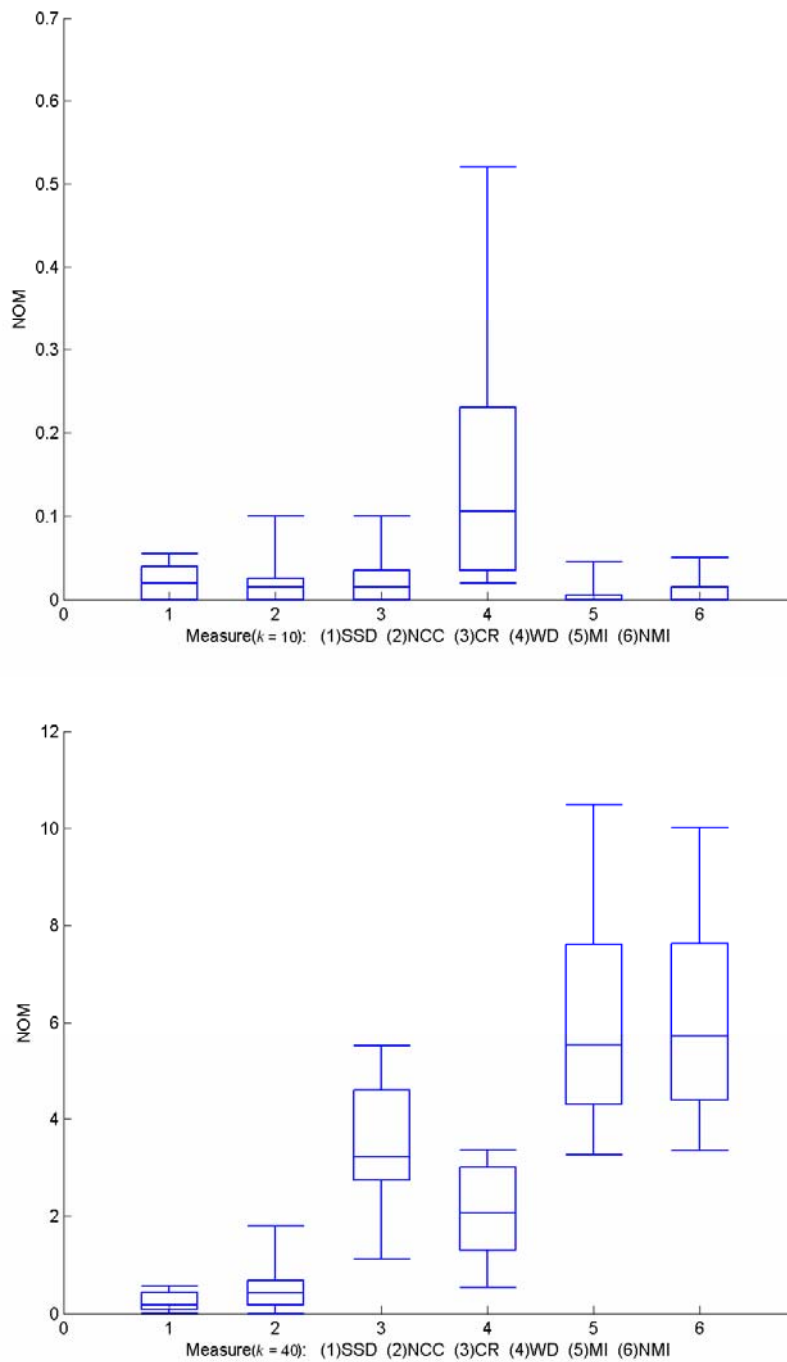
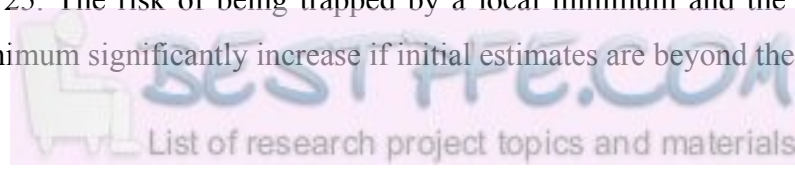


Figure 4.16 Comparison of NOM performances when $k = 10$ and $k = 40$.

4.5.4 Risk of Non-convergence

RON is similar to NOM but provides information about the deepness of each local optimum. Figure 4.17 shows that the RON of each measure reaches its minimum in the areas where k varies from 15 to 25. The risk of being trapped by a local minimum and the difficulty of leaving a local minimum significantly increase if initial estimates are beyond these areas.



The performances of SSD and NCC are quite good over the total region of interest. CR, MI and NMI have good performance at low k values however their performance becomes poor when k is increased. Figure 4.18 shows that the RON property of each measure is very similar to NOM. WD is the worst at low k values and SSD is the best at high k values.

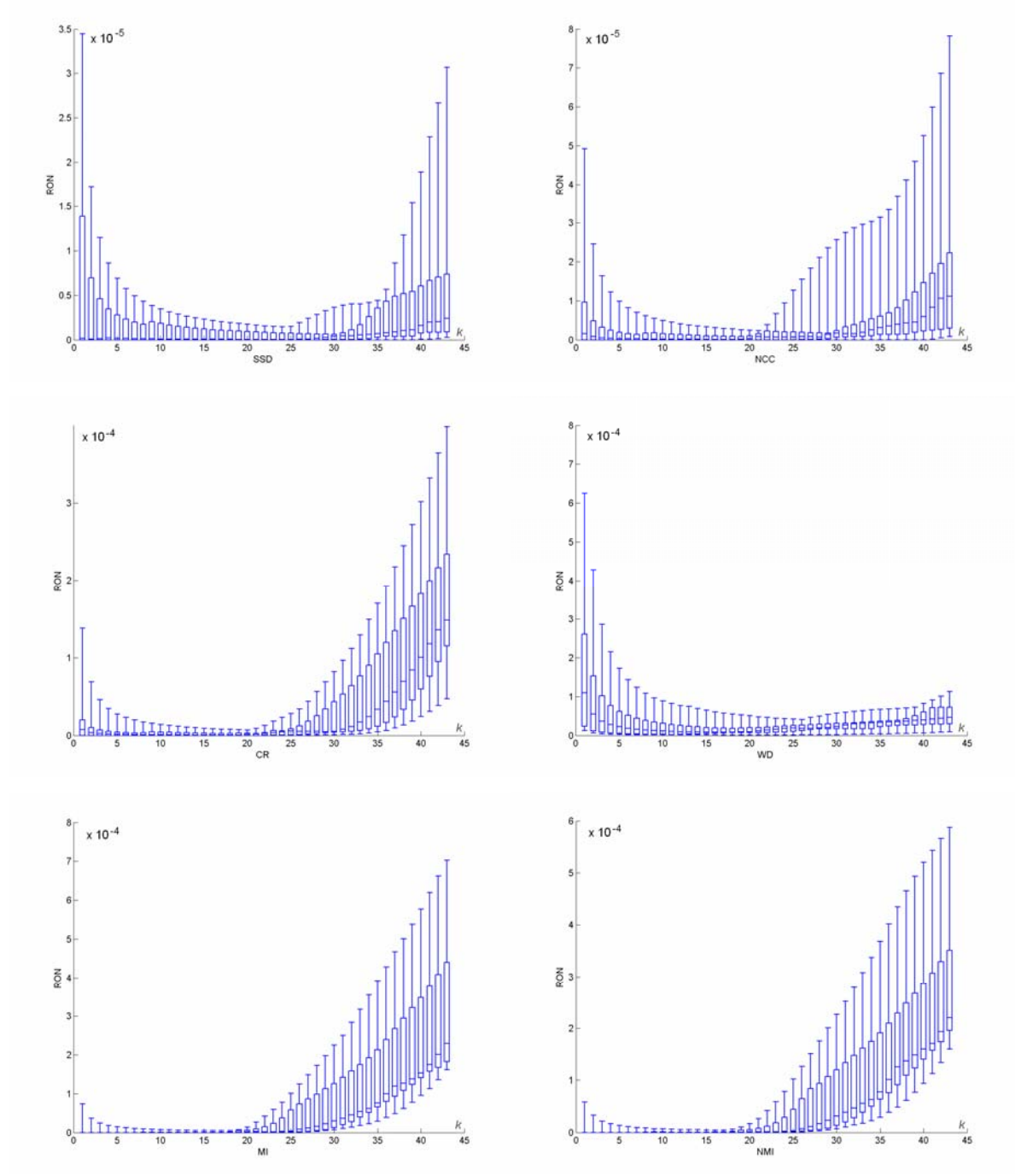


Figure 4.17 Box plot of RON performance of six measures at different k .

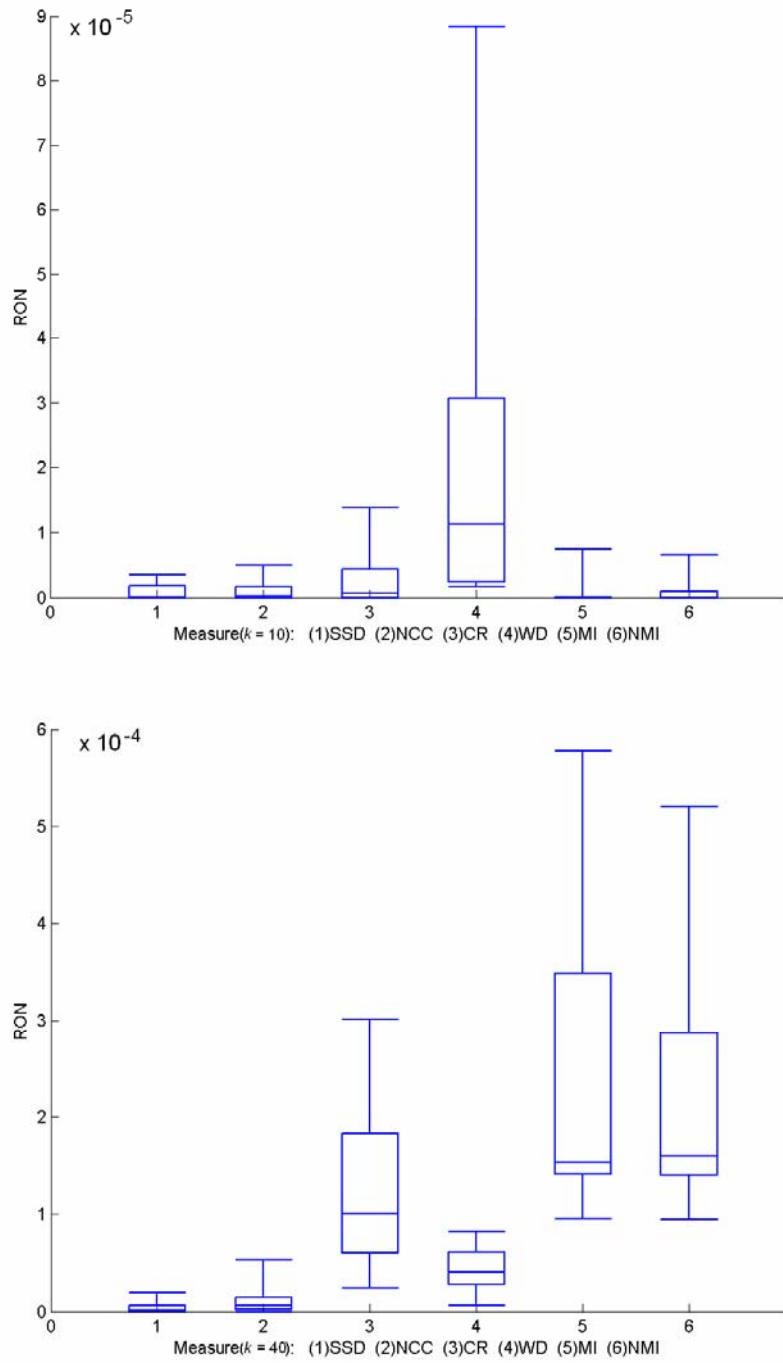


Figure 4.18 Comparison of RON performances when $k = 10$ and $k = 40$.

4.6 Discussion

In this chapter, six popular similarity measures were compared in an atlas-based registration environment. Four important properties of their performances have been investigated. The overall comparisons are discussed in Section 4.6.1. After careful consideration, SSD is selected in Section 4.6.2 as the similarity measure for further development of the new atlas-based segmentation method discussed in the next chapter.

4.6.1 Overall Comparison

- **Computational costs**

It is difficult to compare the computational costs using a Matlab platform. In order to reduce the impact of redundancy in Matlab's internal functions, all time-consuming functions, such as the entropy and the linear interpolation functions, have been implemented in C and called from within Matlab code. Figure 4.19 shows the average computation time spent by each measure for a single sampling of parameter space. NMI was the most time consuming method and SSD was the fastest, being about 30 times faster than NMI. The computational costs of NCC, CR and WD were similar. No obvious difference between MI and NMI was found. The cost of these two measures is dependent on the number of bins because most of time is taken up by the entropy computation. In these experiments, 256 bins were used.

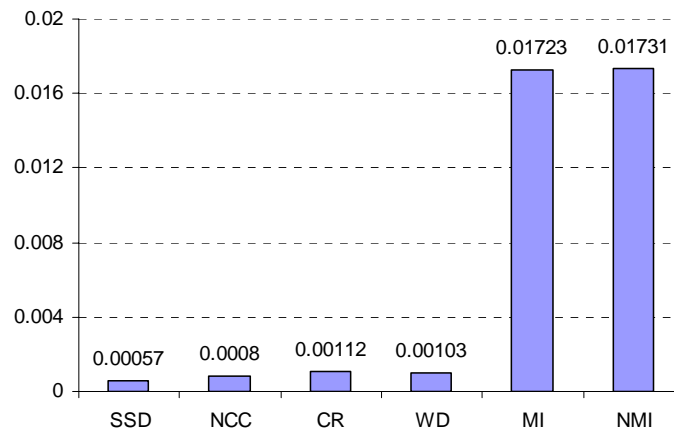


Figure 4.19 Computational cost of each measure in second.

- **Accuracy**

The ACC performances of these measures are all very good. SSD gives the largest average error which is equivalent to 0.6 pixels in T_x . MI and NMI have the best performances with the errors of about 0.3 pixels. However an error of 0.6 pixels is absolutely acceptable in CMR segmentations. MI or NMI may be better in applications where higher accuracy is desired.

- **Distinctiveness of Global Optima**

According to the data provided in Section 4.5.3, MI has the best DOG performance at the area close to the ground truth while CR outperforms the others in the overall region of

interest. This property is not only an indicator of algorithm reliability but also related to the convergence speed. No optimisation is associated with the measures; therefore a comparison of convergence speed is not available in these experiments.

- **Number of Maxima and Risk of Non-convergence**

NOM and RON are two important indicators which decide the robustness and reliability of an algorithm. Low values of these two properties mean that the algorithm has a large capture range and is unlikely to be trapped by local optima. The results in Section 4.5.3 and Section 4.5.4 revealed that all measures except WD are expected to be reliable and robust if initial estimates are close to the ground truth. However, the NOM of MI and NMI is 20 times more than that of the SSD in the areas far from the ground truth. This indicates that the capture range of MI or NMI is much smaller than SSD. Algorithms based on SSD may find it easier to jump out of local minima.

4.6.2 Selection of Similarity Measure

Selection of an efficient similarity measure is one of the key steps in the construction of an atlas-based non-rigid registration. The registration will be used as a fully automated method to map the segmentation information defined on the atlas to the target image. Since the method is expected to be supervision-free, it would be desirable that the algorithm has a large capture range and less local optima in the error surface. These features favour either SSD or NCC as better choices than the others. Furthermore, both algorithms can provide analytic derivatives, which in turn open up more options for selecting an optimisation algorithm, as discussed in the following chapters. After comparison of the overall performance of two methods SSD was finally selected as the more favourable similarity measure for atlas-based registration. MI or NMI may be applied, if higher accuracy is required, to improve the results of the SSD algorithm. The advantages of the SSD are summarised below

- the lowest computational cost,
- reasonably high accuracy,
- better NOM and RON,
- able to provide analytic derivative for optimisation.

4.7 Conclusions

Six widely used similarity measures were examined in the context of rigid atlas-based segmentation, using a comparison framework independent of the optimisation algorithm. The comparisons are based on the SMPL atlas-based registration framework which enables simplifications in the computational complexity of the atlas registration problem. All the similarity measures can be simplified for use in this framework. They were then quantitatively compared with each other in four key aspects: ACC, DON, NOM and RON. It is concluded that both SSD and NCC have wider capture range and less local optima in the total region of interest and MI and NMI have better performance at the areas close to the ground truth. SSD was selected as the similarity measure for the atlas-based non-rigid registration framework which will be further developed in the next chapter.

5 Atlas-based Segmentation of Cardiac MR Images

Atlas-based image segmentation treats the segmentation as a registration problem. The atlas is a labelled image, normally generated by segmenting an actual image. It is used to find the transformation that maps the pre-segmented atlas to the target image (the image to be segmented). After registration, all structural information defined in the atlas is transferred to the target image. The energy function in a traditional atlas-based registration is based on the intensity difference between the atlas pixels and the corresponding pixels in the target image; however, this approach does not have sufficient accuracy [69-71], is easily trapped into local optima [72] and is computationally intensive [69].

In this chapter, the SMPL atlas-based registration framework is further developed. The atlas is not considered as an image; instead, it is treated as a set of mathematical points which have intensity values, weights and anatomical labels. The registration maps each point from the atlas onto its best corresponding position in the target image. Linear interpolation is used to create sub-pixel resolution. The SMPL framework has higher accuracy, lower computational cost and the ability to integrate different kinds of useful information to improve the robustness of the algorithm.

5.1 Introduction

5.1.1 Traditional Atlas-based Registration

In general, an atlas is a labelled image typically generated by manually segmenting an actual image. This provides a spatial map of labels that not only characterizes the intensity information but also implicitly contains the boundary information. Furthermore, a great deal of high-level anatomical information can be defined on the atlas, although to date such high-level information has not been widely exploited.

Traditionally, the atlas is treated as a separate imaging modality and is registered to the target image by computing a coordinate transformation T . T maps the image coordinate of points in the target image I_t onto points in the atlas I_a . For a given pixel $\mathbf{v}(x,y)$ in I_t , its correct label can be found through the mapping relationship [93]:

$$\mathbf{v} \mapsto I_a(T(\mathbf{v}))$$

The transformation T will lead to non-integer pixel co-ordinates consequently a sub-pixel interpolation is required. Nearest Neighbour (NN) interpolation of the atlas is typically employed to determine which labels should be assigned; however, NN interpolation is only on the order of a pixel. Other interpolations such as linear interpolation produce sub-pixel resolution but unfortunately the new grey levels produced may not correspond to any atlas feature. The mapping problem can be solved in the SMPL framework proposed.

Speed is one of the most important disadvantages which must be addressed in traditional atlas-based registration. Because all the pixels in the atlas and the target image are included in the computation, the non-linear approximation in the registration method becomes inefficient. One solution is to manually or automatically define a boundary box in the target image. However, this requires a model of the intensity distribution, as well as the shape and spatial distribution of the background within the box. This task appears very difficult on any large dataset such as ONTARGET due to the variance between patients. Erroneous models create local minima in the error surface and result in incorrect segmentations.

5.1.2 New Atlas-based Registration Framework

In the SMPL framework, the atlas is treated as a set of mathematical points that have no size but have intensity values, weights and anatomical labels. The registration maps each atlas point onto its best corresponding position in the target image. Linear interpolation is used to calculate sub-pixel positions in the target image. Advantages of the SMPL framework were detailed in Section 4.2 and the first two advantages of the framework discussed in that section had been investigated. It was shown that the formulations of similarity measures with high computational costs, such as MI and NMI, can be simplified using the proposed framework. Speed up was obtained by removing background pixels from the registration process. SSD was eventually selected as the similarity measure of the automated 2D CMR segmentation based on the SMPL atlas-based registration framework, due to its large capture range, fewer local optima, lower computational cost and its ability to derive analytic expressions for first and second derivatives.

Other advantages will be investigated in this chapter and the next. Linear interpolation is known to cause artefacts in the error function. It is shown that artefacts can be reduced in the SMPL framework by sub-pixel resampling. Local minima in the error surface are largely

decreased with this strategy. Another advantage of the SMPL framework is that it can assign a different weight to each point in the atlas, which is useful if a statistical or probabilistic atlas is available in the future. The main advantage of the SMPL framework is its ability to integrate different kinds of useful information into one system. Not only does it assign a different grey level to each point but it can also easily define boundary points and other anatomical information. The utilization of such higher level information is introduced in this chapter and further discussed and examined in the next chapter.

5.1.3 Overview

The atlas construction is discussed in Section 5.2. An initial atlas for each image is created from the intersection between the image plane and the 3D finite-element model of the heart (introduced in Section 1.5). The 3D model is initialized in each case by the temporal Fourier analysis method developed in Chapter 2. The grey levels associated with each object in the atlas (blood, muscle etc) are calculated for each individual patient using the EM algorithm. The atlas is then re-sampled, to provide sub-pixel resolution and to reduce the local minima caused by linear interpolation.

The registration aims to map each re-sampled point from the atlas onto its best corresponding position in the target image by minimizing the intensity difference between corresponding pixels. Non-rigid mapping is accomplished using a free-form deformation (FFD) model based on cubic Bézier curves. Section 5.3 introduces the details of the FFD algorithm and Section 5.4 presents the components of the energy function. Since the SSD is selected as the similarity measure, analytic expressions of the derivative of the energy function are available. Optimisation is performed using the Levenberg-Marquardt (LM) algorithm in Section 5.5. A capture range analysis of this new atlas-based segmentation method is examined in Section 5.6 and experiments on data from a large clinical trial is described in Section 5.7. Discussion and conclusions are made in Section 5.8.

5.2 Atlas Construction

Two atlases are used in this Chapter. The first was simply manually segmented from the ED frame of a middle SA CMR slice. This is only used in Section 5.6 for analysis of the capture range. The other atlas was constructed from the 3D heart model in Section 1.5 from a single CMR scan of a normal volunteer. This model was initialized in each case by the localization method developed in Chapter 2. The localization method relied on a temporal Fourier

analysis of the dynamic characteristics of the heart to provide initial estimates for the size, orientation and position of the model. The initialized model was intersected with each image plane to create the initial atlas. This method was implemented in all subsequent experiments in this thesis. Different grey levels were assigned to the objects on the atlas. However, because the intensities varied between cases, each case required a customised grey level. The grey levels were estimated for an individual patient by directly estimating the pixel intensities found within the initial atlas region in the patient images. In the SMPL framework, the atlas was represented by a set of mathematical points which have intensity values; thus, a good sampling strategy is required. With a sub-pixel re-sampling strategy, the local minima caused by linear interpolation will be reduced. In summary, this section will describe:

- the accurate initial estimate of heart model based on temporal Fourier analysis.
- the EM-based algorithm which is used to estimate the greyscale labelling of different objects.
- the sub-pixel resampling solution which reduces the local minima caused by linear interpolation.

5.2.1 Initial Estimation of Heart Model

In Chapter 2, it was shown that the heart can be distinguished from other features on the CMR images by analyzing the temporal changes in pixel intensity that occur at the same frequency as the heart rate. A Fourier transform is applied to every pixel in each SA slice to calculate a H1 image. After removing the noise on the images by thresholding, Figure 5.1a shows the H1 images from six SA slices (SA1 to SA6). These H1 images form a 3D volume called the H1 volume, which is used to provide a highly accurate initial estimate of the size, orientation and position of the heart model.

- **Defining the Initial Position**

The centroid of the H1 volume, marked by the red point in Figure 5.1a, is assumed to be the centre of the heart. The initial position of the model is obtained by matching the centre of the model to that centroid.

- **Defining the Initial Size**

To ensure no deformation is introduced into the initial model, a single (isotropic) scale is used to adjust the size of model in all directions. From experience the parameter is adjusted until 92% of the H1 volume is covered.

- **Defining the Initial Orientation**

The orientation of the model is also estimated from the H1 volume. A ROI is first computed for each H1 image. The long axis \mathbf{V}'_x (Figure 5.1a) is approximated by a 3D line fitted to the centroid of each ROI. To obtain the orientation of the RV from the LV (\mathbf{V}'_y) the H1 volume is collapsed along \mathbf{V}'_x into one plane (Figure 5.1b). \mathbf{V}'_y is determined by the primary eigenvector calculated from the principal component analysis of the collapsed data. \mathbf{V}'_z was computed to complete a right handed coordinate system. The model was orientated by mapping its pre-defined coordinate system to this detected coordinate system. No *a-priori* knowledge, such as the average directions used in the LV localization method described in Chapter 2, was required in this method.

Figure 5.1c presents the model after the initial estimate. The intersection of the model with the middle SA slice is shown in Figure 5.2a. It shows a good agreement on both the position and orientation of the actual LV and RV. Numerical results of the initial estimate's accuracy over the 330 ONTRAEGET cases can be found in Section 5.7.3.

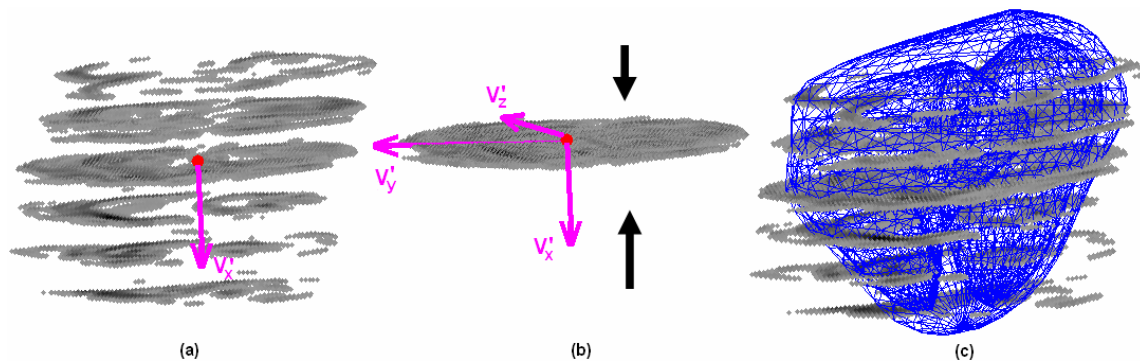


Figure 5.1 (a) model centre and \mathbf{V}'_x defined by the H1 volume, (b) \mathbf{V}'_y defined by the collapsed H1 volume, (c) Initial estimate of the heart model based on the H1 volume.

5.2.2 Grey Level Estimation

The intensity representations of cardiac structures in CMR may vary widely from case to case. It is therefore prudent to estimate these directly from the target image. EM is a popular tool for this purpose as mentioned in Section 1.6.2.

- **EM Algorithm**

EM is an iterative procedure that clusters the unobserved data v from the observed data w by finding the maximum likelihood estimates of parameters in the probabilistic model for v . For each iteration of the EM algorithm two steps are performed, the E-step and the M-step:

- E step: The unobserved data are estimated, using conditional expectation, from the observed data and the current estimate of the model parameters.
- M step: The maximum likelihood function is maximized with the assumption that the unobserved data is known. Instead of the actual unobserved data, the estimate of the unobserved data from the E-step is used.

In image segmentation applications, the observed data are the intensities of the image and the unobserved data are the correct classifications to be computed. The intensity values are modelled by a Gaussian distribution $\theta_k \{ \mu_k, \sigma_k \}$, where μ_k is the mean and σ_k is the variance of each class. $\theta_k, k \in \{1, 2, \dots, K\}$ are the “unobserved data” parameters required to be known. The EM algorithm can be mathematically described by the following:

- E step – calculate the conditional expectation

$$p(v_l = k | w_l, \theta^t) = \frac{p(w_l | v_l = k, \theta^t) p(v_l = k | \theta^t)}{\sum_k p(w_l | v_l = k, \theta^t) p(v_l = k | \theta^t)} \quad (52)$$

- M step – estimate the parameters for next iteration

$$\mu_k = \frac{\sum_{l=1}^L p(v_l = k | w_l, \theta^t) w_l}{\sum_{l=1}^L p(v_l = k | w_l, \theta^t)} \quad (53)$$

$$\sigma_k = \frac{\sum_{l=1}^L p(v_l = k | w_l, \theta^l) (w_l - \mu_k)(w_l - \mu_k)^T}{\sum_{l=1}^L p(v_l = k | w_l, \theta^l)} \quad (54)$$

- **Application in CMR Segmentation**

EM has already been used for CMR image segmentation in many studies such as [4, 14, 43]. From our own experience we found that in order to successfully use this algorithm in CMR segmentations a ROI must be applied to exclude the background pixels. Figure 5.2b shows an example of the intensity distribution of an entire middle SA CMR image. In the histogram, both the myocardium and blood pixels comprise a small part so that they are unlikely to be determined by EM. The initial model is therefore used to provide the required ROI for the algorithm (Figure 5.2a). The objects inside the initial model mostly include only the myocardium and the blood pools even if the initial model is misplaced somewhat. The intensity distributions of the two objects can now be easily estimated by EM (Figure 5.3).

- **Process in CMR Segmentation**

The process of the EM fitting is described as follows. Before the iteration, an initial estimation is required. This was based on the thresholding method proposed by Otsu [133]. The histogram is divided into two parts and the mean and standard deviation values of each part are used for the initial estimation, shown as the green curves in Figure 5.3. The cyan curves is the two EM estimated Gaussian distributions computed by the EM algorithm. They are combined to a pink curve, demonstrating a good agreement with the red histogram curve.

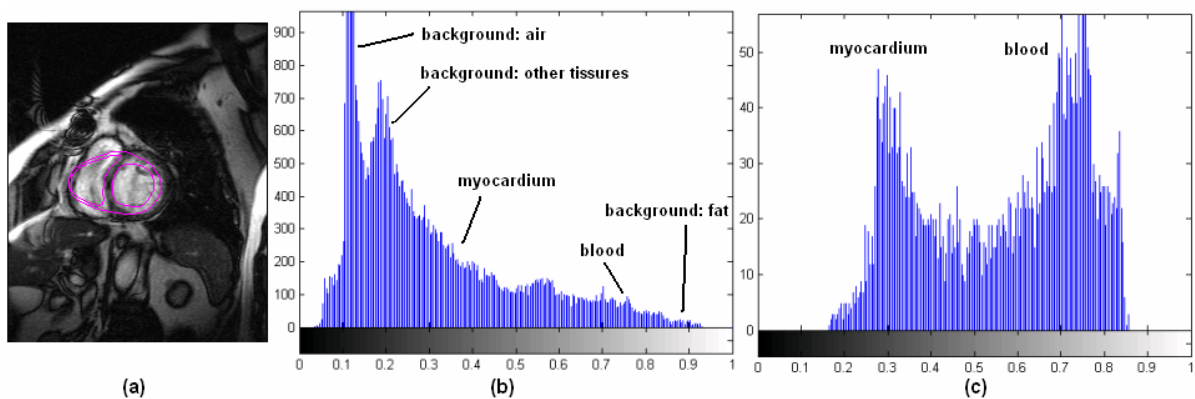


Figure 5.2 Histogram of a middle SA slice with and without initial model. (a) middle SA slice and initial model, (b) histogram of the whole image, (c) histogram inside the model.

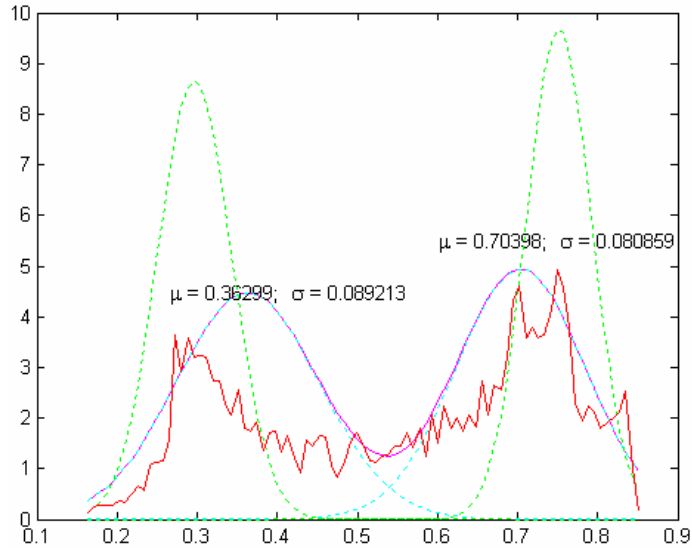


Figure 5.3 EM estimation of the histogram in Figure 5.2c. Red curve – histogram, green curve – initial estimation, cyan curve – two estimated Gaussian distribution and pink curve – combined distribution.

5.2.3 Sub-pixel Sampling

Interpolation is a necessary requirement for atlas-based registration. Nearest-neighbour interpolation is limited in accuracy and spline interpolation is too slow to be applied in practice. Linear interpolation is therefore the best choice in many situations. Unfortunately, it is well known that linear interpolation introduces artefacts into the error surface.

- **Local Minima Caused by Linear Interpolation**

An example is shown below. The atlas in Figure 5.4b was manually extracted from the CMR image in Figure 5.4a. The grey levels of the blood and muscles in the atlas were analyzed by the EM algorithm. The atlas was shifted by one pixel increments within the area bounded by the green frame in Figure 5.4a. The SSD between the atlas and the corresponding image pixels is computed and the error surface is shown in Figure 5.5a. The surface is smooth and would converge to the correct place; however if the atlas is shifted by only half pixel increments and linear interpolation is applied the error surface (Figure 5.5b) is found to be covered by local minima. This artefact persists when the same spacing is used for sampling in both the atlas and the target image.

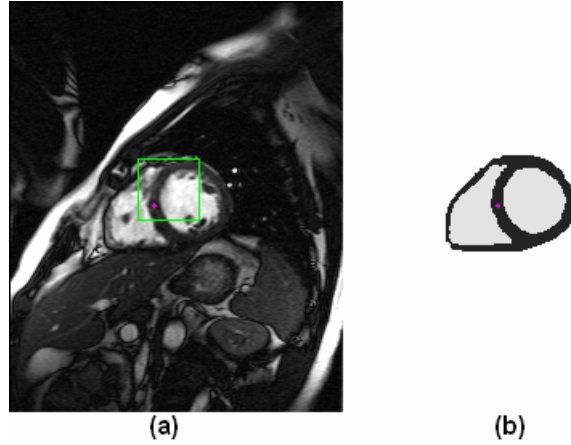


Figure 5.4 An example used for showing artefact of linear interpolation; (a) middle SA image, green rectangle – region for atlas translation, red dot – ground truth of gravity centre; (b) atlas, red dot – gravity centre.

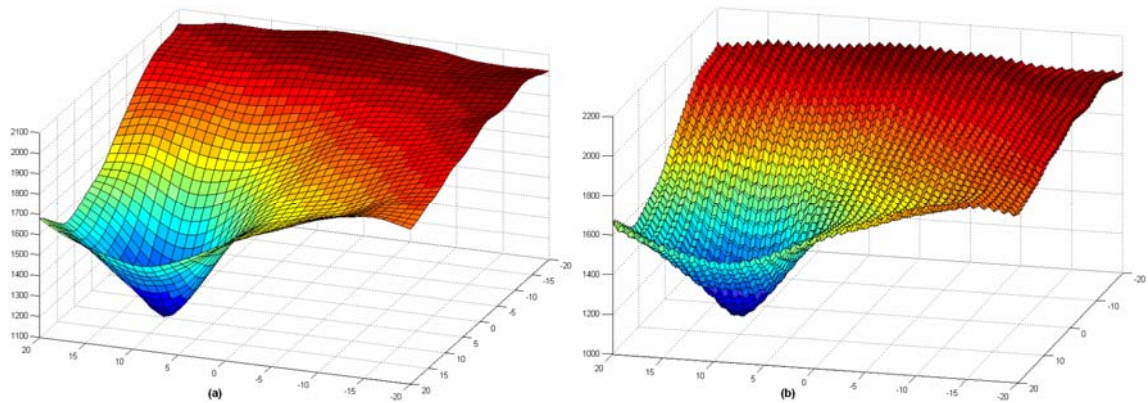


Figure 5.5 Artefact of linear interpolation in error surface; (a) shift one pixel each time, (b) shift half pixel each time.

- **Sub-pixel Resampling**

The local minima cannot be completely removed but they can be reduced by sub-pixel resampling [132]. Let us consider the set of atlas points $P: \{p = (x, y)\}$ where $1 \leq x \leq A_x$, $1 \leq y \leq A_y$. Instead of sampling one pixel apart, the spacing is set slightly smaller than one pixel in both the x and y directions respectively:

$$\begin{aligned} \delta_x &= (A_x - 0.499) / A_x \\ \delta_y &= (A_y - 0.499) / A_y \end{aligned} \tag{55}$$

Figure 5.6 shows an example of the sampling using the above protocol. The green points are the original sampling points and the red and blue points represent the resampling results of

the blood pools and myocardium respectively. The number of local minima is considerably reduced in the resulting error surface, Figure 5.7.

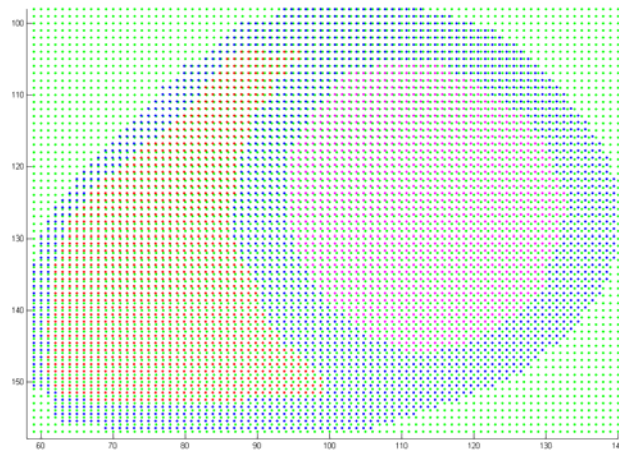


Figure 5.6 Resampling at sub-pixel level: green dots – the pixel centres, red and blue dots – the new locations of the atlas points after sub-pixel resampling.

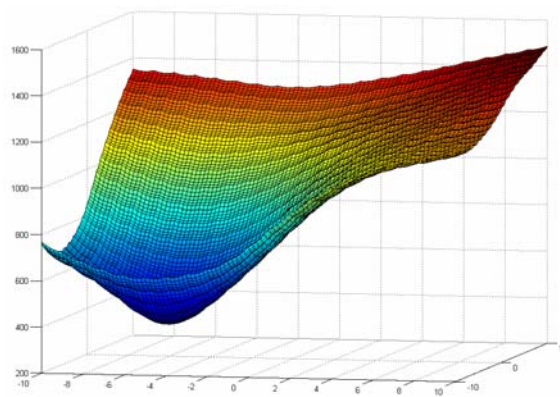


Figure 5.7 Artefact reduced by sub-pixel sampling in comparison to Figure 5.5.

The SMPL framework is readily adaptable to sub-pixel sampling. It is easy to offer different sampling levels, either less or more than one pixel, depending on requirements. This feature is advantageous for multi-resolution strategies. Furthermore, the sampling may not necessarily be evenly distributed over the whole image. Increased sampling can be performed over important areas. Investigation of these strategies is out of the scope of this thesis and further statistical analyses may be required for this purpose.

5.3 FFD for Non-rigid Registration

The non-rigid registration is implemented by the FFD algorithm, also called host mesh fitting in some studies. The object to be deformed, a 1D line, 2D image or 3D volume, is placed into a host mesh that has a simple geometric structure, for example, a rectangle. The

host mesh is made up of multiple elements linked by continuity constraints. In each element, a local coordinate system is established. The position of the object is embedded in the mesh by expressing its object points in terms of global parameters. The grid parameters are also called control points since the deformation of these points produces the deformation of all local points in the mesh, including the embedded object. The advantage of using a host mesh is that the non-rigid deformation can be described with fewer parameters. The minimal number of parameters is the number of the control points used to describe the mesh.

The method has been widely used in many domains such as medical modeling and image analysis. The interpolation system of the individual elements is described by different polynomial curves called basis functions. In medical modeling, cubic-Hermite, B-spline and cubic-Bézier curves are three functions widely used. The cubic-Bézier was selected in this thesis, since existing Matlab code could be applied. Continuity between the elements is obtained by a relationship that maps the global parameters of the host mesh into local parameters of the elements. Compared to the more commonly used cubic B-spline functions, cubic-Bézier splines were defined to have C1, rather than C2 continuity. The cubic-Bézier basis functions therefore have more local flexibility and create a more flexible deformation with a smaller number of elements than in the B-spline formulation.

This chapter will discuss only the application of 2D FFD to the atlas-based registration problem; a 3D FFD implementation will be discussed in Chapter 7.

5.3.1 Cubic Bézier FFD

The cubic Bézier FFD (cubic FFD) used in this thesis is defined below. If a rectangular mesh is selected to construct the FFD grid, the spatial domain can be denoted as $\Omega_I = \{ \mathbf{X} = (X, Y) \mid 0 \leq X < X_{\max}, 0 \leq Y < Y_{\max} \}$. The domain is divided into $n_x \times n_y$ elements with uniform spacing δ_x and δ_y in the two directions. The local coordinates are computed by

$$\xi_x = \frac{X}{n_x} - \left\lfloor \frac{X}{n_x} \right\rfloor \quad (56)$$

$$\xi_y = \frac{Y}{n_y} - \left\lfloor \frac{Y}{n_y} \right\rfloor \quad (57)$$

when \mathbf{X} is located in that element. The displacement of the deformation at $\mathbf{X}(X, Y)$ within an element e can be formulated as:

$$\mathbf{u}(X, Y) = \sum_{a=1}^4 \sum_{b=1}^4 B_a(\xi_X) B_b(\xi_Y) \mathbf{P}_{a,b}^e \quad (58)$$

where $B_a(\xi)$, $\xi \in [0,1]$, are 1D element basis functions, combined into 2D tensor product basis functions, and $\mathbf{P}_{a,b}^e$ are associated element parameters (control points). There are 16 local control points in any element of the cubic Bézier FFD. Cubic Bézier (Bernstein) polynomials, $B_a(\xi)$ are given by:

$$B_1(\xi) = (1 - \xi)^3$$

$$B_2(\xi) = 3\xi(1 - \xi)^2$$

$$B_3(\xi) = 3\xi^2(1 - \xi)$$

$$B_4(\xi) = \xi^3$$

5.3.2 Linear Bézier FFD

A linear Bézier function may be used as the FFD basis functions when speed is the predominant factor. The linear Bézier FFD (linear FFD) has only two basis functions:

$$B_1(\xi) = 1 - \xi$$

$$B_2(\xi) = \xi$$

and the displacement function is:

$$\mathbf{u}(X, Y) = \sum_{a=1}^2 \sum_{b=1}^2 B_a(\xi_X) B_b(\xi_Y) \mathbf{P}_{a,b}^e \quad (59)$$

The linear FFD has fewer degrees of freedom in comparison to the cubic FFD. A linear FFD trades accuracy for a faster expected convergence.

5.3.3 Global to Local Map

A bicubic Bézier FFD has $N = n_x \times n_y \times 16$ local control points and basis functions. If all elements are represented as an element ensemble, the displacement field (Eq. 59) written in terms of the element ensemble becomes:

$$\mathbf{u}(\mathbf{X}) = \sum_{i=1}^N \Psi_i^e(\mathbf{X}) \mathbf{P}_i^e \quad (60)$$

where $\mathbf{P}_i^e = \mathbf{P}_{a,b}^e$ within a particular element e , with a and b derived from n in a modular fashion. $\Psi_i^e(\mathbf{X}) = B_a(\xi_X)B_b(\xi_Y)$ if \mathbf{X} is in the element e , otherwise $\Psi_i^e(\mathbf{X}) = 0$. If the N basis functions are organised into a column vector Ψ^e and the element control points into a $N \times 2$ matrix P^e , then

$$\mathbf{u}(\mathbf{X}) = P^{eT} \Psi^e(\mathbf{X}) \quad (61)$$

Continuity is provided between elements with a general linear global-to-local map, which derives the set of local control points P^e from a smaller set of global control points P :

$$P^e = GP.$$

Equation 61 can be rewritten as

$$\mathbf{u}(\mathbf{X}) = P^T \Psi(\mathbf{X}) \quad (62)$$

where Ψ are global basis functions

$$\Psi(\mathbf{X}) = G^T \Psi^e(\mathbf{X}). \quad (63)$$

5.4 Energy Function

Let \mathbf{X} denote an atlas point at the position (X, Y) with weight $w(\mathbf{X})$ and grey level $I_a(\mathbf{X})$. The transformation T defined by the deformation of the mesh maps points in the atlas image I_a onto the current image I_t , ie $T: \mathbf{X} \rightarrow \mathbf{x}$ or $\mathbf{x} = \mathbf{x}(\mathbf{X}) = \mathbf{X} + \mathbf{u}(\mathbf{X})$. The mapping is optimised so that the pixel value in $I_a(\mathbf{X})$ approximates the pixel value $I_t(\mathbf{x}(\mathbf{X}))$. In this way the current image can be considered to be warp to the reference state. The warped image is given by $M_t(\mathbf{X}) = I_t(\mathbf{x}(\mathbf{X}))$. The SSD measure between the atlas and the deformed image $M_t(\mathbf{X})$ is

$$E_1 = \sum_{\mathbf{X}} w^2(\mathbf{X}) (I_a(\mathbf{X}) - M_t(\mathbf{X}))^2 \quad (64)$$

A smoothness penalty term is included in the energy function to penalize the deformation in areas with sparse data. One option is the biharmonic penalty term [93] which constrains the second-order derivatives:

$$E_s = \int_{\Omega} \beta_1 \left\| \frac{\partial^2 \mathbf{u}}{\partial X^2} \right\|^2 + \beta_2 \left\| \frac{\partial^2 \mathbf{u}}{\partial Y^2} \right\|^2 + \beta_3 \left\| \frac{\partial^2 \mathbf{u}}{\partial X \partial Y} \right\|^2 d\Omega \quad (65)$$

Another option is Sobolev smoothing, which has been widely used in FFD applications [134-136]. This term penalizes both first-order and second-order derivatives. In order to avoid shrinking of the model (a common implementation problem) the smoothing term is defined to act on the displacement $\mathbf{u}(p) = T(p) - p$:

$$E_s = \int_{\Omega} \alpha_1 \left\| \frac{\partial \mathbf{u}}{\partial X} \right\|^2 + \alpha_2 \left\| \frac{\partial \mathbf{u}}{\partial Y} \right\|^2 + \beta_1 \left\| \frac{\partial^2 \mathbf{u}}{\partial X^2} \right\|^2 + \beta_2 \left\| \frac{\partial^2 \mathbf{u}}{\partial Y^2} \right\|^2 + \beta_3 \left\| \frac{\partial^2 \mathbf{u}}{\partial X \partial Y} \right\|^2 d\Omega \quad (66)$$

The two α weights control the variation of displacement and the three β terms penalize the curvature of the displacement. The energy function therefore includes two terms (so far), w_s provides the smoothing weight:

$$E = E_1 + w_s E_s \quad (67)$$

5.5 Optimisation

Using SSD for the similarity measure provides more options for the selection of optimisation methods. One of the most efficient choices is the Levenberg-Marquardt (LM) algorithm, which is specifically designed for solving non-linear least square problems.

Note that the X and Y components of the objective function are independent of each other, in that \mathbf{u}_X is independent of Y components of P , so that each iteration of the LM procedure involves a solution to X and Y components of P separately. We consider only the X component in the following, the Y component is similar.

5.5.1 Gradients of Energy Function

The error function can be written:

$$E = E_1 + w_s E_s = \mathbf{d}^T \mathbf{W}^T \mathbf{W} \mathbf{d} + w_s E_s \quad (68)$$

where \mathbf{d} is a vector of errors with elements $d_q = I_a(\mathbf{X}_q) - M_t(\mathbf{X}_q)$ and W is a (typically diagonal) weighting matrix $W_{ii} = w(\mathbf{X}_p)$ (in general W can be derived from the covariance matrix). The gradient \mathbf{g} is given by

$$\mathbf{g} = \mathbf{g}_I + \mathbf{g}_S = -2JW^T W\mathbf{d} + 2w_S S\mathbf{P} \quad (69)$$

where J is the Jacobian matrix with element

$$J_{ij} = \frac{\partial M_t(\mathbf{X}_i)}{\partial P_j} \quad (70)$$

and S is a matrix given by

$$S_{ij} = 2 \int_{\Omega} \alpha_1 \frac{\partial \Psi_i}{\partial X} \frac{\partial \Psi_j}{\partial X} + \alpha_2 \frac{\partial \Psi_i}{\partial Y} \frac{\partial \Psi_j}{\partial Y} + \beta_1 \frac{\partial^2 \Psi_i}{\partial X^2} \frac{\partial^2 \Psi_j}{\partial X^2} + \beta_2 \frac{\partial^2 \Psi_i}{\partial Y^2} \frac{\partial^2 \Psi_j}{\partial Y^2} + \gamma_1 \frac{\partial^2 \Psi_i}{\partial X \partial Y} \frac{\partial^2 \Psi_j}{\partial X \partial Y} d\Omega \quad (71)$$

5.5.2 Advantages of the Levenberg-Marquardt Method

LM is a blend of simple gradient descent and Gauss-Newton algorithms.

- **Simple Gradient Descent**

For each iteration of the simple gradient descent algorithm the parameters \mathbf{P} are updated to be proportional to the negative of the gradients.

$$\mathbf{P}^{t+1} = \mathbf{P}^t - \lambda \mathbf{g}(\mathbf{P}^t)$$

where \mathbf{P}^t is the current value and \mathbf{P}^{t+1} is the updated value after the iteration. However this method suffers from slow convergence when the error surfaces are irregular.

- **Gauss-Newton Method**

The Gauss-Newton method solves this problem by replacing the fixed size step with the inverse of the Hessian matrix H which comprises the second derivatives of E with respect to \mathbf{P} .

$$\mathbf{P}^{t+1} = \mathbf{P}^t - H^{-1} \mathbf{g}(\mathbf{P}^t)$$



Its disadvantage is that the speed of convergence is sensitive to the quadratic assumption at the starting location.

- **Levenberg-Marquardt**

Levenberg proposed a new update:

$$\mathbf{P}^{t+1} = \mathbf{P}^t - (\mathbf{H} + \lambda \mathbf{I})^{-1} \mathbf{g}(\mathbf{P}^t) \quad (72)$$

where \mathbf{I} is the identity matrix and λ is a scalar. If the error decreases with the step, the quadratic assumption in the Gauss-Newton is assumed correct and λ is reduced in order to weaken the influence of the gradient descent. Otherwise λ will be increased and the optimisation follows the gradient descent algorithm.

LM requires the computation of \mathbf{H} . In practice the Hessian can be approximated by a linearized version calculated from the Jacobian matrix \mathbf{J} :

$$\mathbf{H} = 2\mathbf{J}^T \mathbf{J} + \mathbf{S} \quad (73)$$

Thus, an analytical expression of the first derivative must be available at a reasonable computational cost for using LM. This is not true for some similarity measures such as MI or NMI. Powell's direction set method or Nelder-Mead's downhill simplex method [137] are often applied for those measures.

5.5.3 Implementation of Levenberg-Marquardt

The computation of the first derivatives \mathbf{g} and the Hessian matrix \mathbf{H} is necessary for LM. The derivative of the intensity term w.r.t each unknown FFD parameter is given by:

$$\mathbf{g}_I = -2\mathbf{J}\mathbf{W}^T \mathbf{W}\mathbf{d} \quad (74)$$

where the elements of Jacobian matrix \mathbf{J} (by the chain rule) are

$$\begin{aligned} J_{ij} &= \frac{\partial M_i(\mathbf{X}_i)}{\partial P_j} = \frac{\partial I_t(\mathbf{x}(\mathbf{X}_i))}{\partial P_j} = \frac{\partial I_t(\mathbf{x})}{\partial \mathbf{x}} \bigg|_{\mathbf{x}=\mathbf{x}(\mathbf{X}_i)} \cdot \frac{\partial \mathbf{x}}{\partial P_j} = \frac{\partial I_t(\mathbf{x})}{\partial \mathbf{x}} \bigg|_{\mathbf{x}=\mathbf{x}(\mathbf{X}_i)} \cdot \frac{\partial \mathbf{u}(\mathbf{X}_i)}{\partial P_j} \\ &= \frac{\partial I_t(\mathbf{x})}{\partial \mathbf{x}} \bigg|_{\mathbf{x}=\mathbf{x}(\mathbf{X}_i)} \cdot \Psi_j(\mathbf{X}_i) \end{aligned} \quad (75)$$

$\left. \frac{\partial I_t(\mathbf{x})}{\partial \mathbf{x}} \right|_{\mathbf{x}=\mathbf{x}(X)}$ is defined as the derivative of I_t in the current state with respect to the current coordinate at $\mathbf{x} = \mathbf{x}(X)$.

With this simplification, the computational cost for the derivatives is reduced to a look-up operation using terms which are pre-calculated before the optimisation (the gradient of the target image and the Bézier basis function values).

The intensity term of each element of the Hessian Matrix can be approximated by:

$$H_{kl}^I = 2 \sum \frac{\partial I_t(\mathbf{x}(X))}{\partial P_k} \frac{\partial I_t(\mathbf{x}(X))}{\partial P_l} \quad (76)$$

The optimisation is achieved by iteratively updating the displacement of the parameters from the initial guess. The updates follow:

$$\delta \mathbf{P} = -(\mathbf{H} + \lambda \mathbf{I})^{-1} \cdot \mathbf{g} \quad (77)$$

5.5.4 Termination Criteria for Optimization

Four criteria were used to terminate the optimization. The optimization was successful if the tolerance on parameters or derivatives was met. The optimization also terminated if the total process time exceeded a set value or no correct path was found in the error surface within a limited number of loops.

5.6 Capture Range Analysis

The capture range is a major determinant of the robustness of an automated method. In order to examine the capture range of the new atlas-based segmentation method, experiments were performed using a range of rigid body transformations. These experiments investigated whether large rigid-body transformations could be reliably estimated by a non-rigid registration with simple mesh in cardiac MR applications. If so, it may not be necessary to carry out a rigid-body registration before the non-rigid registration, as is the case in many implementations.

5.6.1 Implementation

In this experiment, the atlas of Figure 5.4b was employed to fit to the same image (Figure 5.4a) from which the atlas was constructed. The ground truth for the solution is therefore the

original atlas shown in Figure 5.4b. The grey levels of the blood and myocardium in the atlas were directly estimated from the corresponding pixels in the image. The atlas was rigidly transformed from the ground truth to create different initial poses. The experiment examines if the registration method is able to deform the atlas from these initial poses back to the ground truth.

Three rigid-body parameters T_x , T_y and R form a 3D parameter space for this experiment. T_x and T_y are the translations in x and y directions and R is defined as a clock-wise rotation as shown in Figure 5.8. No scaling is considered so that the results can be presented in 3D. The parameter space was sampled with an interval of 2 pixels in the range of $[-30 +30]$ for T_x and T_y and 4 degrees in the range of $[-60 +60]$ for R . These result in a total of 14147 different experiments. Figure 5.8 presents three experiments that used the maximal value of one of the parameters.

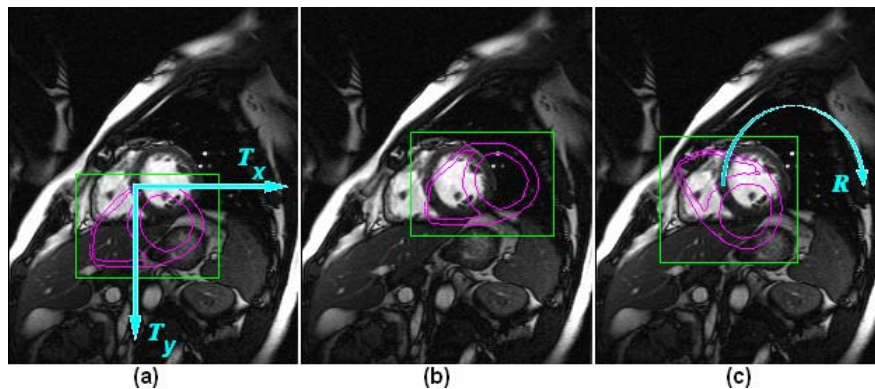


Figure 5.8 Definitions of T_x , T_y and R and examples with single maximal values. (a) $\nabla T_x = +30$, (b) $\nabla T_y = +30$ and (c) $\nabla R = +60$.

MHD was applied to measure the errors between the ground truth and the contours after registration. LV, RV and myocardial contours were independently measured. A one element linear FFD mesh was used for the registration. The smoothing weights were set to 0.5 and the weights of the atlas points were all set to 1.0.

5.6.2 Registration Process

A typical registration procedure with the large initial rotation error is shown in Figure 5.9. The four vertices of the element were moved across the image to create the FFD deformation for the atlas. The intensity difference between the atlas points and their corresponding pixels in the target image reduced in an iterative manner. Figure 5.9 displays the deformation results from every 20th iteration. It shows that the non-rigid registration is achieved by two

shearing-like movements instead of one rigid-body movement. This implies that the FFD-based non-rigid registration prefers local deformation. The changes of the energy function and its separate terms during the registration are shown in Figure 5.10.

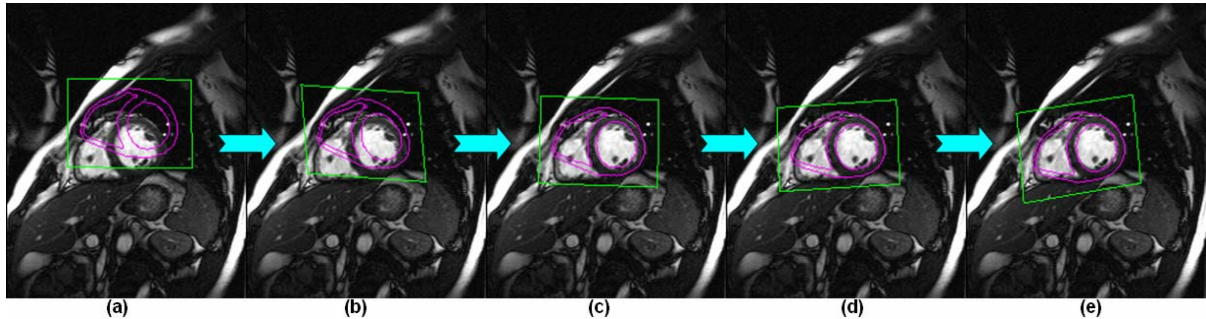


Figure 5.9 An example of the registration process. The initial pose was formed with a large rotation error. 20 loops occur between two neighbouring images.

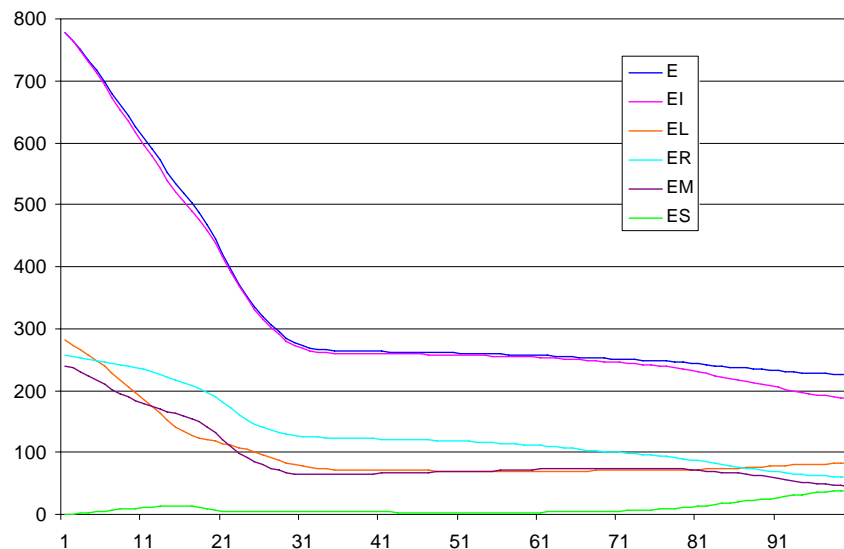


Figure 5.10 Changes in the energy function and its individual terms from the example shown in Figure 5.9. *E* – energy function, *ES* – smoothing term, *EI* – intensity term including LV term *EL*, RV term *ER* and myocardium term *EM*.

5.6.3 Results

- **Qualitative Validation**

Figure 5.11 shows four results from registrations that had large displacements in their initial poses. Figures 5.11a, b and c have large rotations. It was found that the initial rotation error cannot be large if the initial atlas was located at the left side of the ground truth such as the case in Figure 5.11d. This is because more local minima exist in the error surface around the RV than the LV, making it easy for the registration to become trapped in the wrong

minimum. A large initial rotation may prevent the atlas from returning to the ground truth position.

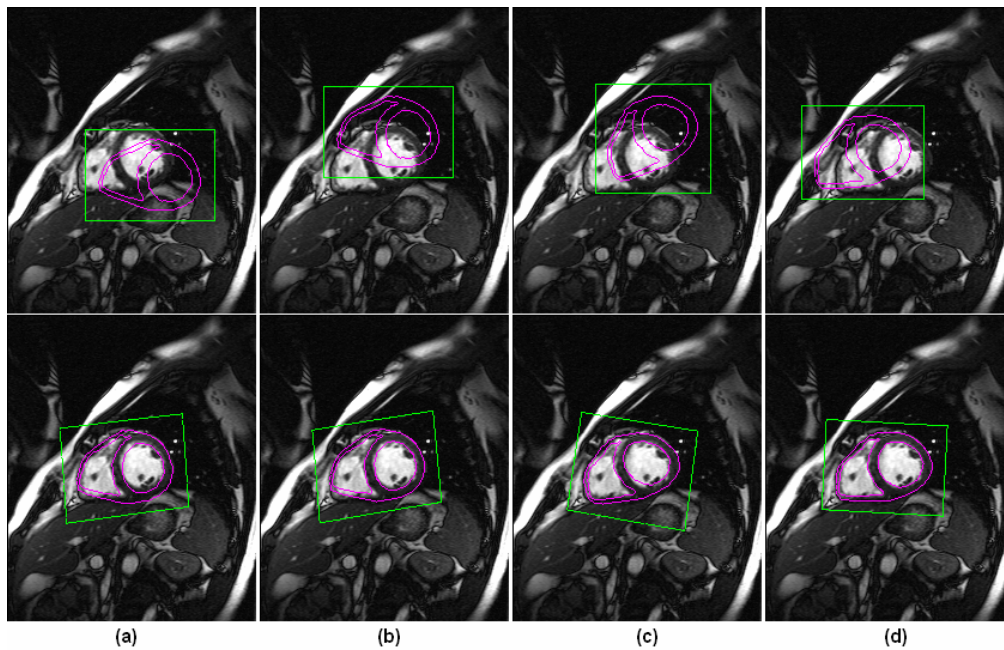


Figure 5.11 Examples of atlas-based registration results. Top row - starting positions, bottom row – positions after registration. (a) $\nabla T_x = 22, \nabla T_y = 10, \nabla R = 20$; (b) $\nabla T_x = 10, \nabla T_y = -26, \nabla R = 20$; (c) $\nabla T_x = 18, \nabla T_y = -18, \nabla R = -20$; (d) $\nabla T_x = -18, \nabla T_y = -6, \nabla R = -4$;

- **Quantitative Validation**

Figure 5.12 shows the distribution of the MHD results of 14147 registration experiments. The LV has better results than the RV and myocardium. In 54% of cases, the LV is able to converge to the correct position (with a distance error of less than two pixels), in comparison to 33% of cases using the RV and 41% with the myocardium.

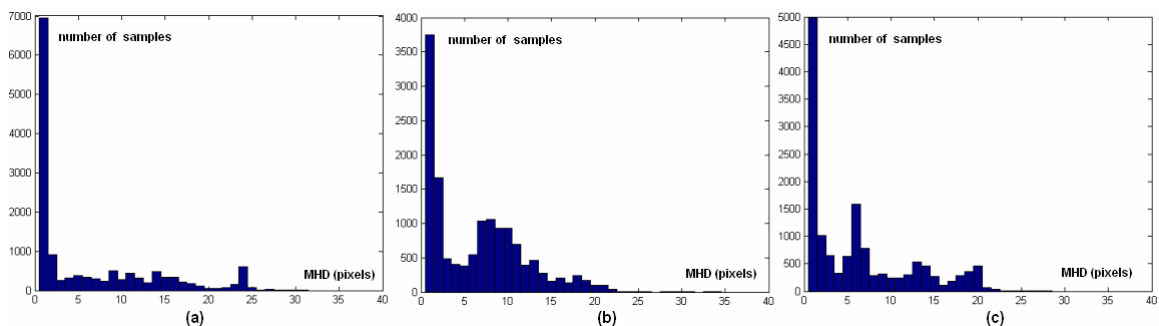


Figure 5.12 Histogram plot of modified Hausdorff distances (MHD) of 14147 registrations with different starting poses. (a) LV, (b) RV, (c) myocardium.

The iso-surfaces of the capture range leading to errors of two pixels or less are shown in Figure 5.13. The top row shows that the LV has better performance in high rotation cases. This may be due to the LV's round shape. The figure also demonstrates that the accuracy of the myocardium is highly dependent on the performance of the RV. The algorithm normally converges if initial poses have rotated by less than 20 degrees. The bottom row reveals that the average translation capture range in any direction is about 25 pixels. There is no obvious bias in $-T_y$ and $+T_y$ directions. In contrast, $+T_x$ translations out perform $-T_x$ translations because the structures around the RV are more complicated than the LV. More local optima are expected to be found in areas close to the RV.

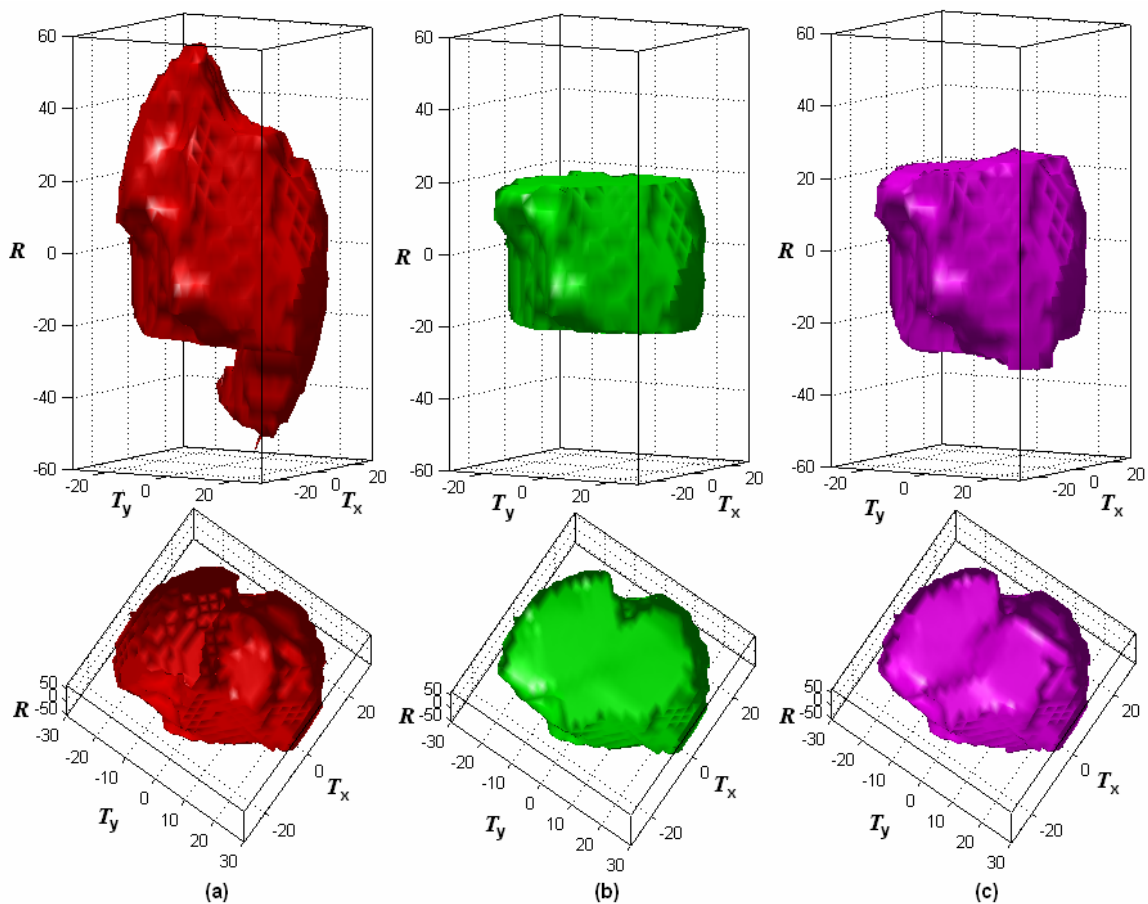


Figure 5.13 Iso-surfaces of MHD at 2 pixels. (a) LV, (b) RV, (c) myocardium.

The results show that the method has a large capture range and it may not be necessary to carry out a rigid-body registration before using non-rigid registration. The rigid-body step can be replaced by a non-rigid registration that uses a low complexity mesh. This strategy is implemented by the multi-grid and multi-resolution framework in Section 5.7.2.

5.7 Large Dataset Analysis

To validate the accuracy of the new atlas-based registration method, the 3D finite element heart model (developed in Section 1.5) was used to register all 330 patients in the ONTARGET dataset. The atlas for each image was constructed from the intersection between the image plane and the initialized model, discussed in Section 5.2. The best initial estimate was found on the middle SA slice. Thus, this slice was selected as the first image for segmentation in this chapter and the other slices will be investigated in Chapter 7. The atlas-based segmentation method was used for the registration of the initial atlas to the image. A coarse-to-fine strategy was employed to improve the robustness of the method and the papillary muscles were removed by morphological methods. The registration results were compared to the ground truth contours manually defined by an experienced analyst.

5.7.1 Ground Truth Data

The ground truth data was manually obtained by clicking on the boundaries between the structures with the spacing of 3-6 pixels (Figure 5.14a,b). In order to remove the impact of the under-sampling of the ground truth data, spline curves were fitted to these points and more points generated by interpolating the curves on a sub-pixel level, Figure 5.14c.

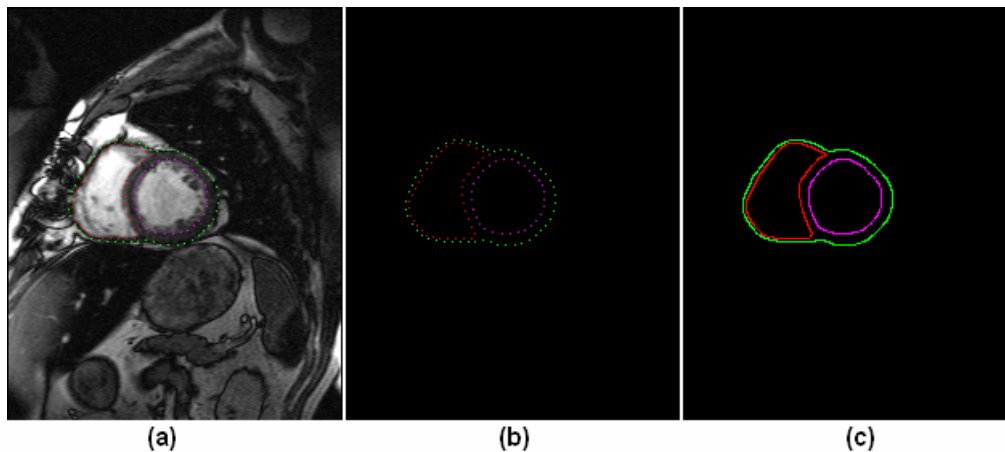


Figure 5.14 Sub-pixel level ground truth data: (a) original image, (b) under-sampling ground truth and (c) ground truth contours after sub-pixel interpolation.

5.7.2 Implementation

This section describes implementation details designed to avoid common problems known to occur when fitting a model to a wide range of patient data. In particular, the algorithm may be attracted to a local minimum for many reasons:

- intensity inhomogeneity problem in the images
- blurred RV free walls
- SA planes not orthogonal to the LA (This causes abnormal LV and RV shapes)
- abnormal shape or size of patients' heart
- papillary muscles in LV and RV cavities

A general solution to this problem is to employ a coarse-to-fine strategy that uses multiple resolution and grids. Multi-resolution has been applied in many automated segmentation or registration applications [34, 38, 64, 70, 121, 138-141]. It not only can improve the robustness but also reduce the computational cost. Multi-grid algorithms are also often used in mesh-based registration methods [139, 140].

Another problem arises when papillary muscles are classified as blood pool for the purposes of clinical analysis. It provides better shape descriptors for the LV and RV; however, it will increase the error of the intensity term in the energy function and lead to smaller contours. The contours can be compensated for by either removing the papillary muscles from the image or by modeling the papillary muscles in the atlas. The first solution is easier to realize. The majority of the papillary muscle in the blood pools can be adequately removed using morphological methods.

- **Coarse-to-fine Framework**

- *Multi-resolution*

Typically, multi-resolution strategies construct a pyramid of images using successive Gaussian smoothing and sub-sampling [142]. The image at each level in the pyramid is half the size of the next level. Registration starts with the lowest resolution image in the pyramid. The parameter estimates obtained from the low level fits become the starting parameter values for the next higher level. Gaussian smoothing is vital for avoiding local minima using these strategies. Speed was not the key target for this experiment; therefore, instead of using a pyramid of images, a set of images with different levels of smoothing but of the same size were created for this coarse-to-fine strategy.

- *Multi-grid*

The purpose of using multi-grid registration is similar to multi-resolution. The error surface of the registration using a low complexity mesh may have less local minima and the global minima may be more easily approximated at that level.

In [139, 140], a multi-grid method was proposed to reduce the computational cost. In their methods, parameters estimated at low complexity levels can be completely propagated to higher levels. The method first examined the deformation of each element in the previous low complexity level. The parameters of the element were only propagated to its high level grid if a large deformation was observed on that element. The total time can be saved in comparison to a more direct use of high complexity meshes; however, local minima are not expected to be efficiently avoided in this method due to minimal changes in the error surfaces.

Instead of propagating the parameters from low complexity levels to higher ones, our strategy performs a completely new registration, starting from an undeformed mesh, at each level. With this strategy, local minima occurring in the error surface of one level may not appear at another level.

- *Multi-weights*

An advantage of the SMPL framework is that it is able to assign a different weight for any single pixel. Normally, the same weight is assigned to each single object. In the coarse-to-fine strategy, the weights of the objects can be different at each level. All objects have similar weights at the coarse level and higher weights are set to myocardial pixels in finer levels. It should be noted that the percentage of blood points in the atlas is higher than that of myocardial points and this needs to be considered when setting the weights.

- *Coarse-to-fine Registration Process*

The whole process consists of four levels of coarse-to-fine FFD registrations (Figure 5.15). Due to the presence of different LV to RV size ratios in the images, it was found that a starting mesh complexity of 2x2 (Figure 5.15a) performed better than 1x1. The highest Gaussian smoothing was applied and the weights of the blood and myocardium were set to 1 and 2 at the coarse level. The mesh complexity is increased by one for each level while the Gaussian smoothing decreased steadily to zero. The weights of myocardial pixels in these four levels were set to 2, 2, 3 and 5 respectively.

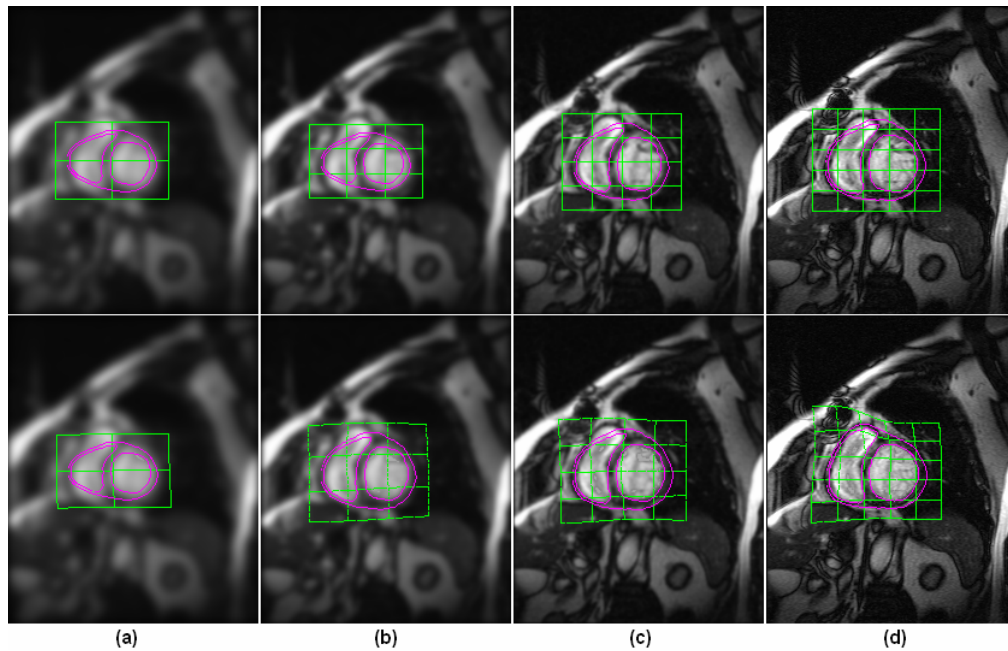


Figure 5.15 Multi-grid and multi-resolution strategy applied in the case of Figure 5.20. Top row – before registration, bottom row – after registration. (a) 2x2 mesh, high smoothing, (b) 3x3 mesh, medium smoothing, (c) 4x4 mesh, low smoothing, (d) 5x5 mesh, no smoothing.

- **Remove Papillary Muscles in LV and RV**

There has been much discussion on whether the papillary muscles should be included as part of the blood pool when determining heart function indices. Some insist that those muscles must be excluded from the blood pool to maintain an accurate measurement of LV volumes [143]; others have shown that the inclusion of papillary and trabecular muscles generates little impact clinically [144]. The American Society of Echocardiography recommends echocardiography should include the papillary muscles and trabeculations in the LV and RV cavities. The different automated approaches for CMR segmentation have usually classified the papillary muscles as part of the blood pool. Their inclusion in the blood pool makes the LV almost circular and the shape of RV becomes more regular in SA slices [6, 37-39, 78, 102, 145, 146].

Morphological methods can be employed to quickly remove the papillary muscles in both the LV and RV cavities. This process was applied once after each level of the coarse-to-fine framework.

- *LV cavity*



Figure 5.16 shows the process for removing the LV papillary muscles. Firstly, a threshold was calculated using the EM algorithm discussed in Section 5.2.2, and applied to the area inside the LV contour to obtain the binary LV blood pool shown in Figure 5.16b. The ROI needed to be restricted to the LV contour to avoid leaking in some cases. A convex hull algorithm was applied to the binary image (Figure 5.16c) to fill the papillary muscle pixels (Figure 5.16d). The grey levels of these pixels were then changed to the mean blood value (Figure 5.16e).

○ *RV cavity*

A similar process was employed for the removal of the RV papillary muscles. Here, the convex hull cannot be used because of the shape of RV, so it was replaced by simply filling the image. The result is shown in Figure 5.17e. The RV free wall may be removed using this method when it is thin and not a continuous curve and further research is required to find a better solution.

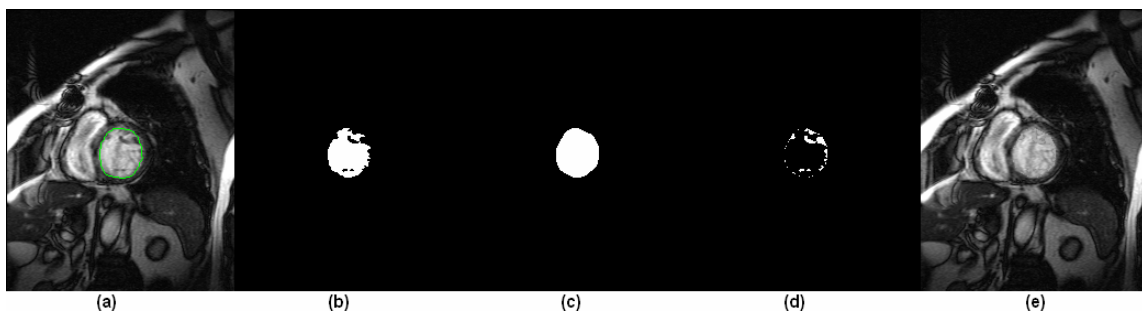


Figure 5.16 Removal of papillary muscles from LV cavity; (a) SA image with LV contour, (b) binary image after thresholding, (c) binary image after convex hull, (d) potential papillary muscle pixels, (e) image after removing LV papillary muscles.

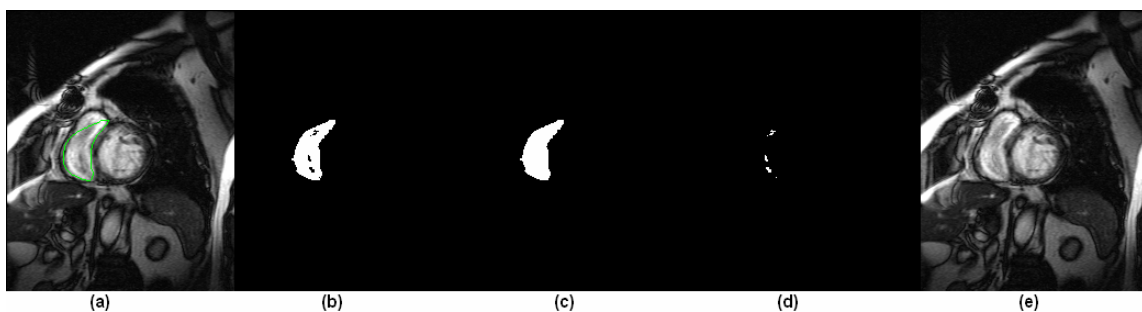


Figure 5.17 Removal of papillary muscles from RV cavity; (a) SA image with RV contour, (b) binary image after thresholding, (c) binary image after image filling, (d) potential papillary muscle pixels, (e) image after removing RV papillary muscles.

5.7.3 Results

- **Case Failures**

The non-rigid atlas-based registration algorithm successfully detected the LV and RV structures in 328 cases out of 330. Two cases, shown in Figure 5.18, completely failed. A large initial rotation error was observed in both cases and this was probably the main reason for their failure. These two cases were not included in the remainder of this Chapter, and in the refinement of the segmentation methods presented in Chapters 6 and 7.

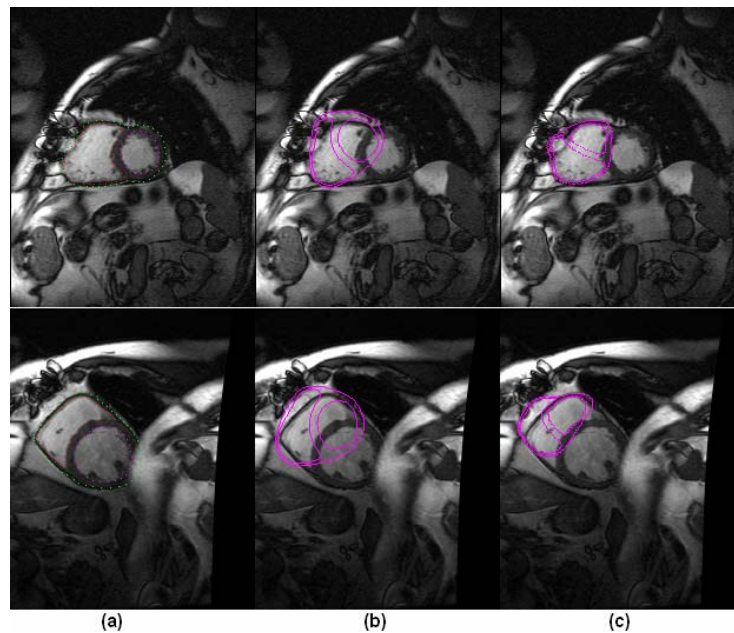


Figure 5.18 Two failed cases with large initial errors. (a) ground truth, (b) initial estimation, (c) registration result.

- **Initial Estimate Results**

Quantitative analysis of the initial estimation results is shown in Figure 5.19. The average MHD measure was about 5 pixels in the LV, RV and myocardium contours. The average SI of the LV and RV were both over 70%. This high coverage is very important in the modified atlas-based registration method discussed in the next chapter. The coverage of the myocardium is relatively low since it is affected by both the LV and RV.

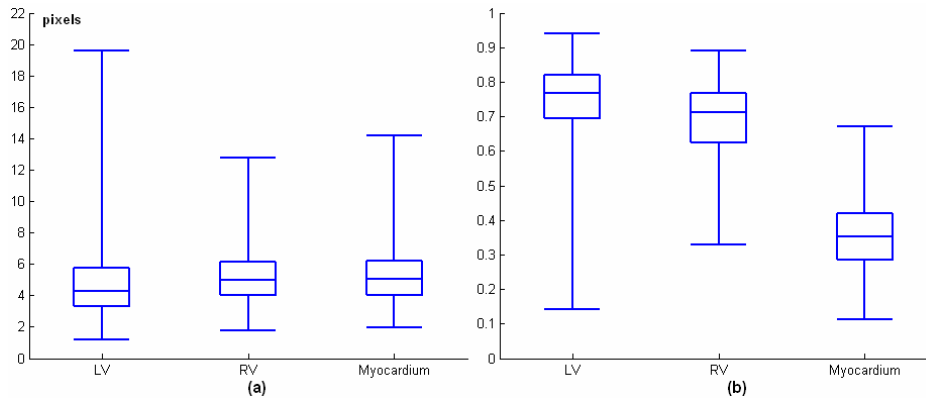


Figure 5.19 (a) MHD errors in pixels and (b) SI results of initial contours on the ED frames of middle SA slices for the ONTARGET dataset.

- **Atlas-based Registration Results**

The atlas-based registration results are shown in Figure 5.21 and Figure 5.22. The figures show a large improvement for the LV contours. The numerical data in Table 5-1 shows that both the mean values and standard deviations of the MHD errors have reduced more than 60% during registration. In the RV, the mean MHD error has a 50% reduction. However, no improvement in the standard derivation was found because there are a few cases where the RV was mis-registered. The mis-registrations were mainly caused by abnormal RV shapes and poor image scans in RV areas. Figure 5.20 shows the case which contributes the peak error in Figure 5.21b. The image has poor quality caused by image aliasing in the RV. If the SI results in Table 5-1 are considered, the improvement in RV area is as good as the improvement in LV area. The myocardium error highly depends on the RV error, which obtains a 50% reduction in the mean MHD error and whose average SI measure is almost doubled.

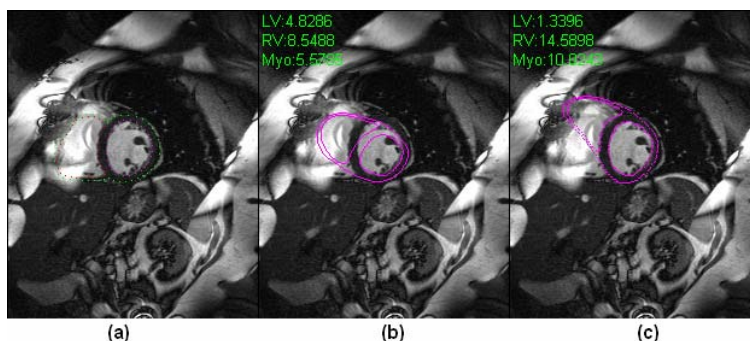


Figure 5.20 The case with the largest RV error. (a) ground truth, (b) initial estimation, (c) registration result.

(mean \pm std)	Modified Hausdorff Distance		Similarity Index	
	Initial position	After registration	Initial position	After registration
LV	4.76 ± 2.35	1.75 ± 0.90	0.75 ± 0.11	0.90 ± 0.05
RV	5.19 ± 1.66	2.59 ± 1.98	0.69 ± 0.10	0.86 ± 0.09
Myocardium	5.21 ± 1.77	2.70 ± 1.67	0.36 ± 0.11	0.63 ± 0.09

Table 5-1 Modified Hausdorff distance and similarity index before and after registration

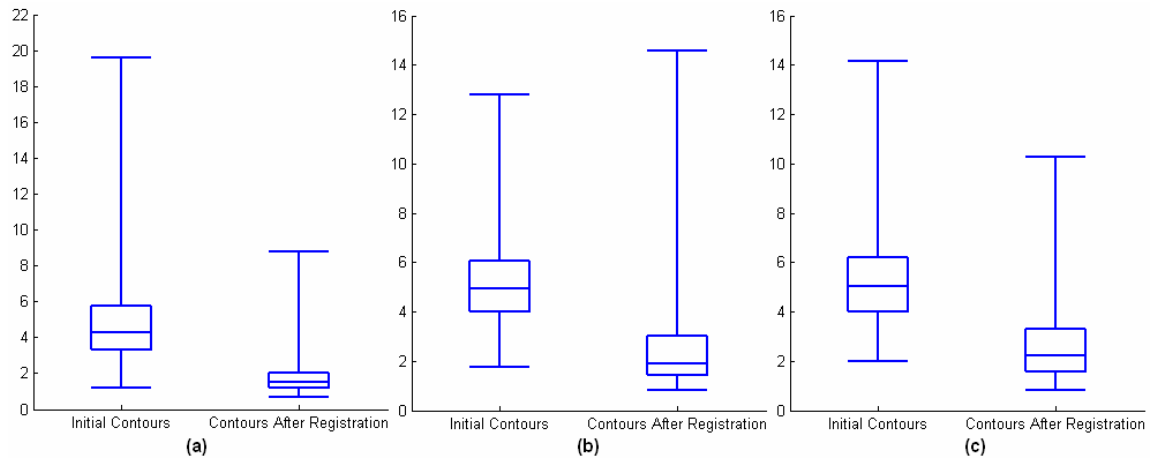


Figure 5.21 Box plot of MHD (unit: pixel) between the ground truth and the detected contours. (a) LV endocardium, (b) RV endocardium and (c) epicardium.

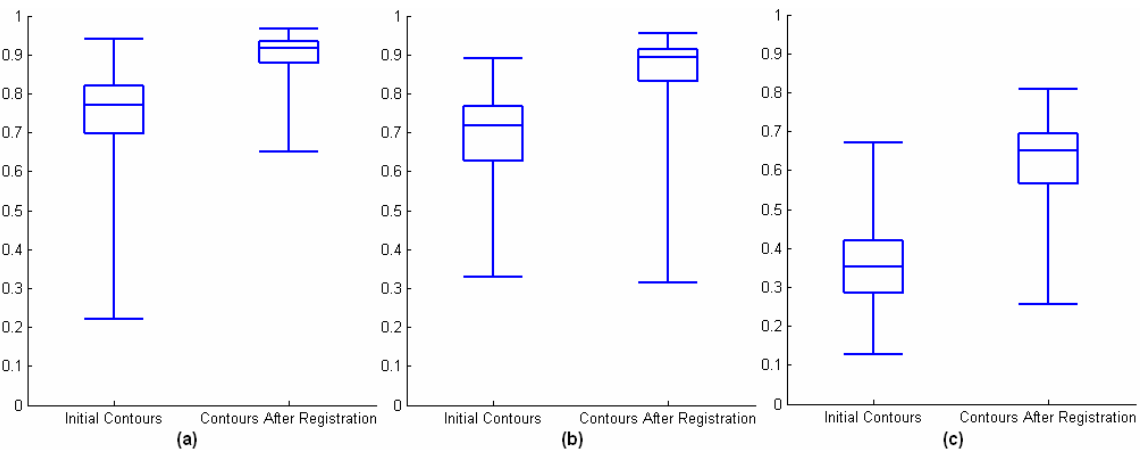


Figure 5.22 Box plot of SI between the ground truth and the detected contours. (a) LV blood pool, (b) RV blood pool and (c) myocardium.

5.8 Discussion and Conclusion

In this chapter, the SMPL atlas-based registration framework is presented. The results show the method has a large capture range and good accuracy. No rigid-body registration was necessary; a non-rigid registration step that uses a low complexity mesh was used instead. The sub-pixel resampling strategy significantly helped to reduce the local optima caused by

linear interpolation and the running time was improved by using fewer pixels in the computation. By using the SSD measure and LM optimisation, the automated atlas-based registration method based on the SMPL framework provided an efficient and accurate solution to the segmentation on the middle SA slices. A method for automatically detecting failure was also developed, which relied on the capability of the SMPL registration framework to integrate anatomical information into the atlas. These advantages will be discussed further in the next chapter.

Similar to other deformable model based registration methods, the algorithm was still found to be insufficiently robust to local minima. The main problems are discussed below..

- *Papillary Muscle Problem*

Figure 5.23 shows the comparison between the results of including and not including the process of removing papillary muscles. No significant improvement was observed using the current removal method. Two possible reasons are:

- 1) the image filling algorithm used in the RV cavity instead of the convex hull. The papillary muscles which are not completely inside the atlas's RV contour can not be removed.
- 2) The removal process is currently only run once at each level of the coarse-to-fine framework. It should be executed at each iteration of the registration process. This can improve the results but at the expense of total computational cost.

A more efficient method is required, especially for the RV. A balloon force is investigated in the following chapter for this purpose.

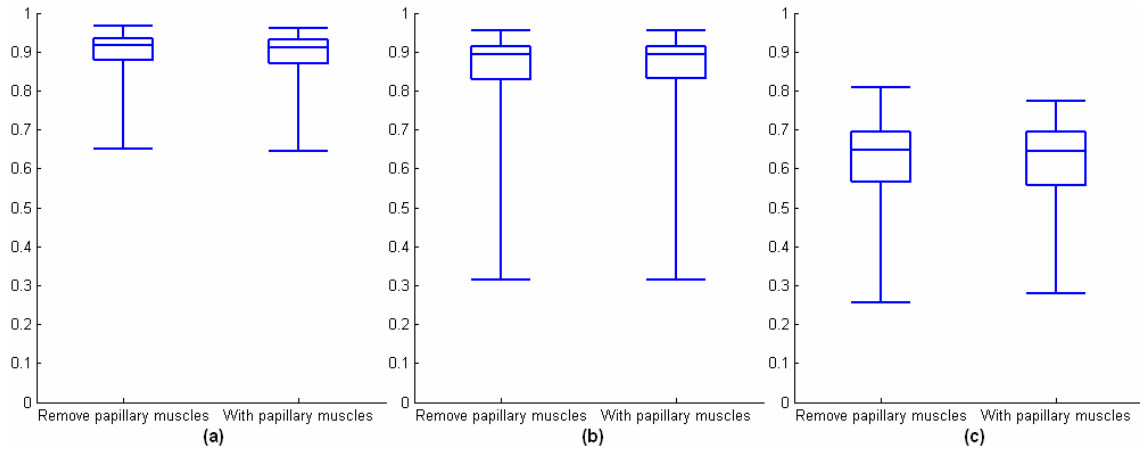


Figure 5.23 Box plot of SI with and without papillary muscle removal process. (a) LV blood pool, (b) RV blood pool and (c) myocardium.

○ *No Background Information Problem*

Another potential problem is that no background was included in the method in order to reduce the computational cost and also to avoid modeling the background which is very variable. Unfortunately, smaller contours may be found if the background is not included, particularly when the myocardial wall on the target image is thicker than in the atlas, Figure 5.24. The atlas will have no desire to expand its contours to the correct position when the energy function is only based on the intensity difference. An image force must be created to solve this problem. A solution is investigated in the next chapter by adding a balloon force.

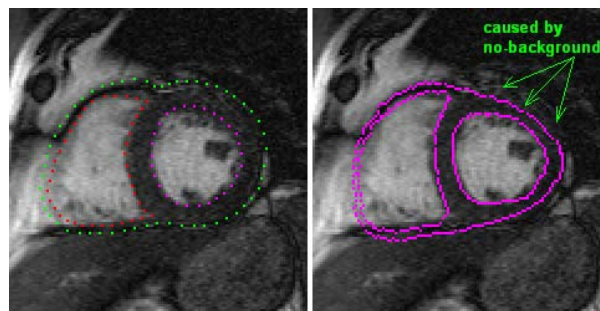


Figure 5.24 A small epicardial contour because of no background information.

○ *Myopic Problem*

The Myopic problem is a common problem in deformable model based methods. The atlas is not attracted to the correct boundaries if they are too far away from its initial position. This is often problematic for the RV contour when the RV shape on the target image is quite

different from the shape in the atlas, as shown in Figure 5.25. The balloon force solution proposed in the next chapter aims to reduce this effect.

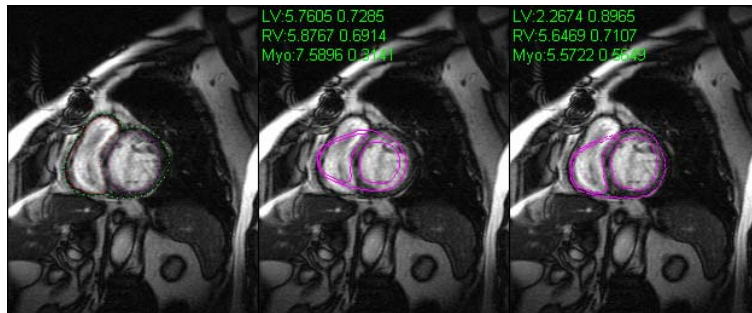


Figure 5.25 Myopic problem in a case with high RV/LV ratio.

6 Modified Atlas-based Segmentation for Cardiac MR Images

This chapter presents a modified atlas-based registration method for CMR segmentation. The method is based on the SMPL framework proposed in the last chapter. The framework efficiently solves the atlas registration using non-linear least squares, incorporating sub-pixel sampling and arbitrary weighting. A coarse-to-fine mesh solution strategy yielded a global minimum in most cases; however, intensity information alone did not produce results of sufficient accuracy because of the myopic problem and lack of background information in some cases.

The SMPL framework can be extended by incorporating additional information, for example labelling specific regions of the heart or defining boundaries. Incorporating more information can improve both the robustness and the accuracy of the solution. A modified method based on this concept is proposed in this chapter for CMR image segmentation. A clinical trial of 328 patients was used to investigate its accuracy and robustness compared to the intensity-based method.

The chapter is organized as follows. Section 6.1 presents how boundaries and anatomical information was defined in the atlas. Section 6.2 proposes a method to construct and integrate a boundary term to the method. Section 6.3 discusses how to construct and integrate an area term that uses the anatomical labelling defined in the atlas. Section 6.4 provides detailed results, investigating the accuracy and robustness of the modified method. Discussions and conclusions can be found in Section 6.5 and 6.6.

6.1 Inclusion of High Level Information

This section will demonstrate how the additional boundaries and anatomical information are included in the atlas.

6.1.1 Atlas

The atlas was constructed from the intersection between the initialized model and the plane of the target image. Object points were obtained by sampling the atlas on a sub-pixel level.

Figure 6.1a shows the object's points, blue being the myocardial points, red RV blood pool points and pink LV blood pool points. The grey levels associated with each object were calculated for each individual patient from the pixel intensities found within the atlas region of the patient images using the EM algorithm. The same grey level was assigned to the LV and RV blood points.

6.1.2 Boundary Points

The boundary points of LV endocardium, RV endocardium and epicardium were defined in the atlas, and are marked as green in Figure 6.1b. These points, when the atlas is registered correctly, are generally located in areas that have a high gradient in the target image. They were used to construct a boundary term for the segmentation method. The boundary term creates a force that attracts these boundary points to the real boundaries in the image. It aims to increase the capture range of the method and to decrease the dependency on the initial position. With this term, various contour-based techniques can be employed and integrated into the SMPL framework.

6.1.3 Anatomical Information

Anatomical information can be manually or automatically defined in the atlas. The information is mapped to the target image by deformation and is used to improve the robustness and accuracy of the method. For example, the two RV inserts, shown as two black dots in Figure 6.1b, can be automatically determined in the atlas. They can be detected as the first and last RV points by a polar scan from the LV centre. The two inserts are used to characterize the region of septal myocardium (marked by the left red polygon, Figure 6.1b) between the two cavities. The points inside the region are called septal-myocardial points in this thesis. In our experience, these points can be detected at a very early stage of the segmentation process because of their distinctive anatomical nature. These points may also be used in the method as a tool to validate registration failures and to improve the estimation of the myocardial grey level.

Another region labelled the LV free wall myocardium (marked by the right red polygon, Figure 6.1b) can also be automatically defined. The two RV inserts detected above are used to compute the LV RV direction \mathbf{V}_y . The LV free wall myocardium is located in $-\mathbf{V}_y$ direction. The region of interest is then defined by the area on the ring with the angle less

than 60 degrees to $-V_y$ w.r.t the LV centre. The contour points of this region are used in Section 6.3 to improve the accuracy of the LV free wall's epicardium.

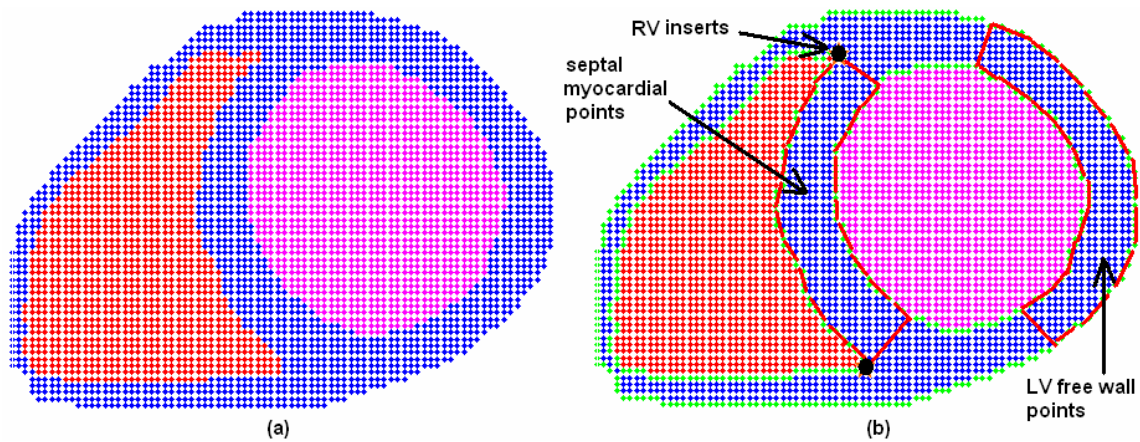


Figure 6.1 (a) atlas points: blue – myocardial points, red – RV points, pink – LV points; (b) boundary and anatomical information defined in atlas, green points – boundary points, black dots – two RV inserts, red contours – two special anatomical regions.

6.2 Integration of the Boundary Term

6.2.1 Introduction

The aim of the boundary term is to solve the myopic problem identified in the intensity-only method implemented in Chapter 5. It will also reduce the local minima caused by the papillary muscles.

The results of the previous chapter showed that in most cases the LV and RV contours detected using just the intensity term were too small. They were normally within the blood cavities. The intensity term worked better for cases where the atlas objects were larger than the corresponding objects in the image, and the atlas could not enlarge as well as it could shrink. Papillary muscles and partial volume effects also lead to the detected LV contours being too small. In the RV, large errors were introduced mainly because of the irregular shapes of the RV, due to the myopic problem. To solve this, a balloon force would expand both the LV and RV boundaries (Figure 6.1b) to more correct positions. Such a force field must meet the following requirements:

- 1) A constant force should be established in homogenous regions to drive the contour out to the boundaries.

- 2) The force should be reduced to zero or very small values in the vicinity of the boundaries.

A distance map is a good option to create such a force field, as previously described for LV segmentations [147]. In this literature, two Euclidian distance maps have been proposed: one created from the boundary information and the other from the intensity information. The following section discusses these two distance maps in detail. Disadvantages are examined and a new ROI distance map based on the fast marching time-crossing map is proposed. The new distance map is shown to have better local performance and is more robust to leaking.

6.2.2 Edge Distance Map

The edge distance map (Figure 6.2c) is derived from a binary edge map (Figure 6.2b). The binary edge map can be computed using the Canny algorithm with appropriate threshold selection, and the edge distance map can be constructed by computing the distance between each pixel and its closest edge pixel on the binary edge map.

One advantage of an edge distance map is that it has a large capture range, since it offers a constant force to the nearest boundaries no matter how far the initial contour is from the boundaries. Unfortunately, two requirements should be met. One is that a high-quality binary edge map should be available. The other is that the nearest boundaries are the correct targets. These conditions are not always satisfied in CMR segmentation.

- **False Edges on Binary Edge Map**

The correct choice for the binary edge map's threshold is essential; however, this is very difficult to automatically determine. An example is shown in Figure 6.2. A high threshold cannot provide enough edges (Figure 6.2b) and a low threshold may produce too many edges (Figure 6.2d). Both will produce unusable distance maps (Figure 6.2c and e).

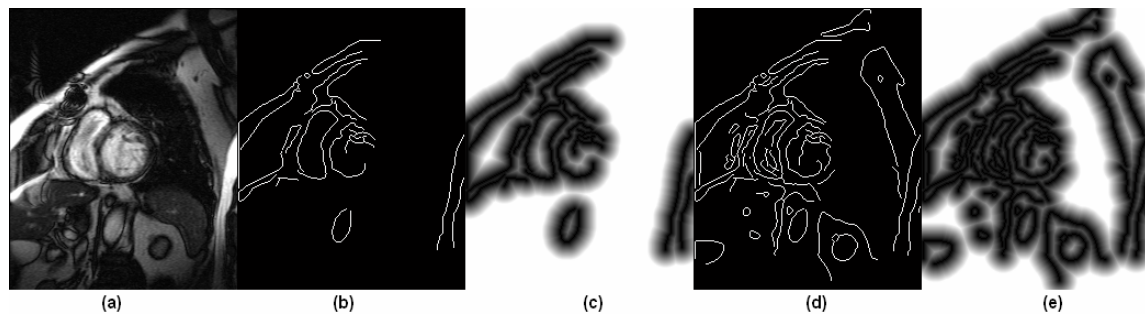


Figure 6.2 Edge distance maps derived from binary edge maps: (a) original image, (b) binary edge image with high threshold, (c) distance map from b, (d) binary edge image with low threshold and (e) distance map from d.

- **Nearest Boundary Problem**

The force field of an edge distance map can only drive the initial contours to their nearest boundaries. The results will be wrong if the nearest boundaries are not the targets. An example is shown in Figure 6.3a. The blue curve represents the actual boundary and the pink is the initial contour. Figure 6.3b gives the edge distance map derived from the blue boundary. The initial contour does not encapsulate the entire peak in the distance map therefore the downhill force (arrows in Figure 6.3b) will drive the initial contour to one side. It is vital that the initial contour encapsulates the distance map's peak.

6.2.3 ROI Distance Map

Another distance map is called the region of interest (ROI) distance map. The object contours are first obtained by a simple thresholding, and ROI distance map is obtained by computing the distance between each pixel to its nearest contour pixel. The map results in a force field that attracts the initial contour to the object contour. This method suffers if the threshold level is inaccurate, the main problem being leaking due to the simple thresholding process.

- **Threshold Level**

It is difficult to obtain accurate information about the threshold level before the registration. If the level is too high or too low the object contour may larger or smaller. If the errors are too large, the map impedes rather than assists the segmentation process.

- **Leaking Problem**

Simple thresholding often causes leaking of the blood pool objects, especially where the boundaries are thin such as in the RV free wall. Fat outside the RV free wall will be included if any leaking occurs around the RV. Thus, ROI distance maps are expected to have good performance in the LV but not the RV.

6.2.4 Proposed ROI Distance Map

A new ROI distance map is designed to solve the above issues, based on the fast marching time-crossing map introduced in Section 1.6.1.

- **Time-cross Map**

An initial contour, derived from the current atlas position, is set as the zero state in the time-cross map T_M . The algorithm drives the contour in the outward directions with a speed that is inversely proportional to the image gradients [31]. The map records the time when the contour will pass that pixel. It is similar to computing the shortest distance between the pixels and the initial contour with Dijkstra's shortest path algorithm. The distance map B_M is constructed by the formula:

$$B_M = \frac{1}{\lambda + T_M}$$

where λ is a small constant. Figure 6.3c shows the new distance map inside the actual contour. The initial contour is set to the highest level in the distance map and evolves to low positions during registration. The level close to zero is expected to be found at the boundaries. The force created by this map is shown by the arrows in Figure 6.3c.

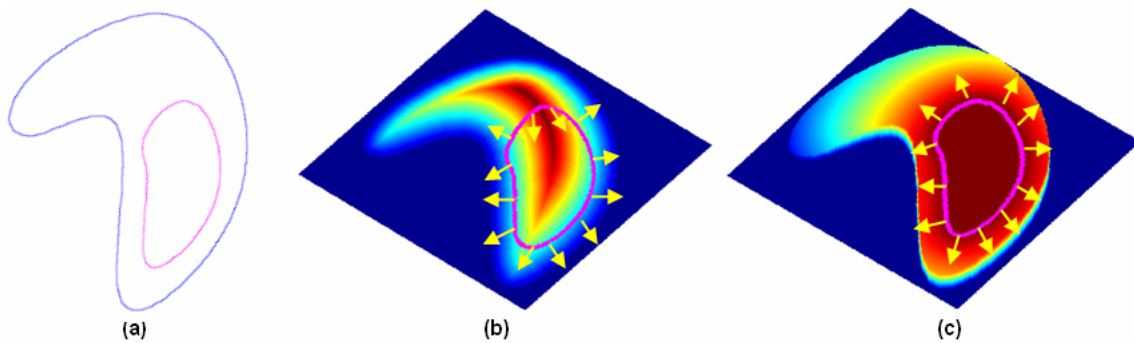


Figure 6.3 (a) pink - initial contour and blue – actual boundary, (b) edge distance map (3D) and (c) ROI distance map (3D) based on fast marching time-cross map.

- **Definition of the Initial Contour**

When using this distance map, it is important to ensure that the actual boundaries are not inside the initial contours. The actual boundaries cannot be reached if they are within the initial contour because the map produces a one-way balloon force. This can be avoided by segmenting object pixels in the initial contour with a threshold level computed by the EM algorithm. The contour of the segmented object is considered as the new initial contour. The threshold level is set slightly higher than the calculated value to ensure that the initial contour only contains object pixels. This results in a small initial contour that does not seriously affect the result. The determination of the threshold level is currently based on experience.

To obtain good results, the initial estimate must cover a large percentage of the object. Only the LV endocardium and RV endocardium from the SI results shown in Figure 5.22 meet this requirement. Since the average myocardial coverage of the initial estimate is only about 35%, this strategy was not used for the myocardium.

- **Construction of LV and RV ROI Distance Maps**

Maps were created respectively for the LV and RV endocardial contours. A representative LV map B_M^{LV} is shown in Figure 6.4 b and d and the RV map B_M^{RV} in Figure 6.4 c and e. The maps were reconstructed in each step of the coarse-to-fine strategy. These maps can efficiently prevent the leaking problem since the values decrease rapidly at the boundaries. The advantages of the new ROI based map are concluded below:

- no edge detection required,
- a guaranteed downhill gradient from the initial contours, avoiding the nearest boundary problem arising from the edge distance map,
- noise impact not as influential as the edge distance map,
- no leaking problem as exhibited in the conventional ROI distance map.

However, disadvantages include:

- a one-way balloon force

- unable to stop by itself
- thresholding required to obtain new initial contours.

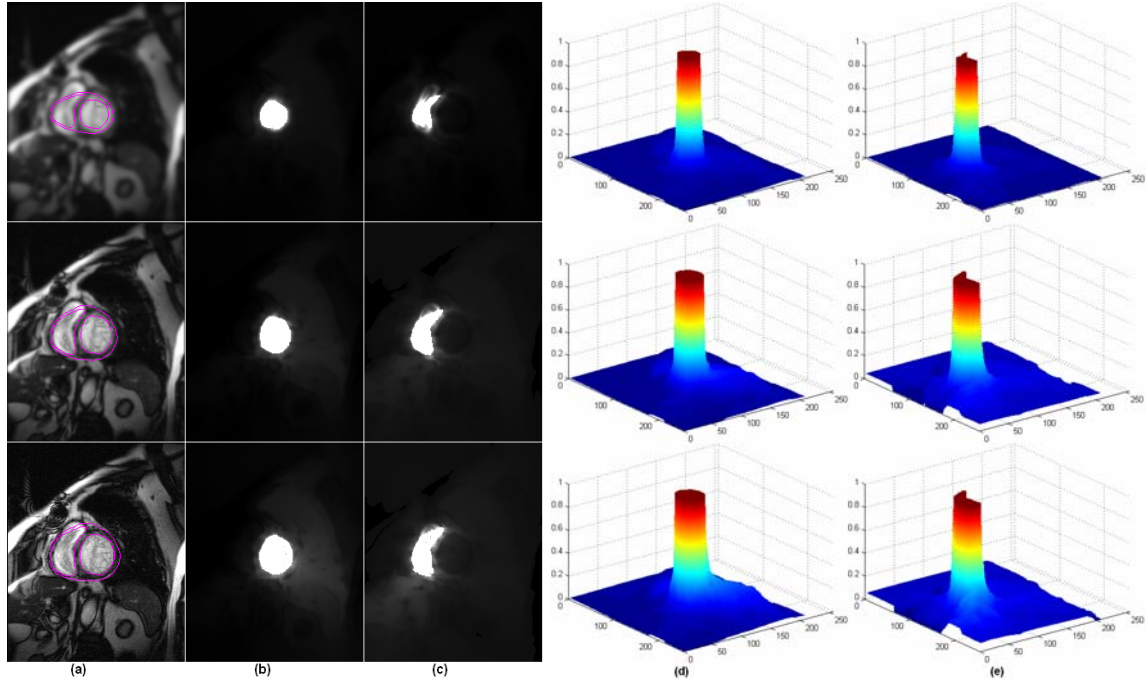


Figure 6.4 Distance maps based on fast marching algorithm and its updates in each step of the multi-grid strategy (each row); (a) image with initial contours before registration (b) B_M^{LV} , (c) B_M^{RV} , (d) B_M^{LV} 3D view and (e) B_M^{RV} 3D view.

6.2.5 Energy Function and Optimisation

- **Energy Function**

The energy function now consists of three terms when the boundary term is added:

$$E = E_I + w_B E_B + w_S E_S \quad (78)$$

E_I and E_S are referred to Eq. 64 and 65 in the last chapter. E_B is the boundary term which creates the balloon force to expand the contours, which is based on the new ROI distance maps.

Let $b_1 = \{b_1 | b_1 \in B_1\}$ denote a LV boundary point and $b_2 = \{b_2 | b_2 \in B_2\}$ a RV boundary point. Assume they have a same weight w_B . $B_M^{LV}(b_1)$ and $B_M^{RV}(b_2)$ respectively represent the distance map value of b_1 in B_M^{LV} and b_2 in B_M^{RV} . If T is the transformation of the non-rigid deformation, E_B is given by:

$$E_B = E_{B1} + E_{B2} = \sum_{b_1} (\mathbf{B}_M^{LV}(T(b_1)))^2 + \sum_{b_2} (\mathbf{B}_M^{RV}(T(b_2)))^2 \quad (79)$$

The boundary points are therefore warped by the mesh deformation in order to find new positions that have low values in the distance maps \mathbf{B}_M^{LV} and \mathbf{B}_M^{RV} . Though E_B is unable to stop by itself at the boundaries, the evolution over the boundaries will be penalized by E_l . Thus, w_B must be carefully selected or leaking will occur.

- **Optimisation**

The optimisation of this term in the LM algorithm is similar to that of the intensity term described in the last chapter. The only change is that the error term is derived from the distance maps instead of the target image.

6.2.6 Issues in Epicardial Application

The boundary term may be used to improve the epicardial contours when the LV and RV have been well registered. However, the intensity term may not be strong enough to prevent excessive dilatation caused by the boundary term. Most of the risk exists in the LV free wall since, in many cases, the boundaries between myocardium and the air in the adjacent lung tissue are not strong enough.

An alternative solution is proposed in the next section, where an area term is introduced to replace the boundary term for the improvement of epicardial contours. The area term is flexible and is defined for local requirements.

6.3 Integration of Area Term

This term was developed to improve epicardial contours caused at the LV free wall, using the area of the polygon defined by the LV free wall in Figure 6.1. The boundary points of this polygon were automatically selected in advance (Section 6.1.3). The area term produces a balloon force to expand this specific area. It is an intensity-independent term therefore not restricted by the image and it can be defined to expand or shrink. The term is also very flexible and can be defined on one or multiple regions of interest. Similar to the boundary term, the term cannot terminate by itself. It therefore causes expansion to obtain more area for myocardium until the gains are balanced by losses in the intensity term.

6.3.1 Energy Function

The new energy function including the area terms E_A is defined by:

$$E = E_I + w_A E_A + w_S E_S \quad (80)$$

where w_A is the weight. E_A is computed by the area function of a polygon.

Consider a polygon made up of line segments between N_A vertices (x_a, y_a) where $a = 1, \dots, N_A$. The last segment is assumed to be the connection between (x_{N_A}, y_{N_A}) and (x_1, y_1) for a closed polygon as shown in Figure 6.5.

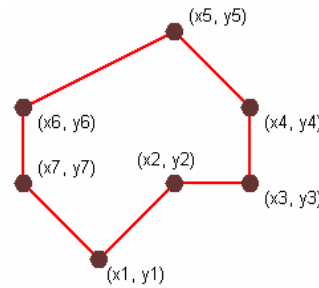


Figure 6.5 Example of a closed polygon with seven vertices

The area of the polygon is given by

$$A = \frac{1}{2} \sum_{a=1}^{N_A} (x_a y_{a+1} - x_{a+1} y_a)$$

where $x_{N_A+1} = x_1$ and $y_{N_A+1} = y_1$. The formula is valid only when the polygon is not self-intersecting. By removing the constant multiplier and adding the negative sign for the minimum, the area term is defined as:

$$E_A = - \sum_{a=1}^{N_A} (x_a y_{a+1} - x_{a+1} y_a) \quad (81)$$

Note that selection of a suitable w_A is critical since the area term needs to be balanced by the intensity term.

6.3.2 Optimisation

The LM algorithm is applied for the optimisation. The gradient and the Hessian matrix are computed for LM as follows.

- **Gradient**

The derivatives of other terms can be found in the previous chapter. The derivative of E_A with respect to each parameter $\mathbf{P}_j = (P_{jx}, P_{jy})$ is given below. The X and Y components of the objective function are independent of each other.

$$\frac{\partial E_A}{\partial P_{jx}} = -\sum_{a=1}^{N_A} y_{a+1} \frac{\partial x_a}{\partial P_{jx}} + \sum_{a=1}^{N_A} y_a \frac{\partial x_{a+1}}{\partial P_{jx}} = -\sum_{a=1}^{N_A} y_{a+1} \Psi_{jx}(\zeta_x^a) + \sum_{a=1}^{N_A} y_a \Psi_{jx}(\zeta_x^{a+1}) \quad (82)$$

$$\frac{\partial E_A}{\partial P_{jy}} = -\sum_{a=1}^{N_A} x_a \frac{\partial y_{a+1}}{\partial P_{jy}} + \sum_{a=1}^{N_A} x_{a+1} \frac{\partial y_a}{\partial P_{jy}} = -\sum_{a=1}^{N_A} x_a \Psi_{jy}(\zeta_y^{a+1}) + \sum_{a=1}^{N_A} x_{a+1} \Psi_{jy}(\zeta_y^a) \quad (83)$$

- **Hessian Matrix**

Since the LM method is robust to approximations of the Hessian, it was found that the method converged at an acceptable rate even when the second derivative of the area term was ignored. Thus, the Hessian matrix is the same as the previous chapter.

6.4 Results

The experiment was based on the segmentation of the middle SA slice of 328 cases in the ONTARGET dataset. Results using the modified segmentation method with the boundary term are first presented. Here, the four-level coarse-to-fine strategy was applied, as well as the morphological algorithm for removal of the papillary muscles. The results are compared to those obtained from the intensity-only method (previous chapter). Results obtained from the inclusion of the area term are then presented.

6.4.1 Results of Integrating Boundary Term

An example shown in Figure 6.6 demonstrates the efficiency of integrating the boundary term. The term creates a balloon force to iteratively expand the RV contour to the correct position. The MHD and SI results of the ONTARGET dataset are respectively presented in Figure 6.7 and Figure 6.8. They are compared to the results of the intensity-only method obtained in the previous chapter. A noticeable improvement in LV endocardium can be found in Figure 6.7a and Figure 6.8a. A reasonable improvement is observed in the RV endocardium and the myocardium (Figure 6.7b,c and Figure 6.8b,c). The figures also show that large errors in a small number of cases still exist. Numerical results, mean \pm standard deviation, are summarized in Table 6-1. When the boundary term is included, the average

MHD error in the LV is reduced by one third, to approximately one pixel, when compared with results obtained without the boundary term. The SI result shows that the average coverage reaches 94% with a low standard deviation. The average MHD errors of both RV and myocardium are reduced by 20% when the boundary term is included.

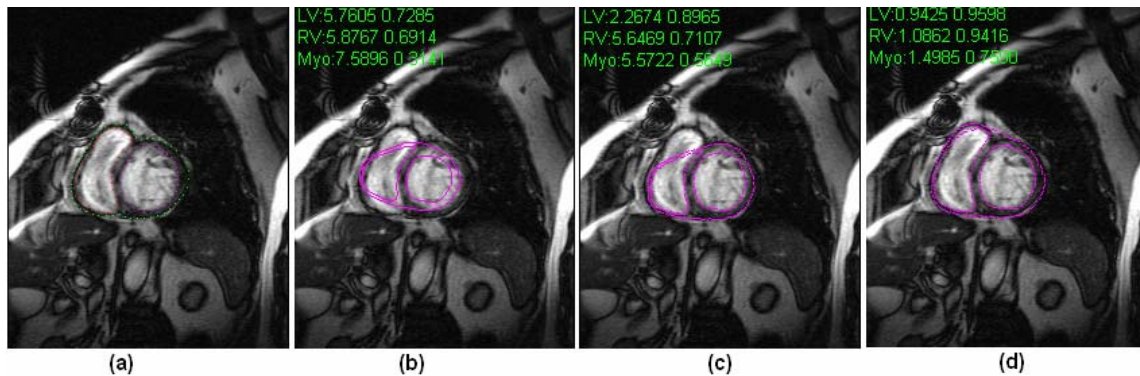


Figure 6.6 Comparison between the results of the method with and without boundary term; (a) ground truth, (b) initial contours, (c) method without boundary term and (d) method with boundary term.

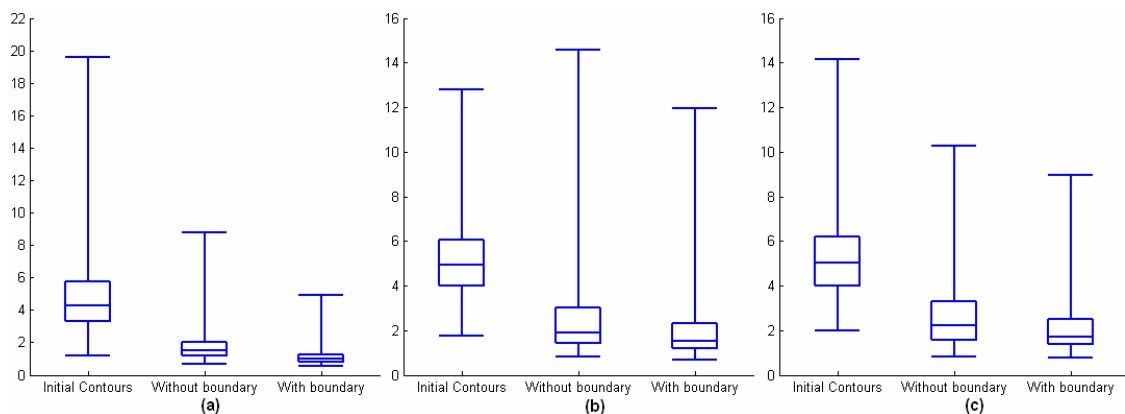


Figure 6.7 MHD comparison of initial contour, registration based on intensity only and registration after adding boundary term. (a) LV, (b) RV and (c) epicardium.

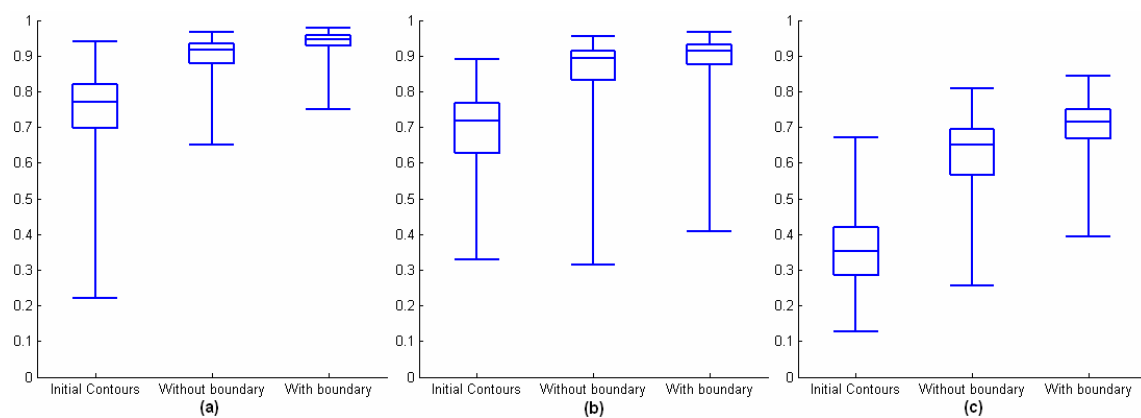


Figure 6.8 SI comparison of initial contour, registration based on intensity only and registration after adding boundary term. (a) LV, (b) RV and (c) myocardium.

	MHD			SI		
	Initial contour	without boundary	with boundary	Initial contour	without boundary	with boundary
LV	4.76 ± 2.35	1.75 ± 0.90	1.15 ± 0.54	0.75 ± 0.11	0.90 ± 0.05	0.94 ± 0.03
RV	5.19 ± 1.66	2.58 ± 1.98	2.06 ± 1.62	0.69 ± 0.10	0.86 ± 0.09	0.89 ± 0.08
Myo	5.21 ± 1.77	2.70 ± 1.67	2.18 ± 1.34	0.36 ± 0.11	0.63 ± 0.09	0.70 ± 0.07

Table 6-1 MHD and SI comparison of initial contour, registration without and with boundary term.

6.4.2 Results of Integrating Area Term

This step attempts to further improve the epicardial results, particularly at the LV free wall. The boundary term was replaced by the area term and an additional registration step performed. w_A was an important parameter in this step. Erroneous deformations were found when w_A was higher than 0.16. A parametric optimisation was performed to compare results with w_A from 0 to 0.16. A zero weight means no area term was included.

The MHD and SI results of the optimisation test are shown in Figure 6.9 and Figure 6.10 respectively. There is no change on the RV side. Both LV and myocardium have small changes in their performance at different weights. It can be observed that in Figure 6.10a and c, both LV and the myocardium have slightly better average SI results at high weights; however, the risk of leaking is also increased.

It can be concluded that the area term may slightly improve the accuracy but it is very sensitive to the weight selection. An optimised weight must be found using a large study. Until such a study is undertaken, inclusion of the area term is not recommended in the atlas-based segmentation method, since no obvious improvement is found.

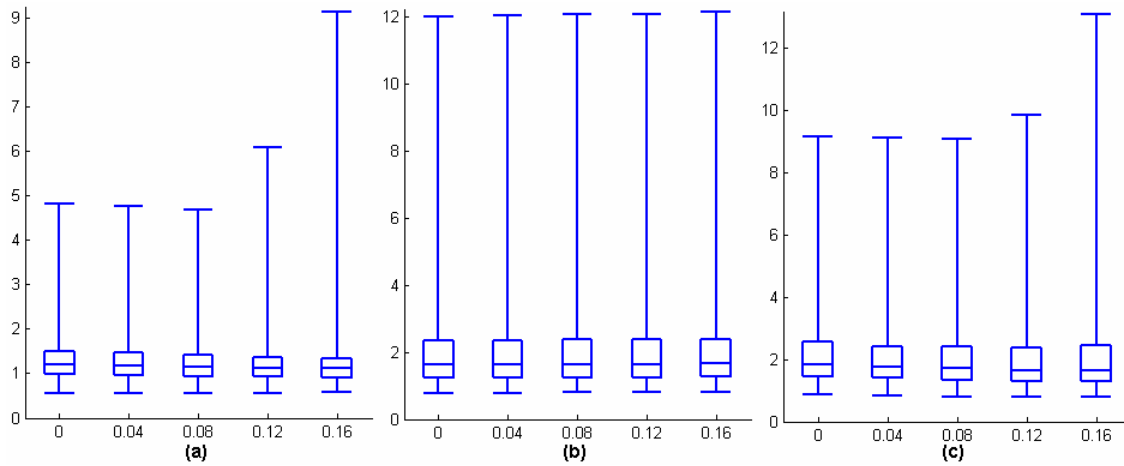


Figure 6.9 MHD comparison of using different area-term weights from 0 to 0.16. (a) LV, (b) RV and (c) epicardium.

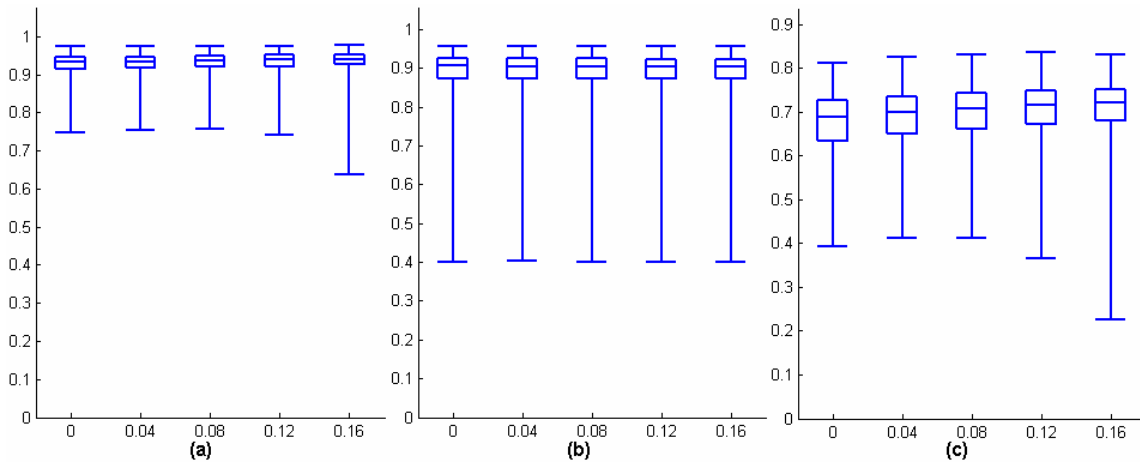


Figure 6.10 SI comparison of using different area-term weights from 0 to 0.16. (a) LV, (b) RV and (c) epicardium.

6.5 Discussion

There are many factors which affect the accuracy and speed of the algorithm. This section discusses additional features and anatomical information that could be considered for further improvement.

6.5.1 Accuracy

Three topics are discussed which may improve the accuracy: the number of coarse-to-fine iterations, more information that could be integrated in the method and a better solution to the papillary muscle removal.

- **Coarse-to-fine Strategy Issues**

Selection of a different number of levels in the coarse-to-fine strategy will affect the results. Higher accuracy may be achieved by adding more high-level registration steps. Figure 6.11 and Figure 6.12 show the results for each level of the current 4-level strategy. After each level the MHD errors were reduced and SI values improved. The incremental improvement reduces in the higher levels. There is an obvious trade-off between accuracy and computational cost. One more high-level registration may double the total computation time for just marginal improvement.

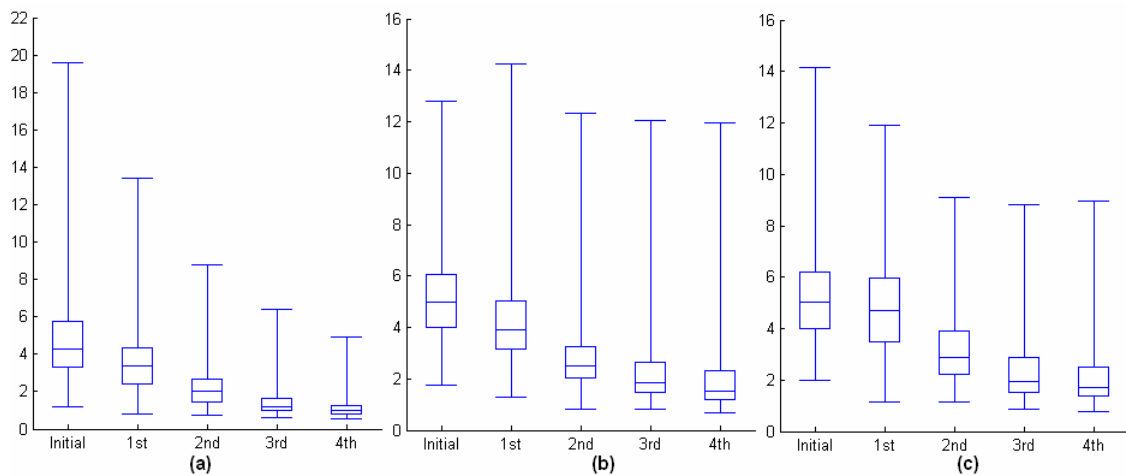


Figure 6.11 MHD comparison of initial contour and each level of the coarse-to-fine strategy, 1st level: 2x2 mesh, 2nd level: 3x3 mesh, 3rd level: 4x4 mesh, 4th level: 5x5 mesh. (a) LV, (b) RV and (c) epicardium.

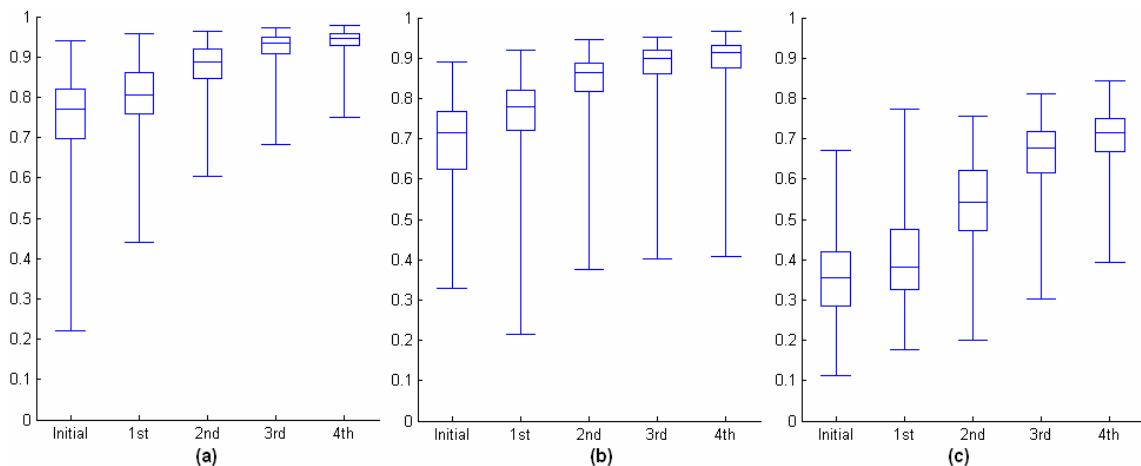


Figure 6.12 SI comparison of initial contour and each level of the coarse-to-fine strategy, 1st level: 2x2 mesh, 2nd level: 3x3 mesh, 3rd level: 4x4 mesh, 4th level: 5x5 mesh. (a) LV, (b) RV and (c) myocardium.

- **More High Level Information**

Adding more information can help the method create an error space with less local minima. For example, statistical analyses of the heart's shape have been performed [4, 38, 64, 66, 92, 102]. Their results can be used to add constraints to the registration. Time constraints were employed to prevent erroneous segmentations in [3]. A method that integrates time dimension into the AAM algorithm was proposed for automated detection of LV endocardial and epicardial boundaries in [148]. More anatomical constraints can be defined in the atlas. For example, the boundary points of the LV endocardium should create a circular shape for the LV contour. The RV contour should also obey a specific shape and the distance constraint between epicardium and endocardium may be formulated into the energy function.

- **RV Papillary Muscles**

Removal of the papillary muscles is one of the main obstacles to accurate RV segmentation. The local minima caused by papillary muscles are often too deep for the method to jump out. The current image filling method for removal is not robust enough to deal with all papillary muscles in the RV cavity, and is not able to remove papillary muscles which are not floating in the blood pool. A more robust method is required to reliably remove them.

6.5.2 Improve Speed

Speed has not considered in these experiments. The process takes about 30 seconds for each case; although this has not been optimised by hard coding computational bottlenecks, this may not be adequate for real-time applications. The computational effort can be improved by the following methods:

- **Speed up Bézier FFD Deformation**

Because cubic Bézier splines have $C1$ continuity and the basis functions have limited local support, changing a single control point only affects the transformation in the local neighbourhood of that control point. This local characteristic can be used to develop a computationally efficient implementation even for a large number of control points. Similar implementations of B-spline curves can be found [68, 149].

- **Use Linear FFD**

The use of linear FFD instead of cubic FFD can help to reduce the computation time at the expense of accuracy. It is possible to use linear FFD at the low level of the coarse-to-fine strategy; however, the total saving on computation cost is not obvious.

- **Reduce the Complexity of FFD**

Another possible option to improve the speed is to reduce the complexity of FFD grid. For example, Figure 6.13 shows the results of two registrations with 4x4 and 5x5 meshes respectively in the fourth level of the coarse-to-fine strategy. No obvious difference in accuracy can be observed but 20% of the total computation time will be saved if a 4x4 mesh is selected.

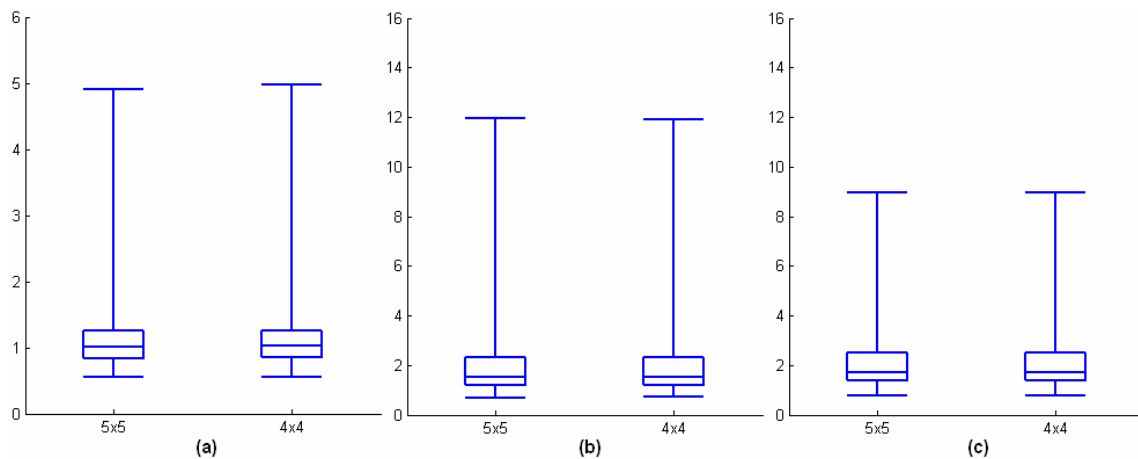


Figure 6.13 MHD Comparison of the registrations with 5x5 mesh and 4x4 mesh used in the last level of the coarse-to-fine strategy.

6.6 Conclusions

A modified method based on the SMPL atlas-based registration framework was proposed in this chapter. The method integrated the intensity, boundary and anatomical information for CMR image segmentation. Experiments using a large clinical dataset proved that this modified method had better accuracy and robustness characteristics. The average MHD error in the LV was reduced to approximately one pixel when the boundary term was included. The SI result showed that the average coverage of LV reaches 94%. Good agreement between the automated method and the ground truth can also be found in the RV and myocardium. No further improvement was observed upon inclusion of an area term designed to expand the LV free wall.

7 Model-based 3D Segmentation

This chapter investigates techniques for 3D model-based segmentation of the LV and RV. A feature-based 3D registration technique is proposed that combines the iterated closest point (ICP) and 3D FFD algorithms to automatically fit the model to pre-detected feature points. The feature points used are the LV and RV contours detected by the atlas-based 2D registration method discussed in the previous chapter.

The results of the 2D and 3D registrations on the middle SA slice are applied to update the initial model and to provide initial estimates for 2D segmentation of the remaining SA slices. The results of these segmentations produce more contours to use as feature points to further update the 3D model. The model is iteratively improved to better match the available data in an incremental manner. To prevent including erroneous feature points, criteria are established to validate the segmentation results. This is particularly important for the apical and basal slices. In particular, insufficient information on the apical area is available from SA slices, and the addition of a 4-chamber LA slice is required to improve the accuracy in this area. The atlas-based 2D registration procedure is used for segmentation of this LA slice, with the addition of a constraint term designed to incorporate information from mid-ventricular SA slices. The final results show that this segmentation strategy provides an efficient, accurate and robust solution for 3D CMR segmentation.

The introduction of the 3D segmentation strategy is provided in Section 7.1. Details about the feature-based 3D registration method and its implementation on the middle SA slice are discussed in Section 7.2. Section 7.3 presents the techniques for the registration of other SA slices. Section 7.4 proposes an atlas-based 2D registration with constraint term for application on the 4-chamber LA slice. The results are presented in Section 7.5. Discussions and conclusions can be found in Section 7.6 and Section 7.7.

7.1 Introduction

7.1.1 3D Segmentation Strategy

The complete segmentation strategy is outlined in Figure 7.1. It starts with an initial estimate of the size, orientation and position of the heart model using the novel method introduced in

Chapter 2 based on the temporal Fourier analysis of the dynamic characteristics of the heart (Step 1, Figure 7.1). The middle SA slice is selected as the first slice for segmentation because the ventricular shapes are less variable and the model has a better initial position on that slice than others. The atlas-based 2D registration method proposed in Chapter 6 (Step 2, Figure 7.1) is used for the segmentation. The method is based on the SMPL atlas-based registration framework that includes boundary, intensity and anatomical information. The detected contours on the middle slice are subsequently used as feature points for updating the model with the feature-based 3D registration method presented in this chapter (Step 4, Figure 7.1). The updated model provides more accurate initial atlases for the segmentation of the other SA slices. The two slices next to the middle SA slice are then segmented using the 2D atlas based method. The resulting contours update the 3D model further and the next slices are segmented. An iterative update procedure is established; the model becomes more accurate as more and more feature points are included. To avoid feature points introduced from an erroneous registration a validation criterion is established (Step 3 in Figure 7.1). One common problem in the segmentation of SA slices is the lack of information at the apex. The appearance of the apex is uncertain due to partial volume effects. The segmentation of an apical slice is therefore more difficult than a middle slice. A 4-chamber LA slice is therefore included to provide more accurate information at the apex. The atlas-based 2D registration method (Chapter 6) is used for the segmentation of the 4-chamber LA slice. To avoid erroneous deformation in the LA direction, a constraint term is added to the atlas-based 2D registration method (Step 5 in Figure 7.1) for the LA slice. The 3D model is eventually updated with feature points from the segmentation of both the SA and LA slices (Step 6 in Figure 7.1).

The automated initialization of the model and the atlas-based 2D registration have been discussed in previous chapters. The additional techniques to be discussed in this chapter are:

- 1) Feature-based 3D registration method
- 2) Segmentation of other SA slices
- 3) Registration of the 4-chamber LA slice

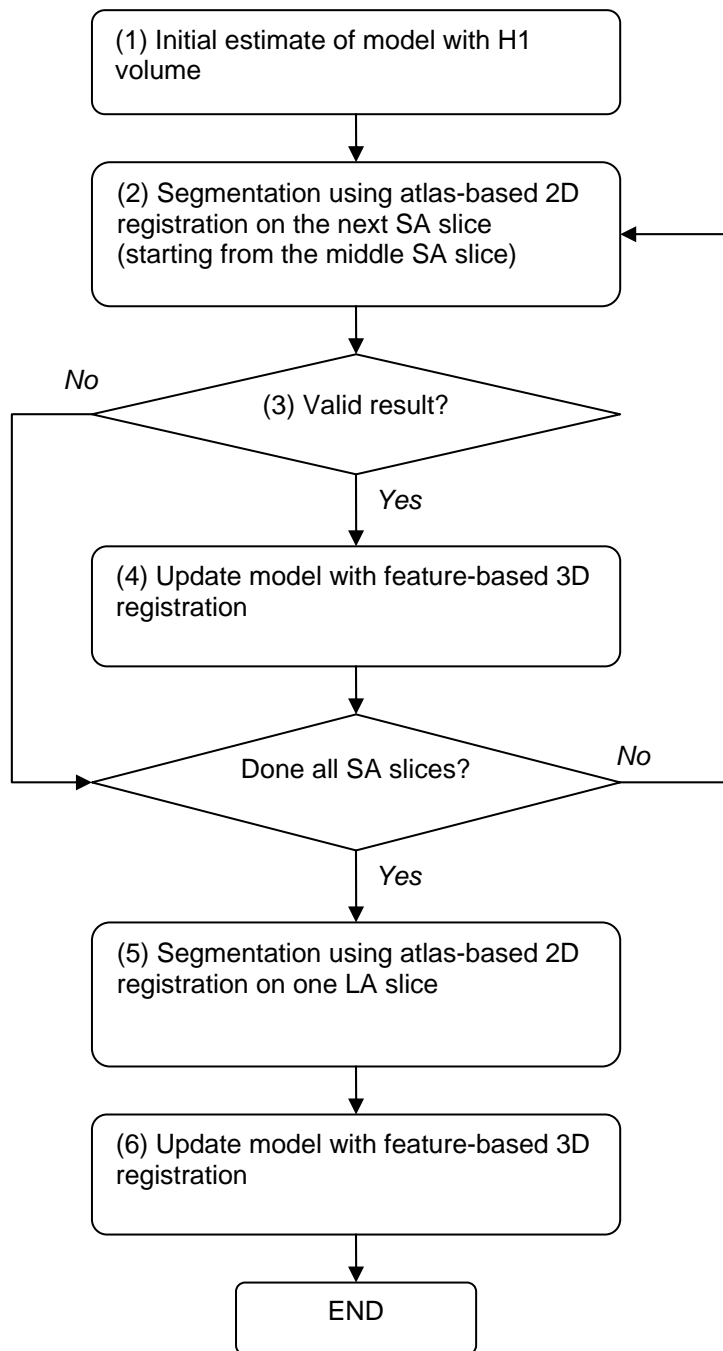


Figure 7.1 Flow chart showing the process of automated 3D model-based CMR segmentation process.

7.1.2 Main Techniques

- **Feature-based 3D Registration Method**

The feature-based 3D registration method is designed to update the heart model from the contours detected by the 2D segmentation. It integrates the ICP and 3D FFD algorithms to enable fully automated model fitting (details are discussed in Section 7.2). The method starts by using the ICP algorithm to find the points on the model that correspond to the contour

points. A 3D FFD deforms the model by reducing the distance between these corresponding point pairs. A linear update method is applied which iteratively approximates the non-linear optimisation to make the method more efficient. Since a limited number of feature points are available, large smoothing weights are applied to avoid any erroneous deformation in areas of sparse data. Under these conditions, it was found that there were only marginal differences between the linear and cubic FFD results. Thus, a linear FFD was selected to further reduce the computational cost.

The initial model was firstly updated using the contours detected on the middle SA slice. The updated model's LV, RV endocardium and epicardium showed good agreement with the middle slice (Section 7.5.2). The same approach, with the 2D segmentation method, was iteratively applied to the other slices. The updated model provides more accurate initial estimate for the successive registrations, and the total time cost is expected to be less than a fully 3D atlas-based registration.

- **Segmentation of other SA slices**

The atlas-based 2D registration and the feature-based 3D registration were iteratively applied on slices adjacent to the middle SA slice. Some registration parameters needed to be adjusted as the model became increasingly closer to the ground truth.

Segmentation of the apical or basal slices is expected to be less accurate than slices close to the middle. The information on the SA slices is of limited value and is less reliable in the apical and basal areas. Partial volume effects, poor image acquisition and flaws in the current model may cause serious problems in these slices. The large variance in the shape and size of the objects also make it difficult to register these slices. To decide if the segmentation results should or should not be included as new feature points to update the 3D model, some criteria were established to validate the reliability of the registration results.

The results in Section 7.5.3 show that the iterative segmentation strategy provides good accuracy in most slices, however the segmentation of the apex and base can be improved by incorporation of long axis slices.

- **Registration of a 4-chamber Long-axis Slice**

The purpose of using a LA slice is to improve the result by introducing more accurate information at the apical area. The 4-chamber LA slice was selected because it contains both

LV and RV information. The atlas-based 2D registration method developed in Chapter 6 was used to detect the LV, RV endocardium and epicardium in this slice. The boundary term was applied to prevent the contours from being too small because of the papillary muscle and the apical shape. Only the LV distance map was used and no balloon force was added to the RV cavity due to the thin RV free wall. To avoid erroneous deformation, a constraint term was added to penalize the displacement of specific ‘constraint points’ derived from the SA slices. The energy function and the optimisation are investigated in Section 7.4.2. Details of implementation can be found in Section 7.4.3. The segmentation results were employed to update the model by the feature-based 3D method. The results in Section 7.5.4 show that the 4-chamber LA slice can improve the performance in the apical area.

7.2 Feature-based 3D Registration Method

7.2.1 Method

The method begins by locating points corresponding to feature points (contour points in this application) on the model using the ICP algorithm. The 3D FFD procedure is applied to deform the model, reducing the distance between the corresponding point pairs. This involves the computation of local coordinates in the deformed meshes and a linear approximation to iteratively approximate the non-linear optimisation. The following five aspects are discussed below:

- 1) ICP algorithm to find the corresponding points,
- 2) 3D FFD framework for registration,
- 3) fast computation of local coordinates in deformed meshes,
- 4) energy function for 3D registration,
- 5) iterative linear solution to approximate the non-linear optimisation.

- **ICP Algorithm**

The ICP algorithm, proposed by [150], has become one of the standard methods for feature-based geometric fitting applications and has been extended for CMR segmentation and registration. [42] used it for the alignment between the landmarks embedded in the cardiac mesh and their candidate model state. In [61] and [3], the algorithm was applied to estimate the initial pose of a model by minimizing the distance between the model and the detected

contour points. A similar concept is used in our application. The contour points detected by atlas-based 2D registration are projected onto the model; however, instead of finite elements [61] or a simple mesh deformation [3], the 3D FFD algorithm is used to minimise the distance between these point pairs. Figure 7.2 shows the contour points x_0 (red) and their corresponding points x (green) on the model. The general routine of finding the closest point on triangular surfaces for a 3D point is described below:

- 1) Find the corresponding surface if there are multiple surfaces
- 2) Project the contour point on each triangle of this surface
- 3) Validate if the projected point is within the triangle
- 4) find the triangle which is valid and has the shortest distance to the point

This routine is computationally expensive when there are a large number of contour points because each point has to be projected on to all triangles. An approximation method is proposed to reduce the computational cost. Before the projections, the distance between the point and the centre of each triangle is computed. The four triangles with the shortest distance are selected. These four triangles only are used in steps 2-4. The number of selected triangles was determined by experience and depends on the surface curvatures.

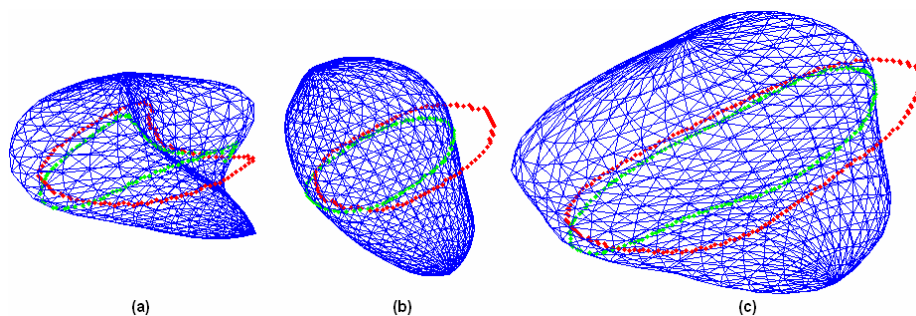
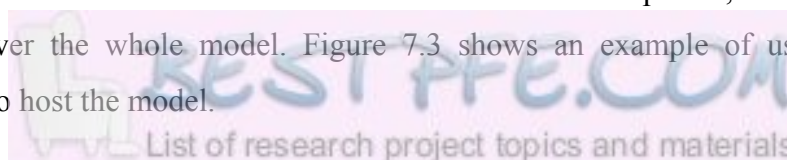


Figure 7.2 Contour points (red) detected in last chapter and their corresponding points (green) on the model surfaces (a) RV endocardium, (b) LV endocardium, (c) epicardium.

- **3D Free-form Deformation**

The 3D FFD algorithm is applied to deform the model to reduce the distance between x_0 and x in Figure 7.2. Similar to the 2D FFD described in Chapter 5, a mesh is first constructed to cover the whole model. Figure 7.3 shows an example of using $3 \times 3 \times 3$ rectangular mesh to host the model.



The deformation is governed by the grid points of the mesh. If a 3D spatial domain $\Omega_I = \{\mathbf{X} = (X, Y, Z) | 0 \leq X < X_{\max}, 0 \leq Y < Y_{\max}, 0 \leq Z < Z_{\max}\}$ is divided into $n_X \times n_Y \times n_Z$ elements with uniform spacing δ_X , δ_Y and δ_Z in three directions. The local coordinates are computed by

$$\xi_X = \frac{X}{n_X} - \left\lfloor \frac{X}{n_X} \right\rfloor \quad (84)$$

$$\xi_Y = \frac{Y}{n_Y} - \left\lfloor \frac{Y}{n_Y} \right\rfloor \quad (85)$$

$$\xi_Z = \frac{Z}{n_Z} - \left\lfloor \frac{Z}{n_Z} \right\rfloor \quad (86)$$

when \mathbf{X} is inside of that element. The displacement of the deformation $\mathbf{u}(\mathbf{X}) = \mathbf{x} - \mathbf{X}$ can be formulated by

$$\mathbf{u}(\mathbf{X}) = \sum_{i=1}^N \Psi_i^e(\mathbf{X}) \mathbf{P}_i^e \quad (87)$$

where N is the number of parameters \mathbf{P}_i^e in that element and $\Psi_i^e(\mathbf{X})$ is the basis function given by the 3D tensor product

$$\Psi_i^e(\mathbf{X}) = B_a(\xi_X) B_b(\xi_Y) B_c(\xi_Z) \quad (88)$$

where $B_a(\xi)$, etc, are the 1D linear or cubic Bézier polynomials listed in Chapter 5. The continuity between elements is provided by a global-to-local map G as stated in Chapter 5 and the displacement of the feature-based 3D and atlas-based 2D registrations have the same formula

$$\mathbf{u}(\mathbf{X}) = \mathbf{x} - \mathbf{X} = P^T \Psi(\mathbf{X}) \quad (89)$$

where Ψ are global basis functions and $\Psi(\mathbf{X}) = G^T \Psi^e(\mathbf{X})$. Ψ^e is the column vector of the basis functions $\Psi_i^e(\mathbf{X})$ in Eq. 87. The parameter matrix P in Eq. 89 controls the deformation of the mesh grid points. If a required deformation is aimed to minimize the distance between

\mathbf{x} and \mathbf{x}_o , then P^T of this deformation can be computed by Eq. 89 at the corresponding model points ξ , or \mathbf{X} . It should be noted that \mathbf{X} is the undeformed global coordinates. If the current mesh is deformed, the corresponding local coordinates ξ of \mathbf{x} need to be computed and then converted to \mathbf{X} .

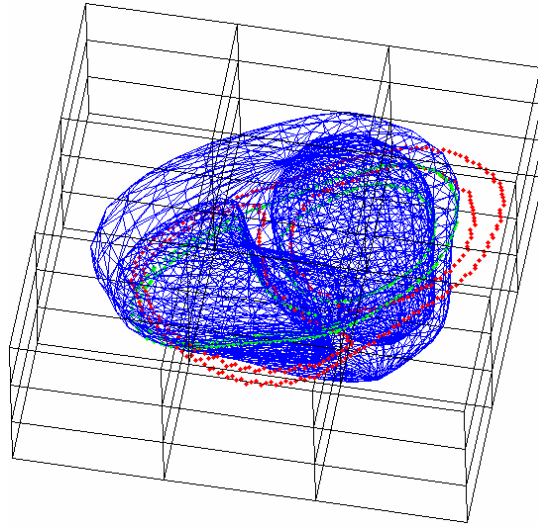


Figure 7.3 Model hosted by 3x3x3 mesh, the contours (red) and their corresponding points (green) on the model surfaces.

- **Calculation of Local Coordinates in Deformed Mesh**

The computation of local coordinates in an undeformed mesh is straightforward since the mesh has a regular shape. A non-linear solution is generally required to convert between local coordinates and global coordinates in a deformed mesh. Assume $\mathbf{x} = (x, y, z)$ is the global coordinate of one point in a deformed mesh. The local coordinate $\xi = (\xi_x, \xi_y, \xi_z)$ is computed by solving the equation:

$$\mathbf{F} = \mathbf{x} - P^T \Psi(\xi) = 0 \quad (90)$$

This can be iteratively approximated by the Newton-Raphson method

$$\xi^{t+1} = \xi^t + J^{-1} \mathbf{F} \quad (91)$$

where J is the Jacobian matrix. Once the local coordinates are obtained, the undeformed global coordinates \mathbf{X} can be computed by

$$\mathbf{X} = P_o^T \Psi(\xi) \quad (92)$$

where P_o^T is the initial positions of grid points of the undeformed mesh.

The computational cost of the non-linear solution is very high; however, the problem can be linearly solved if the deformation of each triangle can be approximated as an affine transformation. This is generally satisfied when reasonable smoothing is considered in the registration, which is also satisfied in this study. High smoothing is often used in this study to avoid erroneous deformation because of a limited number of contour points. In the linear solution, the local coordinate of any point in a triangle ξ can be linearly approximated by the local coordinates of the vertices for that triangle.

Assume a triangle (Figure 7.4) has three vertices with the global coordinates $\mathbf{v}_i = (x_i, y_i, z_i)$ and local coordinates $\xi_i = (\xi_{xi}, \xi_{yi}, \xi_{zi})$ where $i = 1, 2, 3$. The global coordinates of any point \mathbf{x} in the triangle can be represented as a function of the three vertices:

$$\mathbf{x} = \mathbf{v}_1 + \tau_1 \cdot (\mathbf{v}_2 - \mathbf{v}_1) + \tau_2 \cdot (\mathbf{v}_3 - \mathbf{v}_1) \quad (93)$$

where $\tau_1 \in [0,1]$, $\tau_2 \in [0,1]$ and $\tau_1 + \tau_2 \leq 1$. Once τ_1 and τ_2 are computed, ξ can be approximated by the formula

$$\xi = (1 - \tau_1 - \tau_2) \cdot \xi_1 + \tau_1 \cdot \xi_2 + \tau_2 \cdot \xi_3 \quad (94)$$

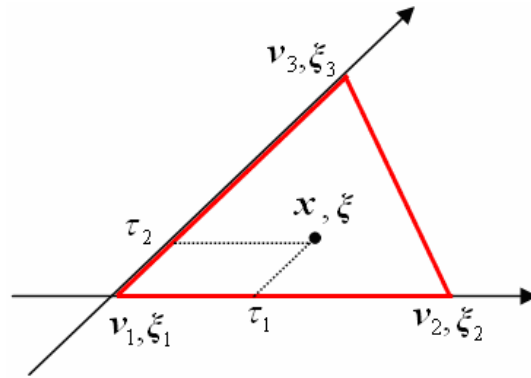


Figure 7.4 Linear solution to the computation of local coordinates.

- **Energy function**

The energy function E in this 3D FFD registration consists of two terms:

$$E = E_D + w_s E_S \quad (95)$$

where E_D is the distance term, E_S is the smoothing term and w_s is the weight for the balance between the two terms. E_D is defined by the sum of squared distances between \mathbf{x}_o and \mathbf{x} :

$$E_D = \sum_x w^2(\mathbf{x})(\mathbf{x} - \mathbf{x}_o)^2 \quad (96)$$

where w is the weight of each point which can be different. To be consistent with the smoothing term, E_S , the formula is reformatted as a function of the displacement,

$$E_D = \sum_x w^2(\mathbf{x})(\mathbf{u}(\mathbf{X}) - \mathbf{u}_o(\mathbf{X}))^2 \quad (97)$$

where $\mathbf{u}(\mathbf{X}) = \mathbf{x} - \mathbf{X}$, $\mathbf{u}_o(\mathbf{X}) = \mathbf{x}_o - \mathbf{X}$ and \mathbf{X} is the undeformed coordinates of \mathbf{x} . $\mathbf{u}_o(\mathbf{X})$ is the target displacement which $\mathbf{u}(\mathbf{X})$ should match.

A Sobolev smoothing term E_S is added to the energy function in order to penalize possible erroneous deformations at the areas with scattered data. The term is the integral over the whole space and consists of ten sub-terms in 3D FFD:

$$\begin{aligned} E_S = \int_{\Omega} & \gamma_1 \left\| \frac{\partial \mathbf{u}}{\partial X} \right\|^2 + \gamma_2 \left\| \frac{\partial \mathbf{u}}{\partial Y} \right\|^2 + \gamma_3 \left\| \frac{\partial \mathbf{u}}{\partial Z} \right\|^2 + \gamma_4 \left\| \frac{\partial^2 \mathbf{u}}{\partial X^2} \right\|^2 + \gamma_5 \left\| \frac{\partial^2 \mathbf{u}}{\partial Y^2} \right\|^2 + \gamma_6 \left\| \frac{\partial^2 \mathbf{u}}{\partial Z^2} \right\|^2 \cdots \\ & + \gamma_7 \left\| \frac{\partial^2 \mathbf{u}}{\partial X \partial Y} \right\|^2 + \gamma_8 \left\| \frac{\partial^2 \mathbf{u}}{\partial Y \partial Z} \right\|^2 + \gamma_9 \left\| \frac{\partial^2 \mathbf{u}}{\partial X \partial Z} \right\|^2 + \gamma_{10} \left\| \frac{\partial^3 \mathbf{u}}{\partial X \partial Y \partial Z} \right\|^2 d\Omega \quad (98) \end{aligned}$$

The ten weights from γ_1 to γ_{10} penalize the deformation in different directions and curvatures. A detailed discussion of the affects of these weights can be found in [135].

The energy function can be assembled in matrix-vector format:

$$E = \left\| \begin{bmatrix} W\boldsymbol{\Psi} \\ \hat{S} \end{bmatrix} P - \begin{bmatrix} WU_o \\ 0 \end{bmatrix} \right\|^2 \quad (99)$$

where W is the weight matrix consisting of w , $\boldsymbol{\Psi}$ is the column of the global basis functions, U_o is the matrix of the target displacement, \hat{S} is derived from the smoothing matrix S (the

3D equivalent of Eq. 71 in Chapter 5) by $\widehat{S}^T \widehat{S} = S$, and P is the parameter matrix. The residual sum of squares (RSS) can be efficiently solved using a linear least squares estimation.

- **Least Squares Minimization**

The FFD minimization problem can be generally considered to be a non-linear least squares optimisation problem because the local coordinates of the data can change during the minimization process. However, it has been shown that an efficient solution, approximating a Newton procedure, involves the iterative solution of the linear least squares problem arising from the assumption of fixed local coordinates, followed by an update of the local coordinates [151].

The closed-form linear solution to the minimization of $\|AX - \mathbf{b}\|^2$ is

$$\mathbf{X} = (A^T A)^{-1} A^T \mathbf{b}.$$

By applying it to Eq. 99, the solution is

$$P = (\Psi^T W^T W \Psi + S)^{-1} \Psi^T W^T W U_0. \quad (100)$$

The iterated closed-form solution provides fast convergence for the non-linear feature-based 3D registration process. Figure 7.5 shows the first three iterations in a typical case. The error curve of the iterative process is shown in Figure 7.6, demonstrating that the errors are reduced by about 90% after the first iteration.

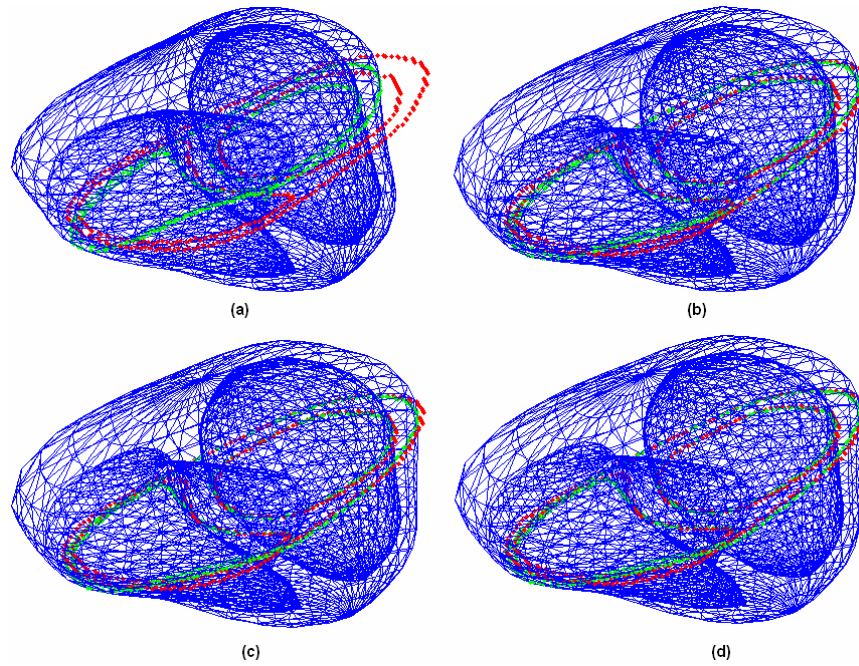


Figure 7.5 First three iterations in the fitting, (a) initial model, (b) after 1st iteration, (c) after 2nd iteration and (d) after 3rd iteration.

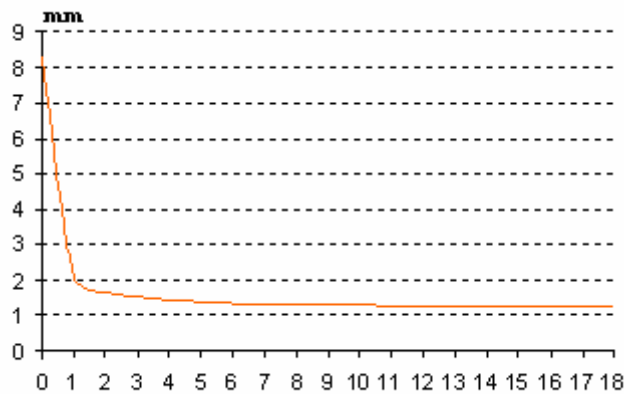


Figure 7.6 Error function change in iterations.

7.2.2 Optimisation

The implementation of the feature-based 3D registration requires the determination of basis functions, weight settings and mesh complexity.

- **Basis function**

A test was performed to compare the results of using cubic and linear FFD models. No obvious difference in MHD errors (Figure 7.7) and SI results (Figure 7.8) was observed. Thus, the linear FFD was selected since it is much faster than the cubic FFD.

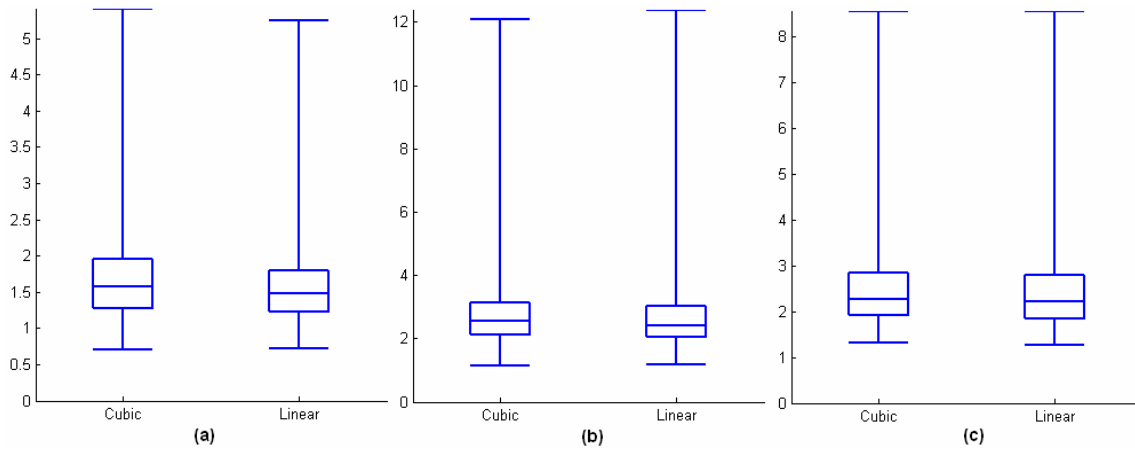


Figure 7.7 Comparison of MHD results of using linear and cubic FFD; (a) LV, (b) RV, (c) myocardium.

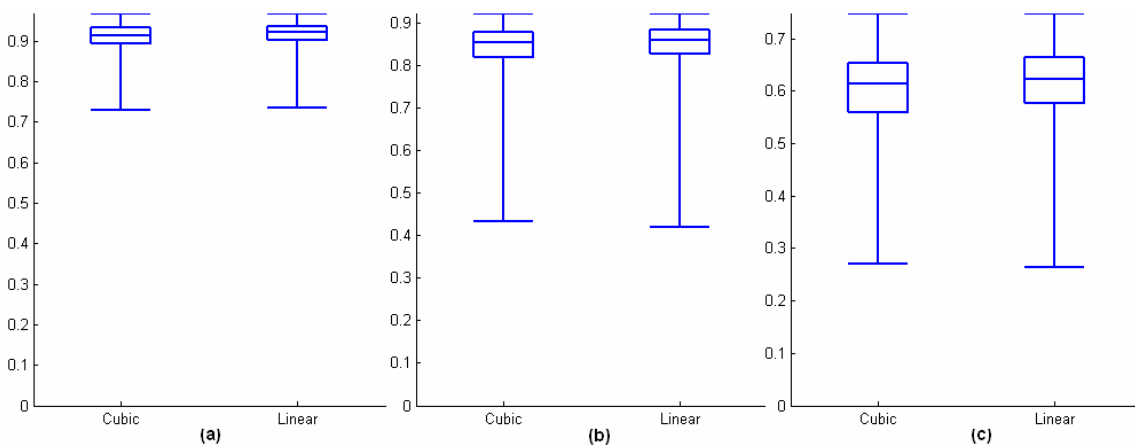


Figure 7.8 SI results of using linear and cubic FFD; (a) LV, (b) RV, (c) myocardium.

- **Weight setting for each point**

Different weights can be assigned via $w(X)$ for each feature point. If it could be set to be proportional to the reliability of each point, the weight may be useful to reduce the impact of some erroneous pairs. This was not very useful in this study because the model was always close enough to the contours so that the erroneous pairs were not a serious problem. Thus, the weights were set to 1.0 for all points.

- **Weight setting for the smoothing term**

The weight of the smoothing term determines the degree of the deformation over the whole space. If the feature points are scattered sparsely, the weight should be set as high as possible. It is important to initially use a high weight when only the contours of middle SA slices are used. A low smoothing weight may cause erroneous deformation, particularly in the LA direction. Different weights were tested from 0.25 to 4. Figure 7.9 and Figure 7.10

show the MHD errors and SI results of these tests. The errors increase slightly when high smoothing weights are applied. The smoothing weights were selected to be 1.0 to keep the balance between accuracy and the degree of deformation.

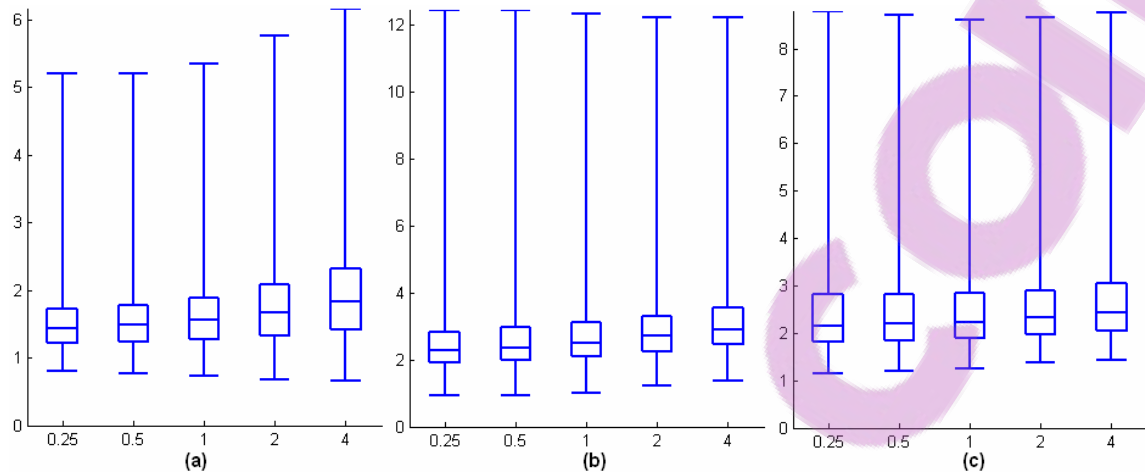


Figure 7.9 MHD results of using different smoothing weights from 0.25 to 4; (a) LV, (b) RV, (c) myocardium.

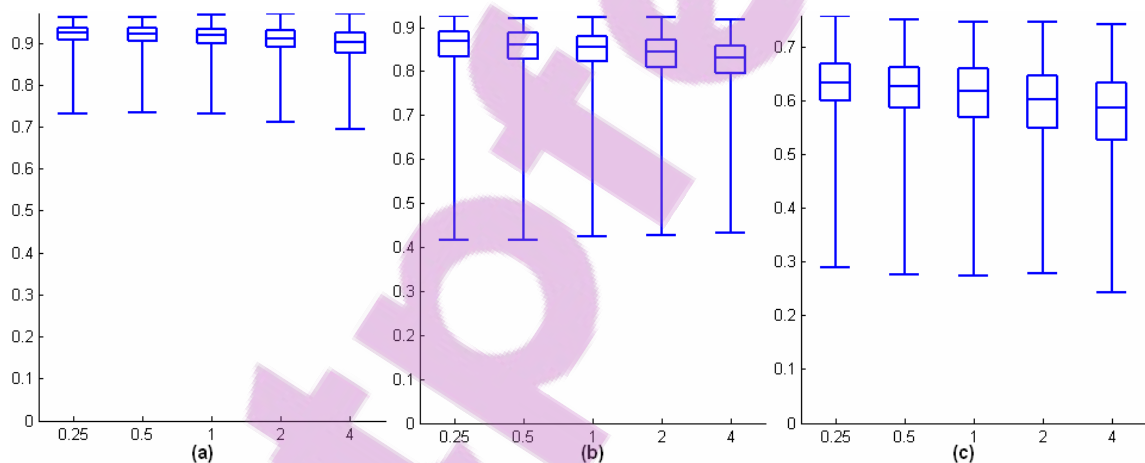


Figure 7.10 SI results of using different smoothing weights from 0.25 to 4; (a) LV, (b) RV, (c) myocardium.

- **Selection of mesh complexity**

Figure 7.11 (MHD errors) and Figure 7.12 (SI results) show the experiment of using meshes with different complexities from 1x1x1 to 4x4x4. No obvious difference was found. The best results on the LV, RV and myocardium were found when a 3x3x3 mesh was selected.

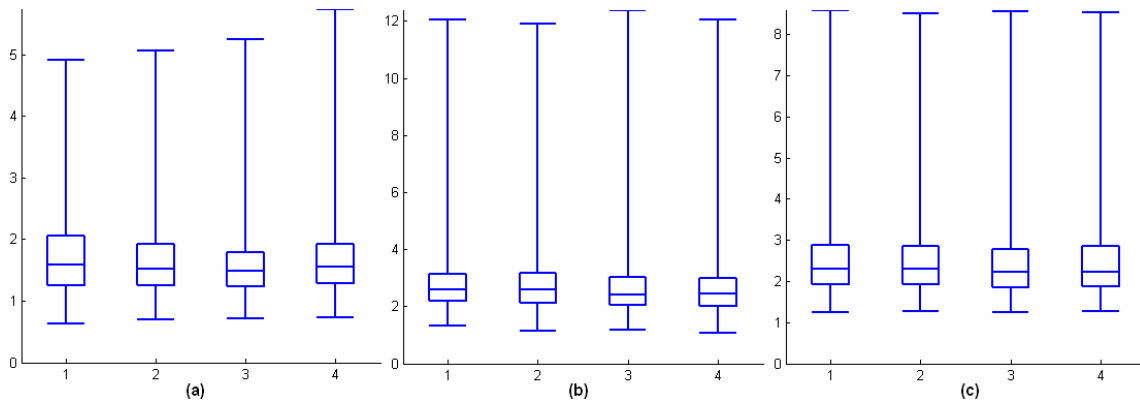


Figure 7.11 MHD results of using different mesh complexities from left to right 1x1x1, 2x2x2, 3x3x3, 4x4x4; (a) LV, (b) RV, (c) myocardium.

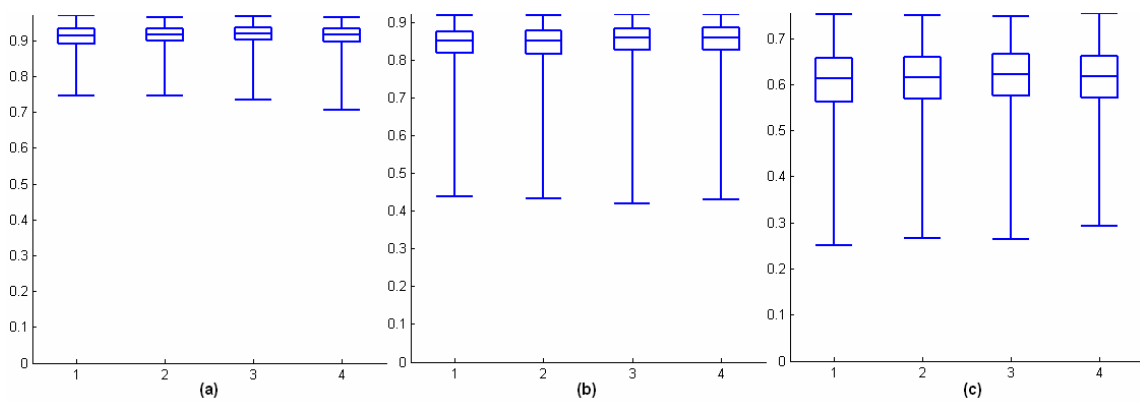


Figure 7.12 SI results of using different mesh complexities from left to right 1x1x1, 2x2x2, 3x3x3, 4x4x4; (a) LV, (b) RV, (c) myocardium.

7.3 Segmentation on Other Short-axis Slices

The 3D heart model, updated by the contours detected on the middle SA slice, provides more accurate initial atlases for the segmentation of the other SA slices. The two slices next to the middle SA slice are first segmented using the same atlas based 2D method. The resulting contours update the 3D heart model further and the next slices are segmented. An iterative update procedure is established; the model becomes more accurate as more and more feature points are included. Some registration parameters needed to be adjusted in the segmentation of those middle SA slices as the model became increasingly closer to the ground truth.

Segmentation of the apical or basal slices is expected to be less accurate than slices close to the middle. The information from the SA slices is of limited value and is less reliable in these areas. Partial volume effects, poor image acquisition and flaws in the current model cause serious problems in these slices. The large variance in the shape and size of the objects also make it difficult. Thus, not all the segmentation results should be included to update the

heart model. In this section, we focus on how to establish criteria to validate the reliability of the segmentation results.

7.3.1 Segmentation Issues

- **Apical Slices**

The errors were worse in the apical area because there was a lack of information available in apical SA slices. Partial volume effects and the placement of the apical SA slice caused large variability in the shape and size of the LV and RV cavities (Figure 7.13). In some cases, only the LV or the RV was shown in the image. It is particularly difficult for the atlas-based 2D registration method if the atlas's shape and size was quite different from the image. In such a situation, the segmentation on the apical SA slices may not be possible or the results may not be reliable. LA slices which have more accurate information in the apical area should be included. Thus, a suitable criterion is needed to establish when apical SA slices should not be included and when to use LA slices instead.

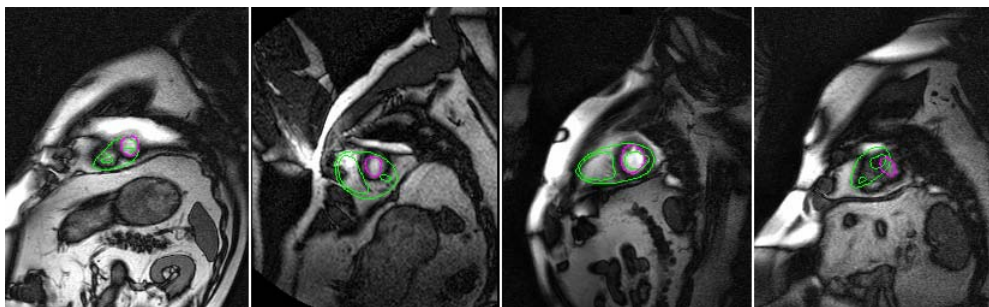
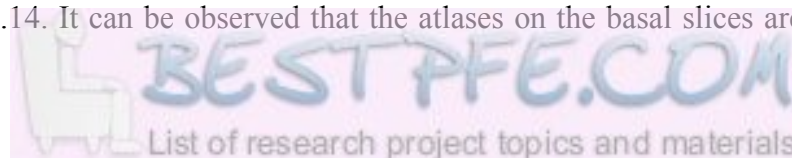


Figure 7.13 Examples of variability of the atlas and the LV RV presentation on apical slices

- **Basal Slices**

More problems were found in the basal area than any other area. The causes of the problems were not confined to the images but were also due to the design of the current model. The basal SA slice was typically the first slice placed in CMR scans. The slice should be parallel to the plane of the atrioventricular ring and pass the two anchor points at rear of the LV and RV myocardium. However, the placement of the slice is currently still based on operator's experience and inter-operator errors will always exist. These small differences in the orientation or position of the slice plane resulted in large differences in the images. The variability of the LV and RV presentation on those slices was often large. Four examples are shown in Figure 7.14. It can be observed that the atlases on the basal slices are completely



different from the images, making it impossible to segment these slices with the atlas-based registration method.

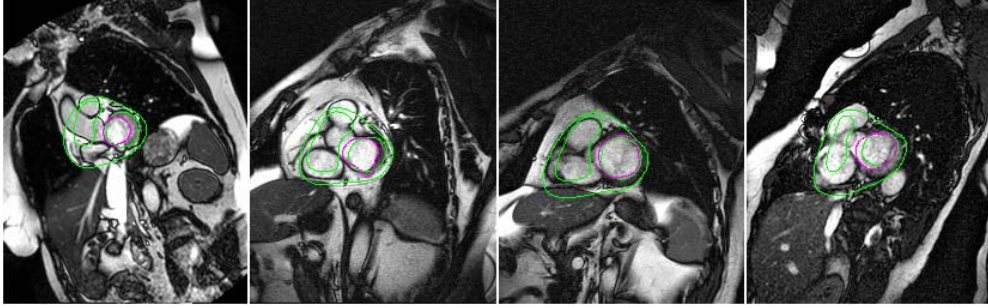


Figure 7.14 Examples of variability of the atlas and the LV RV presentation on basal slices

7.3.2 Validation Criteria

- **Basal Slices**

The validation criterion for basal slices was based on a specific average distance between the epicardium and endocardium. The distance of each epicardial point to its closest endocardial point was computed and averaged. Assume $P = \{\mathbf{p}_1, \mathbf{p}_2, \dots, \mathbf{p}_N\}$ denotes the epicardial points and $O = \{\mathbf{o}_1, \mathbf{o}_2, \dots, \mathbf{o}_M\}$ is the endocardial points in the atlas. The average distance is computed by

$$d(P, O) = \frac{1}{N} \sum_{\mathbf{p}_i \in P} d(\mathbf{p}_i, O) \quad (101)$$

where

$$d(\mathbf{p}_i, O) = \min_{\mathbf{o}_j \in O} \|\mathbf{p}_i - \mathbf{o}_j\| \quad (102)$$

The average distance on the middle SA slice (d_{mid}) was first computed and treated as the standard for comparison to the distance of other slices. If the average distance on any slice was more than twice of d_{mid} , that slice and all other slices closer to the base were discarded. This method may not work for patients with hypertrophic cardiomyopathy whose basal septum has often substantial thickening.

- **Apical Slices**

An apical slice was not considered useful if either the slice had an erroneous registration or the LV cavity was too small. Each apical slice therefore had to satisfy the following two rules:

- 1) After registration, the percentage of myocardial pixels should be over 75% in the septal region of the atlas on the target image; otherwise, the registration would be considered as a failure.
- 2) After registration, the size of the LV cavity should be no less than 25% of the LV size on the middle SA slice; otherwise, the segmentation result should be considered to be not reliable.

Once a failed slice is found, the other slices closer to the apex will also be discarded.

- **Effect of Criteria**

These two criteria affected almost all the cases in terms of the experiment on the ONTARGET dataset, which is shown in Table 7-1. This shows that in 88% cases the first basal slice was removed by the first criterion, and 85% cases do not include the first apical slice because of the second criterion described above. The case that had three apical slices removed is a special case that has duplicated scans at the apex. Although these slices were not included for updating the 3D model, the errors on these slices were still used in Section 7.5.3 for quantitative analysis.

In 328/330 cases	Apex				Base		
	0	1	2	3	0	1	2
Removed slices	0	1	2	3	0	1	2
No. of cases	32	277	18	1	15	288	25
Percentage	10%	85%	5%	0.3%	4%	88%	8%

Table 7-1 Slices removed by the criteria HD and SI comparison of initial contours, contours after atlas-based registration and contours after 3D registration.

7.3.3 Parameter Optimisation

After the segmentation and registration of the middle SA slice, the model was able to provide highly accurate initial estimates for segmentation on other SA slices. Both the

parameters in atlas-based 2D registration and feature-based 3D registration were optimised for the segmentation of the other SA slices.

- **Parameters in Atlas-based 2D Registration**

The coarse-to-fine strategy was used for the registration of each slice. The multi-resolution levels with high smoothing and low mesh complexity could be ignored because the initial atlas was close to the actual boundaries. Figure 7.15 shows a three-level solution to the registration of a SA slice close to the apex. In order to provide enough local deformation, the method started from a 3x3 mesh and with a medium size Gaussian smoothing kernel. The complexity of the mesh increased to 5x5 and the smoothing decreased to zero.

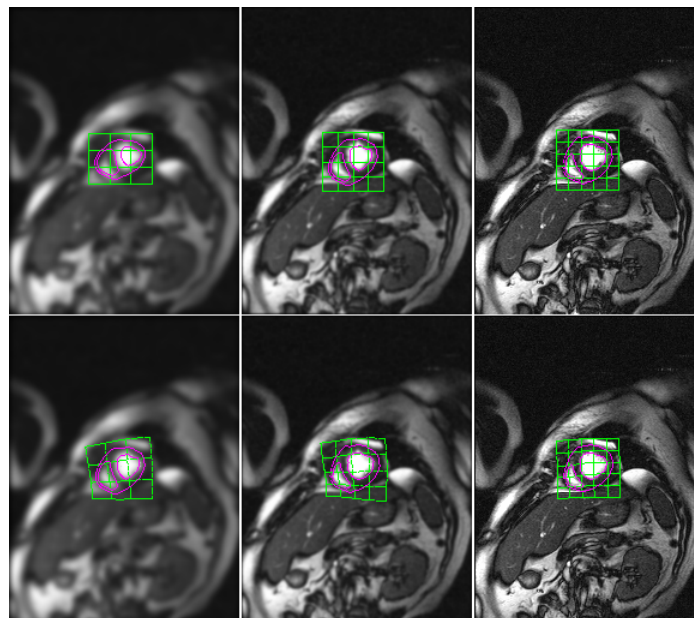


Figure 7.15 Coarse-to-fine strategy for the atlas-based registration of a SA slice close to the apex, top row – before registration, bottom row – after registration.

- **Parameters in Feature-based 3D Registration**

A 3x3x3 linear FFD was used for each 3D registration and a test was performed for the selection of the best smoothing weight. Figure 7.16 shows the results of using different weights from 0.25 to 1. No obvious difference was found except the apical slice. The best performance was found when the weight was set to 1.0. Thus, the parameters were the same as those used for the middle SA slice.

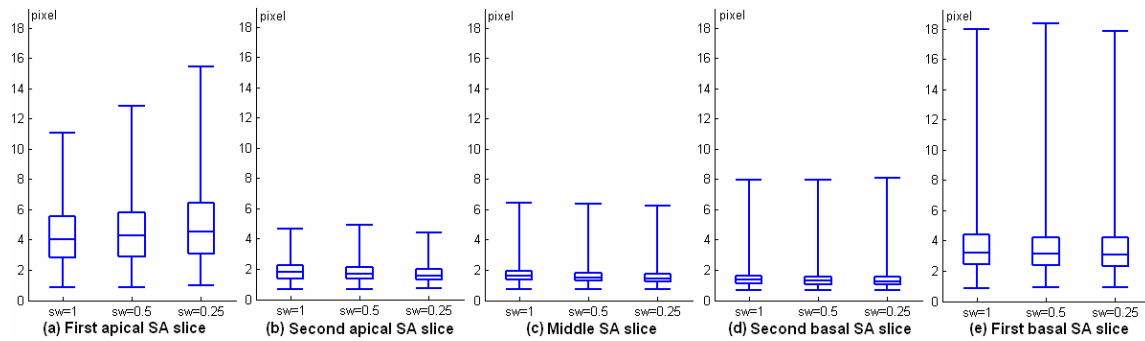


Figure 7.16 Box plot of MHD errors of the experiments using different smoothing weights from 0.25 to 1.

7.4 Segmentation of the 4-chamber Long-axis slice

7.4.1 Problems and Requirements

The atlas-based 2D registration method was used to detect the LV, RV endocardium and epicardium on the 4-chamber LA slice. The challenges in the segmentation of 4-chamber LA slices may arise from the following factors:

- 1) A thin or blurred RV free wall may cause leaking in that area.
- 2) Papillary muscles in LV cavity (often indistinctly imaged due to partial volume effects) will cause the detected contours to be smaller than expected.
- 3) The valves between the ventricles and atria are too thin to be detected by an automated method.

A balloon force and some constraints are required in the algorithm to deal with these problems.

- **A balloon force**

The initial model was normally very close to the ground truth. In some cases, strong local deformations were required when the real heart's shape was significantly different from the atlas. However, this may not be achieved because the smoothing weight must be set to high to avoid leaking at the RV free wall. The detected LV contour is also at risk of being smaller than the actual size due to the papillary muscles in the LV cavity. These can be reduced by adding a balloon force in the LV cavity. The boundary term discussed in Chapter 6 can be used to provide this force. The balloon force in the LV cavity was also found to be useful to overcome short-comings in the design of the current heart model. In the current model the position of RV apex is lower than the LV apex. A large deformation of the LV contour was

therefore needed when this model was registered to the image where the LV apex was lower than the RV apex. The balloon force was able to help the registration of such cases. The balloon force was not used in the RV because the RV free wall was quite thin and suffered from leaking.

- **Constraints**

The valves between the ventricles and atria are often too thin to be used to prevent erroneous translation in the LA direction. To avoid this, a constraint was added to the energy function to penalize any deformation in areas which were already registered quite well, i.e. the area around the middle SA slices. This constraint penalized the displacement of the intersections between the 4-chamber LA slice and the middle SA slice. These intersection points could also be used to help construct a better LV distance map for the boundary term (discussed below).

7.4.2 Atlas-based 2D Registration with Constraint Term

- **Energy Function**

When the above requirements are taken into account, the energy function of the atlas-based registration consists of four parameters, an intensity term E_I , a boundary term E_B , a smoothing term E_S and a constraint term E_C .

$$E = E_I + w_B E_B + w_S E_S + w_C E_C \quad (103)$$

where w_B , w_C and w_S are three weights defining the relative balance between the four terms. w_C is the weight of the constraint term and is typically much larger than the other two. The first three terms have been discussed in the last two chapters. The distance map for E_B will be shown in the next section. E_C penalizes the displacements of the pre-defined constraint points $C = \{c_1, \dots, c_n\}$. The term is given by the sum of squared distances between the deformed and undeformed positions of each point in C :

$$E_C = \sum_{c=1}^C (x(\mathbf{X}_c) - \mathbf{X}_c)^2 = \sum_{c=1}^C \mathbf{u}(\mathbf{X}_c)^T \mathbf{u}(\mathbf{X}_c) \quad (104)$$

where

$$\mathbf{u}(\mathbf{X}_c) = \sum_{i=1}^N \Psi_i(\mathbf{X}_c) \mathbf{P}_i \quad (105)$$

where \mathbf{P} are the parameters and Ψ are the basis functions in the formula.

▪ Optimisation

The optimisation was performed by the LM algorithm, which requires the computation of gradients and the Hessian matrix. The computation of the first three terms is given in previous chapters, and the gradient of the constraint term is given by

$$\mathbf{g}_c = -2J^{cT}U \quad (106)$$

where U is the matrix consisting of the displacement of all constraint points and J^c is the Jacobian matrix with elements

$$J_{cj}^c = \frac{\partial \mathbf{u}(\mathbf{X}_c)}{\partial P_j} = \Psi_j(\mathbf{X}_c) \quad (107)$$

The constraint term of the Hessian matrix is approximated by the Jacobian matrix with elements

$$H_{ij}^c = \sum_{c=1}^c \frac{\partial \mathbf{u}(\mathbf{X}_c)}{\partial P_i} \frac{\partial \mathbf{u}(\mathbf{X}_c)}{\partial P_j} = \sum_{c=1}^c \Psi_i(\mathbf{X}_c) \Psi_j(\mathbf{X}_c) \quad (108)$$

7.4.3 Implementation

▪ Determination of a 4-chamber LA slice

The first step was to automatically determine the 4-chamber LA slice from amongst the LA slices acquired. Figure 7.17a and b show two typical planning strategies of the LA CMR scans used in the ONTARGET dataset. On the middle SA slice, the 4-chamber LA slices are marked in magenta. These could be automatically determined by seeking the minimal angle between the LA slice plane and the RV direction \mathbf{V}_y defined in Figure 2.2. \mathbf{V}_y is the orientation from the LV centre to the middle of the endocardial insertions of the RV free wall, shown in Figure 7.17c. This could be easily computed in the SMPL atlas-based framework. The two RV insertion points were pre-defined in the atlas and the LV centre could be computed from the LV area after registration. In order to find the correct slice in both planning strategies, an offset of $\theta = 15^\circ$ (Figure 7.17c) was added to the \mathbf{V}_y axis. This

method proved to be robust on the 328 ONTARGET cases. Five cases failed to agree with the manual selections. These included one case with no 4-chamber slice and four cases with poor estimation of V_y .

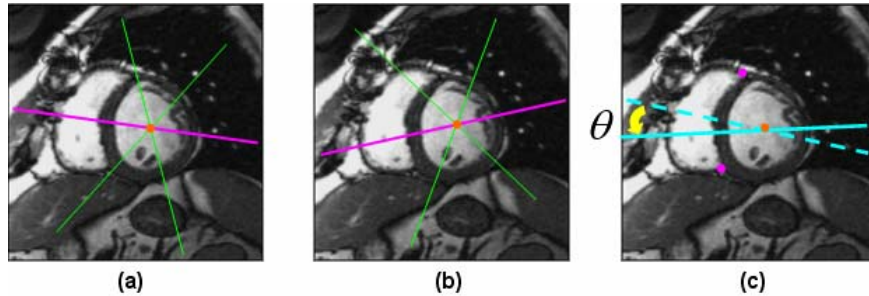


Figure 7.17 (a) and (b) are two different LA planning strategies shown on the middle SA slice, (c) the LV centre (orange), two RV inserts (magenta), the original V_y (cyan dot line) and the V_y rotated by θ (cyan solid line).

- **Determination of Constraint Points**

The constraint points were included to reduce erroneous deformation in the registration of the 4-chamber LA slice. The middle SA slice had the best registration results, therefore the intersection points between the middle SA slice and the 4-chamber LA slice were selected as constraint points. The displacements of these intersection points were highly penalized during the registration process and therefore reduced erroneous deformation in both the LA and SA directions. In practice, to provide more freedom in the apical area, the SA slice next to the middle SA slice but closer to the base was used instead of the middle SA slice. The atlas points on the LA slice which were within two pixels of the intersection line were defined as constraint points, shown in pink on Figure 7.19. Only small deformations occurred around these points during the registration process.

- **Construction of Distance Maps**

The computation of the distance map for this registration was similar to the one outlined in the chapter 6, except only the LV distance map was used. The process began by finding, through image thresholding, an initial contour within the atlas's LV region. The fast marching time map was computed and the distance map was constructed using the inverse of the time map. One limitation of this method was that the balloon force created by the distance map tended to expand the ventricles across into the atria. Unfortunately, there were no clear boundaries between the ventricles and the atria on the image which could prevent such erroneous deformations. Thus, the constraint points were employed to reduce the force

to zero on the basal side (Figure 7.18b and c). The balloon force was therefore only active in the apical half of the atlas.

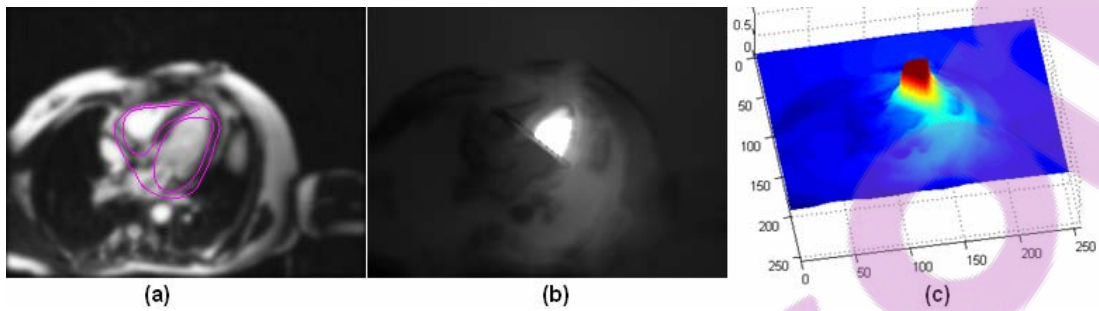


Figure 7.18 (a) atlas on the 4-chamber LA slice, (b) 2D view of LV distance map and (c) its 3d view.

- **Coarse-to-fine Strategy**

A three level coarse-to-fine strategy was applied in the registration, Figure 7.19. The complexity of the mesh increased from 3×3 to 5×5 . The lowest complexity level, used in the middle SA slice, was not required because the initial model was already very close to the actual boundaries.

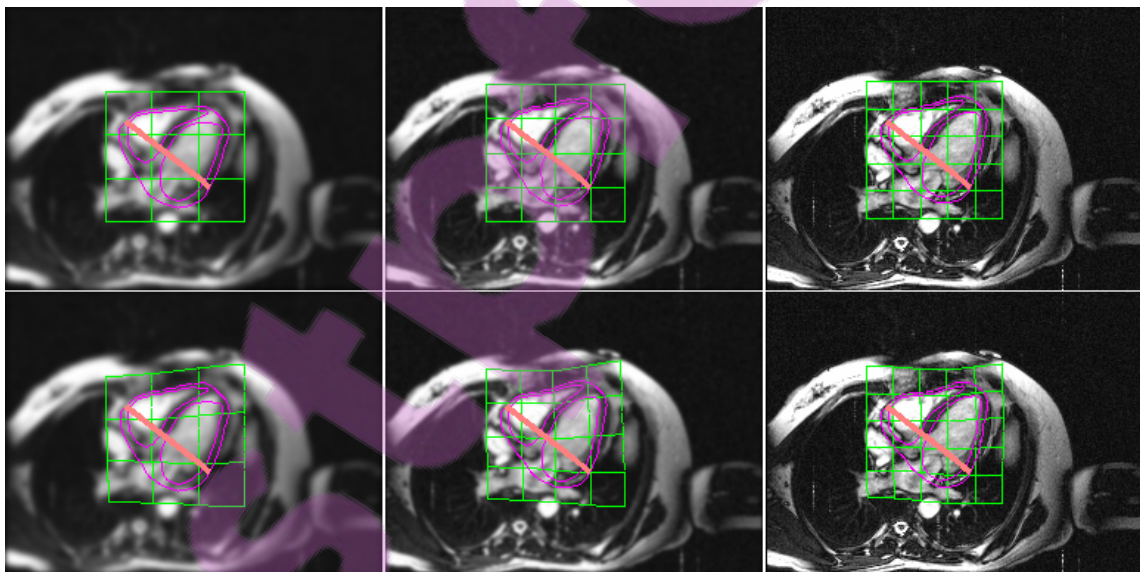


Figure 7.19 Multi-grid and multi-resolution strategy for the atlas-based registration of the LA slice; pink – constraint points, green – mesh, magenta – atlas.

7.5 Results

7.5.1 Ground Truth

The experiments were implemented using 328 ONTARGET cases. The validation of the feature-based 3D registration method was based on the middle SA slices, using the LV, RV

endocardial and epicardial ground truth contours described in Section 5.7.1. For the other SA and LA slices, only the LV endocardial contours from two independent observers were available for comparison. These were previously used in Chapter 2 for the validation of LV localization. With two independent ground truths, the inter-observer error of the LV endocardium is available for comparison with the automated method.

7.5.2 Results on the Middle Short-axis Slice

A typical example is shown in Figure 7.20. The ground truth, Figure 7.20a, includes the LV, RV endocardium and epicardium, and the initial atlas is shown in Figure 7.20b. Figure 7.20c shows that the atlas-based 2D registration provides excellent agreement between the ground truth and the detected contours. The contours are used to update the initial model by the feature-based 3D registration method. The intersection between the updated model and the middle SA slice is shown in Figure 7.20d.

The box plots of the MHD errors and SI results of the contours from the updated model are presented in Figure 7.21 and Figure 7.22. It shows that the model has been successfully fitted to the contours. The smoothing weights were set to high in this initial fit, leading to slightly higher contour errors after the 3D registration. The updated model can provide highly accurate initial estimates for the segmentation of other slices. Numerical results, mean \pm standard deviation, are summarized in Table 7-2.

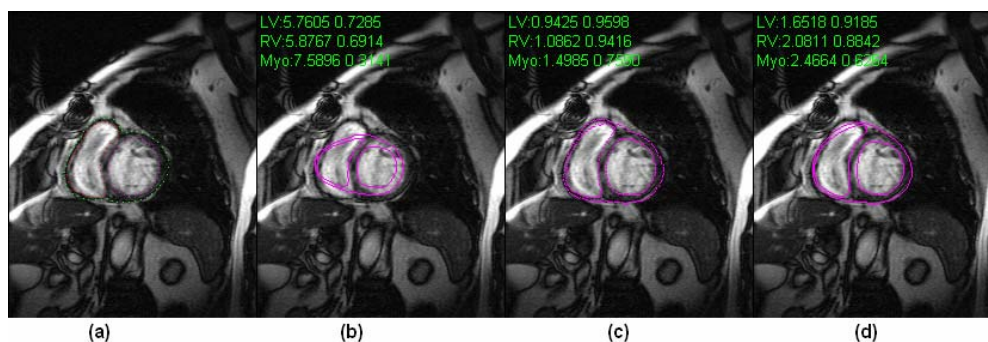


Figure 7.20 Contour comparisons on the middle SA slice used in the last chapter: (a) Ground truth contours, (b) initial model contours, (c) contours after atlas-based registration and (d) model contours after 3D fitting.

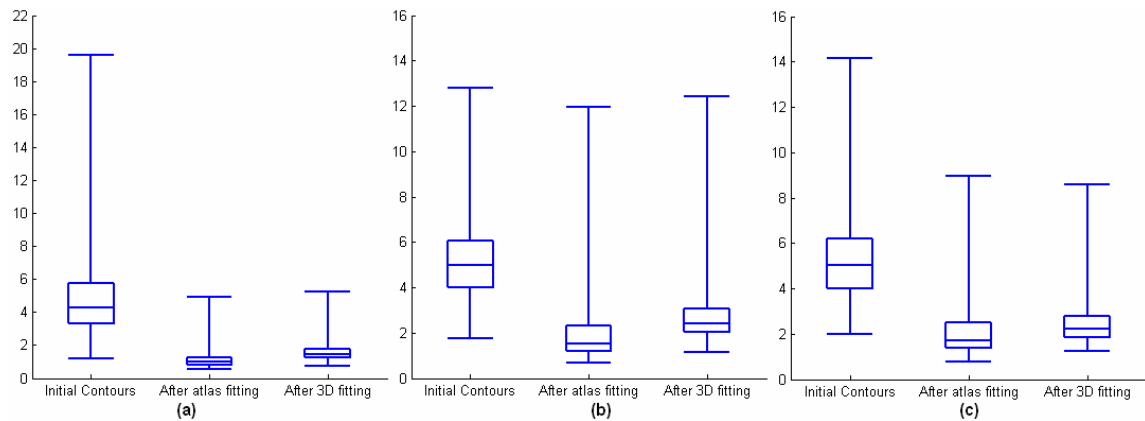


Figure 7.21 MHD comparison of initial contours, the contours after atlas-based registration and contours after 3D model fitting on the middle SA slice. (a) LV, (b) RV and (c) epicardium.

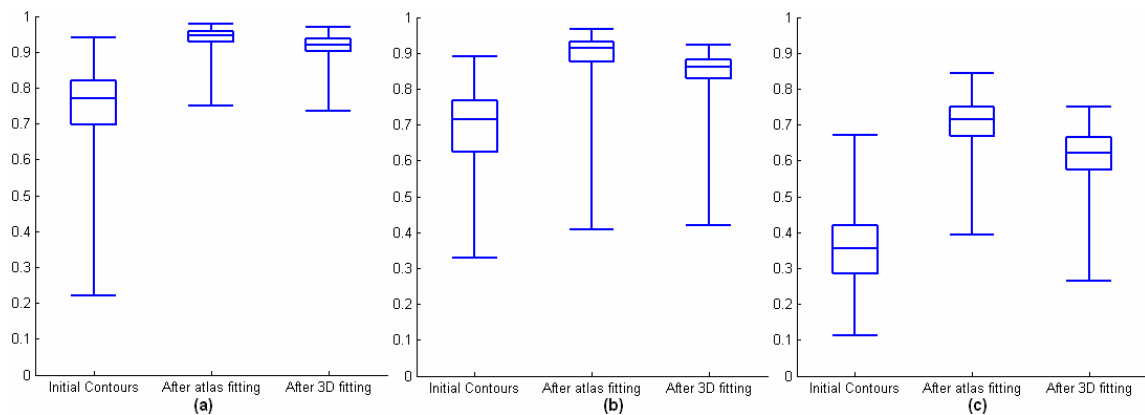


Figure 7.22 SI comparison of initial contours, the contours after atlas-based registration and the contours after 3D model fitting on the middle SA slice. (a) LV, (b) RV and (c) epicardium.

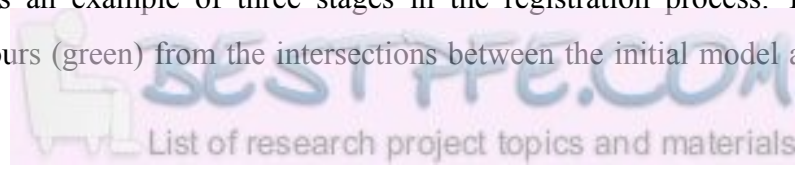
	MHD			SI		
	Initial contour	After atlas fitting	After 3D fitting	Initial contour	After atlas fitting	After 3D fitting
LV	4.76 ± 2.35	1.15 ± 0.54	1.60 ± 0.58	0.75 ± 0.11	0.94 ± 0.03	0.92 ± 0.03
RV	5.19 ± 1.66	2.06 ± 1.62	2.84 ± 1.54	0.69 ± 0.10	0.89 ± 0.08	0.84 ± 0.07
Myo	5.21 ± 1.77	2.18 ± 1.34	2.57 ± 1.19	0.36 ± 0.11	0.70 ± 0.07	0.62 ± 0.07

Table 7-2 MHD and SI comparison of initial contours, contours after atlas-based registration and contours after 3D registration on the middle SA slice.

7.5.3 Results on Other Short-axis Slices

- **Qualitative Analysis**

Figure 7.23 shows an example of three stages in the registration process. The top row provides the contours (green) from the intersections between the initial model and each SA



slice. The magenta contours are the ground truth LV endocardium. It may be noticed that the initial model is quite close to the ground truth in this case. The middle row shows the results of the updated model from the contours detected on the middle SA slice. The middle SA slice is the 4th column in the figure. The contours on this slice are significantly improved after updating but there are still obvious errors on the other SA slices, especially the apical slices. Another two slices (3rd and 5th slices) were then segmented and the detected contours were added to update the model. The bottom row gives the updated results using all SA slices. A good agreement between the ground truth and the model was found except in the first and the last slices which did not pass the validation.

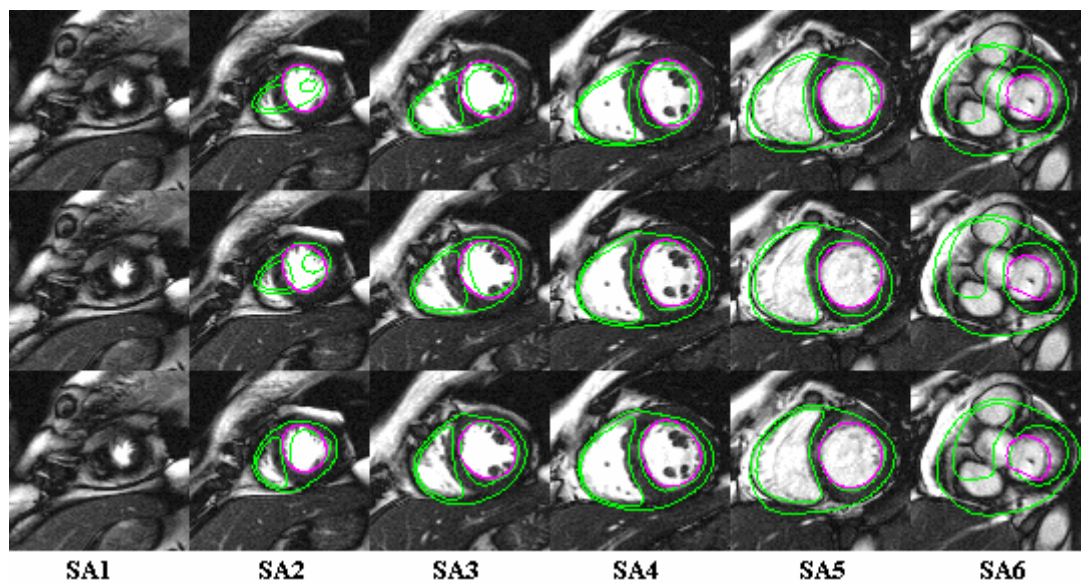


Figure 7.23 Top row – initial model shown on each SA slice, middle row – updated model with the contours computed from the middle SA slice, bottom row – updated model with the detected contours of the 3rd to 5th SA slices; magenta contour – the ground truth of LV endocardium.

- **Quantitative Analysis**

A uniform framework was required to evaluate the 328 ONTARGET cases because each case has a different number of SA slices. Five specific slices were selected in each case as defined in Figure 7.24: (a) first apical slice, (b) second apical slice, (c) middle slice, (d) second basal slice and (e) first basal slice. The evaluations were based on these five slices.

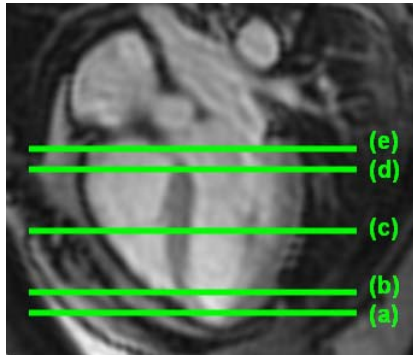


Figure 7.24 Location of five specific slices: (a) first apical slice, (b) second apical slice, (c) middle slice, (d) second basal slice and (e) first basal slice.

Figure 7.25 shows box plots of MHD errors between the ground truth and the updated model on these five slices, compared to the inter-observer errors. The model shows an excellent agreement with the ground truth from the second apical slice to the second basal slice. The average MHD errors in these slices were all less than two pixels. The errors of the first apical and first basal slices were higher than the middle slices and the highest average error was found in the first apical slice, about 4 pixels in average. The numerical results are given in Table 7-3.

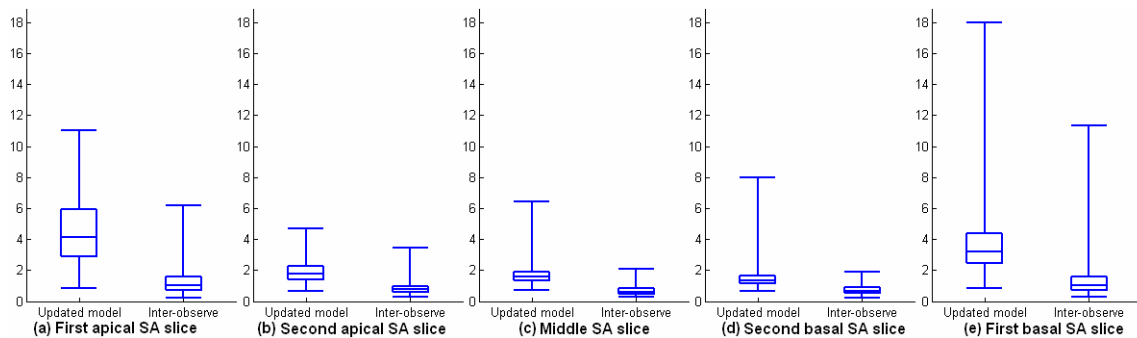


Figure 7.25 Box plots of the modified Hausdorff distances between ground truth and the updated model, in comparison to the inter-observer errors.

7.5.4 Results on 4-chamber Long-axis Slice

The atlas-based 2D registration results on the 4-chamber LA slices are provided, followed by the presentation of the updated model with the detected contours.

- **2D Registration Result of the 4-chamber LA Slice**

Figure 7.26 shows the MHD errors of the LV endocardium between the ground truth and the atlas before and after the LA registration. The error is improved 10% from 2.52 +/- 1.10 (mean +/- std) to 2.25 +/- 1.01 after registration. The result after registration is about twice

the inter-observer error which was 1.01 ± 0.46 . Thus, although the 4-chamber LA slice can improve the apical result, the improvement is not significant.

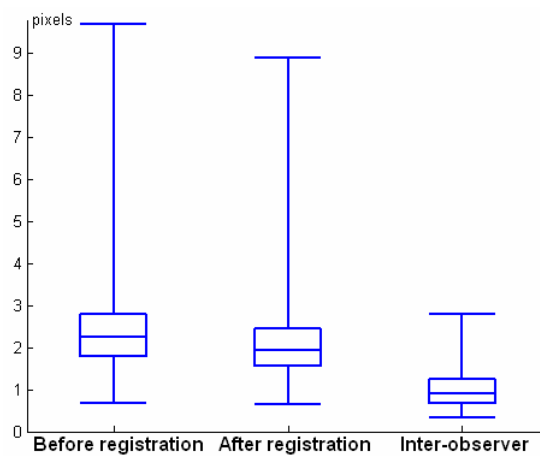


Figure 7.26 MHD errors on the 4-chamber LA slice between the ground truth and (a) the contours before the registration, (b) the contours after registrations and (c) inter-observer error.

▪ **Updated 3D model using the 4-chamber LA Slice**

Figure 7.27 shows the improvement in the case used in Figure 7.23 when the model is updated with the contours detected in both the SA slices and the 4-chamber LA slice. In this case, a large improvement in the first SA slice of the case can be found. The quantitative evaluation over the 328 ONTARGET cases is shown in Figure 7.28.

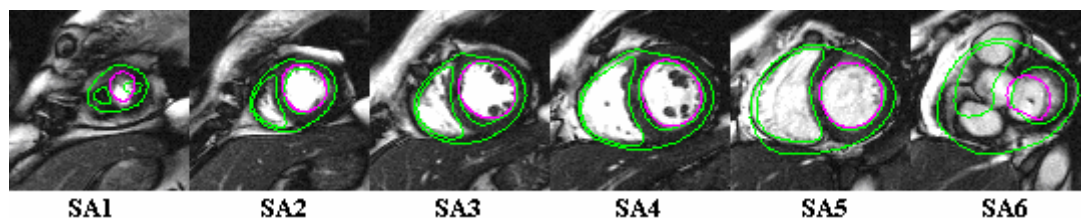


Figure 7.27 Results shown on the SA slices after the fit on the 4-chamber LA slice, in comparison to the results without using the LA slice (Figure 7.23).

7.5.5 Summary of Results

Four important stages were defined in the automated segmentation process:

- 1) the model after initial pose estimation
- 2) the model updated by the contours detected on the middle SA slices
- 3) the model updated by the contours detected on all SA slices

- 4) the model updated by the contours detected on both the SA and LA slices

The achievement at each stage is quantitatively evaluated in comparison to the ground truth. Figure 7.28 presents a detailed comparison of these four stages and the inter-observer errors (labelled as manual in the figure). Five typical SA slices defined in Figure 7.24 were studied. In Figure 7.28, the box plots of MHD errors shows continuing improvements at each stage. The numerical results of the mean and standard deviation are provided in Table 7-3. The improvement of each slice is described below.

- 1) First apical SA slice: This slice had larger initial errors than any other slice. The errors were significantly reduced during the registration of the SA slices. The inclusion of the 4-chamber LA slice (SA+LA, Figure 7.28) further improved the results. The average MHD error of the final result was about 2.5 times greater than the average inter-observer (manual, Figure 7.28) error.
- 2) Second apical SA slice: Similar to the first apical SA slice, the errors were mainly decreased during the SA slice registration. A slight improvement could be found when the 4-chamber LA slice was included. The average error was about 1.7 pixels, double the average inter-observer error.
- 3) Middle SA slice: The initial estimates on this slice were the best. The results were mostly improved by the 2D registration of this slice and almost remained unchanged during later registration steps. The excellent performance of the automated method was shown on this slice.
- 4) Second basal SA slice: Good performances were found in this slice. The initialization of this slice was nearly as good as the middle SA slice. The average MHD error of the final result was the best among all slices: lower than 1.5 pixels.
- 5) First basal SA slice: The final result for this slice was similar to the first apical SA slice. The errors decreased as more SA slices were included in the registration. The 4-chamber LA slice did not help to reduce the errors; in fact it made them slightly worse. The reasons for this will be discussed in the next section.

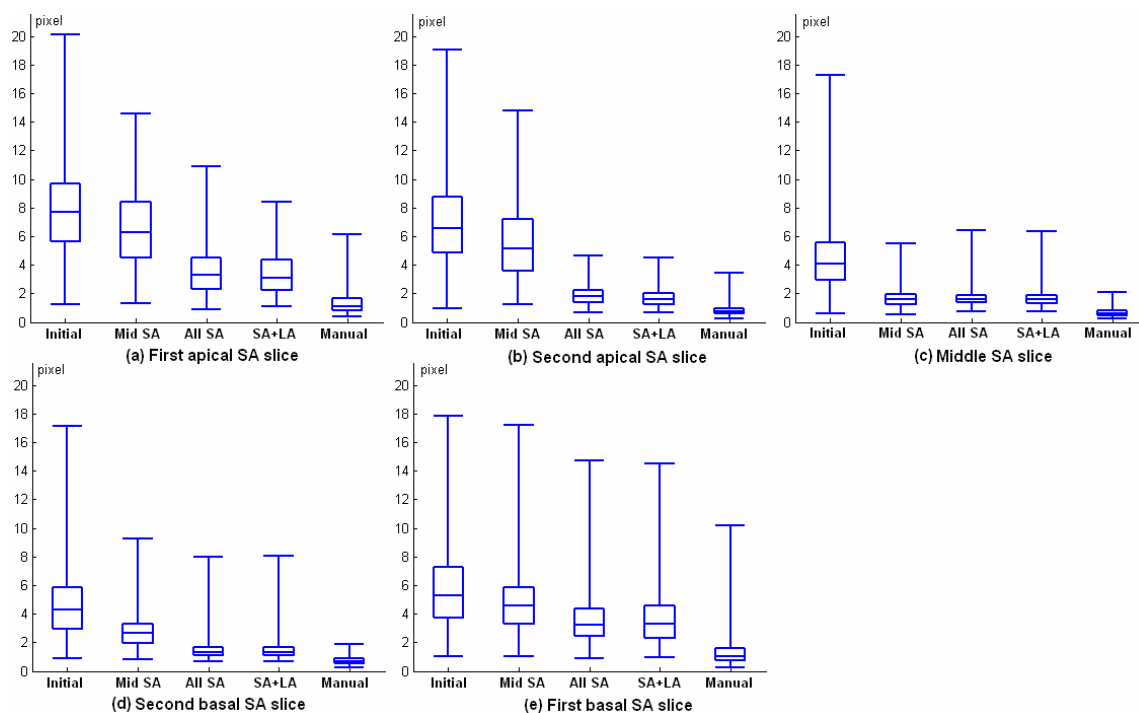


Figure 7.28 Box plot of the modified Hausdorff distance of the correspondence between ground truth and Initial estimate, using the contours detected on Mid SA, All SA, SA+LA, and inter-observer manual error.

	Initial	Mid SA	All SA	SA+LA	Manual
Apical SA	7.64 +/- 3.11	6.55 +/- 2.61	3.70 +/- 1.89	3.49 +/- 1.63	1.37 +/- 0.93
Second to apex	7.07 +/- 3.13	5.60 +/- 2.55	1.90 +/- 0.68	1.72 +/- 0.63	0.82 +/- 0.34
Middle SA	4.51 +/- 2.23	1.65 +/- 0.60	1.68 +/- 0.53	1.67 +/- 0.53	0.70 +/- 0.29
Second to base	4.81 +/- 2.70	2.81 +/- 1.22	1.46 +/- 0.61	1.46 +/- 0.64	0.70 +/- 0.27
Basal SA	5.91 +/- 3.13	4.86 +/- 2.34	3.60 +/- 1.85	3.72 +/- 2.07	1.40 +/- 1.31

Table 7-3 Modified Hausdorff distance between the ground truth and the updated model after initial estimate, using the contours detected on Mid SA, All SA, SA+LA, and inter-observer manual error.

7.6 Discussions

7.6.1 Achievements

A successful automated 3D segmentation of CMR images has been proposed. The method started from the initial estimate derived from the H1 volume, followed by iteratively applying two registration techniques in 2D and 3D domains. The atlas-based 2D registration method detected the LV, RV endocardial and epicardial contours on each image. Feature-based 3D registration was used to update the 3D model with the detected contours. The model was deformed to match the actual boundaries by iteratively including additional

slices. The 4-chamber LA slice was used to improve the accuracy at the apical area. The following achievements can be concluded from the results:

- 1) The automated method was able to successfully segment the 3D LV and RV endocardium and epicardium. The average MHD errors were less than 2 pixels in all slices except the first basal and apical slices, which were about twice of the inter-observer errors. The average MHD errors on the first basal and apical slices were slightly worse (three times the inter-observer errors) than the other slices but are still less than 4 pixels.
- 2) The initial estimation method and the atlas-based segmentation method were shown to be robust and reliable with a large clinical dataset. The strategy of iteratively using atlas-based 2D and feature-based 3D registrations was feasible and efficient.
- 3) The performance of the method was better on the slices close to the mid-ventricle rather than apical and basal slices. The 4-chamber LA slice improved the performance in the apical area, but this was limited.

7.6.2 Limitations and Future Work

The current method is based on an iterative application of 2D and 3D registration algorithms. The deformation in the LA direction was not effectively solved. It may help to increase the accuracy if more LA slices are used. An atlas-based 3D registration is another possibility. Also, the current 3D model needs to be improved, particularly at the apex and base. A statistical analysis may provide good constraints to avoid erroneous deformation. These topics are considered in more detail below.

- **Adding Other LA Slices**

A comparison of the “All SA” and the “SA+LA” results, Figure 7.28, showed the latter can improve the accuracy at the apex by including the 4-chamber LA slice in the registration.

- *More LA Slices*

More LA slices are available in most cases. In general, there were at least three LA slices in each case. If these slices are included, the results can be expected to improve further at the expense of computational cost.

- *Better LA Planning*

The current LA slices were designed to pass the centre of the LV during the data acquisition. Little information about the RV is contained except in the 4-chamber LA slice. Better acquisition would require the operator to focus on both the LV and RV. Figure 7.29 provides two possible new LA acquisition plans. Two more slices passing the RV centre are added to the plan in Figure 7.29a. The plan in Figure 7.29b, maintains all LA slices passing through the LV centre but adds two more slices close to the LV RV orientation to present more information about both. Unfortunately, these extra scans will increase the total acquisition time.

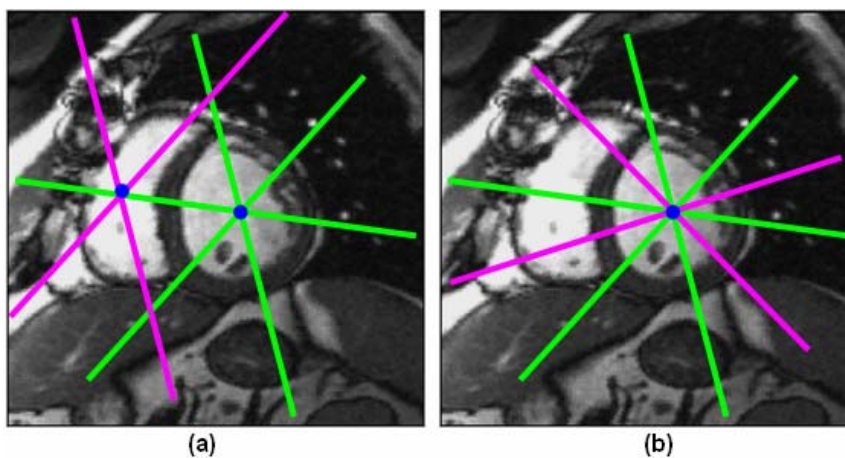


Figure 7.29 Two possible better LA acquisition plans; green – original slices, magenta – new slices added.

- **3D Atlas-based Registration**

It is conceivable that a true 3D atlas-based registration instead of the current iterative 2D and 3D registration could be used to register the model to the CMR data. All SA and LA slices can be included in the registration at the same time. However, the sparsity of the multislice data may make volumetric 3D registration methods problematic. The possible advantages and disadvantages in the robustness, accuracy and computational cost are discussed below.

- *Robustness*

This method may be more robust since including multiple slices at the very beginning may remove the dependency of any artefacts or low image quality found in any single slice. The orientation errors of the SA slice planning in CMR scans could be more easily corrected than with multiple 2D registration steps.

- *Accuracy*

3D atlas-based registration may be more accurate in the LA direction. The current method does not thoroughly consider the registration in LA direction because the registration is slice-based. Only the 4-chamber LA slice helps to adjust the model in this direction; however, applying it in the last registration step does not greatly improve the model if it has been misled by the previous registration steps of the SA slices. The 3D atlas-based registration provides the same freedom of deformation in the LA direction as the other two directions. The LA slices can also supply better constraints in that direction than the SA slices currently do.

- *Computational Cost*

The computational cost will exponentially increase when adding one more dimension. Thus, more time can be expected to be spent on the 3D atlas-based registration compared to a 2D registration. This would be worse if the initial model is not close to the ground truth. In the current method, the middle SA slice is first registered and the feature-based 3D registration moves the model to places very close to the ground truth. This reduces the computation time for the other slices.

- **Improvement of Current Model**

The current heart model has disadvantages at both the base and apex and a better model is required. Some constraints at the base may be necessary to prevent erroneous deformation in the registration of LA slices. A statistical analysis could be implemented to improve the robustness of registering the model to patients with different heart diseases.

- *Improvements at Base*

The current model has no heart valves; rather, a cover was added above the basal slice to make a closed surface for each structure. A thick myocardial wall (Figure 7.30) was thereby formed at the basal area in the atlas, which may cause erroneous deformation. One example of the coarse-to-fine registration process is shown in Figure 7.30. The synthetic myocardial wall at the base attracts the atlas to the top of the atria, deforming it in the wrong direction. This is also the main reason why the performances at the base (Table 7-3) become worse when 4-chamber slices are added, thus more constraints at the base are required.

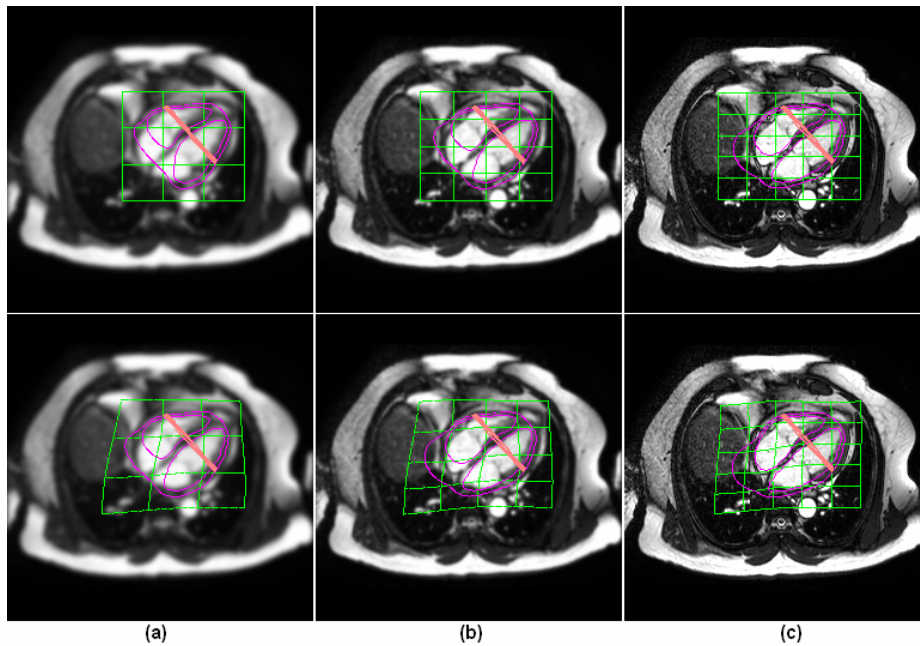


Figure 7.30 Covers above the basal slice and erroneous deformation at the base in a coarse-to-fine registration process; top row – before registration, bottom row – after registration; (a)3x3, (b)4x4, (c)5x5.

○ *Improvements at the Apex*

There exist two problems at the apical area in the current model. Firstly, the myocardium at the apex is relatively thick. This is not always true for all patients and is partly responsible for errors at the apex (Figure 7.31a). One solution may be to add a further registration step at the apical area using a higher complexity mesh. In addition, the RV apex is lower than the LV apex in the atlas and may cause some difficulty in the cases where the LV apex is lower (Figure 7.31b).

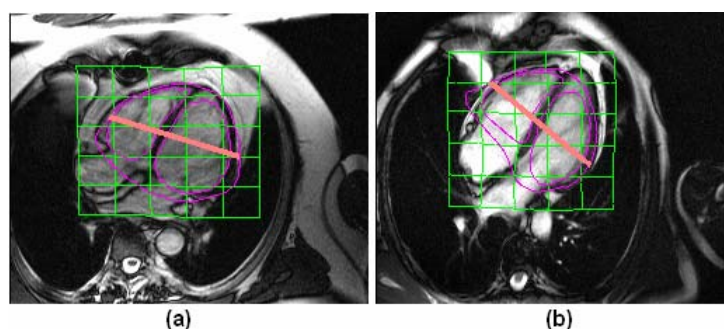


Figure 7.31 Two problems at the apex in current model; (a) thick myocardium, (b) RV apex lower than LV.

○ *Statistical Model*

The current model is constructed from the CMR data of a healthy volunteer. The variance in large datasets makes it difficult to register a single model to all patients. A 3D statistical shape model was constructed in [64] and applied to SA image segmentation in [65]. A 4D statistical model was also investigated in [4, 68] and applications can be found in [4, 66, 67]. Their results show that including statistical constraints can improve the robustness of method and decrease erroneous registration results.

In the extended atlas-based framework, statistical information could easily be integrated to the segmentation method. For example, the distance constraint between endocardium and epicardium used in [20] can be defined by the boundaries points in the atlas. Probabilistic information from the atlas constructed in [4] can be assigned to the different weights of the atlas points. Further research for efficient constraints based on statistical analysis should be performed in the future.

7.7 Conclusions

An efficient feature-based 3D registration method is proposed to fit the initial heart model to the contours detected by the 2D atlas-based registration in the last chapter. These two techniques are iteratively applied for each SA slice. The 3D model becomes closer to the actual shape of the heart in most slices. The 4-chamber LA slices are also exploited for more accurate information at the apical area. The results show that the MHD errors of the automated method are about double the inter-observer errors.



8 Conclusions

The principal contributions of this thesis are summarized in this chapter, followed by suggestions for future research.

8.1 Thesis Summary

The thesis has made novel contributions in five aspects, outlined below:

- 1) Novel method based on temporal Fourier analysis for fast LV localization
- 2) Model-based graph cut method for LV segmentation
- 3) Evaluation of similarity measures for atlas-based rigid-body registration
- 4) New atlas-based registration method for 2D image segmentation
- 5) Model-based segmentation strategy for 3D CMR images

8.1.1 Novel Method for Left Ventricular Localization

In Chapter 2, a novel method was proposed for the automatic detection of the location and orientation of the LV in cine CMR image data. The method exploits the motion of the heart by applying a pixel-based Fourier analysis over time. The dynamic characteristics of the heart can be utilized to make the localization fast and efficient. This is the first time the temporal Fourier analysis has been used to achieve fast localization of the LV.

The method was quantitatively validated on two clinical datasets with a combined total of 395 patients who exhibited a range of cardiac and vascular diseases. Only one case failed and the average bias and precision in the apical, middle and basal SA slices in the remaining 394 were better than 5mm. The errors were similar to the SA image orientations planned by experienced technicians; the accuracy of the method was therefore comparable with current clinical practice. The method also successfully detected LV position and orientation in lower resolution breath-hold cine-scout scans (bias and precision < 6mm) making it suitable for automated scan planning. This method was also used in Chapter 5 for initial estimation of the RVLV model in the automated segmentation method.

8.1.2 Model-based Graph Cut Method

Chapter 3 developed an algorithm for the integration of high-level model-based knowledge into the low-level graph cut segmentation algorithm. This inherits the ability of the traditional graph cuts method to provide a global optimum and overcomes the limitation of using only low-level data. The spatial prior derived from the model was combined into the algorithm as one of the probability terms in the pixels' T-links. This feature is particularly important when low-level information is unable to determine the correct segmentation. The method requires pre-defined seeds and information about intensity probability. However, it was found to be insufficiently robust for the fully automated segmentation of all slices. Though not applied further in this thesis, this method has the potential for higher accuracy in good quality images.

8.1.3 Evaluation of Similarity Measures for Atlas-based Registration

An atlas-based registration framework was designed to achieve a high accuracy with a low computational cost. To this end, a comparison framework independent of the optimisation algorithm was developed to evaluate and find a suitable similarity measures for rigid atlas-based 2D segmentation.

In Chapter 4, six popular inter-modality and intra-modality similarity measures, SSD, NCC, CR, WD, MI and NMI were simplified to fit the new framework. They were quantitatively compared with each other in four key aspects ACC, DON, NOM and RON. The results show that no measure has the overall advantage over the others, rather

- 1) SSD and NCC have wider capture range and less local optima in the total region of interest.
- 2) MI and NMI have better performance in areas close to the ground truth.

SSD was selected as the similarity measure for the atlas-based segmentation method due to its low computational cost, reasonably high accuracy, better NOM and RON, and its ability to provide an analytic derivative for optimisation.

8.1.4 New Atlas-based Segmentation Method

The atlas-based registration framework, and a segmentation method based on this framework, for the segmentation of 2D CMR images was developed in Chapters 5 and 6. In

the new framework, the atlas is not represented as an image but was treated as a set of mathematical points that have intensity values and anatomical labels. The registration maps each point from the atlas onto its best corresponding position in the target image. Linear interpolation was used to achieve sub-pixel resolution and reduce the artefacts caused by image linear interpolation. The framework had a high accuracy, low computational cost and the ability to integrate intensity, anatomical and boundary information. The computational costs were reduced since only objects of interest, rather than the whole image, were included in the atlas. Anatomical information, such as the identification of sub-regions in the heart muscle, could be defined in the atlas so that the weights of object points could be changed during the coarse-to-fine registration process. Boundary points could also be specified in the atlas to help reduce the impact of the myopic problem and the local minima caused by lack of background information.

The automated segmentation method correctly identified the LV, RV and myocardium on the ED frame of middle SA slice in 328/330 cases from the ONTARGET dataset. Failed cases were automatically detected by evaluating the percentage of the pixels in the patient images that lie in the septal region of the atlas and are more likely to be myocardium. The average MHD errors of the automated detected contours in middle SA slices were about 1 pixel in the LV and 2 pixels in the RV and myocardium respectively.

8.1.5 Model-based 3D Segmentation

A segmentation strategy was proposed in Chapter 7 to segment the entire left and right ventricles from multislice CMR images, by iterating between the atlas-based 2D registration and a feature-based 3D registration. The feature-based 3D registration combined the ICP and 3D FFD algorithms to automatically fit the model to pre-detected feature points generated from the LV and RV contours detected by the atlas-based 2D registration. The process started from the 2D segmentation of the middle SA slice and the detected contours were used to update the 3D model. The updated model provided highly accurate initial estimates for 2D segmentation of the other SA slices and their subsequent inclusion allowed the 3D model to be iteratively updated so that it better matched the ground truth. Validation criteria were specified to prevent including any erroneous feature points and the 4-chamber LA slice was added to the analysis to improve the accuracy in the apical region. A specific atlas-based 2D registration with an additional constraint term was proposed for the segmentation of the LA slice.

The results showed that this segmentation strategy had high accuracy and high robustness for a low computational cost. The iterative process is expected to take less time than 3D atlas-based registration because the segmentation on the middle SA slice quickly approximates the initial model to the ground truth. The average MHD errors in most slices were less than 2 pixels – double the inter-observer errors. The errors at the basal and apical slices were within 4 pixels – about triple the inter-observer errors.

8.2 Further Work

Many individual aspects could be investigated to further improve the current segmentation strategy. Some of them were discussed in the previous chapter. They are reorganized into four aspects below in the order of the importance.

8.2.1 Use More LA Slices

Only the 4-chamber LA slice is currently applied in the method. All LA slices can be used to improve the accuracy. The current dataset has limited information on the RV. A better LA planning for CMR scans should be studied to obtain more accurate RV information. Unfortunately, there will be a trade-off between the computational cost and acquisition time versus accuracy.

8.2.2 Better Heart Model

More research should be taken to improve the current model, particularly at the apex and base. The thickness of the myocardium, the statistical LV and RV ventricular shape and the design of the valves require further development. The current thick cover at the base should be replaced by carefully modeled heart valves. It is also important to provide efficient constraints at the base to avoid erroneous deformation. Manual input can be required if no reliable automated method is found.

One option to solve this problem is to develop a model with both atria and ventricles. Such a model was first investigated in [102, 103] and used for heart motion tracking in [102, 152]. Both SA and LA volumes were applied in their experiments. A prior model was first manually deformed to the SA volume and transformed to the coordinates of the corresponding LA volume. Non-rigid 3D atlas-based registration was used for the mapping of the model to the LA volume. Similar models were used for semi-automated [153] and for automated methods [154].

Statistical analysis is important when registering a very limited number of atlases or models to all patient cases in large datasets. It has been proven that statistical constraints can improve the robustness of a method and decrease erroneous registrations. Applications of 4D CMR segmentation can be found in [4, 66, 67]. This statistical information can be easily integrated in the new proposed atlas-based registration framework.

8.2.3 Atlas-based 3D Registration

A complete 3D atlas instead of multiple 2D atlases could be used to register the model to the CMR data. All SA and LA slices can be included in the registration at the same time. The method may be more robust when multiple slices are involved in the registration at the very beginning because any artefacts or low image quality in a single slice will not seriously affect the result. The atlas-based 3D registration can provide the same freedom of deformation in the LA direction as the other directions making the registration in LA direction easier. However, the atlas-based 3D registration may have considerably greater computational cost. The computational cost will exponentially increase when one more dimension is added. This becomes worse if the initial model is not so close to the ground truth. Also, the sparsity of the multislice data may make volumetric 3D registration methods problematic. A hybrid method may provide the best solution. That is, the initial model is first registered on the middle SA slice with the current method before atlas-based 3D registration is applied.

8.2.4 4D Segmentation

4D CMR segmentation can be implemented by propagating 3D detected contours over time. It can also be directly registered by using a 4D model.

In [27], 3D segmentation and tracking was first solved by using a FEM-based deformable model. An active contour based algorithm was used for the temporal propagation. In [148], an AAM motion model was constructed from an image sequence by combining texture and motion information. Contour detection was performed by iteratively deforming the model within statistically allowed limits until an optimal match was found. Similar processes can be found to achieve motion tracking in [61]. [3] attempted to simultaneously solve the segmentation and tracking problems with a 4D deformable model. It extended the deformable surface framework by introducing time-dependent constraints. Prior motion

knowledge was integrated into the deformation process to segment the 4D images. The 4D atlas was also studied in [66] and used for spatial-temporal registration in [67].

In our new proposed framework, there is the potential to interpret 4D segmentation as a 3D segmentation over time which starts from the ED frame. Because the transformations between two neighbouring frames are often very limited, it may be enough to only use the intensity term in the energy function. The speed may be adequate for clinical application because a boundary box can be defined from the 3D segmentation results.

8.2.5 Automatic Breath-hold Registration

One step in our automatic process, which was manually implemented in this Thesis, was the correction of errors in slice position caused by breathing. Experienced analysts translated the slice in the plane of the image by comparing them to all other LA and SA slices, if a large mis-registration was observed. This simple method does not guarantee that the LA and SA slices completely match, but was found to be adequate for clinical purposes. Automated motion correction has recently been investigated in some literature, such as [15], though no clinical application was reported. Several LA slices must be available to register the slices automatically. The current datasets with the acquisition protocol described in Section 1.4.2 are not suitable to this research. New protocols, such as those discussed in Section 7.6.2, should be used for scan planning in the future.

9 Publications

X. Lin, B. Cowan and A. Young: *Localization and Atlas-based Segmentation of the Heart from Cardiac MR Images: Validation with a Large Clinical Trial*. The 2nd International Conference on Bioinformatics and Biomedical Engineering (ICBBE'08), accepted.

X. Lin, B. Cowan and A. Young: *Automated Detection of the Left Ventricle from 4D MR Images: Validation using Large Clinical Datasets*. The 2006 IEEE Pacific-Rim Symposium on Image and Video Technology (PSIVT'06), pp. 218-227. 

X. Lin, B. Cowan and A. Young: *Automated Detection of Left Ventricle in 4D MR Images: Experience from a Large Study*. The 9th International Conference on Medical Image Computing and Computer Assisted Intervention (MICCAI'06), pp. 728-735.

X. Lin, B. Cowan and A. Young: *Model-based Graph Cut Method for Segmentation of the Left Ventricle*. The 27th Annual International Conference of the IEEE Engineering in Medicine and Biology Society (EMBC'05), pp.571-574.

10References

- [1] D. R. Hay, *Cardiovascular disease In New Zealand, 2004*, The National Heart Foundation of New Zealand, 2004.
- [2] S. C. Mitchell, J. G. Bosch, B. P. F. Lelieveldt *et al.*, “3-D active appearance models: segmentation of cardiac MR and ultrasound images,” *IEEE Transactions on Medical Imaging*, vol. 21, no. 9, pp. 1167-1178, 2002.
- [3] J. Montagnat, and H. Delingette, “4D deformable models with temporal constraints: application to 4D cardiac image segmentation,” *Medical Image Analysis*, vol. 9, no. 1, pp. 87–100, 2005.
- [4] M. Lorenzo-Valdes, G. I. Sanchez-Ortiz, A. G. Elkington *et al.*, “Segmentation of 4D cardiac MR images using a probabilistic atlas and the EM algorithm,” *Medical Image Analysis*, vol. 8, no. 3, pp. 255-265, 2004.
- [5] X. Lin, B. Cowan, and A. Young, “Automated detection of the left ventricle from 4D MR images: validation using large clinical datasets,” in *PSIVT*, 2006, pp. 218.
- [6] M. P. Jolly, N. Duta, and G. Funka-Lea, “Segmentation of the left ventricle in cardiac MR images,” *ICCV*, pp. 501–508, 2001.
- [7] G. J. Tortora, and B. H. Derrickson, *Principles of Anatomy and Physiology*, 11th ed., New York: Wiley 2005.
- [8] H. Azhari, S. Sideman, J. L. Weiss *et al.*, “Three-dimensional mapping of acute ischemic regions using MRI: wall thickening versus motion analysis,” *American Journal of Physiology- Heart and Circulatory Physiology*, vol. 259, no. 5, pp. 1492-1503, 1990.
- [9] A. F. Frangi, W. J. Niessen, and M. A. Viergever, “Three-dimensional modeling for functional analysis of cardiac images, a review,” *IEEE Transactions on Medical Imaging*, vol. 20, no. 1, pp. 2-5, 2001.
- [10] D. J. Pennell, “Ventricular Volume and Mass by CMR,” *Journal of Cardiovascular Magnetic Resonance*, vol. 4, no. 4, pp. 507-513, 2002.
- [11] C. H. Lorenz, E. S. Walker, V. L. Morgan *et al.*, “Normal human right and left ventricular mass, systolic function, and gender differences by cine magnetic resonance imaging,” *Journal of Cardiovascular Magnetic Resonance*, vol. 1, no. 1, pp. 7-21, 1999.
- [12] W. J. Manning, and D. J. Pennell, *Cardiovascular Magnetic Resonance*: Churchill Livingstone, 2002.
- [13] A. A. Young, “Assessment of cardiac performance with magnetic resonance imaging,” *Current Cardiology Reviews*, vol. 2, no. 4, pp. 271-282, 2006.
- [14] C. Jackson, M. Robson, J. Francis *et al.*, “Automatic planning of the acquisition of cardiac MR images,” in *MICCAI*, 2003, pp. 541-548.
- [15] J. Lotjonen, M. Pollari, S. Kivisto *et al.*, “Correction of movement artifacts from 4-D cardiac short-and long-axis MR data,” in *MICCAI*, 2004.
- [16] C. Anderson, “Rationale and design of the cardiac magnetic resonance imaging substudy of the ONTARGET trial programme,” *Journal of International Medical Research*, vol. 33, no. Suppl 1, pp. 41A-48A, 2005.
- [17] A. J. Pullen, L. K. Cheng, and M. L. Buist, *Mathematically Modeling the Electrical Activity of the Heart: From Cell to Body Surface and Back Again*: World Scientific, 2005.

- [18] D. L. Pham, C. Xu, and J. L. Prince, "Current methods in medical image segmentation," *Annual Review of Biomedical Engineering*, vol. 2, no. 1, pp. 315–337, 2000.
- [19] J. S. Suri, "Segmentation and quantification techniques for fitting computer vision models to cardiac MR, CT, X-ray and PET image data," *Advanced algorithmic approaches to medical image segmentation: state-of-the-art application in cardiology, neurology, mammography and pathology* pp. 131-227: Springer-Verlag New York, 2002.
- [20] N. Paragios, "A variational approach for the segmentation of the left ventricle in cardiac image analysis," *International Journal of Computer Vision*, vol. 50(3), pp. 345–362, 2002.
- [21] C. Xu, D. L. Pham, and J. L. Prince, "Image segmentation using deformable models," *Handbook of Medical Imaging*, pp. 129–174, 2000.
- [22] M. Kass, A. Witkin, and D. Terzopoulos, "Snakes: Active contour models," *International Journal of Computer Vision*, vol. 1, no. 4, pp. 321-331, 1988.
- [23] V. Caselles, R. Kimmel, and G. Sapiro, "Geodesic active contours," *International Journal of Computer Vision*, vol. 22, no. 1, pp. 61-79, 1997.
- [24] R. Goldenberg, R. Kimmel, E. Rivlin *et al.*, "Fast geodesic active contours," *IEEE Transactions on Image Processing*, vol. 10, no. 10, pp. 1467-1475, 2001.
- [25] T. F. Chan, and L. A. Vese, "Active contours without edges," *IEEE Transactions on Image Processing*, vol. 10, no. 2, pp. 266-277, 2001.
- [26] C. Xu, and J. L. Prince, "Snakes, shapes, and gradient vector flow," *IEEE Transactions on Image Processing*, vol. 7, no. 3, pp. 359-369, 1998.
- [27] Q. C. Pham, F. Vincent, P. Clarysse *et al.*, "A FEM-based deformable model for the 3D segmentation and tracking of the heart in cardiac MRI," in ISPA, 2001, pp. 250-254.
- [28] M. F. Santarelli, V. Positano, C. Michelassi *et al.*, "Automated cardiac MR image segmentation: theory and measurement evaluation," *Medical Engineering & Physics*, vol. 25, no. 2, pp. 149-59, 2003.
- [29] M. Picq, J. Pousin, and Y. Rouchdy, "A linear 3D elastic segmentation model for vector fields: application to the heart segmentation in MRI," *Journal of Mathematical Imaging and Vision*, vol. 27, no. 3, pp. 241-255, 2007.
- [30] S. Osher, and J. Sethian, "Fronts propagating with curvature-dependent speed- Algorithms based on Hamilton-Jacobi formulations," *Journal of Computational Physics*, vol. 79, no. 1, pp. 12-49, 1988.
- [31] J. A. Sethian, *Level Set Methods and Fast Marching Methods*: Cambridge University Press Cambridge, 1999.
- [32] S. J. Osher, and N. Paragios, *Geometric Level Set Methods in Imaging, Vision, and Graphics*, 2003.
- [33] N. Paragios, "A level set approach for shape-driven segmentation and tracking of the left ventricle," *IEEE Transactions on Medical Imaging*, vol. 22, no. 6, pp. 773-776, 2003.
- [34] K. D. Fritscher, and R. Schubert, "3D image segmentation by using statistical deformation models and level sets," *International Journal of Computer Assisted Radiology and Surgery*, vol. 1, no. 3, pp. 123-135, 2006.
- [35] T. Fukami, H. Sato, JinWu *et al.*, "Quantitative evaluation of myocardial function by a volume-normalized map generated from relative blood flow," *Physics in Medicine and Biology*, vol. 52, pp. 4311-4330, 2007.

- [36] M. Lynch, O. Ghita, and P. F. Whelan, "Left-ventricle myocardium segmentation using a coupled level-set with a priori knowledge," *Computerized Medical Imaging and Graphics*, vol. 30, no. 4, pp. 255-262, 2006.
- [37] C. Pluempitwiriyawej, J. M. F. Moura, Y. J. L. Wu *et al.*, "STACS: New active contour scheme for cardiac MR image segmentation," *IEEE Transactions on Medical Imaging*, vol. 24, no. 5, pp. 593, 2005.
- [38] D. Fritz, D. Rinck, R. Unterhinninghofen *et al.*, "Automatic segmentation of the left ventricle and computation of diagnostic parameters using region growing and a statistical model," in Proceedings of SPIE, 2005, pp. 1844-1854.
- [39] C. A. Cocosco, W. J. Niessen, T. Netsch *et al.*, "Automatic image-driven segmentation of cardiac ventricles in cine anatomical MRI," in Proceedings of SPIE, 2005, pp. 59091M.
- [40] G. Mühlenbruch, M. Das, C. Hohl *et al.*, "Global left ventricular function in cardiac CT. Evaluation of an automated 3D region-growing segmentation algorithm," *European Radiology*, vol. 16, no. 5, pp. 1117-1123, 2006.
- [41] M. Lynch, O. Ghita, and P. F. Whelan, "Automatic segmentation of the left ventricle cavity and myocardium in MRI data," *Computers in Biology and Medicine*, vol. 36, no. 4, pp. 389-407, 2006.
- [42] H. C. van Assen, M. G. Danilouchkine, A. F. Frangi *et al.*, "SPASM: A 3D-ASM for segmentation of sparse and arbitrarily oriented cardiac MRI data," *Medical Image Analysis*, vol. 10, no. 286-303, pp. 1, 2006.
- [43] M. P. Jolly, "Automatic segmentation of the left ventricle in cardiac MR and CT images," *International Journal of Computer Vision*, vol. 70, no. 2, pp. 151-163, 2006.
- [44] A. Pednekar, U. Kurkure, R. Muthupillai *et al.*, "Automated left ventricular segmentation in cardiac MRI," *IEEE Transactions on Biomedical Engineering*, vol. 53, no. 7, pp. 1425-1428, 2006.
- [45] M. Lynch, "Automatic seed initialization for the expectation-maximization algorithm and its application in 3D medical imaging," *Journal of Medical Engineering & Technology*, vol. 31, no. 5, pp. 332-340, 2007.
- [46] K. Van Leemput, F. Maes, D. Vandermeulen *et al.*, "Automated model-based tissue classification of MR images of the brain," *Medical Imaging, IEEE Transactions on*, vol. 18, no. 10, pp. 897-908, 1999.
- [47] Y. Boykov, and V. Kolmogorov, "An experimental comparison of min-cut/max-flow algorithms for energy minimization in vision," *IEEE Transactions on Pattern Analysis and Machine Intelligence*, vol. 26, no. 9, pp. 1124-1137, 2004.
- [48] Y. Boykov, and M. P. Jolly, "Interactive organ segmentation using graph cuts," in MICCAI, 2000, pp. 276-286.
- [49] G. Funka-Lea, Y. Boykov, C. Florin *et al.*, "Automatic heart isolation for CT coronary visualization using graph-cuts" in ISBI, 2006.
- [50] G. Kedenburg, C. A. Cocosco, U. Köthe *et al.*, "Automatic cardiac MRI myocardium segmentation using graphcut," in Proceedings of SPIE, 2006, pp. 61440A.
- [51] T. F. Cootes, C. J. Taylor, D. H. Cooper *et al.*, "Active shape models-their training and application," *Computer Vision and Image Understanding*, vol. 61, no. 1, pp. 38-59, 1995.
- [52] T. F. Cootes, G. J. Edwards, and C. J. Taylor, "Active appearance models," in ECCV, 1998.
- [53] A. Suinesiaputra, M. Uzumcu, A. F. Frangi *et al.*, "Detecting regional abnormal cardiac contraction in short-axis MR images using independent component analysis," in MICCAI, 2004, pp. 68-79.

- [54] S. C. Mitchell, B. P. F. Lelieveldt, R. J. van der Geest *et al.*, “Multistage hybrid active appearance model matching: segmentation of left and right ventricles in cardiac MR images,” *IEEE Transactions on Medical Imaging*, vol. 20, no. 5, pp. 415-423, 2001.
- [55] W. R. Crum, T. Hartkens, and D. L. G. Hill, “Non-rigid image registration: theory and practice,” *British Journal of Radiology*, vol. 77, no. suppl_2, pp. S140, 2004.
- [56] J. B. A. Maintz, and M. A. Viergever, “A survey of medical image registration,” *Medical Image Analysis*, vol. 2, no. 1, pp. 1-36, 1998.
- [57] J. P. W. Pluim, J. B. A. Maintz, and M. A. Viergever, “Mutual-information-based registration of medical images: a survey,” *IEEE Transactions on Medical Imaging*, vol. 22, no. 8, pp. 986-1004, 2003.
- [58] F. Maes, D. Vandermeulen, and P. Suetens, “Medical image registration using mutual information,” in *Proceedings of the IEEE*, 2003, pp. 1699-1722.
- [59] B. Zitová, and J. Flusser, “Image registration methods: a survey,” *Image and Vision Computing*, vol. 21, no. 11, pp. 977-1000, 2003.
- [60] T. Mäkelä, P. Clarysse, O. Sipilä *et al.*, “A review of cardiac image registration methods,” *IEEE Transactions on Medical Imaging*, vol. 21, no. 9, pp. 1011, 2002.
- [61] M. Sermesant, C. Forest, X. Pennec *et al.*, “Deformable biomechanical models: Application to 4D cardiac image analysis,” *Medical Image Analysis*, vol. 7, no. 4, pp. 475-488, 2003.
- [62] O. Camara, G. Delso, and I. Bloch, “Free form deformations guided by gradient vector flow: a surface registration method in thoracic and abdominal PET-CT applications,” in *WBIR*, 2003, pp. 224–33.
- [63] H. Chui, A. Rangarajan, J. Zhang *et al.*, “Unsupervised learning of an Atlas from unlabeled point-sets,” *IEEE Transactions on Pattern Analysis and Machine Intelligence*, vol. 26, no. 2, pp. 160-172, 2004.
- [64] A. F. Frangi, D. Rueckert, J. A. Schnabel *et al.*, “Automatic construction of multiple-object three-dimensional statistical shape models: application to cardiac modeling,” *IEEE Transactions on Medical Imaging*, vol. 21, no. 9, pp. 1151-1166, 2002.
- [65] M. Lorenzo-Valdes, G. I. Sanchez-Ortiz, R. Mohiaddin *et al.*, “Atlas-based segmentation and tracking of 3D cardiac MR images using non-rigid registration,” in *MICCAI*, 2002, pp. 642–650.
- [66] D. Perperidis, M. Lorenzo-Valdes, R. Chandrashekhara *et al.*, “Building a 4D atlas of the cardiac anatomy and motion using MR imaging,” in *ISBI*, 2004, pp. 412-415.
- [67] D. Perperidis, R. Mohiaddin, and D. Rueckert, “Spatio-temporal free-form registration of cardiac MR image sequences,” *Medical Image Analysis*, vol. 9, no. 5, pp. 441-456, 2005.
- [68] D. Perperidis, “Spatio-temporal registration and modelling of the heart using cardiovascular MR imaging,” Imperial College, 2005.
- [69] P. A. Yushkevich, J. Piven, H. C. Hazlett *et al.*, “User-guided 3D active contour segmentation of anatomical structures: Significantly improved efficiency and reliability,” *Neuroimage*, vol. 31, no. 3, pp. 1116-28, 2006.
- [70] V. Duay, N. Houhou, and J. P. Thiran, “Atlas-based segmentation of medical images locally constrained by level sets,” in *ICIP*, 2005.
- [71] B. C. Vemuri, J. Ye, Y. Chen *et al.*, “Image registration via level-set motion: Applications to atlas-based segmentation,” *Medical Image Analysis*, vol. 7, no. 1, pp. 1-20, 2003.
- [72] O. Musse, F. Heitz, and J. P. Armspach, “Fast deformable matching of 3D images over multiscale nested subspaces. Application to atlas-based MRI segmentation,” *Pattern Recognition*, vol. 36, no. 8, pp. 1881-1899, 2003.

- [73] M. R. Kaus, J. von Berg, J. Weese *et al.*, “Automated segmentation of the left ventricle in cardiac MRI,” *Medical Image Analysis*, vol. 8, no. 3, pp. 245-254, 2004.
- [74] A. Montillo, D. Metaxas, and L. Axel, “Automated segmentation of the left and right ventricles in 4D cardiac SPAMM Images,” in MICCAI, 2002, pp. 620–633.
- [75] L. Spreeuwens, and M. Breeuwer, “Automatic detection of the myocardial boundaries of the right and left ventricle in MR cardio perfusion scans,” in Proceedings of SPIE, 2001, pp. 1207-1217.
- [76] M. G. Danilouchkine, J. J. M. Westenberg, B. P. F. Lelieveldt *et al.*, “Accuracy of short-axis cardiac MRI automatically derived from scout acquisitions in free-breathing and breath-holding modes,” *Magnetic Resonance Materials in Physics, Biology and Medicine*, vol. 18, no. 1, pp. 7-18, 2005.
- [77] C. E. Jackson, M. D. Robson, J. M. Francis *et al.*, “Computerised planning of the acquisition of cardiac MR images,” *Computerized Medical Imaging and Graphics*, vol. 28, no. 7, pp. 411-418, 2004.
- [78] A. A. Young, B. R. Cowan, S. F. Thrupp *et al.*, “Left ventricular mass and volume: fast calculation with guide-point modeling on MR images,” *Radiology*, vol. 216, no. 2, pp. 597-602, 2000.
- [79] B. M. Dawant, S. L. Hartmann, J. P. Thirion *et al.*, “Automatic 3-D segmentation of internal structures of the head in MR images using a combination of similarity and free-form transformations. I. Methodology and validation on normal subjects,” *IEEE Transactions on Medical Imaging*, vol. 18, no. 10, pp. 909-916, 1999.
- [80] T. Rohlfing, R. Brandt, R. Menzel *et al.*, “Evaluation of atlas selection strategies for atlas-based image segmentation with application to confocal microscopy images of bee brains,” *NeuroImage*, vol. 21, no. 4, pp. 1428–1442, 2004.
- [81] B. J. Wintersperger, S. Sinclair, V. M. Runge *et al.*, “Dual breath-hold magnetic resonance cine evaluation of global and regional cardiac function,” *European Radiology*, vol. 17, no. 1, pp. 73-80, 2007.
- [82] A. Frangi, W. Niessen, M. Viergever *et al.*, "A survey of three-dimensional modeling techniques for quantitative functional analysis of cardiac images," *Advanced Image Processing in Magnetic Resonance Imaging*, L. Landini, V. Positano and M. F. Santarelli, eds.: Taylor & Francis, 2005.
- [83] E. W. Remme, K. F. Augenstein, A. A. Young *et al.*, “Parameter distribution models for estimation of population based left ventricular deformation using sparse fiducial markers,” *IEEE Transactions on Medical Imaging*, vol. 24, no. 3, pp. 381-388, 2005.
- [84] V. Kolmogorov, “Graph based algorithms for scene reconstruction from two or more views,” Cornell University, 2004.
- [85] C. Rother, V. Kolmogorov, and A. Blake, “" GrabCut": interactive foreground extraction using iterated graph cuts,” *ACM Transactions on Graphics*, vol. 23, no. 3, pp. 309-314, 2004.
- [86] E. Dahlhaus, D. S. Johnson, C. H. Papadimitriou *et al.*, “The complexity of multiway cuts (extended abstract),” in STOC, 1992, pp. 241-251.
- [87] K. K. Bhatia, J. V. Hajnal, B. K. Puri *et al.*, “Consistent groupwise non-rigid registration for atlas construction,” in ISBI, 2004, pp. 908-911.
- [88] P. Y. Bondiau, G. Malandain, S. Chanalet *et al.*, “Atlas-based automatic segmentation of MR images: Validation study on the brainstem in radiotherapy context,” *International Journal of Radiation Oncology, Biology, Physics*, vol. 61, no. 1, pp. 289-298, 2005.
- [89] O. T. Carmichael, H. A. Aizenstein, S. W. Davis *et al.*, “Atlas-based hippocampus segmentation in Alzheimer’s disease and mild cognitive impairment,” *NeuroImage*, vol. 27, no. 4, pp. 979–990, 2005.

- [90] M. Wu, C. Rosano, P. Lopez-Garcia *et al.*, "Optimum template selection for atlas-based segmentation," *NeuroImage*, vol. 34, no. 4, pp. 1612-1618, 2007.
- [91] N. Tzourio-Mazoyer, B. Landeau, D. Papathanassiou *et al.*, "Automated anatomical labeling of activations in SPM using a macroscopic anatomical parcellation of the MNI MRI single-subject brain," *NeuroImage*, vol. 15, pp. 273-289, 2002.
- [92] D. Rueckert, A. F. Frangi, and J. A. Schnabel, "Automatic construction of 3-D statistical deformation models of the brain using nonrigid registration," *IEEE Transactions on Medical Imaging*, vol. 22, no. 8, pp. 1014-1025, 2003.
- [93] T. Rohlfing, R. Brandt, R. Menzel *et al.*, "Quo vadis, atlas-based segmentation?," *The handbook of medical image analysis: segmentation and registration models*, J. Suri, D. L. Wilson and S. Laxminarayan, eds.: Kluwer, 2005.
- [94] P. Lorenzen, M. Prastawa, B. Davis *et al.*, "Multi-modal image set registration and atlas formation," *Medical Image Analysis*, vol. 10, no. 3, pp. 440-451, 2006.
- [95] S. Joshi, B. Davis, M. Jomier *et al.*, "Unbiased diffeomorphic atlas construction for computational anatomy," *NeuroImage*, vol. 23, no. Supplement 1, pp. S151-S160, 2004.
- [96] E. D'Agostino, F. Maes, D. Vandermeulen *et al.*, "Non-rigid atlas-to-image registration by minimization of class-conditional image entropy," in MICCAI, 2004, pp. 745-753.
- [97] E. D'Agostino, F. Maes, D. Vandermeulen *et al.*, "An information theoretic approach for non-rigid image registration using voxel class probabilities," *Medical Image Analysis*, vol. 10, no. 3, pp. 413-431, 2006.
- [98] M. B. Cuadra, C. Pollo, A. Bardera *et al.*, "Atlas-based segmentation of pathological MR brain images using a model of lesion growth," *IEEE Transactions on Medical Imaging*, vol. 23, no. 10, pp. 1301-1314, 2004.
- [99] M. B. Cuadra, M. De Craene, V. Duay *et al.*, "Dense deformation field estimation for atlas-based segmentation of pathological MR brain images," *Computer Methods and Programs in Biomedicine*, vol. 84, no. 2-3, pp. 66-75, 2006.
- [100] H. M. Chan, A. C. S. Chung, S. C. H. Yu *et al.*, "2D-3D vascular registration between digital subtraction angiographic (DSA) and magnetic resonance angiographic (MRA) images," in ISBI, 2004, pp. 708-711.
- [101] R. M. Lapp, M. Lorenzo-Valdes, and D. Rueckert, "3D/4D cardiac segmentation using active appearance models, non-rigid registration, and the insight toolkit," in MICCAI, 2004, pp. 419-426.
- [102] J. Lotjonen, S. Kivisto, J. Koikkalainen *et al.*, "Statistical shape model of atria, ventricles and epicardium from short-and long-axis MR images," *Medical Image Analysis*, vol. 8, no. 3, pp. 371-386, 2004.
- [103] J. Lotjonen, J. Koikkalainen, D. Smutek *et al.*, "Four-chamber 3-D statistical shape model from cardiac short-axis and long-axis MR images," in MICCAI, 2003, pp. 459-466.
- [104] A. Rao, G. I. Sanchez-Ortiz, R. Chandrashekhara *et al.*, "Construction of a cardiac motion atlas from MR using non-rigid registration," in FIMH, 2003, pp. 141-50.
- [105] A. F. Frangi, D. Rueckert, J. A. Schnabel *et al.*, "Automatic 3D ASM construction via atlas-based landmarking and volumetric elastic registration," *Information Processing in Medical Imaging*, vol. 2082, pp. 78-91, 2001.
- [106] L. Zhang, E. A. Hoffman, and J. M. Reinhardt, "Atlas-driven lung lobe segmentation in volumetric X-ray CT images," *IEEE Transactions on Medical Imaging*, vol. 25, no. 1, pp. 1-16, 2006.

- [107] J. H. Hipwell, G. P. Penney, T. C. Cox *et al.*, “2D-3D intensity based registration of DSA and MRA - a comparison of similarity measures,” in MICCAI, 2002, pp. 501–508.
- [108] L. Barnden, R. Kwiatek, Y. Lau *et al.*, “Validation of fully automatic brain SPET to MR co-registration,” *European Journal of Nuclear Medicine and Molecular Imaging*, vol. 27, no. 2, pp. 147-154, 2000.
- [109] M. Holden, D. L. G. Hill, E. R. E. Denton *et al.*, “Voxel similarity measures for 3-D serial MR brain image registration,” *IEEE Transactions on Medical Imaging*, vol. 19, no. 2, pp. 94-102, 2000.
- [110] A. Carrillo, J. L. Duerk, J. S. Lewin *et al.*, “Semiautomatic 3-D image registration as applied to interventional MRI liver cancer treatment,” *IEEE Transactions on Medical Imaging*, vol. 19, no. 3, pp. 175-185, 2000.
- [111] S. Clippe, D. Sarrut, C. Malet *et al.*, “Patient setup error measurement using 3D intensity-based image registration techniques,” *International Journal of Radiation Oncology, Biology, Physics*, vol. 56, no. 1, pp. 259-265, 2003.
- [112] N. Williams, K. L. Low, C. Hantak *et al.*, “Automatic image alignment for 3D environment modeling,” in SIBGRAPI, 2004, pp. 388-395.
- [113] M. Jenkinson, and S. Smith, “A global optimization method for robust affine registration of brain images. Medical Image Analysis,” *Medical Image Analysis*, vol. 5, pp. 143-156, 2001.
- [114] N. Wiest-Daessle, P. Yger, S. Prima *et al.*, “Evaluation of a new optimisation algorithm for rigid registration of MRI data,” in Proceedings of SPIE Medical Imaging, 2007.
- [115] J. P. W. Pluim, J. B. A. Maintz, and M. A. Viergever, “Image registration by maximization of combined mutual information and gradient information,” *IEEE Transactions on Medical Imaging*, vol. 19, no. 8, pp. 809-814, 2000.
- [116] D. Škerl, B. Likar, and F. Pernus, “A protocol for evaluation of similarity measures for rigid registration,” *IEEE Transactions on Medical Imaging*, vol. 25, no. 6, pp. 779, 2006.
- [117] D. Škerl, B. Likar, and F. Pernuš, “Evaluation of similarity measures for non-rigid registration,” in WBIR, 2006, pp. 160-168.
- [118] P. Aljabar, R. Heckemann, A. Hammers *et al.*, “Classifier Selection Strategies for Label Fusion Using Large Atlas Databases.” pp. 523–531.
- [119] M. Wierzbicki, M. Drangova, G. Guiraudon *et al.*, “Mapping template heart models to patient data using image registration,” in MICCAI, 2004.
- [120] A. Roche, G. Malandain, X. Pennec *et al.*, “The correlation ratio as a new similarity measure for multimodal image registration,” in MICCAI, 1998, pp. 1115-1124.
- [121] Y. H. Lau, M. Braun, and B. F. Hutton, “Non-rigid image registration using a median-filtered coarse-to-fine displacement field and a symmetric correlation ratio,” *Physics in Medicine and Biology*, vol. 46, no. 4, pp. 1297–1319, 2001.
- [122] C. Grova, P. Jannin, I. Buvat *et al.*, “Evaluation of registration of ictal SPECT/MRI data using statistical similarity methods,” in MICCAI, 2004, pp. 687–695.
- [123] S. Kabus, T. Netsch, B. Fischer *et al.*, “B-spline registration of 3D images with Levenberg-Marquardt optimization,” in Proceedings of SPIE Medical Imaging, 2004, pp. 304–313.
- [124] A. Leroy, P. Mozer, Y. Payan *et al.*, “Rigid Registration of Freehand 3D Ultrasound and CT-Scan Kidney Images,” in MICCAI, 2004, pp. 837-844.
- [125] F. Rousseau, A. Maudsley, A. Ebel *et al.*, “Evaluation of sub-voxel registration accuracy between MRI and 3 D MR spectroscopy of the brain,” in Proceedings of SPIE, 2005, pp. 1213-1221.

- [126] R. P. Woods, J. C. Mazziotta, and S. R. Cherry, "MRI-PET registration with automated algorithm," *Journal of Computer Assisted Tomography*, vol. 17, no. 4, pp. 536-46, 1993.
- [127] C. Studholme, D. L. G. Hill, and D. J. Hawkes, "An overlap invariant entropy measure of 3D medical image alignment," *Pattern Recognition*, vol. 32, no. 1, pp. 71-86, 1999.
- [128] F. Maes, "Segmentation and registration of multimodal medical images: From theory, implementation and validation to a useful tool in clinical practice," Phd, Catholic University of Leuven, Leuven, Belgium, 1998.
- [129] A. Collignon, F. Maes, D. Delaere *et al.*, "Automated multi-modality image registration based on information theory," *Information Processing in Medical Imaging*, vol. 14, no. 6, pp. 263, 1995.
- [130] F. Maes, A. Collignon, D. Vandermeulen *et al.*, "Multimodality image registration by maximization of mutual information," *IEEE Transactions on Medical Imaging*, vol. 16, no. 2, pp. 187-198, 1997.
- [131] J. P. W. Pluim, J. B. A. Maintz, and M. A. Viergever, "Interpolation artefacts in mutual information-based image registration," *Computer Vision and Image Understanding*, vol. 77, no. 2, pp. 211-232, 2000.
- [132] H. M. Chen, P. K. Varshney, and M. K. Arora, "Performance of mutual information similarity measure for registration of multitemporal remote sensing images," *IEEE Transactions on Geoscience and Remote Sensing*, vol. 41, no. 11, pp. 2445-2454, 2003.
- [133] N. Otsu, "A threshold selection method from gray level," *IEEE Transactions on Systems, Man, and Cybernetics*, vol. 9, no. 1, pp. 62-66, 1979.
- [134] A. A. Young, P. J. Hunter, and B. H. Smaill, "Epicardial surface estimation from coronary angiograms," *Computer Vision, Graphics, and Image Processing*, vol. 47, no. 1, pp. 111-127, 1989.
- [135] J. W. Fernandez, and P. J. Hunter, "An anatomically based finite element model of patella articulation: towards a diagnostic tool," Bioengineering Institute, University of Auckland, 2004.
- [136] C. P. Bradley, A. J. Pullan, and P. J. Hunter, "Geometric modeling of the human torso using cubic hermite elements," *Annals of Biomedical Engineering*, vol. 25, no. 1, pp. 96-111, 1997.
- [137] W. H. Press, B. P. Flannery, S. A. Teukolsky *et al.*, *Numerical Recipes in C: the art of scientific computing*, 2 ed.: Cambridge University Press, 1992.
- [138] J. Cizek, K. Herholz, S. Vollmar *et al.*, "Fast and robust registration of PET and MR images of human brain," *Neuroimage*, vol. 22, no. 1, pp. 434-42, 2004.
- [139] P. Hellier, and C. Barillot, "Coupling dense and landmark-based approaches for nonrigid registration," *IEEE Transactions on Medical Imaging*, vol. 22, no. 2, pp. 217-227, 2003.
- [140] P. Hellier, C. Barillot, E. Memin *et al.*, "Hierarchical estimation of a dense deformation field for 3-D robust registration," *IEEE Transactions on Medical Imaging*, vol. 20, no. 5, pp. 388-402, 2001.
- [141] C. Studholme, D. L. G. Hill, and D. J. Hawkes, "Automated three-dimensional registration of magnetic resonance and positron emission tomography brain images by multiresolution optimization of voxel similarity measures," *Medical Physics*, vol. 24, pp. 25, 1997.
- [142] P. Brigger, F. Muller, K. Illgner *et al.*, "Centered pyramids," *IEEE Transactions on Image Processing*, vol. 8, no. 9, pp. 1254-1264, 1999.

- [143] C. E. Barbier, "The exactness of left ventricular segmentation in cine magnetic resonance imaging and its impact on systolic function values," *Acta Radiologica*, vol. 48, no. 3, pp. 285-291, 2007.
- [144] B. Sievers, S. Kirchberg, A. Bakan *et al.*, "Impact of papillary muscles in ventricular volume and ejection fraction assessment by cardiovascular magnetic resonance," *Journal of Cardiovascular Magnetic Resonance*, vol. 6:1, pp. 9 - 16, 2004.
- [145] D. Nguyen, K. Masterson, and J. P. Vallée, "Comparative evaluation of active contour model extensions for automated cardiac MR image segmentation by regional error assessment," *Magnetic Resonance Materials in Physics, Biology and Medicine*, vol. 20, no. 2, pp. 69-82, 2007.
- [146] Y. Rouchdy, J. Pousin, J. Schaerer *et al.*, "A nonlinear elastic deformable template for soft structure segmentation: application to the heart segmentation in MRI," *Inverse Problems*, vol. 23, no. 3, pp. 1017-1035, 2007.
- [147] X. Huang, D. Metaxas, and T. Chen, "MetaMorphs: Deformable shape and texture models," in CVPR, 2004.
- [148] R. J. van der Geest, B. P. F. Lelieveldt, E. Angelié *et al.*, "Evaluation of a new method for automated detection of left ventricular boundaries in time series of magnetic resonance images using an Active Appearance Motion Model," *Journal of Cardiovascular Magnetic Resonance*, vol. 6, no. 3, pp. 609-617, 2004.
- [149] D. Rueckert, L. I. Sonoda, C. Hayes *et al.*, "Nonrigid registration using free-form deformations: application to breast MR images," *IEEE Transactions on Medical Imaging*, vol. 18, no. 8, pp. 712-721, 1999.
- [150] P. J. Besl, and H. D. McKay, "A method for registration of 3-D shapes," *IEEE Transactions on Pattern Analysis and Machine Intelligence*, vol. 14, no. 2, pp. 239-256, 1992.
- [151] W. J. Hedley, "Finite element modelling of the left ventricle using magnetic resonance image data," Department of Engineering Science, University of Auckland, Auckland, 1998.
- [152] J. Lotjonen, D. Smutek, S. Kivisto *et al.*, "Tracking atria and ventricles simultaneously from cardiac short-and long-axis MR images," in MICCAI, 2003, pp. 440-450.
- [153] J. v. Berg, and C. Lorenz, "Multi-surface cardiac modelling, segmentation, and tracking," in FIMH, 2005.
- [154] O. Ecabert, J. Peters, M. J. Walker *et al.*, "Automatic whole heart segmentation in CT images: method and validation," in Proceedings of SPIE, 2007, pp. 65120G.